Experimental approaches toward the deposition of SCMs on surface

Félix Houard

▶ **To cite this version:**

Félix Houard. Experimental approaches toward the deposition of SCMs on surface. Inorganic chemistry. INSA de Rennes, 2021. English. NNT : 2021ISAR0021 . tel-04457235

HAL Id: tel-04457235
https://theses.hal.science/tel-04457235

Submitted on 14 Feb 2024

HAL is a multi-disciplinary open access archive for the deposit and dissemination of scientific research documents, whether they are published or not. The documents may come from teaching and research institutions in France or abroad, or from public or private research centers.

L'archive ouverte pluridisciplinaire **HAL**, est destinée au dépôt et à la diffusion de documents scientifiques de niveau recherche, publiés ou non, émanant des établissements d'enseignement et de recherche français ou étrangers, des laboratoires publics ou privés.

DOCTORAT MATIERE BRETAGNE MOLECULES LOIRE ET MATERIAUX

INSA RENNES

THESE DE DOCTORAT DE

L'INSTITUT NATIONAL DES SCIENCES APPLIQUEES RENNES

ECOLE DOCTORALE N° 596
Matière, Molécules, Matériaux
Spécialité : *Chimie Inorganique*

Par

Félix HOUARD

« Experimental approaches toward the deposition of SCMs on surface »

Thèse présentée et soutenue à l'INSA Rennes, le 6 Décembre 2021
Unité de recherche : Institut des Sciences Chimiques de Rennes (UMR 6226)
Thèse N° : 21ISAR 31 / D21 - 31

Composition du Jury :

Présidente :	Maryline GUILLOUX-VIRY	Professeur des Universités – Université de Rennes 1, France
Rapporteurs :	Marius ANDRUH	Professeur – Universitatea din Bucuresti, Romania
	Guillem AROMÍ	Professeur – Universitat de Barcelona, Spain
Examinatrices :	Valérie MARVAUD	Directrice de Recherche CNRS – Sorbonne Université, France
	Céline PICHON	Chargée de Recherche CNRS – Université de Toulouse, France
Directeur de thèse :	Kévin BERNOT	Professeur des Universités – INSA Rennes, France
Co-directeur de thèse :	Matteo MANNINI	Professeur – Università degli studi di Firenze, Italy

“ The most exciting phrase to hear in science,
the one that heralds new discoveries,
is not 'Eureka!' but 'That's funny...' ”
Isaac Asimov

Acknowledgements

Au moment d'arriver à la conclusion de ces trois années de thèse, l'un des points les plus importants, ou du moins celui dont je me souviendrai le plus, est que la recherche expérimentale est avant tout un effort collectif. Ainsi, les travaux présentés dans les pages qui suivront sont le fait de la contribution de plusieurs personnes aux expertises et personnalités diverses, sans qui cette thèse n'aurait pas pu aboutir.

Tout d'abord, mon directeur de thèse Dr. Kévin Bernot. Doté d'une patience inégalée pour répondre à mes questions les plus évidentes, sa disponibilité et sa positivité m'auront encouragé à mener ces travaux du mieux possible, et ceux au quotidien depuis maintenant trois ans. Son enthousiasme et son ouverture scientifique auront été au final contagieux, ce qui nous aura poussés à nous aventurer dans un domaine que nous n'aurions pas envisagé (« Et il se passe quoi si on met ces gels dans un SQUID ? »).

Je voudrais également remercier mon co-directeur de thèse, Dr. Matteo Mannini, pour nous avoir accueillis dans les meilleures conditions au Laboratorio di Magnetismo Molecolare de Florence, pour ses précieux conseils quant aux mesures de surface et aux meilleures adresses pour trouver un bon *Negroni* !

Je voudrais aussi exprimer ma reconnaissance envers mes collègues du laboratoire CSM de l'INSA, qui nous permettent à nous, les doctorants, de pouvoir travailler dans les meilleures conditions et de faire de la belle science malgré notre petit effectif : les chefs du labo toujours disponibles, Prof. Olivier Guillou et Dr. Carole Daiguebonne; Dr. Guillaume Calvez et Dr. Yan Suffren, qui nous ferait presque penser que les mesures de luminescences sont simples de par leur expertise en spectroscopie ; Dr Christophe Lescop et Dr Nathalie Audebrand pour leur bonne humeur communicative ; Isabelle Morlais pour toute l'aide administrative (ce qui est loin d'être une mince affaire dans notre beau pays !) ; et Stéphane Freslon, sans qui je pense les trois-quarts du labo seraient en ruine à l'heure qu'il est !

Un grand merci aux doctorants et post-docs avec qui j'ai pu passer des bons moments, que ce soit au labo, en conférence ou en ville autour d'une bière ; Ahmad, Ali, Amandine, Chendong, Chloé, Constance, Falou, Florent, Haiyun, Jana, Jinzeng, Roza, Valérie, Youenn… Mention spéciale à Quentin, le « vieux monsieur » qui m'a aidé au tout début de ma thèse, et qui m'a permis de découvrir cette rude épreuve qu'est la *bistecca alla fiorentina* !

À ce titre, je remercie également Guiseppe Cucinotta pour m'avoir suivi et guidé pour les mesures AFM : regarder les lignes de pixels apparaitre du haut en bas de l'écran n'était peut-être pas le plus divertissant, mais on aura quand même réussi à faire quelques clichés qui valent le coup ! Merci aussi à Fabio de m'avoir fait une place dans son labo, Andrea pour m'avoir conseillé lors de mon arrivée à Florence, et Ivan qui m'a fait découvrir les Abruzzi au travers de conversations sur le balcon à grand coup de Montepulciano !

Un grand merci aux collègues du groupe de Chimie Théorique Inorganique, Dr. Boris le Guennic et Dr. Frédéric Gendron, qui ont bien voulu passer du temps sur des systèmes loin d'être triviaux.

Aux collègues du CDiFX, Dr. Thierry Roisnel, Dr. Vincent Dorcet et Dr. Marie Dallon-Cordier, pour avoir fait les mesures de diffractions sur mono-cristaux et nous avoir aidé sur la résolution de certaines structures assez complexes.

Au Prof. Olivier Cador et à Thierry Guizouarn également, pour nous avoir aidés sur les mesures magnétiques, ce qui est le cœur de ce travail de thèse.

Au Dr. Franck Artzner pour sa connaissance des gels et son expertise en SAXS, sans qui la partie finale de ce manuscrit aurait été beaucoup moins intéressante.

Je souhaitais également remercier mes anciens professeurs de l'ENSCR de l'ENSCBP, qui m'ont à la fois donné le goût pour la recherche, mais aussi les clés pour en faire sérieusement.

Pour finir, je remercie chaleureusement tous les membres de mon entourage : mes parents, mes frères, mes amis et mes colocs, pour m'avoir supporté, encouragé et soutenu dans cette belle aventure ; ce travail est aussi le vôtre.

Table of contents

Symbols and abbreviations

Symbols

$\boldsymbol{\mu}$	Magnetic moment
$\boldsymbol{\mu_B}$	Bohr magneton
$\boldsymbol{L}$	Angular momentum
$\boldsymbol{S}$	Spin angular momentum
$\boldsymbol{J}$	Total angular momentum
Ln	Lanthanides
$\boldsymbol{H}$	External magnetic field
$\boldsymbol{M}$	Magnetisation
$\boldsymbol{\chi}$	Magnetic susceptibility
$\boldsymbol{\chi_M}$	Molar magnetic susceptibility
$\boldsymbol{\chi'}$	In-phase (primary) magnetic susceptibility
$\boldsymbol{\chi''}$	Out-of-phase (secondary) magnetic susceptibility
$\boldsymbol{\chi_M}$	Molar magnetic susceptibility
$\boldsymbol{\chi_g}$	Mass magnetic susceptibility
$\boldsymbol{C}$	Curie constant
$\boldsymbol{T_C}$	Curie temperature
$\boldsymbol{\theta}$	Weiss temperature
$\boldsymbol{\mathcal{H}}$	Hamiltonian operator
$\boldsymbol{g}$	g-factor
$\boldsymbol{a_n}$	Hyperfine coupling constant
$\boldsymbol{D}$	Zero-Field Splitting constant
$\boldsymbol{J_{ex}}$	Exchange interaction
$\boldsymbol{M_R}$	Remanent magnetisation
$\boldsymbol{H_C}$	Coercive field
Oe	Oersted
$\boldsymbol{\tau}$	Characteristic relaxation time
$\boldsymbol{\nu}$	Frequency
$\boldsymbol{U_{eff}}$	Effective energy barrier (for SMMs)
$\boldsymbol{\Delta_{eff}}$	Effective energy barrier (for SCMs)
$\boldsymbol{\Delta_\xi}$	Domain wall energy barrier
$\boldsymbol{\Delta_A}$	Anisotropic energy barrier
$\boldsymbol{\Delta_F}$	Finite-size regime energy barrier
$\boldsymbol{\Delta_I}$	Infinite-size regime barrier

Abbreviations

AFM	Antiferromagnetism or Atomic Force Microscopy
EDS	Energy-Dispersive X-ray spectroscopy
emu	Electromagnetic Unit
EPR	Electron Paramagnetic Resonance
ES	Excited State
FM	Ferromagnetism
FTIR	Fourier-Transform Infrared Spectroscopy
GOF	Goodness Of Fit
GS	Ground State
QTM	Quantum Tunnelling of Magnetisation
MPMS	Magnetic Property Measuring System
NIT	Nitronyl Nitroxide radical
NN	Nearest Neighbour
NNN	Next-Nearest Neighbour
SAXS	Small-Angle X-ray Scattering
SCM	Single-Chain Magnet
SEM	Scanning Electron Microscopy
SMM	Single-Molecule Magnet
SQUID	Superconducting Quantum Interference Device
TDA	Thermodifferential Analysis
TGA	Thermogravimetric Analysis
XRD	X-Ray Diffraction
ZFS	Zero-Field Splitting

Introduction

With the multiplication of data generated by human activities (digitalisation of the industry, democratisation of Internet, cloud-computing and big data), the problem of storing this data on physical media arises.[1,2] One of the limits of current technologies lies in the storage density, dictated by the size of the magnetic domains used to encode the bits. Therefore, it would be sufficient to reduce the size of these domains to increase the storage capacity of these hard disk drive (HDDs). However, this approach of nanometrisation ("top-down") comes up against the limits of superparamagnetism.[3] Below a certain critical volume, the energy barrier limiting the transition from one magnetic moment to another (or magnetisation reversal) becomes comparable to thermal energy, the magnetic particles can no longer retain their magnetisation, and information storage becomes impossible.

One of the strategies adopted to obtain nanometric magnets is the reverse approach: synthesise molecular edifices from magnetic metal ions (3*d* and/or 4*f* elements) judiciously coordinated with organic ligands to enhance their magnetic performances. This "bottom-up" approach is the basis of a field of coordination chemistry, namely molecular magnetism.

Thus, many Single-Molecule Magnets (SMMs) have been synthesised over the last 30 years, exhibiting phenomena of slow relaxation of their magnetisation at low temperatures.[4] This lead in some cases to the observation of magnetic hysteresis, a mandatory point for information storage.[5] Advances in understanding these phenomena have made it possible to synthesise more efficient SMMs, which have magnetisation blocking temperatures close to liquid nitrogen.[6–9] In addition, numerous phenomena of quantum origin have also been demonstrated, opening the way to potential applications in spintronics.[10–13]

In parallel to SMMs, one-dimensional magnetic coordination polymers, called Single-Chain Magnets (SCMs),[14–16] have also been synthesised. These magnetic chains are characterised by alternating strongly anisotropic magnetic centres linked together by organic molecules. A correlation phenomenon will be established between the spin carriers at low temperatures, leading to spontaneous magnetisation. The advantage of such chains is that, in addition to allowing remanent magnetisation, they are less subject to the "parasitic" relaxation phenomena present in SMMs (especially quantum tunnelling of the magnetisation).

One of the limiting key points identified for industrial applications is the deposition of these molecules on physical support. Indeed, if the properties of these molecules were first measured on crystals and powders (bulk), what about the properties of an isolated magnet-molecule on a surface? Are there any new phenomena due to interactions with the surface?

Several methods have already been implemented for SMMs,[17–20] such as deposition by sublimation or chemical grafting by functionalisation, with their advantages and limits while.

However, no feasible strategies have been developed yet for SCMs, which will be the goal of this thesis; the synthesis of a new family of SCMs and their deposition on surfaces. Based

on previous work in our laboratory, the systems studied will be composed of lanthanides centres linked by nitronyl nitroxide (NIT) ligands.[21] The use of lanthanide ions is motivated by their strong magnetic anisotropy, inherent to their 4*f* orbitals, which is essential for synthesising effective molecular magnets.[22] They will be associated with nitronyl nitroxide radicals, which are bridging radicals, stable and easily to be functionalised.[23]

In Chapter 1, we will briefly introduce main notions of molecular magnetism relevant to the understanding of this thesis. This will be followed by a brief state of the art of low-dimensional molecular magnets (SMMs and SCMs), their magnetic properties and the synthetic strategies employed.

In Chapter 2, we will investigate the deposition on surface of a, archetypal SCM compound selected from the literature by a conventional method.

In Chapter 3, based on the observations of Chapter 2, we will design and synthesise a new nitronyl nitroxide ligand and its corresponding coordination polymer. Its supramolecular structure and magnetic properties will be carefully investigated.

Starting from the same building blocks as for this SCM, a new finite compound has been isolated and characterised in Chapter 4. The impact of this change in morphology will be investigated by comparing the magnetic properties of these two compounds.

Finally, in Chapter 5, we will take a closer look at the influence of the size of the aliphatic chain of the NIT ligand and we will show the resulting chains can be treated to promote their gelification. These coordination gels will be characterised by magnetic measurements and specific soft matter techniques to determine their supramolecular organisation and their deposition on surface will be demonstrated.[a]

[a] If not stated otherwise, syntheses and characterisations presented in this manuscript have been performed by the author.

References

[1] D. A. Thompson, J. S. Best, *IBM J. Res. Dev.* **2000**, *44*, 311–322.
[2] M. Hilbert, P. Lopez, *Science* **2011**, *332*, 60–65.
[3] L. Néel, *J. Phys. Radium* **1950**, *11*, 49–61.
[4] J. Tang, P. Zhang, in *Lanthan. Single Mol. Magn.*, Springer Berlin Heidelberg, Berlin, Heidelberg, **2015**, pp. 1–39.
[5] R. Sessoli, D. Gatteschi, A. Caneschi, M. A. Novak, *Nature* **1993**, *365*, 141–143.
[6] C. J. Milios, A. Vinslava, W. Wernsdorfer, S. Moggach, S. Parsons, S. P. Perlepes, G. Christou, E. K. Brechin, *J. Am. Chem. Soc.* **2007**, *129*, 2754–2755.
[7] P.-H. Lin, T. J. Burchell, L. Ungur, L. F. Chibotaru, W. Wernsdorfer, M. Murugesu, *Angew. Chem. Int. Ed.* **2009**, *48*, 9489–9492.
[8] C. A. P. Goodwin, F. Ortu, D. Reta, N. F. Chilton, D. P. Mills, *Nature* **2017**, *548*, 439–442.
[9] F.-S. Guo, B. M. Day, Y.-C. Chen, M.-L. Tong, A. Mansikkamäki, R. A. Layfield, *Science* **2018**, *362*, 1400–1403.
[10] L. Bogani, W. Wernsdorfer, *Nat. Mater.* **2008**, *7*, 179–186.
[11] S. Jiang, K. Goß, C. Cervetti, L. Bogani, *Sci. China Chem.* **2012**, *55*, 867–882.
[12] L. Bogani, in *Mol. Nanomagnets Relat. Phenom.* (Ed.: S. Gao), Springer Berlin Heidelberg, Berlin, Heidelberg, **2014**, pp. 331–381.
[13] G. Aromí, O. Roubeau, in *Handb. Phys. Chem. Rare Earths*, Elsevier, **2019**, pp. 1–54.
[14] C. Coulon, H. Miyasaka, R. Clérac, in *Single-Mol. Magn. Relat. Phenom.* (Ed.: R. Winpenny), Springer Berlin Heidelberg, Berlin, Heidelberg, **2006**, pp. 163–206.
[15] C. Coulon, V. Pianet, M. Urdampilleta, R. Clérac, in *Mol. Nanomagnets Relat. Phenom.* (Ed.: S. Gao), Springer Berlin Heidelberg, Berlin, Heidelberg, **2014**, pp. 143–184.
[16] K. Katoh, K. Kagesawa, M. Yamashita, in *World Sci. Ref. Spin Org.*, World Scientific, **2017**, pp. 271–344.
[17] D. Gatteschi, A. Cornia, M. Mannini, R. Sessoli, *Inorg. Chem.* **2009**, *48*, 3408–3419.
[18] A. Cornia, M. Mannini, P. Sainctavit, R. Sessoli, *Chem. Soc. Rev.* **2011**, *40*, 3076.
[19] H. Brune, P. Gambardella, in *Fundam. Picoscience*, CRC Press, **2013**, pp. 447–470.
[20] R. J. Holmberg, M. Murugesu, *J. Mater. Chem. C* **2015**, *3*, 11986–11998.
[21] X. Meng, W. Shi, P. Cheng, *Coord. Chem. Rev.* **2019**, *378*, 134–150.
[22] C. Benelli, D. Gatteschi, *Introduction to Molecular Magnetism: From Transition Metals to Lanthanides*, Wiley-VCH, Weinheim, **2015**.
[23] E. V. Tretyakov, V. I. Ovcharenko, *Russ. Chem. Rev.* **2009**, *78*, 971–1012.

Chapter 1. A Brief Introduction to Single-Chain Magnets

1.1. Fundamentals of molecular magnetism

1.1.1. Magnetism of free atoms and ions

1.1.1.1. Magnetism from a single electron

In order to apprehend the works introduced along with this thesis, it is crucial for the reader to understand the basic notions of magnetism. To this end, in this chapter I will introduce the essential tools needed to characterise and quantify the relevant magnetic phenomena encountered in this work through theory and notable examples taken from the literature.

Let's start with the macroscopic case of the study of a magnetic field induced by a current loop. The Biot-Savart law tells us that the circular movement of the electrons, induced by a current I, gives rise to a magnetic moment μ oriented along the normal axis of the loop of surface $S = \pi r^2$.

A similar treatment can be done following the classical description of an electron rotating uniformly around a nucleus.[1] If one considers an electron of mass m_e, its uniform rotation v around its nucleus of a distance r can be assimilated to the previous current I because of its negative charge $-e$. This definition of the current being a flow of charge as $I = q/t$, and $t = 2\pi.r/v$, then the expression of the magnetic moment μ for a single electron is:

$$\mu = I\pi r^2 = \frac{-e}{2} \cdot r \wedge v \qquad \text{Eq. 1.1}$$

Moreover, the moving electron is characterised by a mass m_e, and a moving mass gives rise to an angular momentum L such as:

$$L = r \wedge p = r \wedge v \cdot m_e \Rightarrow r \wedge v = {}^{L}/_{m_e} \qquad \text{Eq. 1.2}$$

with $L = \hbar$ in this case, $\hbar$ being the reduced Planck constant.

Then, the angular magnetic moment of the electron μ_L can be expressed according to the previous equation Eq.1.1 as:

$$\mu_L = \frac{-eL}{2m_e} = \frac{-e\hbar}{2m_e} = -\mu_B \qquad \text{Eq. 1.3}$$

This unit μ_B, related to the magnetic moment of one electron, is called the Bohr magneton and is helpful for chemists whose objects of study are the size of molecules.

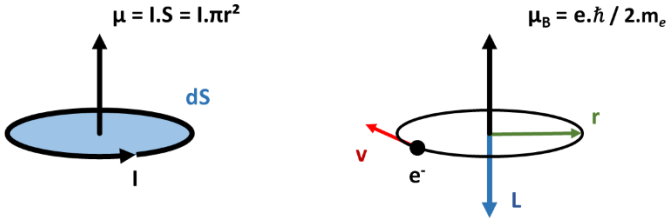

Figure 1.1. Schematic representations of the magnetic moments induced by a current loop (left) and a rotating electron around a nucleus (right).

1.1.1.2. Magnetism from several electrons: the case of atoms and ions

Except in the case of the ^{1}H, atoms possess several electrons distributed on characteristic atomic orbitals. This distribution of electrons will follow the *Aufbau* principle that states that the electrons have to fill first the orbitals of the lowest energy, then the orbitals of higher energy, *etc.*

This electronic configuration will describe the energy level, the localisation around the nucleus, and an electron's behaviour in a given orbital. Indeed, atomic orbitals are described by the three quantum numbers n, l, m_l, with the two last terms directly linked to the angular momentum L of the occupying electron by:

$$L^2 = \hbar\ell(\ell + 1) \qquad \text{Eq. 1.4}$$

$$L_z = \hbar m_\ell \qquad \text{Eq. 1.5}$$

with L_Z the projection of the angular momentum along the z-axis.

The following quantum number required to describe the magnetic property of an electron entirely is the projection m_S of the spin angular momentum S. In the case of the electron, $s = \hbar/2$, its projection along the z-axis has only two solutions $m_S = \pm ½$ (with $+ ½ = \uparrow$ and $- ½ = \downarrow$), and the corresponding magnetic moment is:

$$\mu_S = -g_S \frac{e}{2m_e}\frac{\hbar}{2} = -g_S \frac{e}{2m_e}\frac{\hbar}{2} \approx \mu_B \qquad \text{Eq. 1.6}$$

with g_S the Landé factor being approximately equal to 2.

Added to the Aufbau principle, the distribution of the electrons in atomic orbitals has to fulfil the Pauli principle: two electrons cannot share the same quantum numbers. Thus, the maximum number of electrons in one orbital is two, and their only possible configuration in this orbital is $\uparrow\downarrow$. Such electrons are said to be paired, and the total spin momentum for this orbital is $S_{tot} = \sum m_S = + ½ - ½ = 0$.

The last conditions are described by Hund's rules to minimise the overall energy by minimizing the multiplicity of spin $2.S_{tot} + 1$ and maximizing the total angular momentum $L_{tot} = \sum m_l$. Indeed, many electronic configurations are possible because of the distribution of the electrons within the orbitals and the value of the total orbital momentum L_{tot} define the energy level attributed to each configuration. These notations S_{tot} and L_{tot} will be replaced by

S and *L* later in this thesis because we will deal principally with atoms (hence more than one electron) for the sake of clarity.

We can illustrate these rules and their consequences on the magnetic properties of the two different oxidation states of the copper, the Cu^{I} and the Cu^{II}. From the case of the Cu^{I} example, one can easily conclude that filled orbitals do not participate in the magnetic properties (with no magnetic and orbital moments), contrary to the unfilled Cu^{II} orbitals. Then, in applying Hund's rules, the configuration with the higher L_{tot} = 2 corresponds to the ground state (lowest energy), while the other lies at higher energy; this splitting is called the interelectronic repulsion.

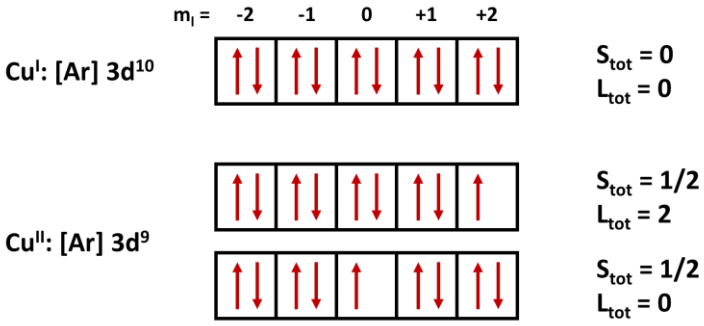

Figure 1.2. Examples of the electronic configuration of the 3d orbitals of the Cu^{I} and the Cu^{II} ions.

These different electronic configurations are grouped terms ^{2S+1}L, the value of *L* corresponding to a letter following the spectroscopic notation (0 = S, 1 = P, 2 = D, *etc.*).

1.1.1.3. The particular case of the 4*f* ions

We will now take a closer look at the properties of the lanthanide (Ln) ions, which have a special place among the periodic table of elements and in this thesis. According to the principles that govern electrons' distribution in atomic orbitals described above, they can adopt two different electronic configurations depending on their relative energy levels: $[Xe]4f^{n-1}5d^{1}6s^{2}$ for the Lanthanum (La), Cerium (Ce) and Gadolinium (Gd), and $[Xe]4f^{n}6s^{2}$ for the others. Finally, the Scandium (Sc) and the Yttrium (Y) with close $(n-1)d^{1}ns^{2}$ configurations are often included in this family and thus called *lanthanoids*.[2]

Because of their predisposition to lose their valence electrons, lanthanides are usually found in their +3 oxidation states (Ln^{III}) in aqueous solutions, although the +2 and +4 states were also reported under specific conditions.[3,4] This chemical similarity is stressed by the fact that they have comparable electronegativity χ_P, large hydration enthalpies $\Delta H_h°$ and their corresponding hydroxydes precipitate in a narrow pH range in a $[Ln(NO_3)_3]$ solution.[5] All these characteristics make them hardly separable, hence their expensive cost.[6]

The main particularity of these 4*f* orbitals resides in the fact that they are shielded by filled orbitals of higher energy and localised near the nucleus because of greater penetration, as represented in Figure 1.3. This particularity makes the 4*f* electrons weakly effective on chemical bonding and poorly sensitive to external perturbations such as the vibrations of the lattice or the ligand field effect observed for the 3*d* ions.

A second particularity, called the *lanthanide contraction*, is observed when filling these 4*f* orbitals. 4*f* electrons have a poor shielding effect on the nuclear charge and do not fully compensate for the increasing electrostatic force felt by the outer shell electrons from the nucleus. These electrons being more attracted by the nucleus results in a decrease of the ionic radius across the lanthanide series, as reported in Table 1.1.

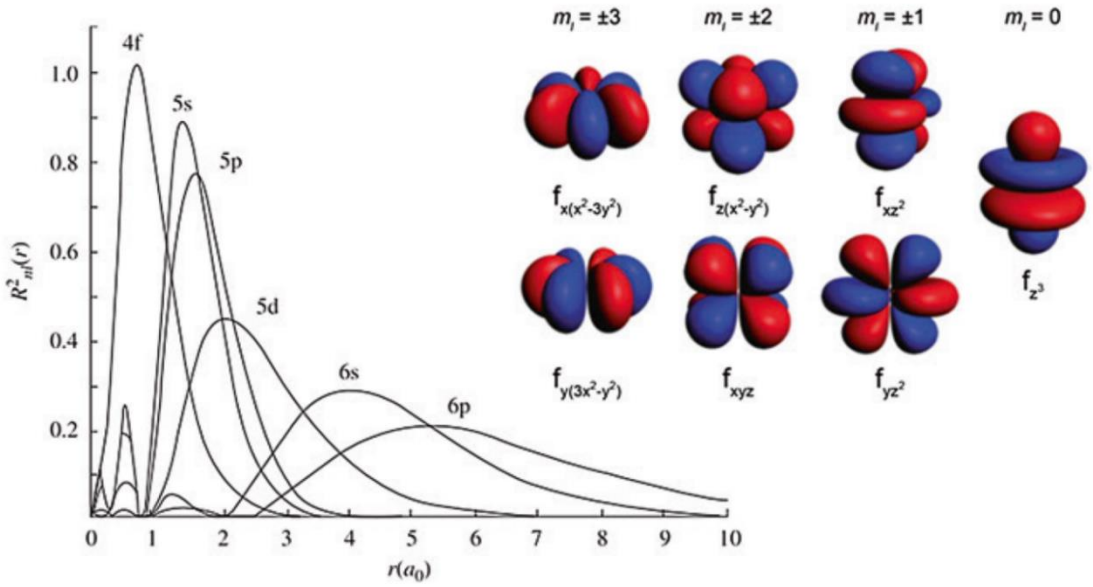

Figure 1.3. Radial distribution functions of 4*f*, 5*s*, 5*p*, 5*d*, 6*s*, and 6*p* electrons for cerium (left) and representation of the 4*f* orbitals according to their m_l number (reproduced from Ref.[7])

Table 1.1. Chemical properties of the trivalent lanthanide ions Ln^{III} (reproduced from Ref.[5])

Ln symbol	Electronic configuration	$E°(Ln^{III}/Ln^{II})$ (V)	χ_P	$\Delta H_h°$ (kJ.mol^{-1})	pH	Ionic radius r_i (pm)*
La	[Xe]4f^0	-3.1	1.10	-3326	7.47	116
Ce	[Xe]4f^1	-2.92	1.12	-3380	7.10	114
Pr	[Xe]4f^2	-2.84	1.13	-3421	6.96	112
Nd	[Xe]4f^3	-2.62	1.14	-3454	6.78	111
Pm	[Xe]4f^4	-2.44	1.13	-3482	n.a.	109
Sm	[Xe]4f^5	-1.5	1.17	-3512	6.65	108
Eu	[Xe]4f^6	-0.34	1.2	-3538	6.61	106
Gd	[Xe]4f^7	-2.85	1.20	-3567	6.58	105
Tb	[Xe]4f^8	-2.83	1.1	-3600	6.47	104
Dy	[Xe]4f^9	-2.56	1.22	-3634	6.24	103
Ho	[Xe]4f^{10}	-2.79	1.23	-3663	6.20	101
Er	[Xe]4f^{11}	-2.87	1.24	-3692	6.14	100
Tm	[Xe]4f^{12}	-2.22	1.25	-3717	5.98	99
Yb	[Xe]4f^{13}	-1.18	1.1	-3740	5.87	98
Lu	[Xe]4f^{14}	n.a.	1.27	-3759	5.74	98

* For a coordination number CN = 8

This inner nature of the 4*f* orbitals and the number of electrons they can accommodate (up to 14) allow strong spin *S* and unquenched orbital *L* moments among the trivalent lanthanide ions (except for Gd^{III} with *L* = 0). The mutual interaction between these intense moments is called spin-orbit coupling. Because the relativistic effects at the origin of this coupling are far from trivial, let us explain it with a simplified comparison from the electron point of view.

The latter is now static, and it is the positive nucleus that orbits around. This change of coordinate conserves the relative speed of rotation ($v_e = v_n$) and the orbit ($r_{e\text{-}n} = r_{n\text{-}e}$), so the angular orbital moment of the nucleus is proportional to the one deduced before for the electron. The nucleus being positively charged, its circular motion creates an induced magnetic field that will interact with the intrinsic spin moment of the electron.

This coupling, if negligible for lighter elements (*Z* < 30), has to be taken into account for the heavier ones as the lanthanides, and require to define a new total momentum *J*, more accurate to describe the magnetic properties of these ions:

$$|L - S| \leq J \leq |L + S| \qquad \text{Eq. 1.7}$$

with *J* = *L* – *S* for *n* < 7 (La^{III} - Eu^{III}) and *J* = *L* + *S* for *n* > 7 (Gd^{III} - Lu^{III}).

One can notice the peculiar case of the Eu^{III} ion, with *L* = *S* = 3 and hence *J* = 0, a diamagnetic ground-state.

From this additional splitting induced by the spin-orbit coupling arise the energy levels noted $^{2S+1}L_J$, each with a 2*J*+1 multiplicity, and whose energy is:

$$E(^{2S+1}L_J) = (\lambda/2)[J(J+1) - L(L+1) - S(S+1)] \qquad \text{Eq. 1.8}$$

with λ the spin-orbit coupling constant of the ion.

Until now, we only have considered 4*f* free ions and neglected the external influences because of the inner nature of the 4*f* orbitals and the predominance of the spin-orbit coupling. The reality is however somewhat different, and these ions are often surrounded by ligands. These ligands will create a static electrostatic field around the positive cation, called the ligand field. According to its spatial distribution around the cation, this static field will lower the system's symmetry and lift the energy level degeneracy by stabilizing the energy of some orbitals to the detriment of others.

This phenomenon is particularly true for highly directional orbitals such as the 3*d* ones, where the ligand field effect is of the utmost importance to rationalise the optical and magnetic properties of 3*d* complexes. In the case of the lanthanide-based compounds, the ligand field has a minor influence on the energy levels of the 4*f* orbitals: it can be considered as a perturbation that splits the energy levels $^{2S+1}L_J$ by few hundreds of cm^{-1} into so-called Stark sublevels. On the other hand, one has to pay close attention to the resulting symmetry modifications that can have profound implications on the properties of some magnetic compounds. This point will be discussed later in this chapter.

The last interaction presented in this introduction arises when applying an external magnetic field to the ion: the degeneracy of these $^{2S+1}L_J$ is lifted by the Zeeman effect, ultimately providing a series of $-J < m_J < J$ magnetic sublevels. The corresponding magnetic moment can be expressed as:

$$\mu_J = g_J \cdot \mu_B \cdot J \qquad \text{Eq. 1.9}$$

with g_J the Landé factor that is:

$$g_J = \frac{3}{2} + \frac{S(S+1) - L(L+1)}{2J(J+1)} \qquad \text{Eq. 1.10}$$

These different interactions described previously on the energy levels are represented in Figure 1.4, and the main spectral and magnetic ground state terms for trivalent 4*f* ions are listed in Table 1.2.

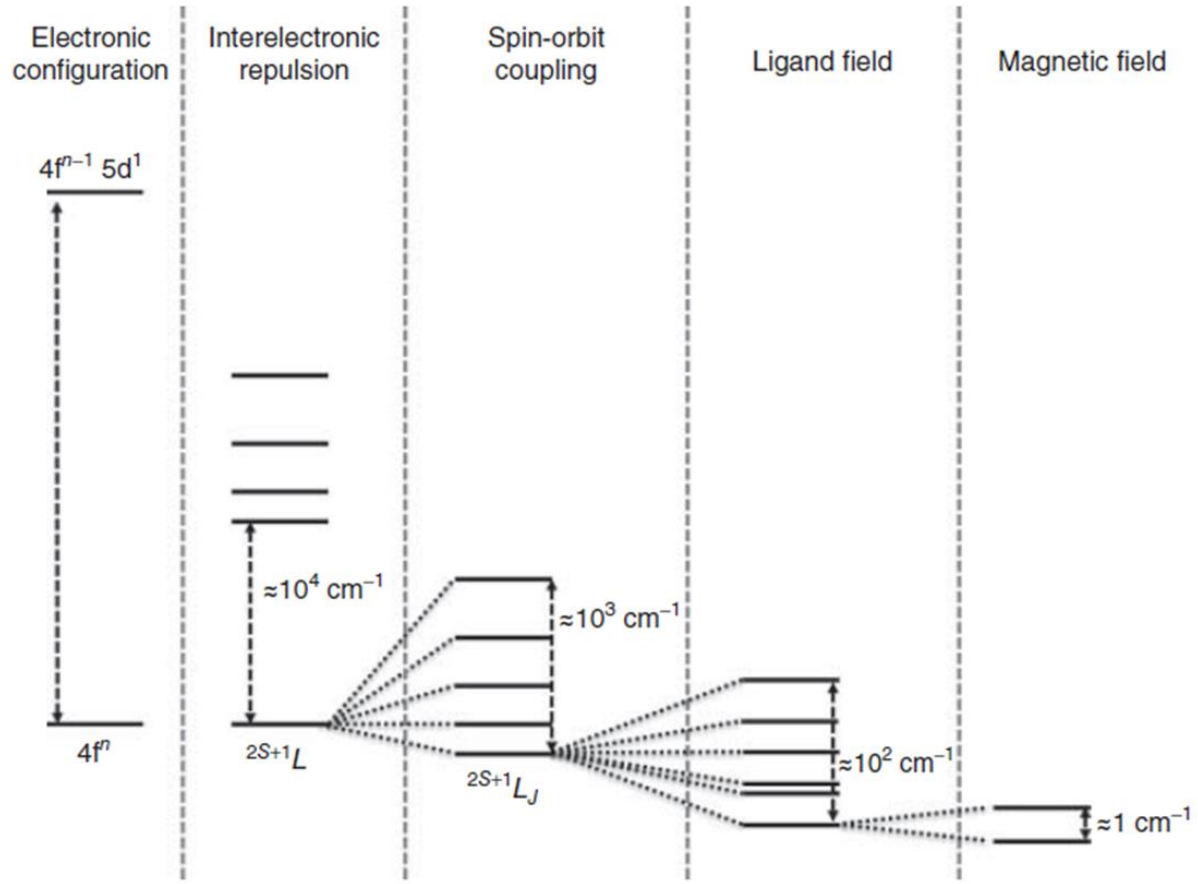

Figure 1.4. Energy level diagram on a given 4*f*n configuration for a trivalent ion Ln^{III} (reproduced from Ref.[8]).

Table 1.2. Ground state spectral and magnetic parameters for the trivalent ions Ln^{III}.

Ln symbol	Ground state $^{2S+1}L_J$	*L*	*S*	*J*	g_J	μ_{theo} (μ_B)	χT_{theo} (emu.K.mol^{-1})
La	$^1S_0$	0	0	0			
Ce	$^2F_{5/2}$	3	1/2	5/2	6/7	2.14	0.80
Pr	$^3H_4$	5	1	4	4/5	3.20	1.60
Nd	$^4I_{9/2}$	6	3/2	9/2	8/11	3.27	1.64
Pm	$^5I_4$	6	2	4	3/5	2.40	0.90
Sm	$^6H_{5/2}$	5	5/2	5/2	2/7	0.71	0.09
Eu	$^7F_0$	3	3	0			
Gd	$^8S_{7/2}$	0	7/2	7/2	2	7.00	7.87
Tb	$^7F_6$	3	3	6	3/2	9.00	11.82
Dy	$^6H_{15/2}$	5	5/2	15/2	4/3	10.00	14.17
Ho	$^5I_8$	6	2	8	5/4	10.00	14.07
Er	$^4I_{15/2}$	6	3/2	15/2	6/5	9.00	11.48
Tm	$^3H_6$	5	1	6	7/6	7.00	7.15
Yb	$^2F_{7/2}$	3	1/2	7/2	8/7	4.00	2.57
Lu	$^1S_0$	0	0	0			

1.1.2. Bulk magnetism

1.1.2.1. The magnetic susceptibility

Because a bulk molecular compound is made of a large number of atoms, we have to find a convenient physical quantity to express this macroscopic magnetic behaviour. This quantity is the magnetisation *M*, which express the magnetic moment μ per unit volume *V*:

$$M = \frac{\partial \mu}{\partial V} \qquad \text{Eq. 1.11}$$

Considering a uniform distribution within the bulk, *M* can be approximated as the contribution resulting from the sum of the magnetic moments μ. The response of the magnetisation *M* when an external magnetic field *H* is applied to the compound is called magnetic susceptibility χ expressed as:

$$\chi = \frac{\partial M}{\partial H} \qquad \text{Eq. 1.12}$$

with χ a tensor of rank 2, to translate a possible anisotropy of the magnetic response ($\chi_x \neq \chi_y \neq \chi_z$ in the cartesian coordinate system).

In the case of isotropic susceptibility and at low field *H*, χ is a scalar, and the Eq. 1.12 become:

$$\chi = \frac{M}{H} \qquad \text{Eq. 1.13}$$

Finally, a more convenient way to express this magnetic susceptibility for chemists is to normalise this quantity by the number of moles of the considered molecular compound as:

$$\chi_M = \frac{M}{H} \cdot \frac{\mathcal{M}}{m} \qquad \text{Eq. 1.14}$$

with χ_M the molar magnetic susceptibility, $\mathcal{M}$ the molar weight and m the mass of the sample, respectively.

The representation of the $\chi_M T$ product plotted against the temperature T gives insights into the magnetic interactions occurring within the sample, described in the following parts.

1.1.2.2. The diamagnetic susceptibility

As we have seen in Part.1.1.1.2, all the electrons do not contribute equally to the magnetic response of the sample: the paired electrons lying in the fully occupied orbitals do not have total spin (S = 0) or orbital (L = 0) momenta. Applying an external magnetic field will change the motion of the inner electrons (the Lorentz force) and then their induced electric current. This modification creates a small internal magnetic field as opposed to the external one, thus a repellent force between the applied field and the material.

This "negative" contribution is called diamagnetism, with a corresponding susceptibility χ_P < 0, and is a common property of the matter. The magnitude of this contribution can be determined, knowing the composition of the studied molecule, thanks to Pascal's constants.[9] These tables list the diamagnetic contributions of a large set of atoms ($\chi_{D,a}$) weighted by the type of bonds or functional groups between them ($\lambda_{D,a}$), which are typically small ($\chi_D \approx -10^{-6}$ emu·mol^{-1}).

$$\chi_D = \sum_a \chi_{D,a} + \sum_a \lambda_{D,a} \qquad \text{Eq. 1.15}$$

1.1.2.3. The paramagnetic susceptibility

On the contrary, applying an external field on unpaired electrons will tend to align their magnetic moments parallel to the field: this is the paramagnetism. This collective orientation will "reinforce" the overall magnetisation M, hence the paramagnetic susceptibility $\chi_P > 0$. It is several orders of magnitude higher than the diamagnetic susceptibility ($\chi_P \approx 10^{-3}$ emu·mol^{-1}), and therefore the dominant contribution to the magnetism of the compound.

Taking into account the two contributions of the para- and diamagnetism phenomena, the molar susceptibility can be expressed as:

$$\chi_M = \chi_P + \chi_D \qquad \text{Eq. 1.16}$$

This molar susceptibility is inversely proportional to the temperature T and follows the Curie law as:

$$\chi_M = \frac{C}{T} \qquad \text{Eq. 1.17}$$

For Ln ions, *C*, the Curie constant, is given by:

$$C = \frac{\mathcal{N}_a \cdot \mu_B^2 \cdot g_J^2 \cdot J(J+1)}{3k_B} \qquad \text{Eq. 1.18}$$

with $\mathcal{N}_a$ the Avogadro number, g_J the Landé factor (see Eq. 1.10) and k_B the Boltzmann constant. In the case of negligible spin-orbit coupling (light elements Z < 30) and/or $L = 0$, then $J = S$ and $g_J = g_S \approx 2.0023$.

However, the paramagnetism itself is not sufficient to observe a long-range order within the system because these microscopic moments lose their orientation once the external field is removed under the influence of the thermal agitation k_BT.

1.1.3. Magnetic interactions

To overcome this spontaneous loss of magnetisation, we must pay attention to the interactions between the magnetic moments within the molecule (or the extended network) to preserve an overall arrangement. Some of them will be discussed in this part.

1.1.3.1. Dipolar interaction

The dipolar interaction is the interaction between the moments generated by magnetic dipoles, as experienced by anyone who tried to bring closer or take away massive magnets by hand. Its energy for two parallel dipoles μ_A and μ_B is:

$$E_{dip} = -\frac{\mu_A \cdot \mu_B (3\cos^2(\alpha) - 1)}{d_{AB}^3} \qquad \text{Eq. 1.19}$$

with α the angle between the direction of the dipoles and the segment connecting their centre, and d_{AB} the distance between them.

By considering the cosine term, the most stable configuration is reached when $\alpha = 0$ or 180°, *i.e.,* when the poles of opposite signs face each other. This interaction works for any magnetic dipoles through space at long-range and is strongly anisotropic.

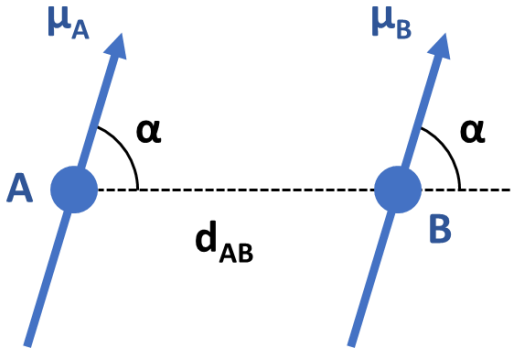

Figure 1.5. Schematic representation of the dipolar interaction between two dipoles μ_A and μ_B.

1.1.3.2. Exchange coupling

The exchange coupling arises from the overlapping of atomic orbitals with unpaired electrons, and the need to reduce the overall energy by reducing the electrostatic space charges while respecting the Pauli exclusion principle. The related spin Hamiltonian for two spins S_A and S_B respectively is:

$$\mathcal{H}_{dip} = -2J_{ex} \cdot S_A S_B \qquad \text{Eq. 1.20}$$

with J_{ex} the exchange integral, the energy difference between the singlet and triplet states as $J_{ex} = E_S - E_T$.

The sign of J_{ex} depends on the considered ground state of the system:

- If the triplet state (↑↑, S_{tot} = 1) corresponds to the ground state, then $J_{ex} > 0$ and the magnetic coupling is called ferromagnetic (FM);
- If the singlet state (↑↓, S_{tot} = 0) corresponds to the ground state, then $J_{ex} < 0$ and the magnetic coupling is antiferromagnetic (AFM).

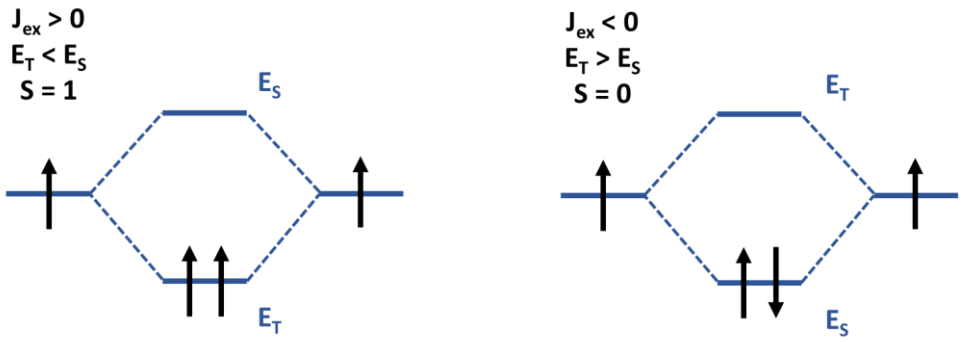

Figure 1.6. Energy diagram representation of the exchange interaction in the case of $J_{ex} > 0$ (ferromagnetic, left) and $J_{ex} < 0$ (antiferromagnetic, left).

Because this coupling refers to the atomic orbitals that decay with the distance, it is highly localised, contrary to the previous dipolar interaction. This constraint explains the scarcity and the weakness of such interaction for 4*f*-based systems (because of the shielded 4*f* orbitals) compared to the 3*d* ones.

1.1.3.3. Super-exchange coupling

From a certain point of view, the super-exchange coupling is an extension of the previous exchange interaction but between next-nearest neighbouring atoms, mediated by a non-magnetic one. This behaviour, deduced from empirical observations on metal oxides and coined under the term of GKA rules (for Goodenough, Kanamori and Anderson),[10–13] stated that the reported magnetic coupling depends on the M_A-O-M_B angle between the two metallic M_A and M_B 3*d* orbitals with respect to the 2*p* one from the intermediate oxygen. Hence, if this angle is close to 90°, the resulting magnetic interaction will be ferromagnetic, while axially aligned orbitals will induce an antiferromagnetic interaction.

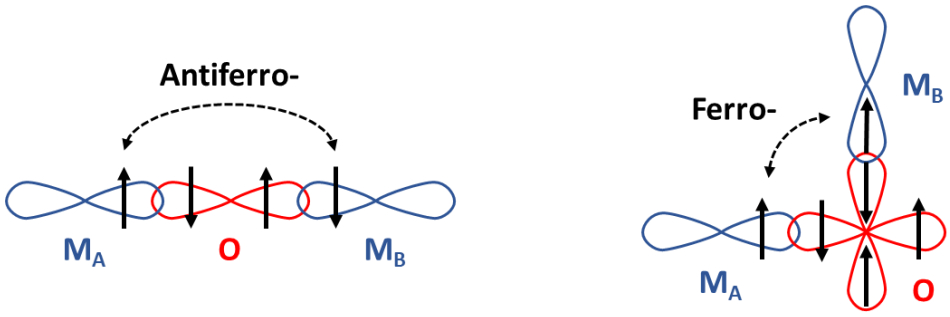

Figure 1.7. Schematic representation of the super-exchange interactions in the case of the M_A-O-M_B angle is equal to 180° (left) and 90° (right).

In addition to these three principal interactions, several others are involved in specific cases to explain the magnetic coupling between two ions with different oxidation states (double exchange) or arising from the conduction electrons in metals, but are beyond the scope of this thesis. However, the reader can refer to excellent state-of-the-art books for further details.[14,15]

1.1.4. Cooperative magnetic behaviours

If the interactions described above are sufficiently strong to propagate among the system, a macroscopic long-range order will arise spontaneously below a given finite temperature.

The Hamiltonian of these magnetic interactions between neighbouring spins *i* and *j* is expressed as follows:

$$\mathcal{H} = -2J_{ex}\sum_{i \neq j}(S_i^x S_j^x + S_i^y S_j^y + S_i^z S_j^z) \qquad \text{Eq. 1.21}$$

with S^x, S^y and S^z the components of the spin anisotropy.

Three different cases of spin anisotropy can be encountered and are represented in Figure 1.8 below:

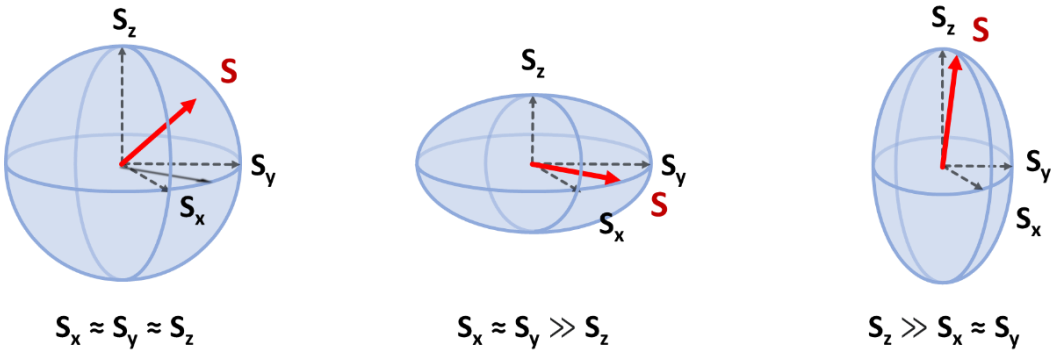

Figure 1.8. Representation of the Heisenberg (left), XY (middle) and Ising (right) models.

By applying the thermodynamics principles to the spin model and the dimensionality of the molecular network, the possibility of a long-range ordering long-range order can occur or not.[16]

Table 1.3. Observation of a long-range ordering at $T \neq 0$ K for different spin models and lattice dimensions.

	Dimension of the molecular network		
Spin model	**d = 1, chain**	**d = 2, plan**	**d = 3, volume**
Ising	No	Yes	Yes
XY	No	BKT transition*	Yes
Heisenberg	No	No	Yes

* Berezinsky-Kosterlitz-Thouless transition[17,18]

1.1.4.1. Ferromagnetic, antiferromagnetic and ferrimagnetic orders

We have described in Part.1.1.2.3 the paramagnetic case when non-interacting magnetic moments align themselves with respect to an applied field, then relax randomly once the latter is removed. However, this orientation can be preserved if dipolar, ferromagnetic or antiferromagnetic interactions occur.

In the case of the ferromagnetic order, the ferromagnetic interaction $J_{ex} > 0$ favour the parallel alignment of the magnetic moments below a finite temperature T_C (the Curie temperature), resulting in a significant magnetic moment.

Similarly, an antiferromagnetic interaction $J_{ex} < 0$ will lead to the orientation of the magnetic moments below a characteristic T_N temperature, but in an antiparallel fashion. This compensation of the magnetic moments will lead to a zero magnetic moment (in the case of a homospin system).

To take into account these interactions between the individual spin carriers, we have to introduce an additional term θ to the Curie law (Eq. 1.17):

$$\chi_M = \frac{C}{T - \theta} \qquad \text{Eq. 1.22}$$

with θ the Weiss temperature (θ = T_C for FM order, and -T_N for AFM order).

The latter is related to a mean-field term imprinted by the J_{ex} interactions of z neighbouring atoms as:

$$\theta = \frac{2z \cdot J_{ex} \cdot J(J+1)}{3k_B} \qquad \text{Eq. 1.23}$$

Finally, an intermediate case can be observed in heterospin systems with antiferromagnetic interactions; despite being oriented in an antiparallel fashion, the non-compensation of the magnetic moments ($S_A \neq S_B$ and/or $n_A \neq n_B$) give rise to an overall magnetic moment below of the T_C temperature. Interestingly, this last phenomenon, called ferrimagnetism is the source of the magnetism observed for centuries in the lodestone Fe_3O_4, the first known-magnet thanks to the non-compensation of antiferromagnetically coupled Fe^{II} (S = 2) and the Fe^{III} (S = 5/2) spins.

The characteristic behaviours of these long-range magnetic orders can be highlighted by magnetic susceptibility measurements, as represented in Figure 1.9.

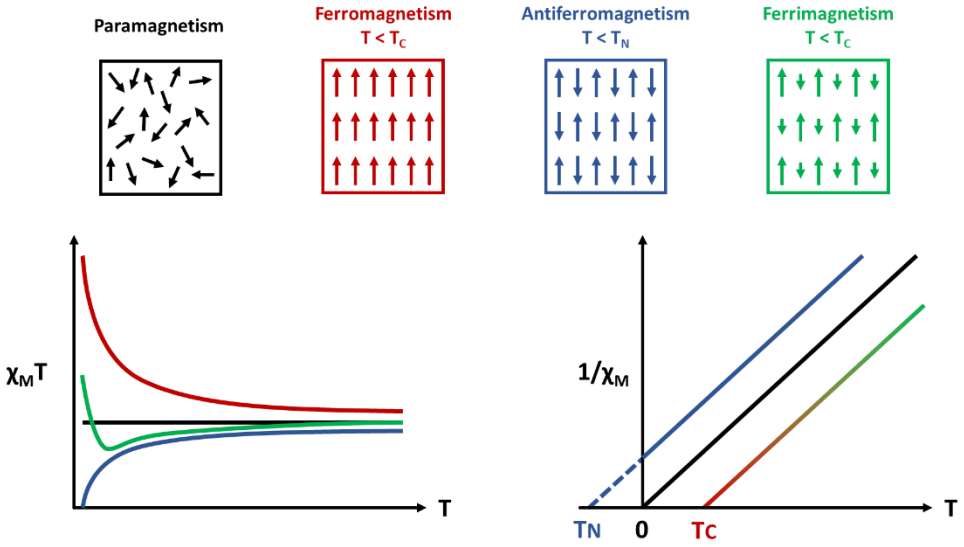

Figure 1.9. Top: Schematic representations of the spin orientations according to the magnetic order. Bottom: Temperature dependencies of the corresponding $\chi_M T$ products (left) and $1/\chi_M$ (right).

Ferro- and ferrimagnetism are although not sufficient to observe a spontaneous magnetisation of the material, and that is why an introduction to the concept of the domains is needed. Indeed, ferro- and ferrimagnetic materials are subdivided into microscopic regions called domains, where all the spins are effectively coupled yet randomly oriented to minimise the magnetic energy from the bulk.

To cover this issue, one has to apply an external magnetic field strong enough to align the magnetisation of all the domains along with the same orientation until saturation: this is the first magnetisation. After removal of this external field, the sample will preserve a non-zero magnetisation called remanent magnetisation M_R. This magnetisation can be suppressed by applying a field of value H_C, called coercive field.

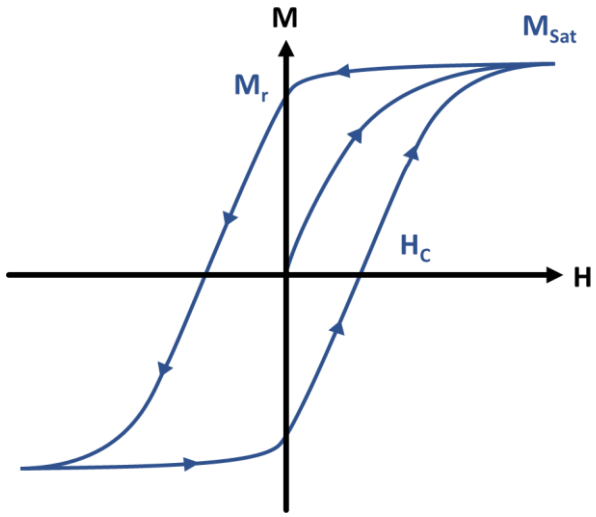

Figure 1.10. Schematic representation of a magnetic hysteresis loop for a permanent magnet.

To address the magnetisation of a persistent magnet along a given axis was employed by manufacturers for decades to store numeric data efficiently. For instance, a classial magnetic hard drive disk (HDD) is made of a thin magnetic layer (commonly Co alloys), subdivided into magnetic domains. A read-and-write head can individually address the magnetisation of each grain by imprinting a small magnetic field $H > H_C$, either up (↑) or down (↓), which can be assimilated to a binary system with↑ = 1 and ↓ = 0. Then, this very same head just has to measure the domain's magnetisation to translate it in terms of data.

Several improvements on the design of the HDDs have been made to decrease the grain size: smaller addressable magnetic grains for a given surface should allow higher data storage areal density.[19] This quest is particularly relevant nowadays to face the digitalisation of societies and industries encouraged by the promises of informatics and the internet in the 1990-2000s and the rise of Artificial Intelligence and Big Data nowadays.

Unfortunately, this miniaturisation approach (or top-down) is hindered when magnetic domains reach nanometric dimensions: this is the superparamagnetic limit.

1.1.4.2. Superparamagnetism

Superparamagnetic properties arise from considering nanometric ferro- or ferrimagnetic particles (usually below 100 nm), analogous to a single magnetic domain with a giant magnetic moment. Because of their magnetic and/or shape anisotropy, only two stable orientations of the magnetisation are possible, "up" (↑) or "down" (↓), separated by an energy barrier *ΔE*.

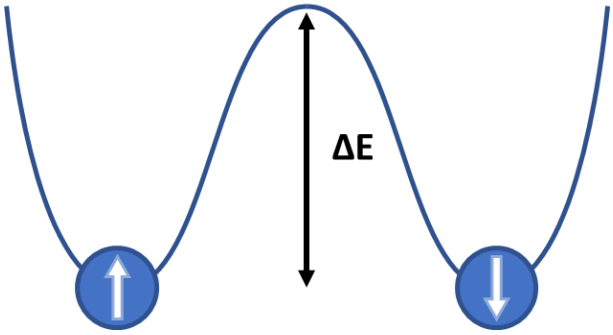

Figure 1.11. Schematic representation of the energy barrier *ΔE* between a magnetic nanoparticle's "up" and "down" configurations.

The relaxation dynamics or the flip between these two states is ruled by a thermally activated process whose characteristic time τ is described by an Arrhenius law as:

$$\tau = \tau_0 \exp\left(\frac{\Delta E}{k_B T}\right) = \tau_0 \exp\left(\frac{KV}{k_B T}\right) \qquad \text{Eq. 1.24}$$

with τ_0 the pre-exponential term, *ΔE* the energy barrier, *K* the magnetocrystalline anisotropy constant and *V* the volume of the particle.

1.2. Single-Molecule Magnets

Physicists and chemists have adopted the strictly opposite approach of the manufacturers. Instead of starting from macroscopic magnets and trying to divide them while preserving their magnetic properties ("top-down"), they chose to start from the elementary units of matter that are atoms with relevant magnetic properties (3*d*/4*f*) and designed coordinating molecules to tailor them.

From Eq. 1.24, it is clear that the relaxation time decreases at a given temperature while lowering the volume V. Because of the small volume of single molecules, the associated energy barrier $\Delta E = KV$ quickly competes with the thermal energy k_BT. This intrinsic characteristic leads to low blocking temperatures T_B, a temperature below which the magnetic relaxation of the particle is slow enough to restrain its magnetisation. Only remain the magnetocrystalline term *K* to optimise, proportional to the anisotropy and the magnitude of the magnetic moment.

Anyways, these favourable conditions were encountered 30 years ago by the group of Gatteschi with $[Mn_{12}O_{12}(AcO)_{16}(H_2O)_4].2AcOH$, or $[Mn_{12}]$,[20] synthesised for the first time by Lis in 1980.[21] In this molecule, four Mn^{IV} (S = 3/2) and eight Mn^{III} (S = 2) ions are coupled through antiferromagnetic interactions to give rise to a high spin *S* = 10, an axial anisotropy *D* = - 0.46 cm^{-1} and a high energy barrier U_{eff} = 70 K.

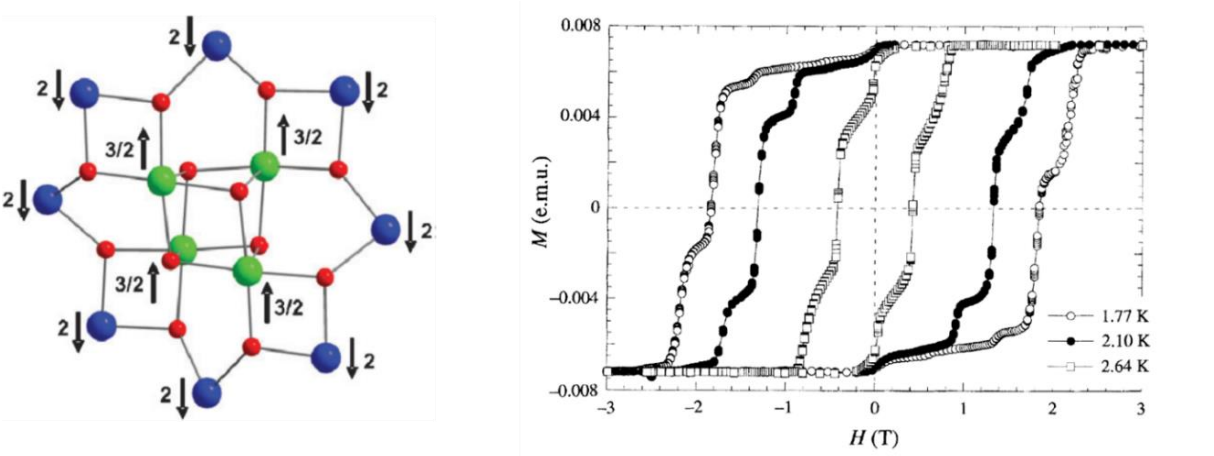

Figure 1.12. Simplified representation of the $[Mn_{12}]$ (acetate and water molecules omitted for clarity) with in green the Mn^{IV}, and in blue the Mn^{III} (left, reproduced from Ref.[22]). Magnetic hysteresis loops measured on $[Mn_{12}]$ single-crystals with various temperatures (right, reproduced from Ref.[23]).

These properties have led to the first observation of slow relaxation of the magnetisation and an open magnetic hysteresis from a molecular origin, called thereafter Single-Molecule Magnets (SMMs). In addition, the steps of this hysteresis loop were attributed to a quantum tunnelling of magnetisation (QTM), further discussed in the following part.[23,24] Due to these unique properties at that time, extensive magnetic studies have been carried out on this textbook molecule and functionalised carboxylic derivatives to unravel their underlying causes.[22,25,26]

1.2.1. Relaxation dynamics of the magnetisation in SMMs

First of all, SMMs can be assimilated to superparamagnets: the energy barrier ΔE becomes U_{eff}, proportional to the value of the ground-state spin S and its axial anisotropy with a zero-field splitting (ZFS) constant $D < 0$. This energy is given by:

$$U_{eff} = \begin{cases} |D|S^2 & S \in \mathbb{Z} \\ |D|(S^2 - \frac{1}{4}) & S \in \mathbb{Z} + \frac{1}{2} \end{cases} \qquad \text{Eq. 1.25}$$

This zero-field interaction splits the S state into $2S+1$ m_S multiplets (or m_J for 4*f* SMMs), leading to an energy level diagram close to the double-well potential for superparamagnetic nanoparticles as depicted in Figure 1.13.

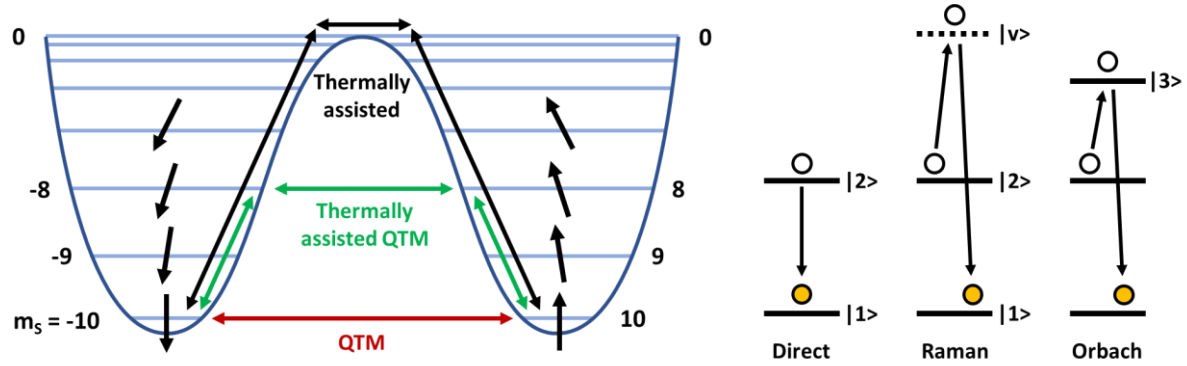

Figure 1.13. (Left) Double well potential energy diagram for an S = 10 SMM, with single arrows representing the spin orientations related to each m_S state, and the double arrows the relaxation pathways. (Right) Mechanisms of the spin-lattice relaxations (adapted from Ref.[27]).

At higher temperatures, vibrations of the molecular lattice are effective and generate phonons that can interact with the spins (spin-phonon coupling).

The first coupling mode, the Direct process, correspond to a spin transition from an excited state to a lower one (|2> →|1>) that generate a phonon matching with one of the vibrational modes of the lattice. The Raman process involve two phonons and a virtual excited state; a first phonon of energy $\Delta E_{2\to v}$ is absorbed by the excited spin system |2> to reach a virtual state with a short lifetime |v>, and relaxes to a lower state |1> while emitting a second phonon of higher energy $\Delta E_{v\to 1}$. Finally, a similar mechanism occurs for the Orbach process, but the intermediate state is not virtual anymore but real.

Lowering the temperature decreases the vibration of the lattices, then the number of phonons and the influence of the previous mechanisms. However, it does not mean that no relaxation can occur: this is the quantum tunnelling of magnetisation (QTM). This tunnel effect is observed due to the alignment (or degeneracy) of the opposite ± m_S energy levels.[24] Besides being remarkable, this is a double-edged property depending on the targeted application: if it can open the way to possible spintronic devices,[28] it is a significant drawback to design nanomagnets because of spontaneous loss of the magnetisation, and *de facto* the stored information.

Finally, an intermediate situation is possible when both thermally assisted relaxations and QTM are observed. The expression of these relaxation processes is the following:

$$\tau^{-1} = \tau_{Orbach}^{-1} + \tau_{Direct}^{-1} + \tau_{QTM}^{-1} + \tau_{Raman}^{-1} = \tau_0^{-1} \exp\left(\frac{-U_{eff}}{k_B T}\right) + AH^m T + \frac{B_1}{1 + B_2 H^2} + CT^n \quad \text{Eq. 1.26}$$

with *A* and *m* being empirical terms for the Direct process, *C* and *n* for the Raman one, and B_1 and B_2 the constants associated with tunnel splitting.[29]

1.2.2. Strategies to improve SMM performances

The first strategy adopted to improve the SMM performances could be sum up as a simple statement; "the greater the total spin *S*, the higher the energy barrier U_{eff}, the slower the relaxation". This motivation has led to extensive (but mostly serendipitous) investigations by the molecular magnetism community to design polynuclear 3*d*-based SMMs. This resulted in an impressive bestiary of SMMs, with spin centres spanning from the Vanadium (V) to the Nickel (Ni), and even attempts of heterosystems with 4*d*/5*d* ions (Molybdenum Mo, Tungsten W, Rhenum Re) with varying degrees of success. A detailed description of these polynuclear SMMs can be found in Ref.[25].

The most notable examples illustrating the limit of this approach are the famous [Mn_{84}] and [Mn_{19}] clusters. The [Mn_{84}] is a colossal cluster synthesised in 2004 by the group of Christou from [Mn_{12}] units, with 84 Mn^{III} that arranged themselves into a torus with a diameter of 4.2 nm and an inner pore of 2 nm.[30] Besides the evident beauty of this edifice, the resulting ground state spin was only *S* = 6 and the energy barrier U_{eff}/k_B = 18 K. For the [Mn_{19}], synthesised in 2006 by the group of Powell, the favourable coupling between seven Mn^{II} (*S* = 5/2) and twelve Mn^{III} allowed to reach an unprecedented *S* = 83/2 spin, but still with poor SMM performances (U_{eff}/k_B = 5.8 K).[31]

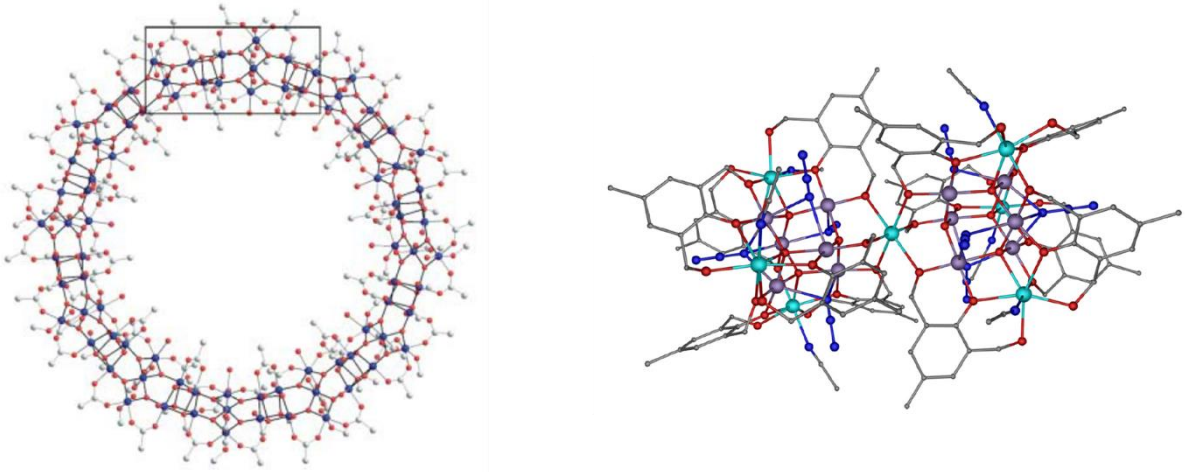

Figure 1.14. Representation of the [Mn_{84}] crystal structure with in the rectangle, the [Mn_{14}] asymmetric unit (reproduced from Ref.[30], left) and of the [Mn_{19}] crystal structure (with Mn^{II} in light blue and Mn^{III} in purple, reproduced from Ref.[26], right).

In fact, increasing the nuclearity of the clusters was backing the wrong horse: if each spin carrier has an effective anisotropy (thanks to the distortions of 3*d* polyhedra and the resulting ligand-field effect), the fact that these easy axes are not collinear and compensate each other lead to a small overall anisotropy.[32] A second limiting factor, based on *ab-initio* investigations from archetypal SMMs and raised first by Waldmann then by Neese and Pantazis,[33,34] pointed out the overestimated dependence of the energy barrier U_{eff} toward the term S^2 (Eq.1.25). The two last authors conclude their article as follows: "*A more promising avenue of research might be to enhance the anisotropy of 'designer' mononuclear species*", further described in the following part.

For that purpose, let us go back a few years, in 2003. Ishikawa *et al.* have reported a series of mononuclear complexes, with lanthanide ions Ln^{III} confined between two phthalocyanine ligands (Pc^{2-}). The Tb^{III} sandwich-like derivative exhibited outstanding SMM properties, with an energy barrier of U_{eff}/k_B = 331 K, outperforming by far most of the polynuclear complexes synthesised until then.[35]

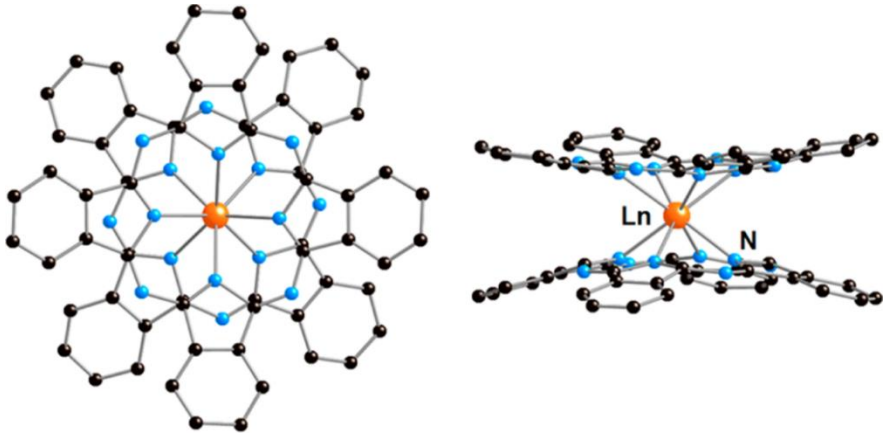

Figure 1.15. Top (left) and side (right) representations of the $[Ln(Pc)_2]^-$ crystal structure (hydrogen atoms omitted for clarity, reproduced from Ref.[36]).

As for the pioneer works for the $[Mn_{12}]$, $[Ln(Pc)_2]^-$ have been widely investigated by doping experiments with diamagnetic ions, substitution and/or functionalisation of the phthalocyanine moieties, varying its oxidation states, *etc.* The reader can refer to the recent book chapter Ref.[37], that summarises a large part of these investigations.

The critical point to understand this leap forward is the magnetic anisotropy of the 4*f* ions, briefly teased in Part.1.1.1.3.

Indeed, we have stated that the inner nature of the 4*f* orbitals led to a large spin-orbit coupling and more accurate $^{2S+1}L_J$ states. Although treated as a perturbation, the ligand field split these states into 2*J*+1 magnetic sublevels m_J. This splitting generates an energy barrier between the doubly degenerates $\pm m_J$ levels of opposite orientation, leading to a strong axial (or Ising-like) anisotropy that increases while increasing $|J|$. The magnitude of this anisotropy can be quantified, from Eq. 1.9, by projecting the moment μ_J along the axial *z*-axis as:

$$\mu_J^{eff} = g_J \mu_B \sqrt{J(J+1)} \qquad \text{Eq. 1.27}$$

In the case of the 4*f* ions with given $^{2S+1}L_J$ states, the Landé factor g_J is a tensor of rank 2 with $g_J = g_x + g_y + g_z$. However, a more convenient notation $g_J = g_\perp + g_\parallel$ (with $g_\perp = g_x + g_y$ and $g_\parallel = g_z$) can be adopted to represent the different kinds of anisotropy encountered, already depicted in Figure 1.8; isotropic ($g_\perp \approx g_\parallel$), planar ($g_\perp > g_\parallel$) or axial ($g_\perp < g_\parallel$).

The value of this tensor $g_\parallel$ can also be determined following:[38]

$$g_\parallel^{eff} = 2g_J|m_J| \qquad \text{Eq. 1.28}$$

High $g_\parallel$ values can then be reached with the Tb^{III} ($g_\parallel = 18$), the Dy^{III} ($g_\parallel = 20$) and the Er^{III} ($g_\parallel = 18$) ions, making them the principal candidates for high-performance SMMs.

In addition to this intrinsic magnetic anisotropy, one can stabilise these low-lying ± m_J ground states by adjusting the symmetry of the ligand field according to the shape of the electron density of 4*f* orbitals (see Figure 1.16 below) to maximise the splitting between ground and excited states.[39]

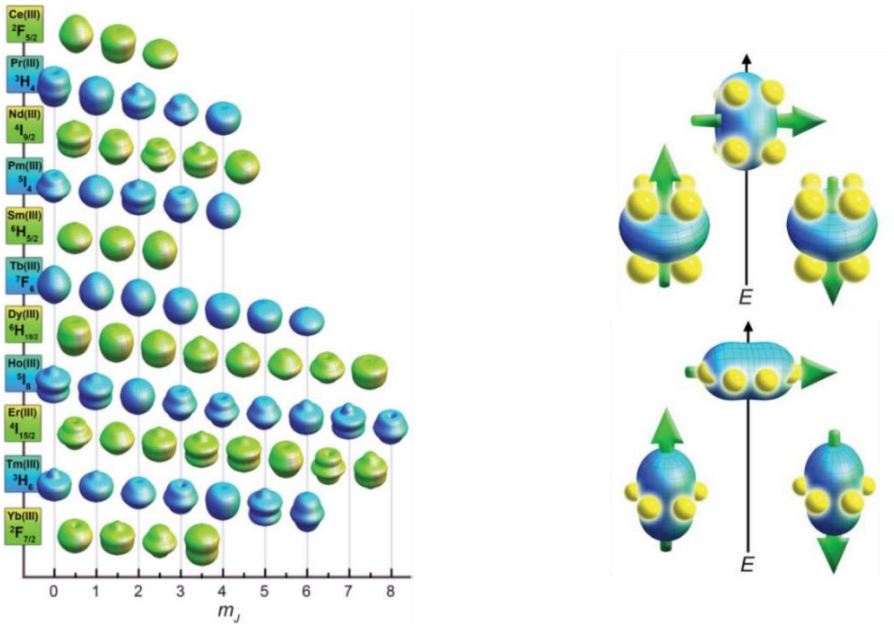

Figure 1.16. Quadrupole approximations of the electron density for the m_J states for each lanthanide (left) and energy configurations of the respect to the crystal field environment for an oblate (top) and a prolate (bottom) ion (reproduced from Ref.[39]).

The shape of these orbitals is either axially or equatorially elongated, and therefore called "prolate" or "oblate", respectively (the specific cases of the Gd^{III}, isotropic, and the Eu^{III}, $J = 0$, are not considered). For example, in the case of the Dy^{III} ion, the shape of electron density related to the $m_J = \pm 15/2$ ground state is oblate. By designing a low symmetry ligand field with the electron density localised on each side, the repulsive electrostatic interactions between their mutual electronic clouds can stabilise either the parallel and antiparallel m_J configurations while destabilizing the low m_J ones. This was supported by theoretical studies on perfectly axial diatomic $[DyO]^+$ that predicted a maximum energy barrier $U_{eff}/k_B \approx 3000$ K.[40]

This intuitive approach, which strongly recalls the case of the $[Tb(Pc)_2]^-$, was provided in 2011 by Rinehart and Long and paved the way to the rational design of axial mononuclear lanthanide SMMs with outstanding U_{eff}/k_B > 1000 K values for the years to come.[41–43]

However, these strongly axial SMMs failed to exhibit large blocking temperature: for instance, the $[Dy(O^tBu)_2(py)_5]^+$ (O^tBu^- = tert-butoxide and py = pyridine) compound, depicted in Figure 1.17 with an angle O-Dy-O = 178.9°, show a comparatively small blocking temperature T_B = 14 K despite a record energy barrier U_{eff}/k_B = 1815 K.[41]

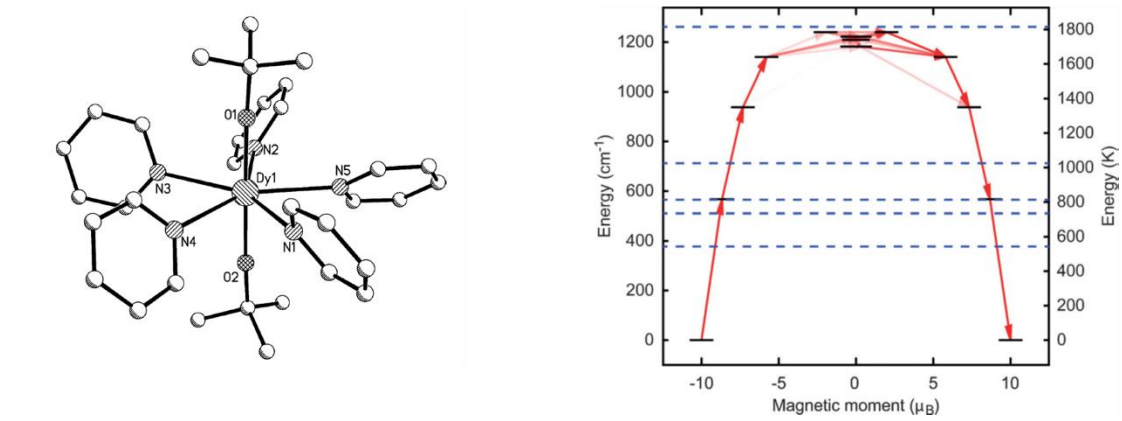

Figure 1.17. Representation of the $[Dy(OtBu)_2(py)_5]^+$ crystal structure (left) and corresponding energy levels diagram from ab-initio simulation (right, reproduced from Ref.[41]).

Indeed, this strategy was focused on the increase of the energy barrier that is related to the thermally-assisted Orbach relaxation. However, we have seen in Part.1.2.1 that the Raman process, related to spin-phonon coupling and thus the vibration of the molecular structure, was also involved in the relaxation of the SMMs.[44,45] How to rigidify these molecules enough to prevent these parasitic relaxation phenomena? This task was far from easy because the trivalent lanthanide ions can accommodate a large number of coordination bonds (even if the 8- and 9-coordinated compounds are the more usual),[46] making them quite flexible by nature.[47] The salvation came from a class of molecules already well known in organometallic chemistry, namely dysprosocenium.

Considering the principles established earlier, these are sandwich-like molecules with a centring Dy^{III} atom coordinated on each side by cyclopentadienyl (Cp) derivatives. The latter provides the expected rigidity by the internal steric constraints imposed by their substituents. In 2017, Goodwin *et al.* have synthesised the cation $[Dy(Cp^{ttt})_2]^+$ (with Cp^{ttt-} = Cp^tBu_3-1,2,4) that is slightly less axial than the previous $[Dy(OtBu)_2(py)_5]^+$ compound (Cp-Dy-Cp = 152.8°), but with a close energy barrier U_{eff}/k_B = 1760 K and above all, a hysteresis loop opens up to 60 K.[48] The authors explained this outstanding result thanks to a high crossover temperature between the Orbach and the Raman processes, due to a less efficient spin-phonon coupling imprinted by the vibrational modes of the rigid Cp^{ttt} groups. Several examples of dysprosocenium molecules have been synthesised with Cp derivatives to correlate their crystal structure and magnetic performances, concluding that compromise has to be found between the angle Cp-Dy-Cp, and the Cp-Dy distance to enhance the ligand field splitting.[49]

These conditions were fulfilled in the latest record-holding example that is an heteroleptic complex $[(Cp^{iPr5})Dy(Cp^*)]^+$ (with Cp^{iPr5} = Cp-penta-isopropyl and Cp* = Cp-penta-methyl) reported by Guo *et al.* in 2018.[50] The use of two different bulky ligands provides a wider Cp-Dy-Cp angle than the homoleptic $[Dy(Cp^{ttt})_2]^+$ (Cp-Dy-Cp = 165.5°) with shorter Dy-Cp distances (see the Figure 1.18 below), thus a stronger ligand field and a higher U_{eff}/k_B = 2217 K.

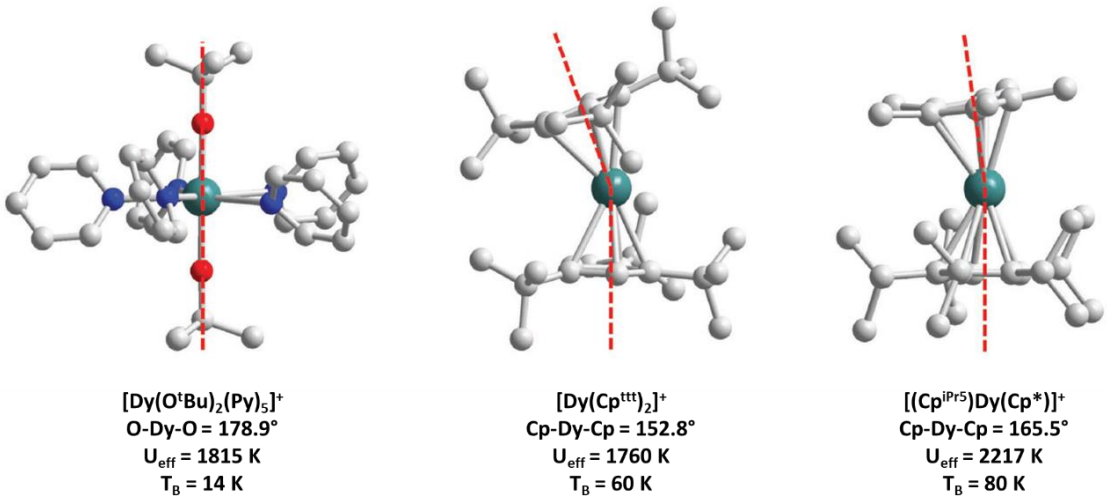

Figure 1.18. Comparison between the crystal structures and the magnetic performances of the principal dysprosocenium SMMs (with the axial angle as dashed red lines, adapted from Ref.[51]).

This improved axiality allowed to observe an open hysteresis loop up to 80 K, which means a major paradigm for the applicability of SMMs: it is the first time that an SMM operates at a temperature above the boiling point of liquid nitrogen (T_b = 77 K), clearing the way to potential industrial applications. However, besides improving the magnetic performances of these metallocenes, one has to keep in mind that these molecules are still highly sensitive to air and moisture. And this issue strongly hampers their integration into spintronic or data storage devices for the time being and should constitute a parallel research axis for the researchers.

1.3. Single-Chain Magnets

So far, we have focused on giving a brief description of discrete (0D) molecular magnets that are SMMs. However, extended magnetic networks (1D, 2D and 3D) may also be important in understanding complex magnetic phenomena to use them to obtain novel and technologically relevant magnets. However, increasing the dimensionality of a lattice drastically increases the difficulty of making an accurate interpretation; this is why physicists and chemists have initially focused their efforts on low-dimensional systems (one-dimensional molecular magnets in our case), easier to rationalize.[52]

If the reader is reminded of what was established in Part.1.1.4.1, he may legitimately ask the following question: why focus our interest on compounds that theoretically do not exhibit long-range order? Indeed, a demonstration was provided by Landau[53] and reproduced by Launay and Verdaguer in their book "Electrons in Molecules".[14] Because of its clarity, we feel it is important to quote this demonstration here as well.

"Let us take a ferromagnetic chain. The ground state should correspond to a configuration where all the spins S are aligned parallel, due to the ferromagnetic interaction J > 0 between neighbouring spins. The total spin is simply S_{GS} = N.S. An excited state can be built by reversing part of the spins. The enthalpy cost is the coupling constant, ΔH = J. For any system, change is determined by the free enthalpy ΔG = ΔH - T.ΔS, where ΔS is the entropy change. As the previous spin-reversing process can occur at N-1 positions along the chain, ΔS = k_B.ln(N-1). Then:

$$\Delta G = \Delta H - T.\Delta S = J - k_B T ln(N-1)Z \qquad \text{Eq. 1.29}$$

which means that when the number of spins N is large enough (and clearly for N → ∞), at a given T ≠ 0 K, the negative entropy term can become higher in absolute value than the positive enthalpy on, J. Then ΔG < 0. Spontaneously, the system abandons the ordered configuration (a) for a disordered one (b). There is no long-range order in 1D at T ≠ 0 K."

Indeed, the last sentence of this paragraph exclude local ordering. We will describe the implications of this statement and how it can be used to build 1D chain magnets, which will be called hereafter Single-Chain Magnets (SCMs).

1.3.1. Static magnetic properties of SCMs

Let us continue our description with the model considered in the previous demonstration, which is the Ising one: the chain is made of an infinite alternation of identical spins *S*, aligned along the *z*-axis and coupled to each other by a constant magnetic interaction *J*.

The related spin Ising Hamiltonian of this system is the following:

$$\mathcal{H} = -J \sum_{i=0}^{\infty} S_i \cdot S_{i+1} = -JS^2 \sum_{i=0}^{\infty} \sigma_i \cdot \sigma_{i+1} \qquad \text{Eq. 1.30}$$

with $\sigma = \pm 1$ (S being constant) depending on the spin orientation along the *z*-axis.

Because of its simplicity, this Ising model does not take into account the anisotropy of the spins, due to the ligand field (3*d* ions) and/or intrinsic properties (4*f* ions) in real systems. The resulting anisotropic Heisenberg Hamiltonian become then:

$$\mathcal{H} = -J\sum_{i=0}^{\infty} S_i \cdot S_{i+1} + D\sum_{i=0}^{\infty} S_{i,z}^2 = -JS^2\sum_{i=0}^{\infty} u_i \cdot u_{i+1} + DS^2\sum_{i=0}^{\infty} u_{i,z}^2 \quad \text{Eq. 1.31}$$

with *u* the unit vector depending on the orientation of the spin along the easy *z*-axis, and *D* the anisotropy parameter of the considered ion ($D < 0$ for the axial anisotropy and $D > 0$ for plane one).[54]

Just from this Hamiltonian, one can intuitively understand the prerequisites to stabilise the system (or minimise its energy): the spin *S* has to be the higher as possible, the coupling ferromagnetic ($J > 0$) and the anisotropy strongly axial ($D < 0$). In this specific case, a magnetic correlation phenomenon can occur between the spin carriers: by lowering the temperature, the spin correlation ξ, mediated by the term *D* and *J*, propagates and increases along the chain, creating oriented domains of $L = 2\xi$ length separated by domain walls.

The energy Δ_ξ associated with the creation of such domain wall was linked with the characteristic magnetic parameters (*S*, *J* and *D*), as is their width:[55,56]

- If the parameter $|D/J| < 4/3$, the transition between two oriented domains is progressive, *i.e.*, the domain walls are broad, with $\Delta_\xi \approx 4S^2\sqrt{|JD|}$;
- If the parameter $|D/J| > 4/3$ (the Ising limit), the transition between two oriented domains is abrupt, *i.e.*, the domain walls are narrow, and the related energy is $\Delta\xi = 4|J|S^2$.

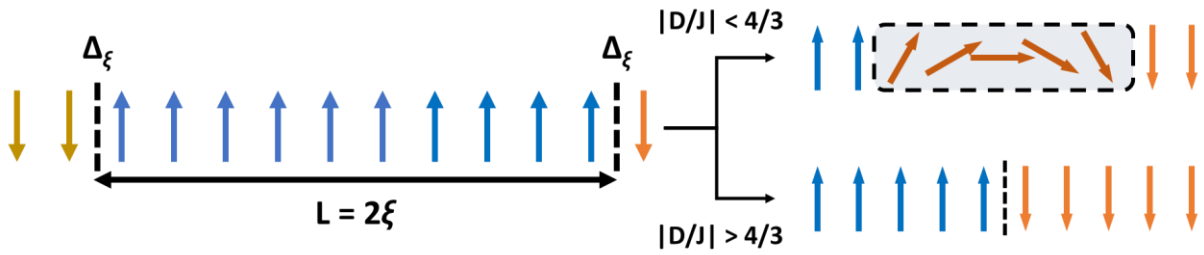

Figure 1.19. Representation of the correlation length *L* in a spin chain (left) and the cases of broad (top) and narrow (bottom) domain wall width.

For the sake of clarity, we will consider in this thesis only the case of SCMs that satisfy the Ising limit, which corresponds to most of the experimental SCMs reported (other models are further detailed in the Ref.[57–60]).

In this case, the correlation length <L> = 2ξ along the chain diverge exponentially while the temperature is lowered, as does the magnetic susceptibility:

$$\chi_M T = C_{eff}.\exp\left(\frac{\Delta_\xi}{k_B T}\right) \quad \text{Eq. 1.32}$$

with C_{eff} the effective Curie constant.

Therefore, the domain wall energy Δ_ξ can be extracted from the linear slope of the ln($\chi_M T$) *vs* 1/*T* plot, helpful in estimating the mean domain length <*L*>. This approximation is however valid if structural defects do not hinder the correlation phenomenon along the chains (diamagnetic ions, length polydispersity, *etc.*) or magnetic saturation (too high magnetic field *H* applied), highlighted by a plateau in the high 1/*T* (or low *T*) region.

1.3.2. Relaxation dynamics of the magnetisation in SCMs

Now, the issue is to know if these chains of infinite oriented domains can maintain their magnetisation after the removal of an applied magnetic field, like the SMMs. To tackle this, R. J. Glauber has described in 1961 the probability of a spin reversal (or flip) within an Ising chain that interacts with a thermal bath by stochastic functions of time.[61]

This pioneering work made it possible to describe the slow relaxation of the magnetisation, whose characteristic time τ follows an Arrhenius law (as for the Orbach process of SMMs):

$$\tau = \tau_0 \exp\left(\frac{\Delta_{eff}}{k_B T}\right) \qquad \text{Eq. 1.33}$$

with Δ_{eff} the activation energy for the flipping of a spin unit deduced from the slope of the ln(τ) = 1/*T* plot (called Arrhenius plot).

Until now, we only have considered the perfect case of study where the spins chains are infinitely long. However, in real systems, these chains obviously include some defects, and this has implications for the correlation propagation and the value of the activation energy Δ_{eff}, which we will detail.

At higher temperatures, the correlation length is small compared to the effective size of the chain; it is the infinite regime. The activation energy Δ_{eff} for the reversal of the magnetisation has to overcome the energy barrier Δ_ξ at each side of the chain (so $2\Delta_\xi$), in addition to the anisotropic contribution $\Delta_A \approx |D|S^2$. Its value becomes then:

$$\Delta_I = 2\Delta_\xi + \Delta_A = 8|J|S^2 + |D|S^2 \qquad \text{Eq. 1.34}$$

At low temperatures, the propagation of the correlation length ξ is hampered by the size of the chain (or the presence of diamagnetic defects); it is the finite regime.[62–65] In this case, as depicted in Figure 1.20, the flipping energy Δ_τ has to overcome only one energy barrier Δ_ξ instead of two, and its expression is now:

$$\Delta_F = \Delta_\xi + \Delta_A = 4|J|S^2 + |D|S^2 \qquad \text{Eq. 1.35}$$

Knowing the values of Δ_I and Δ_F, we can determine the value of Δ_ξ ($\Delta_\xi = \Delta_I - \Delta_F$), as well as the crossover temperature *T**, which allows estimating the mean the correlation length <*L*> with the distance *a* between the two consecutive magnetic centres considererd, and therefore the number *n* of coupled units, thanks to the following equation:

$$n = \frac{\langle L \rangle}{a} \approx \exp\left(\frac{\Delta_\xi}{k_B T^*}\right) \qquad \text{Eq. 1.36}$$

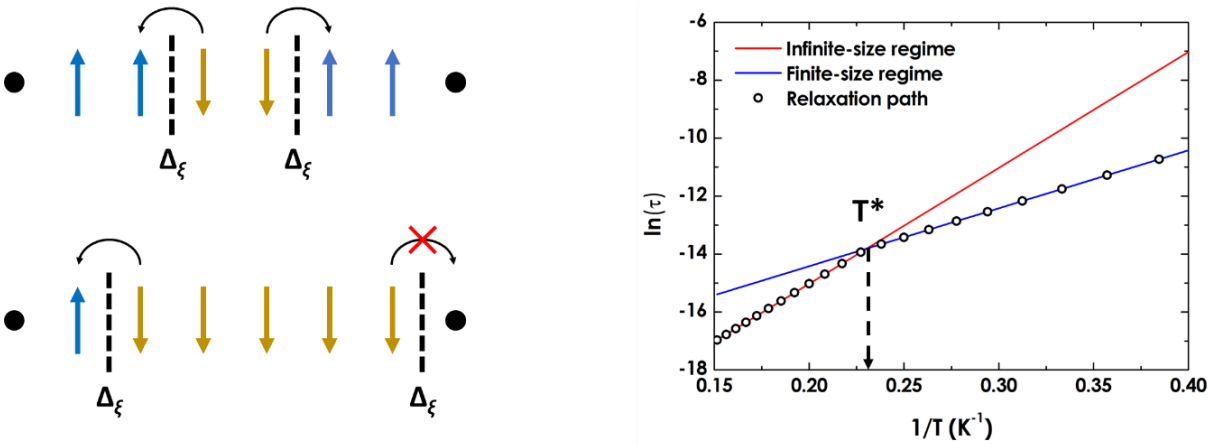

Figure 1.20. Representation of the relaxation dynamics in the infinite (top) and finite (bottom) regimes, and a simulated Arrhenius plot of the corresponding relaxation times τ (right).

The main advantage of the SCMs over the SMMs lies in this relaxation process described above. Because of their mesoscopic dimensions, they are less prone to parasitic relaxation modes such as Direct or Raman, and especially the QTM one (excepted in the cases of very short chains and at very low temperatures).[66] This relaxation "robustness" makes SCMs a good candidate for the design of nanoscale molecular magnets.

To summarise, by taking into account the considerations we have detailed in the last two parts, several key points are necessary to obtain a coordination polymer with a slow relaxation of its magnetisation:

1. The magnetic centres should exhibit a high spin and a significant axial anisotropy to favour a bistable orientation of the magnetisation;
2. Moreover, the individual chains must be effectively magnetically isolated from each other to preserve their peculiar 1D relaxation dynamics;
3. The magnetic interactions between the latter have to be sufficient enough to propagate a correlation phenomenon through ferro- or ferrimagnetic interactions.

1.3.3. Synthetic strategies towards SCMs

These points were used as guidelines to conceptualise strategies for the design of SCMs, which are nicely summarised in the reviews Ref.[67,68]. Among them, one of the most straightforward would be to use SMMs as buildings blocks,[69–72] thanks to their intrinsic spin and axial anisotropy, and arrange them ferro- or ferrimagnetically in one dimension. This approach has proven successful in providing SCMs, the most notable of which is the $(NEt_4)[Mn_2(5\text{-MeOsalen})_2Fe(CN)_6]$ (with 5-MeOsalen^{2-} = N,N'-ethylenebis-5-methoxysalicyl-ideneiminate) synthesised in 2005 by Ferbinteanu *et al.*[73] The magnetic properties of this coordination polymer, made of a linear arrangement of SMM Mn^{III}-Fe^{III}-Mn^{III} trimers, was accounted for a SCM behaviour, with the peculiar crossover between the finite- and infinite relaxation regimes (Δ_I/k_B = 31 K and Δ_F/k_B = 25 K) and an open hysteresis loop up to 1.4 K.

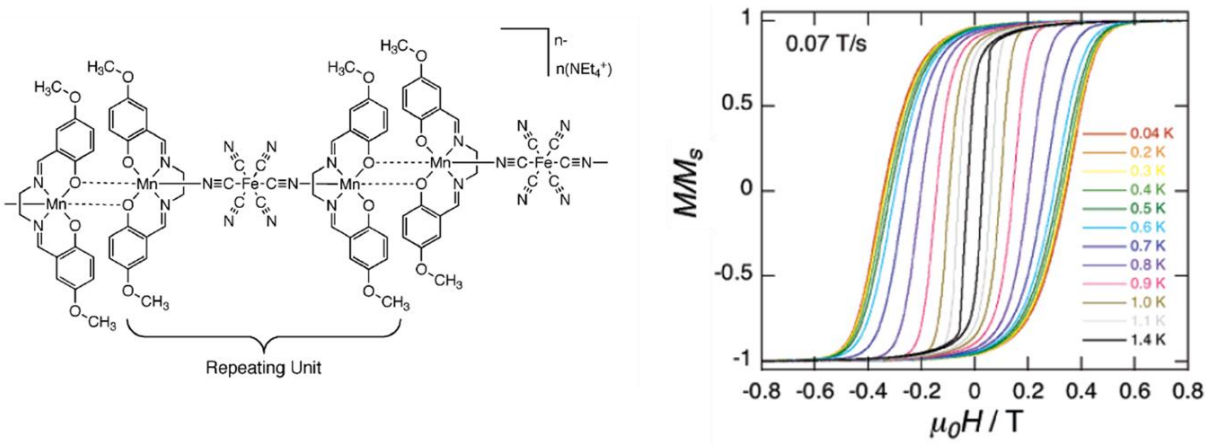

Figure 1.21. Schematic representation (left) and magnetic hysteresis curves (right) of the $(NEt_4)[Mn_2(5\text{-}MeOsalen)_2Fe(CN)_6]$ (reproduced from Ref.[73]).

The attractivity of this family of salmen-derivative ligands as building blocks for SCM, extensively studied by the groups of Clérac and Miyazaka,[74–78] is due to its coordination mode. It occupies the equatorial plane of the metal ion, improving its axial anisotropy (through the Jahn-Teller effect) and giving access to the apical positions to form 1D linear arrangements.

However, obtaining linear chains of SMMs does not guarantee an effective SCM behaviour. The use of building blocks susceptible to show a QTM relaxation can induce analogous spontaneous nucleation of domain walls.[58,79] Additionally, if the interactions between the SMMs subunits are too weak, the latter will act as independent SMMs and not as SCM.[80,81]

A way to prevent this is to use paramagnetic linkers as relays or enhancers of the exchange interaction. The first class of molecules to achieve this are the 3*d* cyanide complexes. They allow short connectivity between metal ions, enabling strong exchange interactions, and their multiple coordination modes make them very versatile building blocks for constructing molecular magnetic materials.[82–84] In the case of the SCMs, the cyanide complexes used can be classified as either homoleptic, $[M^m(CN)_n]^{m-n}$ (with n = 6 or 8)[78,85–90] or heteroleptic, $[M^mx.L^l(CN)_n]^{m+x.l-n}$,[91–93] if some cyanides have been replaced by one or several organic ligands. According to the type of ligand used, one can tailor the axial anisotropy metal ion and the magnetic interactions, as nicely demonstrated by Pichon *et al.* recently.[94]

They have designed a Fe^{II} centre with a planar pentadentate macrocycle (L^{N3O2Ph} = 2,6-diacetylpyridine-bis(phenyl-hydrazone)) to impose a pentagonal pyramid coordination environment, favouring an axial anisotropy along with the free apical positions.[95–97] It was coupled with a Cr^{III}-cyanide complex in the same coordination environment to enhance this anisotropy, known to give rise to a ferromagnetic coupling with the Fe^{II} unit. The resulting chain is quite linear, and the equatorial Fe^{II}-ligand planes defined by the two non-equivalent units are nearly parallel (with a slightly tilted angle of around 4°).

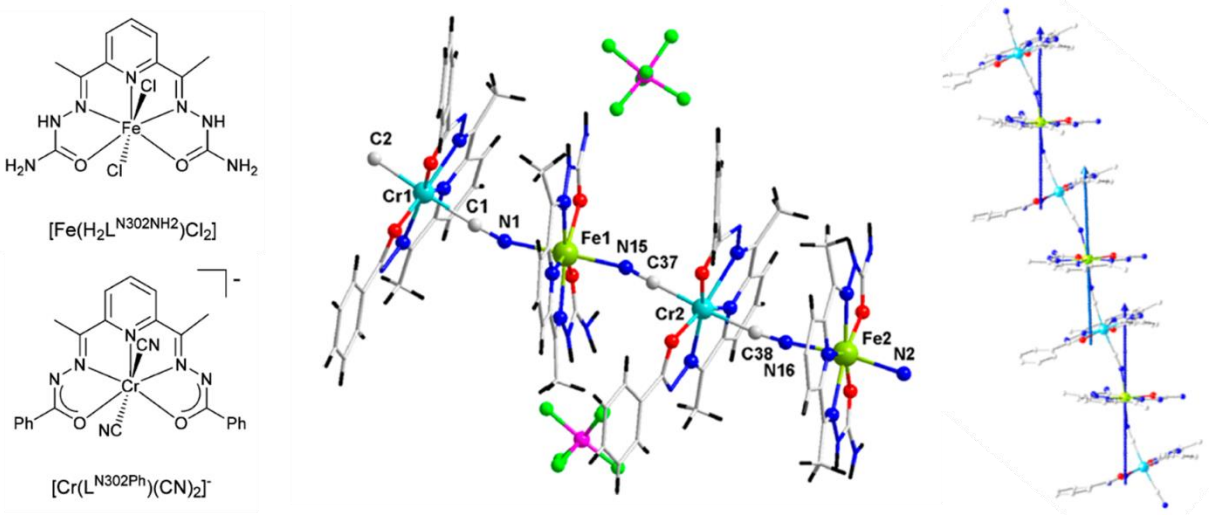

Figure 1.22. Schematic representations of the starting Fe^{II} and Cr^{III} building blocks (left), of the resulting $[Cr(L^{N3O2Ph})(CN)_2Fe(H_2L^{N3O2NH2})]$ crystal structure (middle) and the corresponding easy magnetic axis of the Fe^{II} centres (right) (reproduced from Ref.[94]).

The resulting magnetic properties are in accordance with a SCM behaviour characterised by the crossover between the finite- and infinite relaxation regimes. Despite a weak ferromagnetic exchange coupling (J/k_B = 3.4 K) between the Cr^{III} and Fe^{II} centres, the relative orientation of the uniaxial anisotropy of the latter, oriented along the C≡N-Fe-N≡C axes, are nearly collinear and contribute to the high energy barrier values reported (Δ_I/k_B = 113 K and Δ_F/k_B = 96 K).

Interestingly, this family of cyanide ligands is also at the origin of a particular kind of magnetic chain, whose SCM behaviour is due to photoinduced spin-crossover (SCO) effects between heterometallic centres.[98–102]

1.3.3.1. The metal-radical approach

In this thesis, however, we will focus on the use of organics radicals as ligands. Indeed, this *metal-radical approach*,[103,104] developed simultaneously by the groups of Miller and Gatteschi, has led to several notable achievements in molecular magnetism,[105,106] among which the synthesis of the first SCM, the $[Co(hfac)_2(NITPhOMe)]$ (with NIT = nitronyl nitroxide), which will be detailed further in the Part.1.3.3.3.[107] The design of 4*f*-based molecular magnets has also taken advantage of organic radicals: the diffuse spin orbitals of the radicals can reach the inner 4*f* orbitals, leading to stronger super-exchange coupling as demonstrated in dinuclear lanthanides complexes[108–110] (the reader interested in radical-based SMMs can refer to the exhaustive reviews in Ref.[111,112]).

1.3.3.2. The nitronyl nitroxide radicals

In the following sections, we will take a closer look at NIT radicals and their applications in the design of SCMs.

The nitronyl nitroxides are a class of free radicals, firstly synthesised in the late 1960s by Ullmann *et al.*[113–116] The first step of this synthesis, whose protocol is detailed in Part.3.A.1.1, is the partial reduction of the 2,3-dimethyl-2,3-dinitrobutane by a mild reducing agent, leading to the N,N'-di(hydroxylamino)-2,3-dimethylbutane (or "BHA"). Unfortunately, the latter is obtained with poor reproducibility, although improvements to the procedure have been made recently.[117,118] Then, its condensation with an aldehyde *R*-CHO leads to the 1,3-Dihydroxy-2-(*R*)-4,4,5,5,-tetramethylimidazolidine called after "PreNIT-*R*". The PreNIT is partially oxidised to obtain the corresponding 2-(*R*)-4,4,5,5,-tetramethylimidazolidine-1-oxyl-3-oxide, or "NIT-*R*". At this point of the synthesis, precautions have to be taken because too severe oxidation could lead to the irreversible formation of the imino-nitroxide (IMN) derivative.

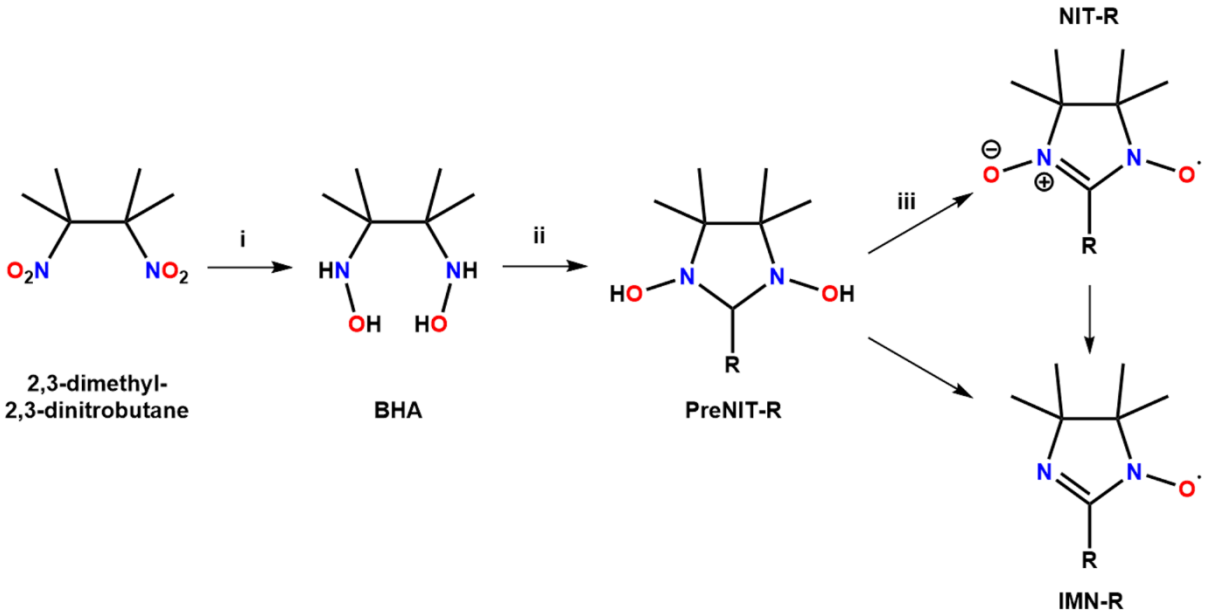

Figure 1.23. Synthetic pathways toward nitronyl nitroxides: i) Zn powder, THF:H_2O; ii) R-CHO, MeOH; iii) $NaIO_4$, CH_2Cl_2:H_2O.

The two equivalent NO groups allow the delocalisation of the unpaired electron along with the O-N-C-N-O group[119–121] (which explain its unusual stability as a free radical) and act as coordinating donor sites. This symmetrical structure allows them to bind as monodentate ligands in a μ-1,1 fashion, which is particularly interesting to build alternating 1D coordination polymers and especially SCMs.

However, the NIT radicals' weak coordination ability[122] limits their bonding to metal ions whose Lewis acidity has been exacerbated by electron-withdrawing groups, such as hfac$^-$ (hexafluoroacetylacetonate) β-diketonates bearing two -CF_3 moieties. Fortunately, the corresponding 3*d* and 4*f* complexes are usually coordinated by two and three β-diketonate molecules, respectively,[123] leaving two coordinating positions free.

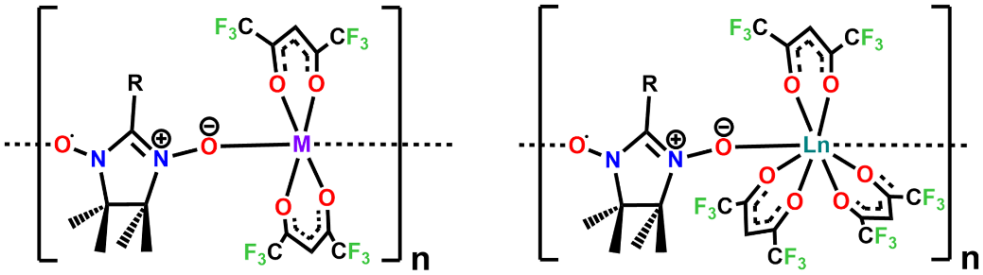

Figure 1.24. Schematic representations of the coordination bonding for a 3*d* (left) or 4*f* (right) NIT-based chain.

Thanks to these structural features, a large number of metal-NIT linear chains[124] (and even wheels)[125,126] have been studied, and their magnetic behaviour rationalised. Indeed, the straightforward condensation step between the BHA and an aldehyde derivative has permitted to finely design the resulting NITs with diverse functional groups, according to the targeted application.[127–129]

1.3.3.3. Examples of notable NIT-based SCMs

We will now describe some remarkable NIT-based SCMs from the literature, a recent exhaustive review by Meng *et al.* can be found in Ref.[124] for more examples.

The first experimental observation of SCM behaviour was reported in 2001 by Caneschi *et al.* in a [Co(hfac)$_2$(NITPhOMe)] coordination polymer (with NITPhOMe = 4'-(methyloxy)phenyl -4,4,5,5-tetramethyl-imidazolin-1-oxyl-3-oxide), where Co(hfac)$_2$ and NITPhOMe moieties are alternately arranged (see Figure 1.25).[107] Besides preventing interchain interaction by steric hindrance, the advantage of the phenyl group is explained by the π- interactions it forms with the aromatic hfac ones bearded by the 3*d* ion, which reinforces the rigidity of the molecule's "skeleton".[130] Combined with the symmetry operations of the non-centrosymmetric $P3_1$ space group, the chain grows in helix, a feature already reported in the Mn^{II} derivative,[131] and is at the origin of second harmonic generation[132], magneto-chiral dichroism[133] and electric field modulation of magnetic exchange effects.[134]

From a magnetic point of view, the coupling exchange between the NIT radical and the Co^{II} moieties is antiferromagnetic. However, because of the magnetic anisotropy of the Co^{II} ions ($g_{\parallel}$ = 9 for a given S = ½) compared to the isotropic NIT (g = 2 and S = ½), the magnetic moments do not compensate, and the resulting chain behaves as a 1D ferrimagnet.[135]

As expected for SCM magnetic properties, the temperature dependence of the $\chi_M T$ product measured on single-crystals show a clear divergence at low temperature that indicate an Ising-type anisotropy[135] and a correlation onset along the chain (Eq. 1.32), as well as a slow relaxation of its magnetisation with an energy barrier Δ_{eff}/k_B = 153 K. This latter led to the opening of the magnetic hysteresis loop up to 4.0 K (with a coercive value of H_C = 4 kOe), unprecedented at this time for 1D molecular compounds. The visible steps are not due to quantum effect (Figure 1.25), contrary to the ones observed for SMMs, but because of the spin-canted structure generated by the non-collinearity of the easy-axes that finally align along the same axis by applying a sufficiently strong H_{DC} field.

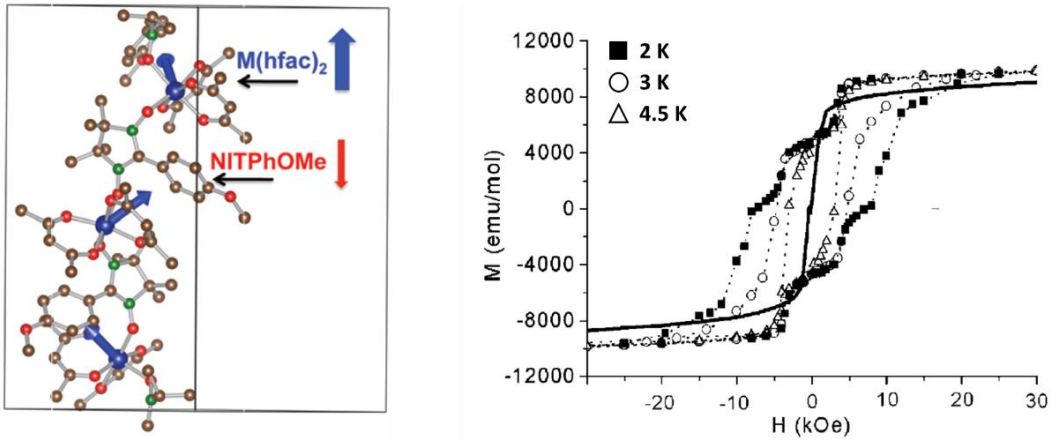

Figure 1.25. Representation of the [Co(hfac)$_2$(NITPhOMe)] crystal structure (hydrogen and fluorine atoms omitted for clarity) with easy magnetic axes as blue arrows (left, reproduced from Ref.[136]) and magnetic hysteresis loop measured at different temperatures (right, adapted from Ref.[107]).

A few years after, the group of Ishida have studied similar Co^{II} systems but based on a family of NITs with longer carbon chains, from C2 to C5, in para- or ortho- position of the phenyl groups. The resulting Co-NIT chains, deduced from the *p*-C4, *p*-C5 and *o*-C2 derivatives,[137–139] crystallise in a usual P2$_1$ system and adopt a zig-zag conformation, the angles NIT-Co^{II}-NIT chain imposed by the π- interactions compensating to form a linear chain.

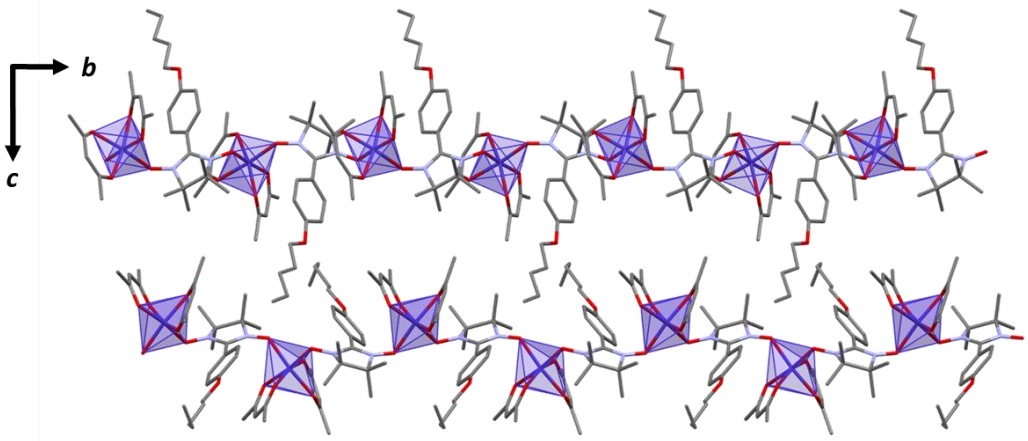

Figure 1.26. Representation of the two crystallographically independent chains of the [Co(hfac)$_2$(NITPhO-*p*-C5)] crystal structure along the *a*-axis (hydrogen and fluorine atoms omitted for clarity).

However, if their molecular structures are far from remarkable, their magnetic properties are worth looking at. Indeed, they gather some of the characteristics expected for SCMs: divergence of the $\chi_M T$ product at low T and slow relaxation of the magnetisation. However, the corresponding energy barriers are more than twice as large as those reported for the previous [Co(hfac)$_2$(NITPhOMe)], with values around $\Delta E/k_B \approx 300$ - 360 K. This resulted in open hysteresis curves with colossal coercive field values $H_C \approx 50$ kOe and a record blocking temperature $T_B = 14$ K at that time.[140]

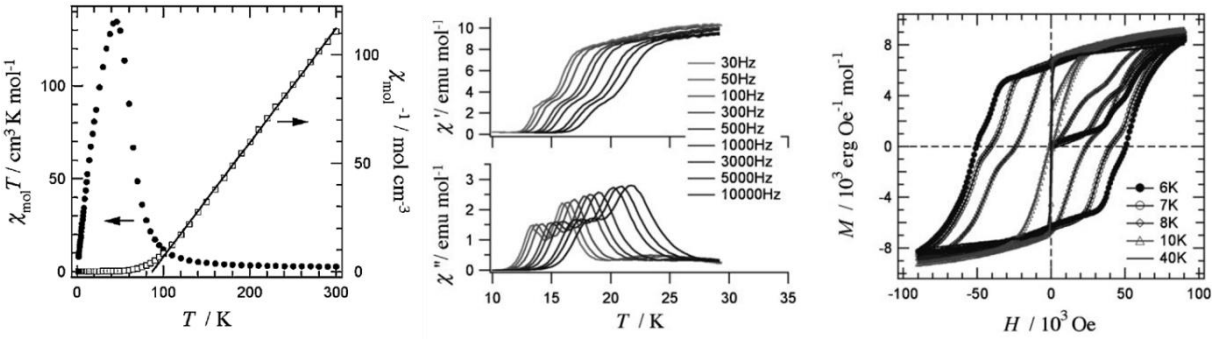

Figure 1.27. Temperature dependence of χ_M and $\chi_M T$ (left), of the AC susceptibilities at various frequencies (middle) and hysteresis curves at various temperatures (right) of the [Co(hfac)$_2$(NITPhO-*p*-C5)] (reproduced from Ref.[138]).

Unfortunately, such impressive performances were not only due to pure SCM behaviour but also to the rise of a 3D ordered phase because of non-negligible interchain interactions, as probed by muon-spin spectroscopy.[141]

Despite this, interest in the Co^{II}-NIT system has persisted, with the syntheses of highly performant Co-NIT SCMs *via* polycyclic aromatic hydrocarbon groups. The first, reported by Vaz *et al.* in 2014, was obtained by the coordination of Co(hfac)$_2$ with a pyrenyl derivative NIT, the NITPyr,[142,143] to form a twofold helical chain.

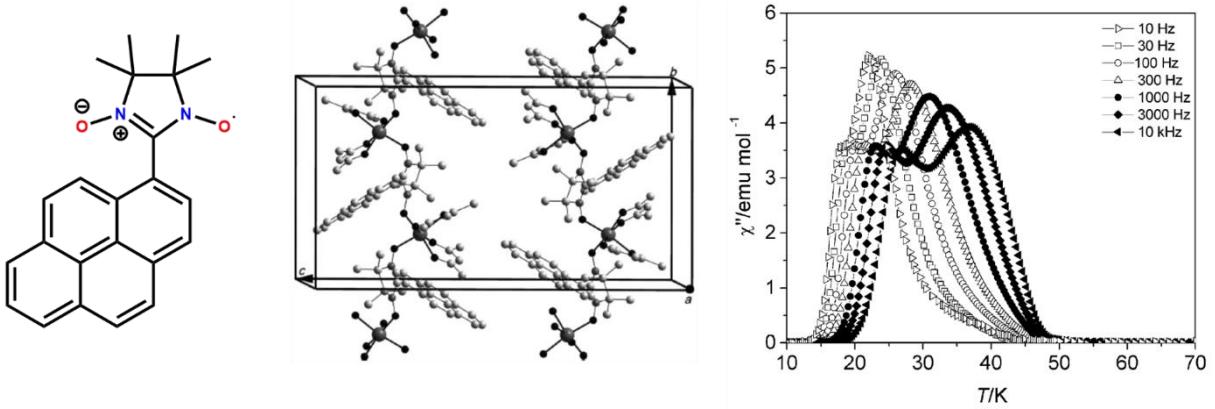

Figure 1.28. Representation of the NITPyr (left) and the crystal structure (hydrogen atoms and hfac groups omitted for clarity) of the resulting [Co(hfac)$_2$(NITPyr)] along the *a*-axis (middle). Temperature dependence of out-of-phase susceptibility at various frequencies (right) for [Co(hfac)$_2$(NITPyr)] (reproduced from Ref.[143]).

The blocking temperature was estimated at T_B = 17 K, with open magnetic hysteresis loops below this temperature (H_C = 32 and 9 kOe at 8 and 2 K, respectively), thanks to dominant intrachain interactions shielded by the large polyaromatic groups. Interestingly, two distinct peaks are observed in AC susceptibility measurements, indicating two distinct relaxation processes, but with similar finite-regime energy barriers $\Delta_{\tau.(1)}/k_B$ = 377 K and $\Delta_{\tau.(2)}/k_B$ = 396 K. This unexpected feature was accounted by the authors for the simultaneous presence of long and short chains, due to the loss of solvent molecules, which would also be responsible for the decrease of the coercive field at lower temperature.

The last examples were provided very recently by Liu *et al.*, based on the [Co(hfac)$_2$(NITPhO-*o*-C2)] and the [Co(hfac)$_2$(NITPyr)] mentioned previously. They have designed NIT radicals bearing a naphthalene derivative with methyloxy- (NITNaphOMe) or ethyloxy- (NITNaphOEt) chains in ortho- position of the central phenyl to investigate the role in their orientation on the magnetic properties.[144] The corresponding [Co-NIT] chains crystallise in a chiral P2$_1$22 space group. The 2$_1$ screw axes combination gives rise to two different spatial arrangements of alternating chains, despite a single crystallographically independent Co^{II} centre. The contribution of these two "sublattices" result in hysteresis loops with coercive fields of 59 and 65 kOe and unprecedented squarenesses of 91 and 97 % at 7 K, for the [Co(hfac)$_2$(NITNaphOMe)] and [Co(hfac)$_2$(NITNaphOEt)], respectively.

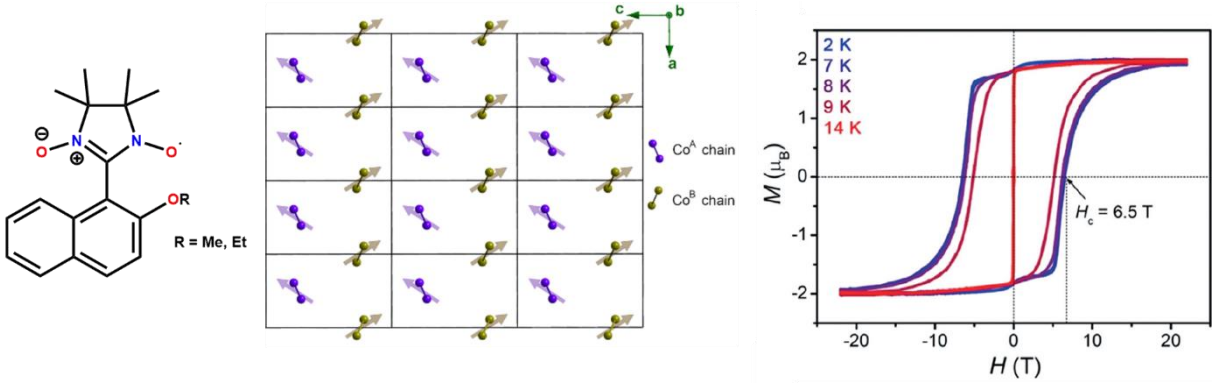

Figure 1.29. Representation of the NITNaphOR (left), extended spatial array of the two non-equivalent Co^{II} sublattices (middle) and hysteresis curves at various temperatures (right) of the [Co(hfac)$_2$(NITNaphOEt)] (reproduced from Ref.[144]).

So far, we have only discussed the 3*d*-NIT SCMs. Indeed, preserving a SCM behaviour while replacing the 3*d* ions by 4*f* ones is not an easy task; although the latter are good candidates due to their strong Ising anisotropies, the buried character of their orbitals prevents efficient exchange interactions.

This challenge has nevertheless been met by Benelli and co-workers in the early 90's, who have synthesised a first series of [Ln(hfac)$_3$(NITEt)] chains (Ln = Y, Gd, Eu, Tb, Dy, Ho and Er).[145–149] Magnetic properties of such chains have revealed the presence of dominant antiferromagnetic next-nearest neighbour (NNN) interactions $J_{NIT\text{-}NIT}$ and $J_{Ln\text{-}Ln}$, that compete with the usual ferromagnetic next-nearest (NN) one $J_{Ln\text{-}NIT}$.[147] The chains made of the most anisotropic centres (from the Tb to the Ho) display an antiferromagnetic 3D ordering around 4 K, which was accounted for through-space dipolar interactions between the interchain Ln centres.

To suppress these interactions, Bogani *et al.* have decided to increase this interchain distance by designing a NITPhOPh radical with bulky aromatic groups as spacers.[150] The shortest interchain Dy-Dy distance has effectively increased, from 10.76 Å (for [Dy-NITEt]) to 11.35 Å, and the resulting [Dy(hfac)$_3$(NITPhOPh)] coordination polymer displayed the first SCM behaviour from a 4*f* chain.

However, the energy barriers deduced from the Arrhenius plot (see Figure 1.30 below) are relatively smaller (Δ_I/k_B = 69 K and Δ_F/k_B = 42 K) than the ones reported for the Co^{II}-based SCMs, because of less intense NN and NNN exchange couplings ($J_{NIT\text{-}NIT}$ = - 6.5 K, $J_{Dy\text{-}Dy}$ = - 4 K and $J_{Ln\text{-}NIT}$ = 19 K). The latter are also at the origin of the steps at 50 Oe and 15 kOe visible on the hysteresis curve.

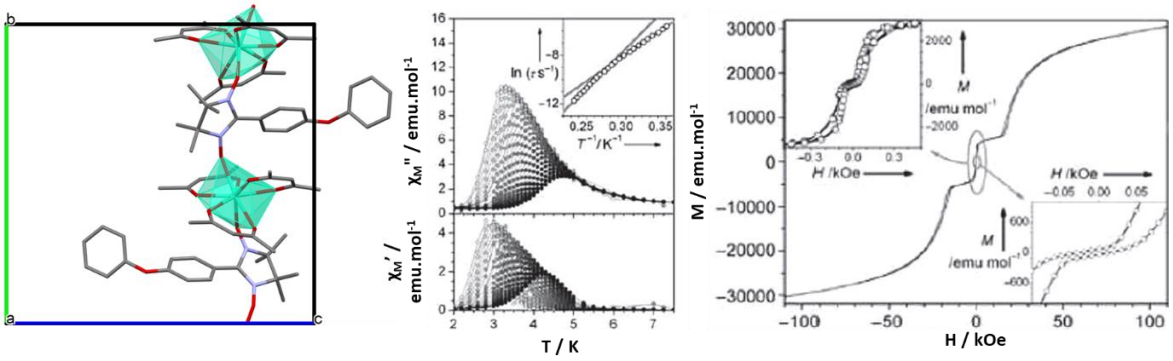

Figure 1.30. Representation of the crystal structure (hydrogen and fluorine atoms omitted for clarity) (left), temperature dependence of AC susceptibilities at various frequencies, with in inset the resulting Arrhenius plot (middle) and hysteresis curve at 1.6 K (right) of the [$Dy(hfac)_3$(NITPhOPh)] (reproduced from Ref.[150]).

As for the [Ln-NITEt] chains described above, a systematic magnetic comparison has been carried out between isostructural [$Ln(hfac)_3$(NITPhOPh)] (with Ln from Gd to Yb) by Bernot *et al.*, to rationalise the influence of the Ln anisotropy on the SCM behaviour.[151,152] Without surprise, the isotropic derivatives (Gd and Yb) did not exhibit a divergence of the $\chi_M T$ product at low T. Instead of an Ising-type arrangement, the spins arrange themselves helically and compensate along the chain, leading to a decrease of the $\chi_M T$ product, already observed for the [Gd-NITEt].[153] For the other ions with Ising-type anisotropies, the domain wall energy barrier Δ_ξ (deduced from Eq. 1.32) increases while increasing the ion anisotropy, as well as the temperature range of the out-of-phase susceptibility signal.

Crossover between SCM and SMM behaviours have also been reported in NIT SCMs with the [{$Dy(hfac)_3$(NITPhIm)}$Dy(hfac)_3$] (with Im = imidazole).[154] Contrary to the examples we have described above, the Dy^{III} and NIT moieties are not coordinated in a μ-1,1 fashion to form a nearly linear chain: in this case, the NITIm bridges two Dy^{III} units, one classically coordinated by one of the two N-O sites, and the other one by the imidazole unit. While decreasing the temperature down to 2 K, an out-of-phase susceptibility signal is observed only if a static field H_{DC} = 3 kOe is applied, reminiscent of the QTM phenomenon for SMMs. The Arrhenius plot displays two linear regions, either at high or low T, the former attributed to a SCM relaxation (Δ_τ = 83 K) and the latter, an SMM [NITIm-Dy-NITIm] one (U_{eff} = 17 K). It is noteworthy that if such NIT-Ln-NIT complexes (or "monomers") are isolated, they can give reliable information on the anisotropy of the Ln centres, useful to explain the magnetic behaviour of the corresponding chain.[155,156] This compound is a good example that the correlation phenomenon can also propagate other than through the N-O-C-N-O group of the NIT radical, within this case weak ferromagnetic couplings between the Dy(hfac) and the phenyl and imidazole rings.

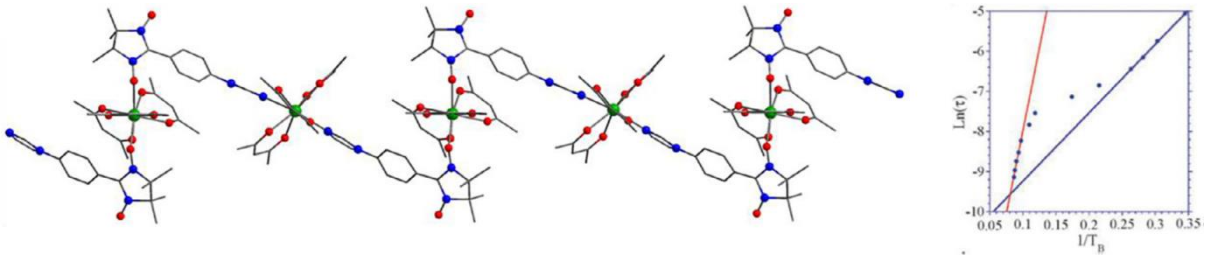

Figure 1.31. Representation of the crystal structure (hydrogen and fluorine atoms omitted for clarity) of the [{Dy(hfac)$_3$(NITPhIm)}Dy(hfac)$_3$] (left), and corresponding Arrhenius plot of the relaxation times measured at H_{DC} = 3 kOe, with the blue and the red lines fitting for the SMM and SCM dynamics, respectively (reproduced from Ref.[154]).

The concepts that have emerged from these works have made it possible to expand the family of 4*f*-SCMs, even though they remain quite scarce in the literature.[156–162]

An alternative way was to combine the 3*d* and 4*f* ions to modulate further the magnetic interactions.[163–165] Because we will focus on the 3*d*-4*f* NIT SCMs, the interested reader is encouraged to refer to the recent reviews of Andruh and co-workers on the added value of such heterospin systems in the design of molecular magnetic materials.[165,166]

Encouraged by the early works on Cu^{II}-Gd^{III} complexes showing ferromagnetic interactions,[167–169] they have substituted the isotropic Gd^{III} towards more anisotropic Ln^{III} ions (Tb and Dy), mandatory for the design of SCMs.

The first example of 3*d*-4*f* NIT SCMs was reported by Zhu *et al*. among a family of [{Ln(hfac)$_3$}$_3$.Cu(hfac)$_2$NITPhO-*R*] to investigate the role of the -*R* group spacers (with Ln = Gd, Tb, Dy, Ho and Yb and *R* = All, Pr and Bnz).[170,171] All the chains are made of an unusual linear arrangement [Cu-Ln-Ln-Ln] bridged by the NIT radicals.

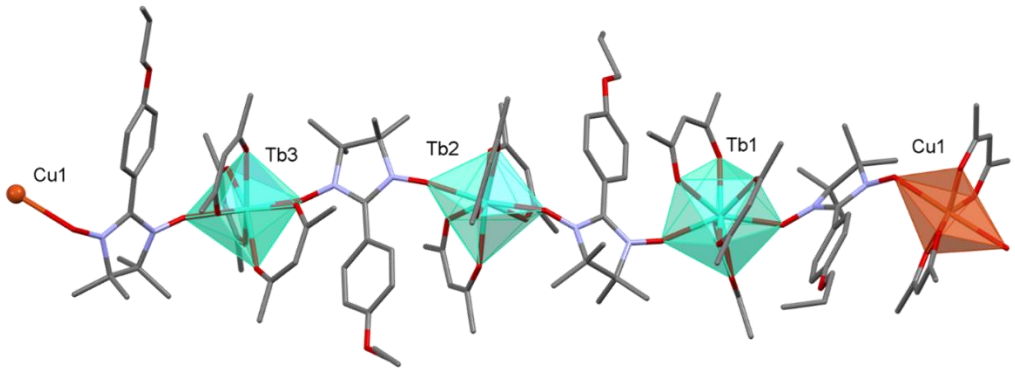

Figure 1.32. Representation of the crystal structure of [{Tb(hfac)$_3$}$_3$.Cu(hfac)$_2$NITPhOPr] (hydrogen and fluorine atoms omitted for clarity).

Only the [{Tb(hfac)$_3$}$_3$.Cu(hfac)$_2$NITPhOPr] derivative shows a divergence of the $\chi_M T$ susceptibility at low *T* and slow relaxation of the magnetisation with a frequency dependence of the AC susceptibility signals, characterized by an energy barrier Δ_τ = 21.4 K. The exchange interactions, investigated through the Gd derivative, have been found to be ferromagnetic between the nearest neighbours ($J_{NIT\text{-}Gd}$ = 7 K and $J_{NIT\text{-}Cu}$ = 25 K) with a smaller antiferromagnetic contribution between next-nearest neighbours ($J_{NIT\text{-}NIT}$ = - 5 K and $J_{Gd\text{-}Gd}$ = - 0.35 K).

However, the control of the arrangement is rather serendipitous in this case and lead to complicated magnetic pathways. By substituting the pendant group of the radical with nitrogen heterocycles (such as pyridine, imidazole or triazole), one can obtain a regular alternation [Cu-Ln], favoured by the selective coordination sites of the latter according to the Pearson's HSAB principles (Hard-Soft-Acid-Base).

The last example we wanted to illustrate provided by Huang et *al.* with the synthesis of a series $[Ln(hfac)_3Cu(hfac)_2(4\text{-NIT-MePyz})_2]$ (with Ln = Gd, Tb and Dy and MePyz = (1-methyl)-pyrazolyl).[172] The $Ln(hfac)_3$ moiety is coordinated to one of the NO groups of the NIT radical (the "hard" site), while the $Cu(hfac)_2$ will bond with the free nitrogen donor atom of the pyrazolyl cycle. As for the previous example, a SCM behaviour is observed for the Tb derivative, this time with the simultaneous presence of two relaxation contributions, one due to a SCM relaxation process, the origin of the second one being not yet identified.

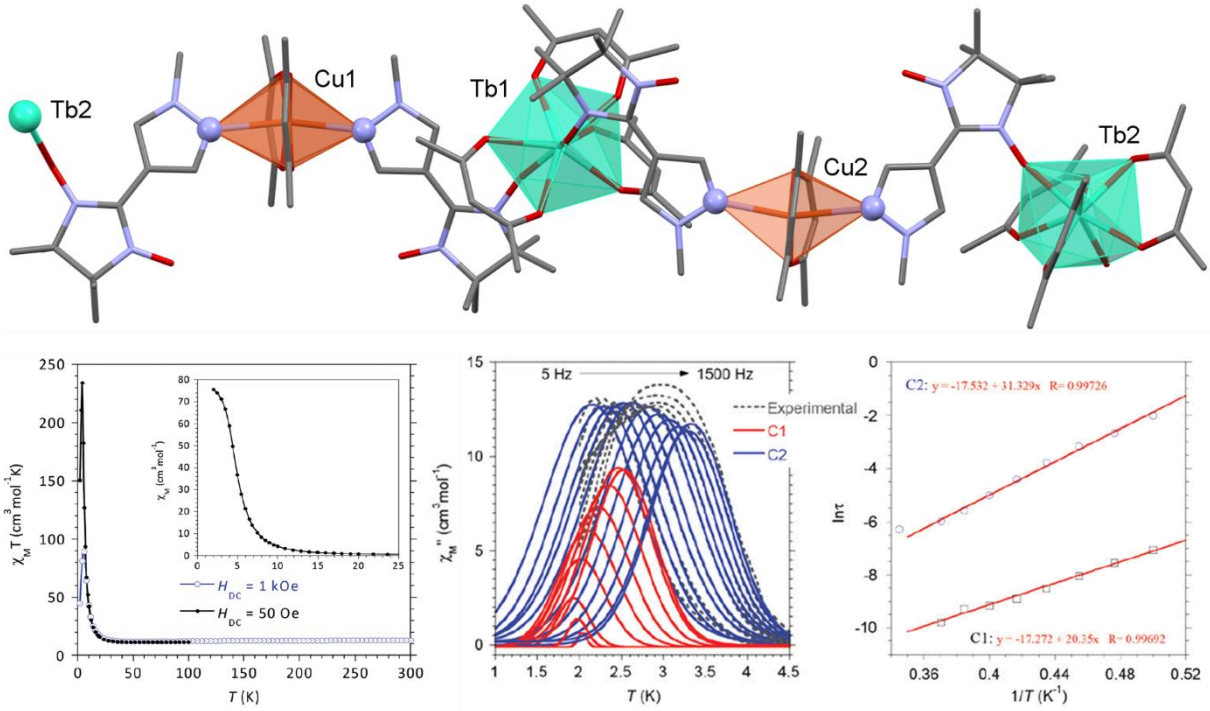

Figure 1.33. Representation of the crystal structure of $[Tb(hfac)_3Cu(hfac)_2(4\text{-NIT-MePyz})_2]$ (hydrogen and fluorine atoms omitted for clarity). Bottom: Temperature dependence of $\chi_M T$ under H_{DC} = 50 and 1000 Oe (left), temperature dependence of the out-of-phase AC susceptibility at various frequencies (middle) and corresponding Arrhenius plots with two distinct relaxation processes (reproduced from Ref.[172]).

1.4. References

[1] E. du Trémolet de Lacheisserie, L. Néel, M. Cyrot, M. Décorps, B. Dieny, *Magnétisme. I - Fondements*, Presses Universitaires De Grenoble, Grenoble, **1999**.

[2] C. Huang, Ed. , *Rare Earth Coordination Chemistry: Fundamentals and Applications*, Wiley, Singapore, **2010**.

[3] M. E. Fieser, M. R. MacDonald, B. T. Krull, J. E. Bates, J. W. Ziller, F. Furche, W. J. Evans, *J. Am. Chem. Soc.* **2015**, *137*, 369–382.

[4] T. P. Gompa, A. Ramanathan, N. T. Rice, H. S. La Pierre, *Dalton Trans.* **2020**, *49*, 15945–15987.

[5] J.-C. G. Bünzli, *J. Coord. Chem.* **2014**, *67*, 3706–3733.

[6] D. A. Atwood, Ed. , *The Rare Earth Elements: Fundamentals and Applications*, Wiley, Chichester, **2012**.

[7] J. Tang, P. Zhang, in *Lanthanides Single Molecules Magnets*, Springer Berlin Heidelberg, Berlin, Heidelberg, **2015**, pp. 1–39.

[8] R. A. Layfield, M. Murugesu, *Lanthanides and Actinides in Molecular Magnetism*, Wiley-VCH, Weinheim, **2015**.

[9] G. A. Bain, J. F. Berry, *J. Chem. Educ.* **2008**, *85*, 532.

[10] P. W. Anderson, *Phys. Rev.* **1950**, *79*, 350–356.

[11] J. B. Goodenough, *Phys. Rev.* **1955**, *100*, 564–573.

[12] J. B. Goodenough, *J. Phys. Chem. Solids* **1958**, *6*, 287–297.

[13] J. Kanamori, *J. Phys. Chem. Solids* **1959**, *10*, 87–98.

[14] J.-P. Launay, M. Verdaguer, *Electrons in Molecules: From Basic Principles to Molecular Electronics*, Oxford Univ. Press, Oxford, **2014**.

[15] B. Sieklucka, D. Pinkowicz, Eds. , *Molecular Magnetic Materials: Concepts and Applications*, Wiley-VCH Verlag GmbH & Co. KGaA, Weinheim, **2017**.

[16] L. J. De Jongh, A. R. Miedema, *Adv. Phys.* **2001**, *50*, 947–1170.

[17] V. L. Berezinskii, *Sov. Phys. JETP* **1972**, *34*, 610–616.

[18] J. M. Kosterlitz, D. J. Thouless, *J. Phys. C Solid State Phys.* **1973**, *6*, 1181–1203.

[19] D. A. Thompson, J. S. Best, *IBM J. Res. Dev.* **2000**, *44*, 311–322.

[20] R. Sessoli, D. Gatteschi, A. Caneschi, M. A. Novak, *Nature* **1993**, *365*, 141–143.

[21] T. Lis, *Acta Crystallogr. B* **1980**, *36*, 2042–2046.

[22] R. Bagai, G. Christou, *Chem. Soc. Rev.* **2009**, *38*, 1011.

[23] L. Thomas, F. Lionti, R. Ballou, D. Gatteschi, R. Sessoli, B. Barbara, *Nature* **1996**, *383*, 145–147.

[24] D. Gatteschi, R. Sessoli, *Angew. Chem. Int. Ed.* **2003**, *42*, 268–297.

[25] C. J. Milios, R. E. P. Winpenny, in *Molecular Nanomagnets & Relatated Phenomena* (Ed.: S. Gao), Springer Berlin Heidelberg, Berlin, Heidelberg, **2014**, pp. 1–109.

[26] A. Zabala-Lekuona, J. M. Seco, E. Colacio, *Coord. Chem. Rev.* **2021**, *441*, 213984.

[27] K. L. M. Harriman, D. Errulat, M. Murugesu, *Trends Chem.* **2019**, *1*, 425–439.

[28] M. N. Leuenberger, D. Loss, *Nature* **2001**, *410*, 789–793.

[29] A. Singh, K. N. Shrivastava, *Phys. Status Solidi B* **1979**, *95*, 273–277.

[30] A. J. Tasiopoulos, A. Vinslava, W. Wernsdorfer, K. A. Abboud, G. Christou, *Angew. Chem. Int. Ed.* **2004**, *43*, 2117–2121.

[31] A. M. Ako, I. J. Hewitt, V. Mereacre, R. Clérac, W. Wernsdorfer, C. E. Anson, A. K. Powell, *Angew. Chem. Int. Ed.* **2006**, *45*, 4926–4929.

[32] J. Cirera, E. Ruiz, S. Alvarez, F. Neese, J. Kortus, *Chem. - Eur. J.* **2009**, *15*, 4078–4087.

[33] O. Waldmann, *Inorg. Chem.* **2007**, *46*, 10035–10037.

[34] F. Neese, D. A. Pantazis, *Faraday Discuss* **2011**, *148*, 229–238.

[35] N. Ishikawa, M. Sugita, T. Ishikawa, S. Koshihara, Y. Kaizu, *J. Am. Chem. Soc.* **2003**, *125*, 8694–8695.

[36] D. N. Woodruff, R. E. P. Winpenny, R. A. Layfield, *Chem. Rev.* **2013**, *113*, 5110–5148.

[37] Y. Lan, S. Klyatskaya, M. Ruben, in *Lanthanides & Actinides in Molecular Magnetism* (Eds.: R.A. Layfield, M. Murugesu), Wiley-VCH Verlag GmbH & Co. KGaA, Weinheim, Germany, **2015**, pp. 223–292.

[38] J. Jung, Étude ab initio de molécules aimants à base d'ions lanthanides, Université Rennes 1, **2015**.

[39] J. D. Rinehart, J. R. Long, *Chem. Sci.* **2011**, *2*, 2078.

[40] L. F. Chibotaru, L. Ungur, *J. Chem. Phys.* **2012**, *137*, 064112.

[41] Y.-S. Ding, N. F. Chilton, R. E. P. Winpenny, Y.-Z. Zheng, *Angew. Chem. Int. Ed.* **2016**, *55*, 16071–16074.

[42] Y.-C. Chen, J.-L. Liu, L. Ungur, J. Liu, Q.-W. Li, L.-F. Wang, Z.-P. Ni, L. F. Chibotaru, X.-M. Chen, M.-L. Tong, *J. Am. Chem. Soc.* **2016**, *138*, 2829–2837.

[43] J. Liu, Y.-C. Chen, J.-L. Liu, V. Vieru, L. Ungur, J.-H. Jia, L. F. Chibotaru, Y. Lan, W. Wernsdorfer, S. Gao, X.-M. Chen, M.-L. Tong, *J. Am. Chem. Soc.* **2016**, *138*, 5441–5450.

[44] A. Lunghi, F. Totti, R. Sessoli, S. Sanvito, *Nat. Commun.* **2017**, *8*, 14620.

[45] M. J. Giansiracusa, A. K. Kostopoulos, D. Collison, R. E. P. Winpenny, N. F. Chilton, *Chem. Commun.* **2019**, *55*, 7025–7028.

[46] F. Ortu, D. P. Mills, in *Handb. Phys. Chem. Rare Earths*, Elsevier, **2019**, pp. 1–87.

[47] S. A. Cotton, *Comptes Rendus Chim.* **2005**, *8*, 129–145.

[48] C. A. P. Goodwin, F. Ortu, D. Reta, N. F. Chilton, D. P. Mills, *Nature* **2017**, *548*, 439–442.

[49] K. Randall McClain, C. A. Gould, K. Chakarawet, S. J. Teat, T. J. Groshens, J. R. Long, B. G. Harvey, *Chem. Sci.* **2018**, *9*, 8492–8503.

[50] F.-S. Guo, B. M. Day, Y.-C. Chen, M.-L. Tong, A. Mansikkamäki, R. A. Layfield, *Science* **2018**, *362*, 1400–1403.

[51] K. Bernot, *Tech. Ing.* **2019**, *RE277*, 22.

[52] M. Verdaguer, A. N. Gleizes, *Eur. J. Inorg. Chem.* **2020**, *2020*, 723–731.

[53] L. D. Landau, E. M. Lifshits, *Statistical Physics*, Pergamon Press, Oxford, **1958**.

[54] J. M. Loveluck, S. W. Lovesey, S. Aubry, *J. Phys. C Solid State Phys.* **1975**, *8*, 3841–3856.

[55] B. Barbara, *J. Magn. Magn. Mater.* **1994**, *129*, 79–86.

[56] V. Pianet, M. Urdampilleta, T. Colin, R. Clérac, C. Coulon, *Phys. Rev. B* **2017**, *96*, 214429.

[57] C. Coulon, H. Miyasaka, R. Clérac, in *Single-Molecule Magnets and Related Phenomena* (Ed.: R. Winpenny), Springer Berlin Heidelberg, Berlin, Heidelberg, **2006**, pp. 163–206.

[58] C. Coulon, V. Pianet, M. Urdampilleta, R. Clérac, in *Mol. Nanomagnets Relat. Phenom.* (Ed.: S. Gao), Springer Berlin Heidelberg, Berlin, Heidelberg, **2014**, pp. 143–184.

[59] V.-M. Pianet, Propriétés statiques et dynamiques des chaînes aimants, Université de Bordeaux, **2014**.

[60] V. Pianet, M. Urdampilleta, T. Colin, R. Clérac, C. Coulon, *Phys. Rev. B* **2016**, *94*, 054431.

[61] R. J. Glauber, *J. Math. Phys.* **1963**, *4*, 294–307.

[62] J. H. Luscombe, M. Luban, J. P. Reynolds, *Phys. Rev. E* **1996**, *53*, 5852–5860.

[63] L. Bogani, A. Caneschi, M. Fedi, D. Gatteschi, M. Massi, M. A. Novak, M. G. Pini, A. Rettori, R. Sessoli, A. Vindigni, *Phys. Rev. Lett.* **2004**, *92*, 207204.

[64] A. Vindigni, L. Bogani, D. Gatteschi, R. Sessoli, A. Rettori, M. A. Novak, *J. Magn. Magn. Mater.* **2004**, *272–276*, 297–298.

[65] L. Bogani, R. Sessoli, M. G. Pini, A. Rettori, M. A. Novak, P. Rosa, M. Massi, M. E. Fedi, L. Giuntini, A. Caneschi, D. Gatteschi, *Phys. Rev. B* **2005**, *72*, 064406.

[66] J. Shibata, S. Takagi, *Phys. Rev. B* **2000**, *62*, 5719–5732.

[67] H.-L. Sun, Z.-M. Wang, S. Gao, *Coord. Chem. Rev.* **2010**, *254*, 1081–1100.

[68] S. Dhers, H. L. C. Feltham, S. Brooker, *Coord. Chem. Rev.* **2015**, *296*, 24–44.

[69] H. Miyasaka, R. Clérac, *Bull. Chem. Soc. Jpn.* **2005**, *78*, 1725–1748.

[70] L. Lecren, O. Roubeau, C. Coulon, Y.-G. Li, X. F. Le Goff, W. Wernsdorfer, H. Miyasaka, R. Clérac, *J. Am. Chem. Soc.* **2005**, *127*, 17353–17363.

[71] H. Miyasaka, M. Yamashita, *Dalton Trans* **2007**, 399–406.

[72] H.-B. Xu, B.-W. Wang, F. Pan, Z.-M. Wang, S. Gao, *Angew. Chem. Int. Ed.* **2007**, *46*, 7388–7392.

[73] M. Ferbinteanu, H. Miyasaka, W. Wernsdorfer, K. Nakata, K. Sugiura, M. Yamashita, C. Coulon, R. Clérac, *J. Am. Chem. Soc.* **2005**, *127*, 3090–3099.

[74] H. Miyasaka, R. Clérac, K. Mizushima, K. Sugiura, M. Yamashita, W. Wernsdorfer, C. Coulon, *Inorg. Chem.* **2003**, *42*, 8203–8213.

[75] H. Miyasaka, T. Nezu, K. Sugimoto, K. Sugiura, M. Yamashita, R. Clérac, *Chem. - Eur. J.* **2005**, *11*, 1592–1602.

[76] H. Miyasaka, A. Saitoh, S. Abe, *Coord. Chem. Rev.* **2007**, *251*, 2622–2664.

[77] A. Saitoh, H. Miyasaka, M. Yamashita, R. Clérac, *J Mater Chem* **2007**, *17*, 2002–2012.

[78] H. Miyasaka, T. Madanbashi, A. Saitoh, N. Motokawa, R. Ishikawa, M. Yamashita, S. Bahr, W. Wernsdorfer, R. Clérac, *Chem. - Eur. J.* **2012**, *18*, 3942–3954.

[79] W. Wernsdorfer, R. Clérac, C. Coulon, L. Lecren, H. Miyasaka, *Phys. Rev. Lett.* **2005**, *95*, 237203.

[80] S. Dhers, H. L. C. Feltham, M. Rouzières, R. Clérac, S. Brooker, *Inorg. Chem.* **2019**, *58*, 5543–5554.

[81] S. Dhers, R. K. Wilson, M. Rouzières, R. Clérac, S. Brooker, *Cryst. Growth Des.* **2020**, *20*, 1538–1542.

[82] R. Lescouëzec, L. M. Toma, J. Vaissermann, M. Verdaguer, F. S. Delgado, C. Ruiz-Pérez, F. Lloret, M. Julve, *Coord. Chem. Rev.* **2005**, *249*, 2691–2729.

[83] E. V. Alexandrov, A. V. Virovets, V. A. Blatov, E. V. Peresypkina, *Chem. Rev.* **2015**, *115*, 12286–12319.

[84] J.-H. Wang, Z.-Y. Li, M. Yamashita, X.-H. Bu, *Coord. Chem. Rev.* **2021**, *428*, 213617.

[85] D. Visinescu, A. M. Madalan, M. Andruh, C. Duhayon, J.-P. Sutter, L. Ungur, W. Van den Heuvel, L. F. Chibotaru, *Chem. - Eur. J.* **2009**, *15*, 11808–11814.

[86] T. S. Venkatakrishnan, S. Sahoo, N. Bréfuel, C. Duhayon, C. Paulsen, A.-L. Barra, S. Ramasesha, J.-P. Sutter, *J. Am. Chem. Soc.* **2010**, *132*, 6047–6056.

[87] R. Gheorghe, A. M. Madalan, J.-P. Costes, W. Wernsdorfer, M. Andruh, *Dalton Trans.* **2010**, *39*, 4734.

[88] J. H. Yoon, D. W. Ryu, S. Y. Choi, H. C. Kim, E. K. Koh, J. Tao, C. S. Hong, *Chem. Commun.* **2011**, *47*, 10416.

[89] I. Bhowmick, E. A. Hillard, P. Dechambenoit, C. Coulon, T. D. Harris, R. Clérac, *Chem. Commun.* **2012**, *48*, 9717.

[90] L. Shi, D. Shao, X. Wei, K. R. Dunbar, X. Wang, *Angew. Chem. Int. Ed.* **2020**, *59*, 10379–10384.

[91] J.-F. Guo, X.-T. Wang, B.-W. Wang, G.-C. Xu, S. Gao, L. Szeto, W.-T. Wong, W.-Y. Wong, T.-C. Lau, *Chem. - Eur. J.* **2010**, *16*, 3524–3535.

[92] D. Zhang, L.-F. Zhang, Y. Chen, H. Wang, Z.-H. Ni, W. Wernsdorfer, J. Jiang, *Chem. Commun.* **2010**, *46*, 3550.

[93] T. D. Harris, C. Coulon, R. Clérac, J. R. Long, *J. Am. Chem. Soc.* **2011**, *133*, 123–130.

[94] C. Pichon, N. Suaud, C. Duhayon, N. Guihéry, J.-P. Sutter, *J. Am. Chem. Soc.* **2018**, *140*, 7698–7704.

[95] A. K. Bar, N. Gogoi, C. Pichon, V. M. L. D. P. Goli, M. Thlijeni, C. Duhayon, N. Suaud, N. Guihéry, A.-L. Barra, S. Ramasesha, J.-P. Sutter, *Chem. - Eur. J.* **2017**, *23*, 4380–4396.

[96] K. Bretosh, V. Béreau, C. Duhayon, C. Pichon, J.-P. Sutter, *Inorg. Chem. Front.* **2020**, *7*, 1503–1511.

[97] C. Pichon, N. Suaud, V. Jubault, C. Duhayon, N. Guihéry, J. Sutter, *Chem. – Eur. J.* **2021**, chem.202102571.

[98] T. Liu, Y.-J. Zhang, S. Kanegawa, O. Sato, *J. Am. Chem. Soc.* **2010**, *132*, 8250–8251.

[99] N. Hoshino, F. Iijima, G. N. Newton, N. Yoshida, T. Shiga, H. Nojiri, A. Nakao, R. Kumai, Y. Murakami, H. Oshio, *Nat. Chem.* **2012**, *4*, 921–926.

[100] T. Liu, H. Zheng, S. Kang, Y. Shiota, S. Hayami, M. Mito, O. Sato, K. Yoshizawa, S. Kanegawa, C. Duan, *Nat. Commun.* **2013**, *4*, 2826.

[101] Q. Liu, J. Hu, Y. Meng, W. Jiang, J. Wang, W. Wen, Q. Wu, H. Zhu, L. Zhao, T. Liu, *Angew. Chem. Int. Ed.* **2021**, *60*, 10537–10541.

[102] L. Zhao, Y.-S. Meng, Q. Liu, O. Sato, Q. Shi, H. Oshio, T. Liu, *Nat. Chem.* **2021**, *13*, 698–704.

[103] A. Caneschi, D. Gatteschi, R. Sessoli, P. Rey, *Acc. Chem. Res.* **1989**, *22*, 392–398.

[104] I. Ratera, J. Veciana, *Chem Soc Rev* **2012**, *41*, 303–349.

[105] J. S. Miller, A. J. Epstein, *Chem. Commun.* **1998**, 1319–1325.
[106] P. Perlepe, I. Oyarzabal, A. Mailman, M. Yquel, M. Platunov, I. Dovgaliuk, M. Rouzières, P. Négrier, D. Mondieig, E. A. Suturina, M.-A. Dourges, S. Bonhommeau, R. A. Musgrave, K. S. Pedersen, D. Chernyshov, F. Wilhelm, A. Rogalev, C. Mathonière, R. Clérac, *Science* **2020**, *370*, 587–592.
[107] A. Caneschi, D. Gatteschi, N. Lalioti, C. Sangregorio, R. Sessoli, G. Venturi, A. Vindigni, A. Rettori, M. G. Pini, M. A. Novak, *Angew Chem Int Ed* **2001**, *40*, 1760–1763.
[108] J. D. Rinehart, M. Fang, W. J. Evans, J. R. Long, *Nat. Chem.* **2011**, *3*, 538–542.
[109] S. Demir, M. Nippe, M. I. Gonzalez, J. R. Long, *Chem Sci* **2014**, *5*, 4701–4711.
[110] V. Vieru, N. Iwahara, L. Ungur, L. F. Chibotaru, *Sci. Rep.* **2016**, *6*, 24046.
[111] S. Demir, I.-R. Jeon, J. R. Long, T. D. Harris, *Coord. Chem. Rev.* **2015**, *289–290*, 149–176.
[112] K. Katoh, K. Kagesawa, M. Yamashita, in *World Sci. Ref. Spin Org.*, World Scientific, **2017**, pp. 271–344.
[113] J. H. Osiecki, E. F. Ullman, *J. Am. Chem. Soc.* **1968**, *90*, 1078–1079.
[114] D. G. B. Boocock, R. Darcy, E. F. Ullman, *J. Am. Chem. Soc.* **1968**, *90*, 5945–5946.
[115] E. F. Ullman, Ludwig. Call, J. H. Osiecki, *J. Org. Chem.* **1970**, *35*, 3623–3631.
[116] E. F. Ullman, J. H. Osiecki, D. G. B. Boocock, R. Darcy, *J. Am. Chem. Soc.* **1972**, *94*, 7049–7059.
[117] V. Ovcharenko, S. Fokin, P. Rey, *Mol. Cryst. Liq. Cryst. Sci. Technol. Sect. Mol. Cryst. Liq. Cryst.* **1999**, *334*, 109–119.
[118] C. Hirel, K. E. Vostrikova, J. Pécaut, V. I. Ovcharenko, P. Rey, *Chemistry* **2001**, *7*, 2007–2014.
[119] A. Zheludev, *J. Magn. Magn. Mater.* **1994**, 14.
[120] M. Bonnet, D. Luneau, E. Ressouche, P. Rey, J. Schweizer, M. Wan, H. Wang, A. Zheludev, *Mol. Cryst. Liq. Cryst. Sci. Technol. Sect. Mol. Cryst. Liq. Cryst.* **1995**, *271*, 35–53.
[121] Y. Pontillon, T. Akita, A. Grand, K. Kobayashi, E. Lelievre-Berna, J. Pécaut, E. Ressouche, J. Schweizer, *J. Am. Chem. Soc.* **1999**, *121*, 10126–10133.
[122] Y. Y. Lim, R. S. Drago, *Inorg. Chem.* **1972**, *11*, 1334–1338.
[123] K. Binnemans, in *Handb. Phys. Chem. Rare Earths*, Elsevier, **2005**, pp. 107–272.
[124] X. Meng, W. Shi, P. Cheng, *Coord. Chem. Rev.* **2019**, *378*, 134–150.
[125] Andrea. Caneschi, Dante. Gatteschi, Jean. Laugier, Paul. Rey, Roberta. Sessoli, Claudia. Zanchini, *J. Am. Chem. Soc.* **1988**, *110*, 2795–2799.
[126] J. Omata, T. Ishida, D. Hashizume, F. Iwasaki, T. Nogami, *Inorg. Chem.* **2001**, *40*, 3954–3958.
[127] H. Feuer, Ed. , *Nitrile Oxides, Nitrones, and Nitronates in Organic Synthesis*, John Wiley & Sons, Inc., Hoboken, NJ, USA, **2007**.
[128] E. V. Tretyakov, V. I. Ovcharenko, *Russ. Chem. Rev.* **2009**, *78*, 971–1012.
[129] H. Karoui, F. L. Moigne, O. Ouari, P. Tordo, in *Stable Radic.* (Ed.: R.G. Hicks), John Wiley & Sons, Ltd, Chichester, UK, **2010**, pp. 173–229.
[130] A. Caneschi, D. Gatteschi, N. Lalioti, C. Sangregorio, R. Sessoli, *J. Chem. Soc. Dalton Trans.* **2000**, 3907–3912.

[131] Andrea. Caneschi, Dante. Gatteschi, Paul. Rey, roberta. Sessoli, *Inorg. Chem.* **1991**, *30*, 3936–3941.
[132] L. Cavigli, R. Sessoli, M. Gurioli, L. Bogani, *Phys. Status Solidi A* **2006**, *203*, 1402–1408.
[133] R. Sessoli, M.-E. Boulon, A. Caneschi, M. Mannini, L. Poggini, F. Wilhelm, A. Rogalev, *Nat. Phys.* **2015**, *11*, 69–74.
[134] M. Fittipaldi, A. Cini, G. Annino, A. Vindigni, A. Caneschi, R. Sessoli, *Nat. Mater.* **2019**, *18*, 329–334.
[135] A. Caneschi, D. Gatteschi, N. Lalioti, R. Sessoli, L. Sorace, V. Tangoulis, A. Vindigni, *Chem. - Eur. J.* **2002**, *8*, 286–292.
[136] M. Scarrozza, P. Barone, R. Sessoli, S. Picozzi, *J. Mater. Chem. C* **2016**, *4*, 4176–4185.
[137] N. Ishii, Y. Okamura, S. Chiba, T. Nogami, T. Ishida, *J. Am. Chem. Soc.* **2008**, *130*, 24–25.
[138] Y. Okamura, N. Ishii, T. Nogami, T. Ishida, *Bull. Chem. Soc. Jpn.* **2010**, *83*, 716–725.
[139] Y. Okamura, T. Nogami, T. Ishida, *Chem. Lett.* **2009**, *38*, 740–741.
[140] R. Sessoli, *Angew. Chem. Int. Ed.* **2008**, *47*, 5508–5510.
[141] T. Ishida, Y. Okamura, I. Watanabe, *Inorg. Chem.* **2009**, *48*, 7012–7014.
[142] M. G. F. Vaz, R. A. Allão, H. Akpinar, J. A. Schlueter, S. Santos, P. M. Lahti, M. A. Novak, *Inorg. Chem.* **2012**, *51*, 3138–3145.
[143] M. G. F. Vaz, R. A. A. Cassaro, H. Akpinar, J. A. Schlueter, P. M. Lahti, M. A. Novak, *Chem. - Eur. J.* **2014**, *20*, 5460–5467.
[144] X. Liu, X. Feng, K. R. Meihaus, X. Meng, Y. Zhang, L. Li, J. Liu, K. S. Pedersen, L. Keller, W. Shi, Y. Zhang, P. Cheng, J. R. Long, *Angew. Chem. Int. Ed.* **2020**, *59*, 10610–10618.
[145] C. Benelli, A. Caneschi, D. Gatteschi, L. Pardi, P. Rey, *Inorg. Chem.* **1989**, *28*, 275–280.
[146] C. Benelli, A. Caneschi, D. Gatteschi, L. Pardi, P. Rey, *Inorg. Chem.* **1989**, *28*, 3230–3234.
[147] C. Benelli, A. Caneschi, D. Gatteschi, L. Pardi, P. Rey, *Inorg. Chem.* **1990**, *29*, 4223–4228.
[148] C. Benelli, A. Caneschi, D. Gatteschi, R. Sessoli, *Adv. Mater.* **1992**, *4*, 504–505.
[149] C. Benelli, A. Caneschi, D. Gatteschi, R. Sessoli, *Inorg. Chem.* **1993**, *32*, 4797–4801.
[150] L. Bogani, C. Sangregorio, R. Sessoli, D. Gatteschi, *Angew. Chem. Int. Ed.* **2005**, *44*, 5817–5821.
[151] K. Bernot, L. Bogani, A. Caneschi, D. Gatteschi, R. Sessoli, *J. Am. Chem. Soc.* **2006**, *128*, 7947–7956.
[152] K. Bernot, L. Bogani, R. Sessoli, D. Gatteschi, *Inorganica Chim. Acta* **2007**, *360*, 3807–3812.
[153] C. Benelli, D. Gatteschi, R. Sessoli, A. Rettori, M. G. Pini, F. Bartolomé, J. Bartolomé, *J. Magn. Magn. Mater.* **1995**, *140–144*, 1649–1650.
[154] R. Liu, L. Li, X. Wang, P. Yang, C. Wang, D. Liao, J.-P. Sutter, *Chem. Commun.* **2010**, *46*, 2566.
[155] K. Bernot, Lanthanides in Molecular Magnetism: From Mononuclear Single Molecule Magnets to Single Chain Magnets, INSA Rennes / Università degli Studi di Firenze, **2007**.
[156] C. Li, J. Sun, M. Yang, G. Sun, J. Guo, Y. Ma, L. Li, *Cryst. Growth Des.* **2016**, *16*, 7155–7162.

[157] R. Liu, C. Zhang, X. Mei, P. Hu, H. Tian, L. Li, D. Liao, J.-P. Sutter, *New J. Chem.* **2012**, *36*, 2088.
[158] P. Hu, X. Wang, Y. Ma, Q. Wang, L. Li, D. Liao, *Dalton Trans* **2014**, *43*, 2234–2243.
[159] X. Wang, Y. Li, P. Hu, J. Wang, L. Li, *Dalton Trans.* **2015**, *44*, 4560–4567.
[160] X. Liu, Y. Zhang, W. Shi, P. Cheng, *Inorg. Chem.* **2018**, *57*, 13409–13414.
[161] X. Liu, Y.-X. Wang, Z. Han, T. Han, W. Shi, P. Cheng, *Dalton Trans.* **2019**, *48*, 8989–8994.
[162] C. V. Sarmiento, T. A. Araujo, S. G. Reis, M. S. de Souza, R. A. Allão Cassaro, M. A. Novak, M. G. F. Vaz, *RSC Adv.* **2019**, *9*, 30302–30308.
[163] M. Andruh, J.-P. Costes, C. Diaz, S. Gao, *Inorg. Chem.* **2009**, *48*, 3342–3359.
[164] M. Zhu, L. Li, J.-P. Sutter, *Inorg. Chem. Front.* **2016**, *3*, 994–1003.
[165] M. G. F. Vaz, M. Andruh, *Coord. Chem. Rev.* **2021**, *427*, 213611.
[166] M. Briganti, F. Totti, M. Andruh, *Dalton Trans.* **2021**, 10.1039.D1DT02511B.
[167] A. Bencini, C. Benelli, A. Caneschi, R. L. Carlin, A. Dei, D. Gatteschi, *J. Am. Chem. Soc.* **1985**, *107*, 8128–8136.
[168] C. Benelli, A. Caneschi, D. Gatteschi, O. Guillou, L. Pardi, *Inorg. Chem.* **1990**, *29*, 1750–1755.
[169] M. Andruh, I. Ramade, E. Codjovi, O. Guillou, O. Kahn, J. C. Trombe, *J. Am. Chem. Soc.* **1993**, *115*, 1822–1829.
[170] M. Zhu, X. Mei, Y. Ma, L. Li, D. Liao, J.-P. Sutter, *Chem. Commun.* **2014**, *50*, 1906.
[171] M. Zhu, P. Hu, Y. Li, X. Wang, L. Li, D. Liao, V. M. L. Durga Prasad Goli, S. Ramasesha, J.-P. Sutter, *Chem. - Eur. J.* **2014**, *20*, 13356–13365.
[172] X. Huang, K. Wang, J. Han, J. Xie, L. Li, J.-P. Sutter, *Dalton Trans.* **2021**, *50*, 11992–11998.

Chapter 2. Deposition Attempts of a Single-Chain Magnet by Drop-casting

2.1. Introduction

As stated in Chapter 1, one of the obvious applications of such nanometric molecular magnets would be data storage: SMMs are discrete entities that do not interact with each other and should therefore act as individual bits at the molecular scale. In addition, they also exhibit quantum properties that could be used for the development of devices, such as quantum computing and spintronics.[1–4] However, two technological obstacles must be overcome before these potential applications reach technological maturity.

The first relies on the operating conditions of these molecular compounds. Ideally, they should be chemically stable under ambient conditions (temperature, humidity, *etc.*) and preserve their inherent magnetic properties at reasonable temperatures (as a reminder, the blocking temperature of the record SMM, [(Cp^{iPr5})Dy(Cp*)], is 80 K under inert conditions).[5]

Putting this aside, the second issue is to arrange these molecules on a surface so that they can be manipulated individually and integrated into devices, which is also particularly challenging.[6–9] Pioneer works, conducted by physicists on single-atoms arrays,[10–12] have demonstrated that one has to pay close attention to the interactions with the substrate.[13,14] Indeed, the SMMs do not undergo any interactions that could alter their magnetic properties in the bulk crystalline phase, which is not the case when isolated on the surface. The various possible interactions between the latter and the metal centre can be detrimental to the chemical integrity and to the preservation of magnetic behaviour.[15–20]

Nevertheless, several methods have already been successfully implemented for SMMs deposition. One of the most popular is the physisorption by evaporation in ultra-high vacuum (UHV).[21–26] It allows a high degree of control of the deposition process and the formation of homogeneous surface arrays, but it requires molecules with high thermal stability under vacuum.

The second alternative, the chemisorption, is easier to implement and relies on the bonds and interactions that can be set up between the molecule and the substrate. At this end, both SMMs and substrate can be functionalised with chemical “anchoring point” targeting specific grafting: hydrosilylation of unsaturated compounds on silicon,[27–30] formation of bonds between sulphur S- groups and the Au surface,[31–35] π- interactions for grafting on HOPG, graphene or graphene nanotubes,[36–39] *etc.* However, no reliable attempt has been successfully implemented in the case of Single-Chain Magnets up to now.

Infinite molecular chains are by nature less prone to such deposition processes because of their infinite dimensionality and periodic arrangement, and few examples on surface are reported in the literature.[40,41]

The first way to obtain such molecular compounds on a surface is to make reacting the corresponding building blocks by *in-situ* synthesis through simultaneous or sequential sublimation or drop-casting of diluted solutions.[42–47] However, this method could lead to the formation of undesirable compounds and structural defects, highly detrimental to the onset of a magnetic correlation phenomenon and thus the preservation of a SCM behaviour.

To preserve the single chains, one can dissociate them from the crystalline bulk by sonication in a poor solvent. The result is a diluted solution that is subsequently drop-casted, and the single chains are adsorbed on the substrate.[48–51]

In this chapter, we will first focus on the implementation of the latter strategy to investigate the deposition of a well-known SCM, the [Tb(hfac)$_3$(NITPhOPh)], characterised by Atomic Force Microscopy.

In the second part, we will detail the deposition optimisation of [Tb(hfac)$_3$·2H$_2$O] on mica substrate, as well as a comparison of its magnetic and luminescent properties with the corresponding bulk crystalline phase.[b]

[b] This study has been published under the reference: Q. Evrard, G. Cucinotta, F. Houard, G. Calvez, Y. Suffren, C. Daiguebonne, O. Guillou, A. Caneschi, M. Mannini, K. Bernot. Self-assembly of a terbium(III) 1D coordination polymer on mica. *Beilstein J. Nanotechnol*. **2019**. 10, 2440–2448.

2.2. Deposition attempts of a SCM by drop-casting

2.2.1. Choice of the SCM candidate

As described in the introduction, the deposition strategy adopted in the framework of this thesis relied on a controlled degradation of the bulk SCM crystals into smaller fragments by the mean of sonication, followed by a drop-casting step on a substrate.

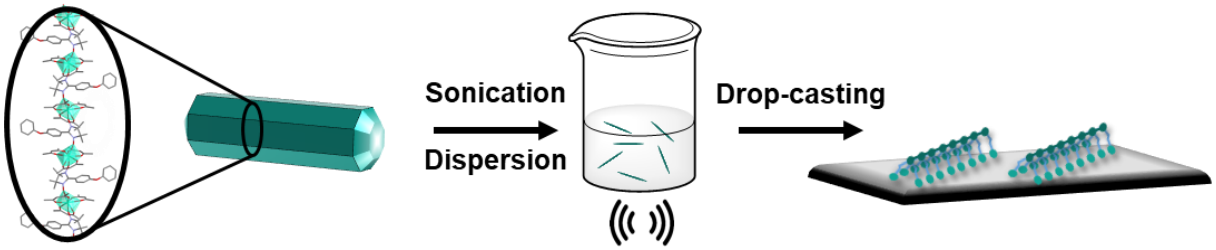

Figure 2.1. Strategy targeted for the deposition of SCMs on surface.

The choice of the SCM aimed for the dispersion and deposition investigations and was driven by the following requirements:

1) The individual polymeric chain should be robust from a chemical and structural point of view, to hamper its degradation/solubilisation into uncoordinated building blocks (which could lead to uncontrolled *in-situ* rearrangements and by-product impurities);
2) Nevertheless, the neighbouring chains should not present too strong supramolecular interactions, to facilitate their dissociation from the bulk crystal to isolated polymers during the sonication step;
3) It should exhibit an open hysteresis preferentially at zero field to allow an easy magnetic characterisation and to act as a relevant magnet.

Based on these prerequisites and the SCM chemistry background developed in our group, the SCM system targeted for this study is a member of the isostructural family **$[Ln(hfac)_3(NITPhOPh)]_n$** (with NITPhOPh = 2,4'-benzoxo-4,4,5,5-tetramethylimidazoline-1-oxyl-3-oxide), studied by Bernot *et al.* to evaluate the influence of the anisotropy of substituted Ln centres (with Ln = Gd to Yb) on the resulting magnetic SCM behaviour (see Part.1.3.3.3).[52–54]

Indeed, the molecular structure of these chains can be described as an alternation of Ln centres and NIT ligands, bridged by bis-μ coordination bonds but also reinforced by π-interactions between aromatic phenyl and $hfac^-$ planes, as represented below in Figure 2.2.[55] This intra-chain robustness coupled with an effective inter-chain separation by terminal phenyl groups with no supramolecular interactions between them should facilitate the liquid dissociation of these SCMs in an appropriate solvent.

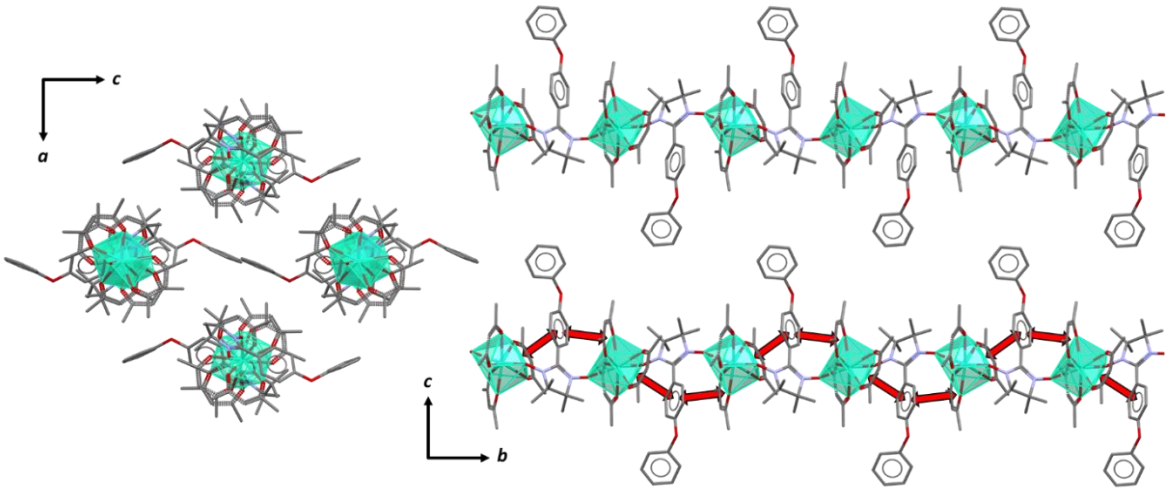

Figure 2.2. Representations of the molecular structure of the **[Ln(hfac)$_3$(NITPhOPh)]$_n$** chain family along the *b*-axis (left) and the *a*-axis, with π- interactions drawn as red arrows.[52–54]

The last point to address was observing an open hysteresis loop, the key point to store magnetic information and obtain a storage device. As stated in Chapter 1, the magnetic relaxation dynamics of the SCMs relies on the Ising-type anisotropy of the Ln^{III} centres in this case, with slowest relaxation times obtained for highly anisotropic ions as depicted in Figure 2.3 below. Among them, the Tb^{III} chain featured the highest temperature range where a frequency dependence of the out-of-phase (χ_M'') susceptibility was observed because of the onset of slow relaxation dynamics. This feature was further confirmed at lower temperature by observing a hysteresis loop open at zero field at 1.8 K, less pronounced for the Dy chain (see Figure 1.30).

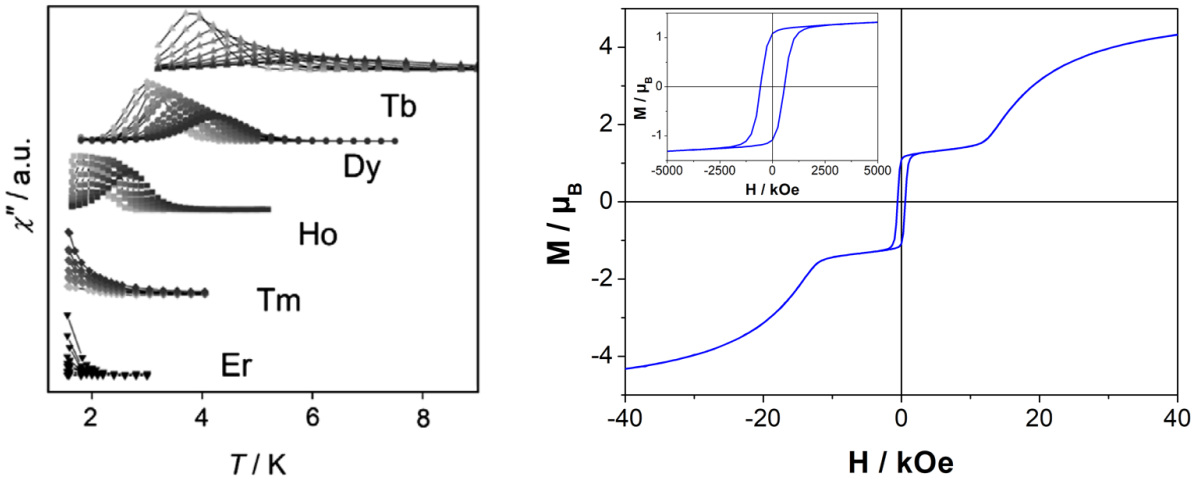

Figure 2.3. Temperature dependency of the out-of-phase (χ_M'') susceptibility for the **[Ln(hfac)$_3$(NITPhOPh)]$_n$** derivatives (left) and magnetic hysteresis curve of the **[Tb(hfac)$_3$(NITPhOPh)]$_n$** at 1.8 K with a magnetic field sweep rate of 15.5 Oe·s^{-1} (right) (reproduced and adapted from Ref.[52,54,56]).

By considering these structural and magnetic considerations, the best SCM candidate designated for this surface deposition study was the **[Tb(hfac)$_3$(NITPhOPh)]$_n$**.

2.2.2. High-power ultrasonication for sonocrystallisation[57]

We thus had to find a way to obtain batches of highly pure crystals of **[Tb(hfac)$_3$(NITPhOPh)]$_n$** with a homogeneous crystallite size distribution, fundamental to undergo a proper solubilization process for surface deposition.

For this purpose, a study was conducted in our group in collaboration with Dr. Q. Evrard about the ultrasonication processing of SCM powders.[57] Indeed, ultrasounds can have many uses in chemical synthesis, depending on the stage at which they are applied. The creation of cavitation bubbles allows, at certain local points, to reach very high values of temperature and pressure (up to 5000 K and 1000 atm), thus giving access to chemical reactions limited by usual experimental conditions (this is called *sonochemistry*).[58,59] In addition, the collapse of these cavitation bubbles generates shock waves that homogenizes the system, prevents secondary nucleation and fragments asymmetrically the crystal germs limiting the dispersity of crystal dimensions. When applied to a cooling reaction mixture (out of equilibrium system), this is called *sonocrystallization*. Finally, when sonication is applied to a large amount of matter on a stable system, it is called *sonofragmentation*. The latter is the most common use of sonication and does not require high-power sonicators, contrary to sonochemistry and sonocrystallization.

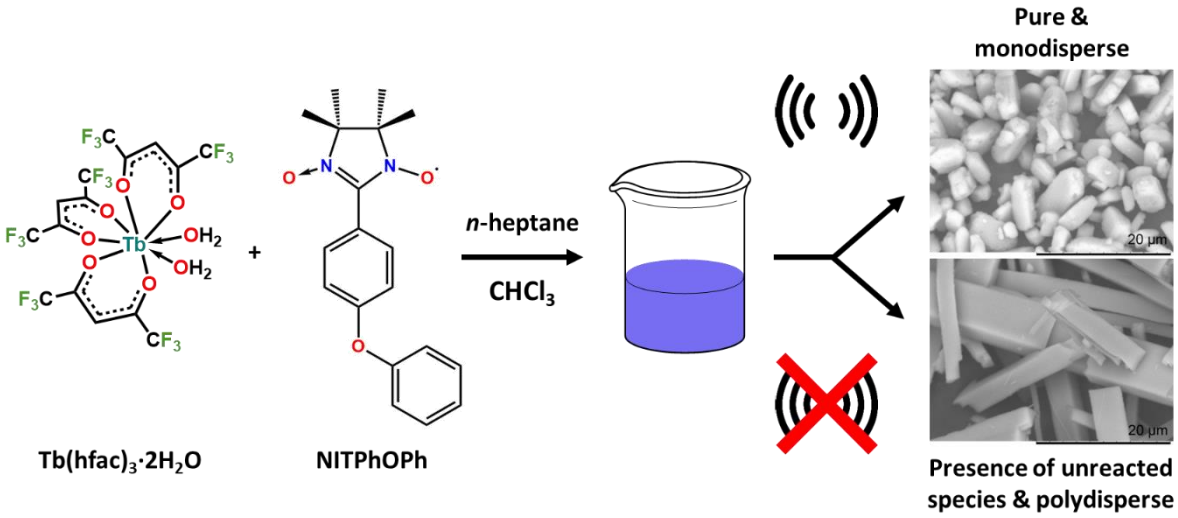

Figure 2.4. Principle scheme of the sonocrystallisation of **[Tb(hfac)$_3$(NITPhOPh)]$_n$** (adapted from Ref.[57]).

In our case, the addition of an ultrasonication step during the crystal growth (detailed in Part.2.A.1.2) afforded monodisperse crystalline powder of **[Tb(hfac)$_3$(NITPhOPh)]$_n$** with a low aspect ratio (for a homogeneous dispersion in solvent), and similar chemical purity and magnetic properties as reported from the corresponding single-crystals. Additionally, the luminescence measurements performed to exclude the presence of uncoordinated reactants did not show traces of impurities.

2.2.3. Drop-casting of $[Tb(hfac)_3(NITPhOPh)]_n$ on mica

A drop-casting protocol has been established (detailed in Part.2.A.1.3) and evaluated by atomic force microscopy (AFM) at the LaMM (Laboratorio di Magnetismo Molecolare, Firenze, ITA, with the help of Dr. G. Cucinotta and Prof. M. Mannini). The mica substrate was chosen because of its low roughness[60] making it particularly suitable for atomic force microscopy (AFM) imaging[61] as well as for its hydrophilic nature promoting the interaction with the deposited molecules. Indeed, muscovite mica has already been used for the deposition of magnetic materials such as FeCoN magnetic films[62] or tungsten oxide nanowires.[63] The deposition was carried out at room temperature by drop-casting of 0.35 mmol·L^{-1} cyclohexane solution of dispersed **$[Tb(hfac)_3(NITPhOPh)]_n$** onto the mica surface.

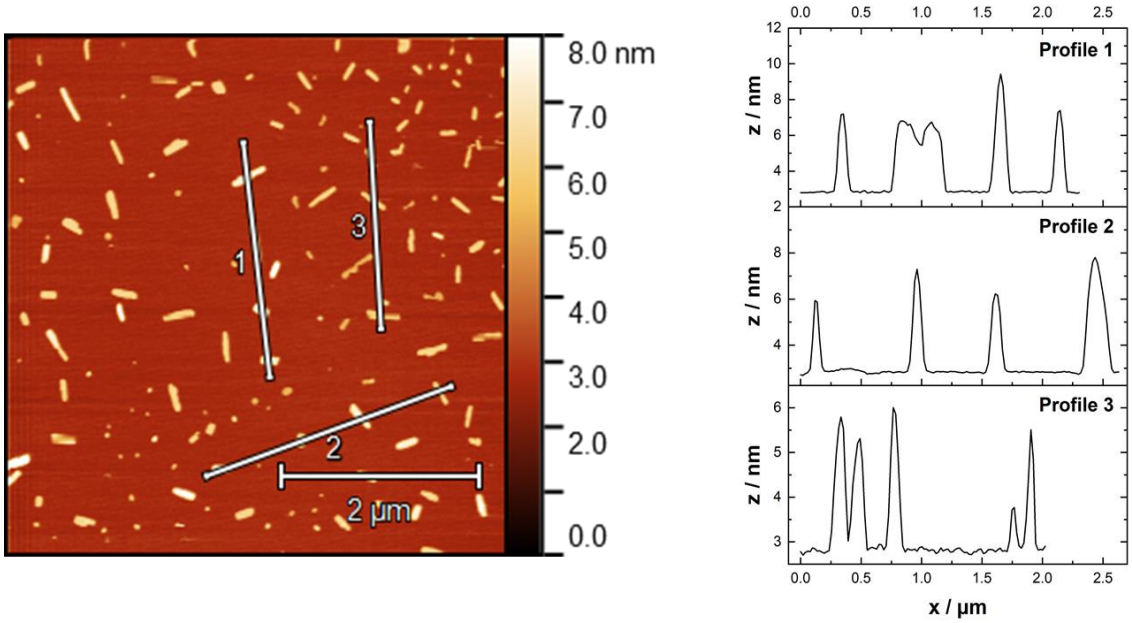

Figure 2.5. AFM topography image of a 0.35 mmol·L^{-1} cyclohexane solution of **$[Tb(hfac)_3(NITPhOPh)]_n$** drop-casted on mica (left) and corresponding height profiles (right).

As depicted in Figure 2.5, the mica surface was covered by elongated small aggregates between tens and hundreds of nanometres long. We also noticed that the aggregates moved with the contact of the AFM tip because interactions with the surface are weak. The distribution height profiles are not homogeneous, spreading from less than 1 nm for the smaller aggregates up to 8 nm, with an average of around 3 nm. The dimensions are far greater than the ones expected for a single isolated chain of **$[Tb(hfac)_3(NITPhOPh)]_n$**. This strongly suggests an incomplete fragmentation of the single crystals into smaller inhomogeneous crystallites or on-surface recrystallization from the cyclohexane solution.

Further studies varying the deposition parameters (changes of sonication time or drop-casted volume) demonstrated that these observations were not reproducible.

Based on these observations, we investigated the deposition of diluted solutions of the **$[Tb(hfac)_3{\cdot}2H_2O]$** and **NITPhOPh** building blocks separately first, then mixed in order to probe a possible growth of **$[Tb(hfac)_3(NITPhOPh)]_n$** on surface through *in-situ* reactions.[43,64]

2.3. Deposition of $[Tb(hfac)_3.2H_2O]$

Following strictly the deposition protocol established in Part.2.2.3, 0.35 mmol·L^{-1} cyclohexane solutions of **$[Tb(hfac)_3{\cdot}2H_2O]$**, **NITPhOPh** and an equimolar amount of these two compounds were sonicated, drop-casted on mica, dried by an N_2 flux and directly mounted on the AFM sample holder. Unfortunately, no particular deposit could be observed on surface irrespectively of the sample.

If these results were expected for the solution of **$[Tb(hfac)_3{\cdot}2H_2O]$** and **NITPhOPh**, the absence of reaction for the equimolar mix could be explained by the fast drying of the solvent that hampers the diffusion of the single molecules on the surface, and then their self-organisation into coordination polymers.

2.3.1. Deposition and *in-situ* assembly of $[Tb(hfac)_3{\cdot}2H_2O]$

To verify this hypothesis, we allowed the solvent to dry slowly (by removing the nitrogen flux step) at ambient atmosphere and the topological evolution of the surface was monitored by AFM measurements carried out over several hours. No deposits were observed for **NITPhOPh** and the equimolar mix. However, small one-dimensional structures have emerged from the deposited **$[Tb(hfac)_3{\cdot}2H_2O]$** but only when the relative humidity of the laboratory was high enough (during rainy days). To verify the reproducibility of these observations and the influence of the atmospheric moisture on the deposition process, freshly prepared samples were kept at room temperature and in a relative humidity of 90% for 24 h.

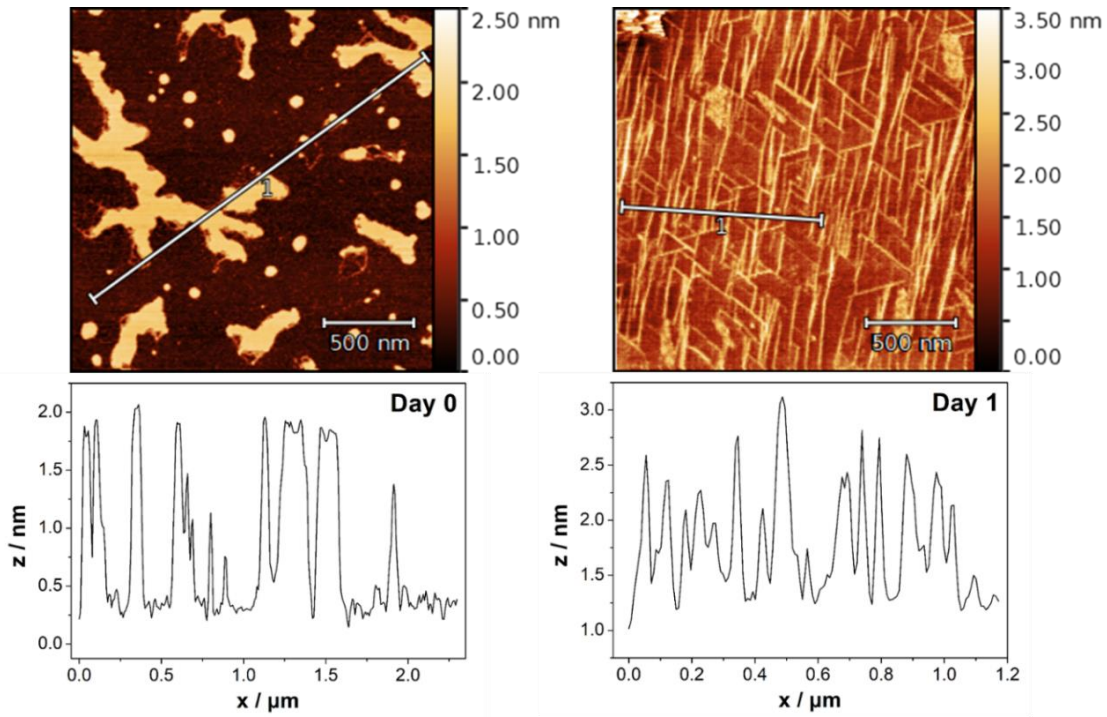

Figure 2.6. AFM topography images of **$[Tb(hfac)_3{\cdot}2H_2O]_n$@mica** and their corresponding height profiles after 30 minutes (left) and 1 day (right).

Initially, amorphous structures were observed on the surface due to the gradual evaporation of solvent and moisture. Interestingly, this morphology changes drastically with the ageing of the samples under controlled moisture conditions, highlighting the critical role of the presence of the Tb^{III} compound. Needle-like objects with lengths of hundreds of nanometres and heights of approximately 1.2 nm can be observed and have to be compared with the molecular structure of **[Tb(hfac)$_3$·2H$_2$O]** already reported in the literature.[65]

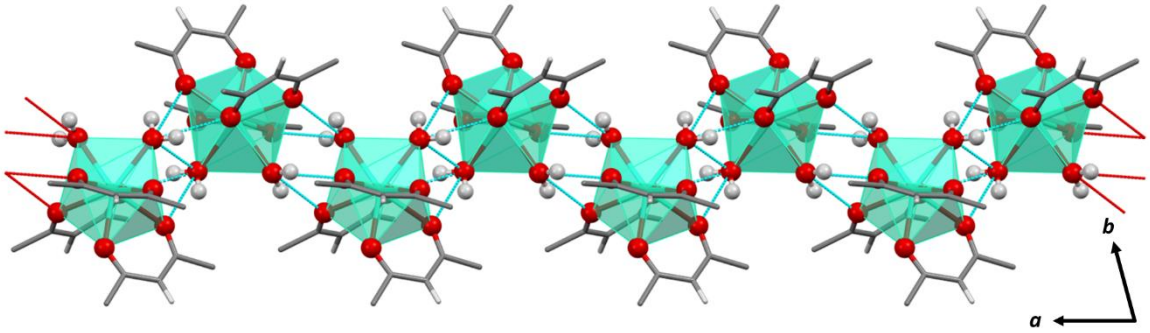

Figure 2.7. Crystallographic representation of **[Tb(hfac)$_3$·2H$_2$O]$_n$** with H-bond network highlighted as blue dotted bonds along the *a*-axis (fluorine atoms are omitted for clarity, adapted from Ref.[65]).

The **[Tb(hfac)$_3$·2H$_2$O]** crystal structure contains one single crystallographically independent Tb^{III} ion. The ion is eightfold coordinated by six oxygen atoms coming from three chelating $hfac^-$ ligands and two additional water molecules. Overall, this coordination pattern leads to a slightly distorted square antiprism D_{4d} coordination polyhedron ($CShM_{D4d}$ = 0.762) around the Tb^{III} ion. The two water molecules play a major role in organizing the Tb(hfac)$_3$ molecules in the crystal packing as they form a strong H-bond network with two $hfac^-$ ligands through the oxygen atoms of the neighbouring molecules. This gives rise to a supramolecular chain along the crystallographic *a*-axis. From the crystallographic data, the dimension of these chains can be estimated to be 10 Å in height and 13 Å in width,[65] that match quite well with the 1.2 nm estimated height deducted from the AFM cliches, as well as the one-dimensional arrangement of the Tb^{III} moieties driven by H-bonding supramolecular interactions.

These objects are aligned along three preferential directions on the muscovite (001) mica surface. The two-dimensional fast Fourier transform (2D-FFT) analysis of the AFM images shown in Figure 2.8 reveals that the needles indeed form an ordered arrangement along three preferential directions separated by 60° from each other. These directions recall the three main crystallisation directions of the hexagonal pattern formed by the tetragonal Si/Al atoms on the muscovite (001) mica surface. Some disordered objects that are roughly 1.5 nm high are also present on the surface, which could be due to residual amorphous **[Tb(hfac)$_3$·2H$_2$O]** formed by a less controlled evaporation of the solvent in these areas. Under high moisture conditions, the presence of these disordered areas could be minimised, thus optimizing the overall quality of the deposit. We stress that the moisture conditions are crucial for developing ordered features on the mica surface. Indeed, as soon as drier conditions (ambient relative humidity or dry conditions) were employed, no organised deposits could be observed.

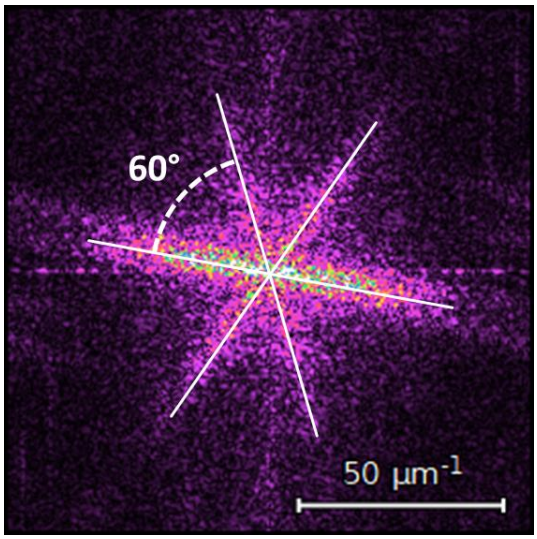

Figure 2.8. 2D-FFT analysis highlighting the three preferential directions of orientation of the needle-like objects on mica (left), distribution of the measured length (top) and height values (bottom).

Two different hypotheses regarding the origin of this orientation of the supramolecular chains on the mica surface can be proposed. The first hypothesis relies on the presence of K^+ ions on the mica surface that can lead to the formation of potassium carbonate (K_2CO_3) when mica is air-cleaved. Recent findings[66–69] show that the mechanism of K^+ depletion from air-cleaved mica is not fully known but resembles the one observed on aluminium oxide,[70] iron oxide[71] or cerium oxide[72] surfaces and is favoured by the presence of moisture.[69] As far as surface deposits are concerned, the epitaxial orientation of tungsten oxide (WO_3) nanowires upon deposition on air-cleaved mica[63] has been linked to the formation of K_2CO_3 acting as a precursor for the pure WO_3 nanowires. For **[Tb(hfac)$_3$·2H$_2$O]$_n$@mica** a similar growth of the chains along preferential directions on the mica substrate is observed. However, it is very unlikely that K_2CO_3 acts as a precursor for our compound, making this hypothesis irrelevant.

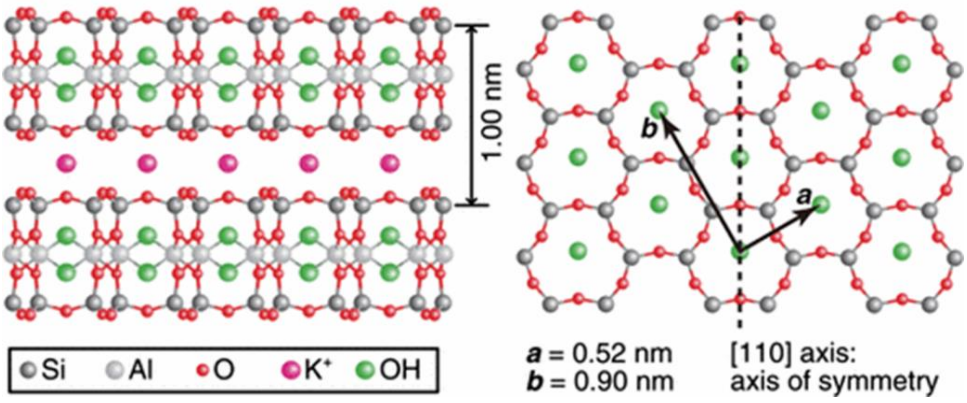

Figure 2.9. Crystal structure of muscovite mica along the [110] plane (left) and cleaved, along the [001] plane (reproduced from Ref.[73]).

The second hypothesis, which we consider more probable, is that the self-assembly of **[Tb(hfac)$_3$·2H$_2$O]** molecules into chains is likely to be triggered by the presence of –OH groups and water on the air-cleaved mica surface.

Indeed, reactions between the mica surface, atmospheric CO_2 and water occur instantaneously after cleavage in air.[74] The high wettability of mica under these conditions favours water condensation.[75] Indeed, it has been demonstrated that epitaxial adsorption of water on the hexagonal lattice of mica[76] is observed above 45% of relative humidity.[77,78] These findings were confirmed by theoretical simulations.[79] Accordingly, this is a favourable thermodynamic environment for the molecules to reproduce the H-bonded network observed in the crystal packing of **$[Tb(hfac)_3{\cdot}2H_2O]_n$**.

The occurrence of this second process is supported by the fact that deposits can be observed only when the samples are aged under significantly moist conditions (90% relative humidity). As soon as dryer conditions were tested, no chains were found on the surface. If this second hypothesis is correct, it can be reasonably inferred that water molecules are adsorbed along with preferential directions of the mica hexagonal network tailoring the organisation of the **$[Tb(hfac)_3{\cdot}2H_2O]_n$** chains along these directions.

One can note that the AFM tip gradually damages the chains during scanning by scratching, as shown below by a series of snapshots collected consecutively at the same location on the substrate. As the number of scans increases, the needles on the surface gradually disappear even when operating in tapping mode (semi-contact mode). This indicates the labile nature of the obtained deposit.

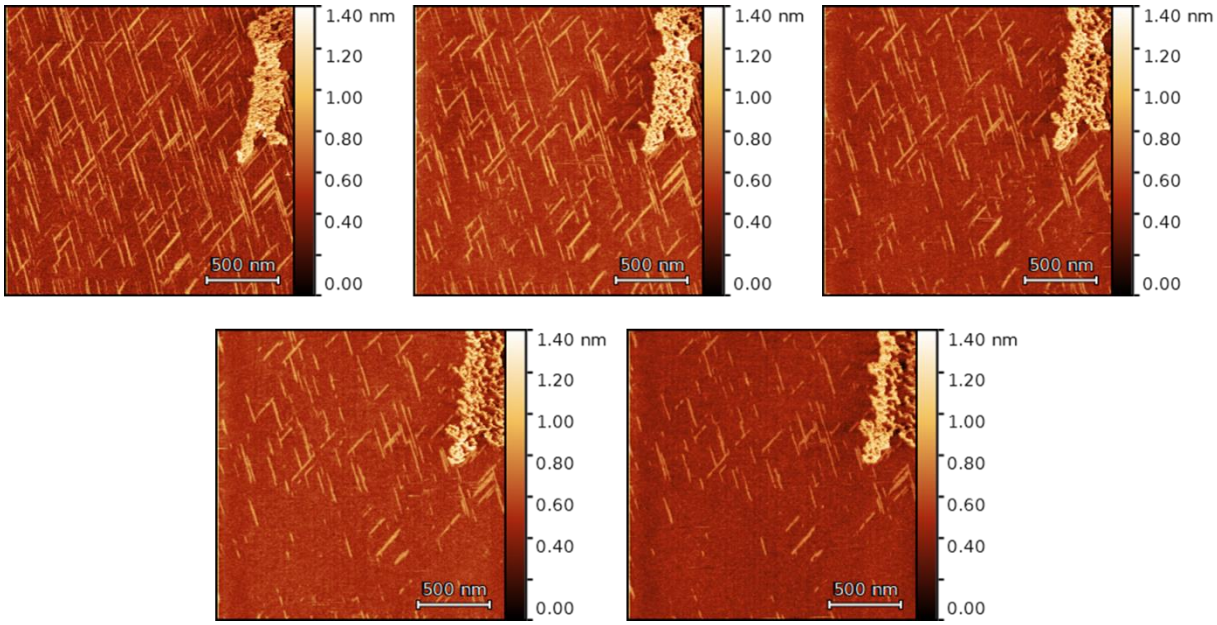

Figure 2.10. AFM images of **$[Tb(hfac)_3{\cdot}2H_2O]_n$@mica** taken in semi-contact mode consecutively in the same region of the sample (from left to right, and top to bottom).

Regardless, the good reproducibility of this deposition protocol allowed us to perform further characterisations on freshly prepared samples of **$[Tb(hfac)_3{\cdot}2H_2O]_n$@mica**, which relied on the inherent magnetic and luminescent properties of the **$[Tb(hfac)_3{\cdot}2H_2O]$**.

2.3.2. Magnetic properties of $[Tb(hfac)_3{\cdot}2H_2O]_n$@mica

Indeed, as discussed in Chapter 1, 4*f* ions are characterized by a large magnetic anisotropy due to unquenched orbital angular momentum and high magnetic moments, making them particularly appealing as building blocks for efficient molecular magnets.[80,81] It also makes them more sensitive to magnetic measurements, and therefore easier to identify even for small amounts, as in our case.

However, as a mineral, the muscovite mica substrate can occur with different chemical compositions, hosting randomly iron atoms by replacing SiO_4 tetrahedrons with iron oxides or by substituting the aluminium ions in the octahedral positions of the mica 2D network.[63] Consequently, the free substrate may have a significant magnetic response that could be of the same order of magnitude as the deposited material. This is why magnetic measurements have first been performed on the bare cleaved mica, which has subsequently been used to grow the supramolecular chains.

Dynamic magnetic measurements were performed with an oscillating field (H_{AC} = 3 Oe) on a freshly cleaved mica substrate (*m* = 11.6 mg) at various frequencies and external static fields to probe any dynamic contribution. No out-of-phase χ_g'' signal is observed, excluding the possibility of a parasitic relaxation process (Figure 2.A.15). The constant value of the in-phase χ_g' susceptibility (1.0 x 10^{-7} emu·g^{-1}), as well as the very weak hysteresis magnetic signal (Figure 2.A.16), will be subtracted from the signal obtained for the deposited **$[Tb(hfac)_3{\cdot}2H_2O]_n$** on mica in the following.

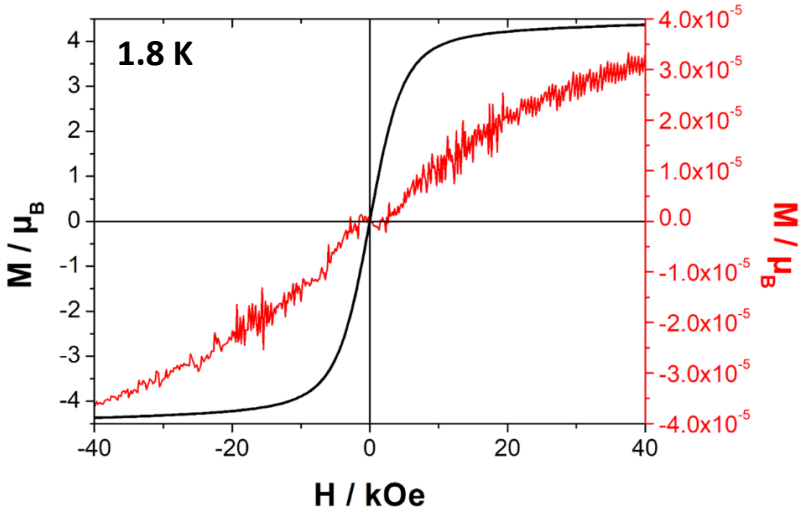

Figure 2.11 Magnetisation curves of **$[Tb(hfac)_3{\cdot}2H_2O]$** (black) and **$[Tb(hfac)_3{\cdot}2H_2O]_n$@mica** (red) with a magnetic field sweep rate of 15.5 Oe·s^{-1}.

In order to compare the static behaviour of the Tb^{III} molecules from the bulk crystalline and deposited states, magnetic hysteresis measurements of both **$[Tb(hfac)_3{\cdot}2H_2O]$** and **$[Tb(hfac)_3{\cdot}2H_2O]_n$@mica** have been performed. If a correct signal-to-noise ratio is observed on the deposits, which validates the use of Tb^{III} as a spin carrier, complete saturation of the magnetisation is not observed even at H_{DC} = 40 kOe, probably because of a partial loss of the magnetic anisotropy of Tb^{III} in the deposits (*vide infra*).

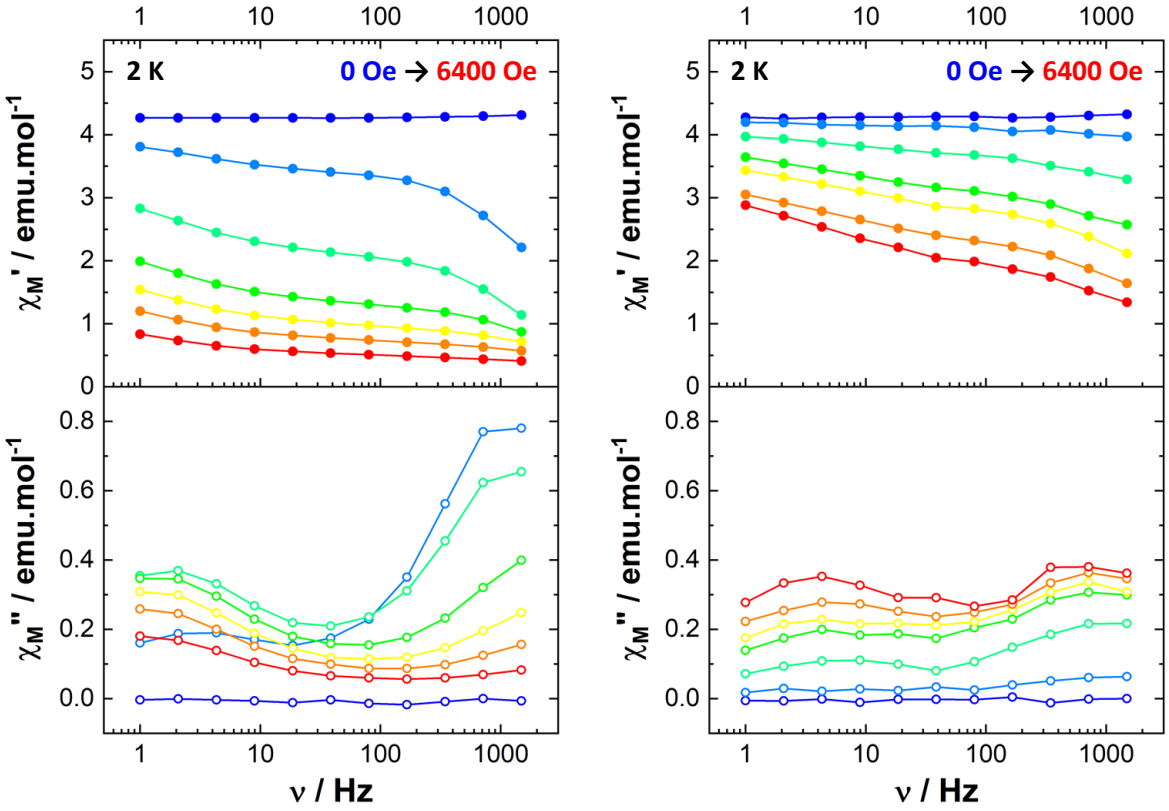

Figure 2.12. Frequency dependence of the in-phase (χ_M') and the out-of-phase (χ_M'') susceptibilities of bulk **[Tb(hfac)$_3$·2H$_2$O]** (left) and **[Tb(hfac)$_3$·2H$_2$O]$_n$@mica** (right) with different H_{DC} static fields.

The out-of-phase magnetic susceptibility of both the **[Tb(hfac)$_3$·2H$_2$O]** and the **[Tb(hfac)$_3$·2H$_2$O]$_n$@mica** samples is frequency-dependent, a feature characteristic of SMM behaviour. The frequency dependence of χ_M'' of the **[Tb(hfac)$_3$·2H$_2$O]$_n$@mica** sample is similar to that of crystalline bulk **[Tb(hfac)$_3$·2H$_2$O]$_n$**. Namely, two maxima of χ_M'' are observed, which however differently depend on the static magnetic field applied probably due to a partial loss of the magnetic anisotropy of Tb^{III} upon layering on the mica substrate. This may be a result of *i)* the geometric distribution of the Tb coordination environment in the deposits similar to what has been observed when SMMs are dissolved in liquid matrixes[82] or *ii)* a modification of the spin-phonon coupling, as the phonon bath of such deposits is drastically different from the one of the bulk material.

2.3.3. Luminescence of [Tb(hfac)$_3$·2H$_2$O]$_n$@mica

Lanthanide ions also have unique luminescence properties because of the negligible influence of the crystal field, resulting in narrow line-shaped bands due to the inner nature of their 4*f* orbitals. Indeed, the intense green luminescence of the Tb^{III} ion arises from the forbidden f → f transitions between the radiative level $^5D_4$ to the ^7F_J lower states (with J = 6 - 1). These well-localised emission bands are especially interesting in our case to probe the presence of lanthanide-functionalised surfaces,[83,84] thus luminescence properties of both **[Tb(hfac)$_3$·2H$_2$O]** and **[Tb(hfac)$_3$·2H$_2$O]$_n$@mica** have been measured.

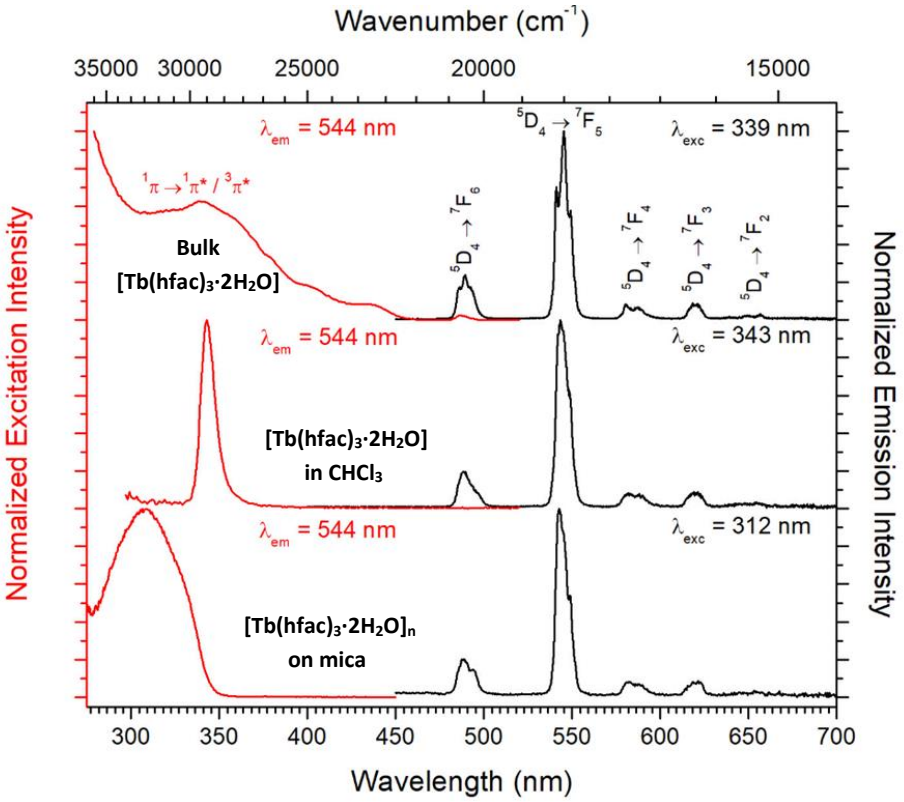

Figure 2.13. Excitation (red) and emission (black) spectra of bulk **[Tb(hfac)$_3$·2H$_2$O]** (top), 10^{-5} mol·L^{-1} $CHCl_3$ solution of **[Tb(hfac)$_3$·2H$_2$O]** (middle) and **[Tb(hfac)$_3$·2H$_2$O]$_n$@mica** (bottom).

As shown above, the luminescence spectrum of the chains of Tb^{III} on the mica substrate is preserved,[85] *i.e.,* an efficient ligand-to-terbium energy transfer is observed in the excitation spectra with a maximum of the excitation observed for the $^1\pi \rightarrow {}^1\pi^*/{}^3\pi^*$ absorption transitions coming from the ligand at around 339 nm in the solid-state, at 343 nm in $CHCl_3$ solution and at 312 nm on mica. The emission bands at 489, 544, 580 and 620 nm are attributed to the $^5D_4 \rightarrow {}^7F_6$, $^5D_4 \rightarrow {}^7F_5$, $^5D_4 \rightarrow {}^7F_4$ and $^5D_4 \rightarrow {}^7F_3$ transitions, respectively.[86] The presence of the $^5D_4 \rightarrow {}^7F_2$ transition can be observed only in the spectrum of the bulk at 656 nm due to the relatively high emission intensity, which cannot be observed accurately for the deposits of Tb^{III} on mica.

We note that the relative luminescence intensities greatly depend on the nature of the sample. The luminescence observed for the chains on the mica substrate is weaker than that of the bulk by several orders of magnitude. This variation could be explained by water-induced quenching or oxygen quenching[87] and by the decrease of the lifetime τ from 375 µs for **[Tb(hfac)$_3$·2H$_2$O]** to 132 µs for **[Tb(hfac)$_3$·2H$_2$O]$_n$@mica** (see Table 2.1 below).

Table 2.1. Luminescence lifetimes τ of bulk **[Tb(hfac)$_3$·2H$_2$O]$_n$**, **[Tb(hfac)$_3$·2H$_2$O]$_n$@mica** and 10^{-5} mol·L^{-1} $CHCl_3$ solution of **[Tb(hfac)$_3$·2H$_2$O]$_n$**.

Sample	τ (µs)
$[Tb(hfac)_3{\cdot}2H_2O]_n$	375 ± 0.6
$[Tb(hfac)_3{\cdot}2H_2O]_n$@mica	129 ± 0.8
$[Tb(hfac)_3{\cdot}2H_2O]$ in $CHCl_3$	13 ± 0.1

Furthermore, the very small amount of luminescent material present on the mica substrate reduces the luminescence intensity. The quantum yields could not be measured because of the geometry of the sample (large anisotropic plates) and the weakness of the emission signal.

The excitation spectrum of the bulk is similar to the one already reported in the literature[88] with a main band at 339 nm and three small shoulders around 378 nm ($^5G_6 \leftarrow {}^7F_6$), as well as another direct metal-centred transition ($^5D_4 \leftarrow {}^7F_6$) at 486 nm. Once the solid is dissolved in $CHCl_3$, the only remaining transition in the excitation spectra is characterized by a very narrow band at 343 nm attributed to the $^1\pi \rightarrow {}^1\pi^*/{}^3\pi^*$ transition. The spectrum of the supramolecular chains on mica, however, exhibits a wide excitation band around 312 nm, which could arise from an important change of the local environment of **[Tb(hfac)$_3$·2H$_2$O]** with the presence of water and potassium ions close to the $hfac^-$ ligands.

2.4. Conclusion

In this chapter, we have determined a protocol aiming at the deposition of single chains of **[Tb(hfac)$_3$(NITPhOPh)]$_n$** on surface. The first step of this protocol was to evaluate the stability of the SCM crystals and their dispersion in an appropriate solvent under sonication conditions. This was followed by deposition attempts by drop-casting on mica, characterised by AFM measurements.

If the reported results were non-conclusive (because of the observation of poorly adherent fragmented crystals), the tests carried out with the constituent building blocks were more successful. Indeed, depositions of one-dimensional chains were obtained from diluted solutions of **[Tb(hfac)$_3$·2H$_2$O]**. The optimal conditions of reproducibility were identified, the crucial one being the ageing in humid atmosphere of the fresh samples; the presence of atmospheric water molecules, coupled to the hydrophilic nature of the mica surface allows the Tb^{III} complexes to stabilise into a supramolecular structure *via* hydrogen bonds.

Accordingly, the very strong magnetic moment and the high luminescence of the Tb^{III} ion allow the observation of the magnetic and the luminescent behaviour of **[Tb(hfac)$_3$·2H$_2$O]$_n$@mica** without any particular surface-dedicated instrumentation. In particular, a significant magnetic signal is observed from the deposits, which is used to approximate the mass of the deposited material. The luminescence lifetime measured for **[Tb(hfac)$_3$·2H$_2$O]$_n$@mica** is smaller than that of bulk **[Tb(hfac)$_3$·2H$_2$O]$_n$** but larger than that of a diluted solution of **[Tb(hfac)$_3$·2H$_2$O]$_n$**. This gradual lifetime reduction from bulk to surface to liquid could be associated with the diminution of the number of neighbouring terbium ions and, hence, the reduction of Tb^{III} self-quenching possibilities.

However, the strategy adopted in this study failed to achieve the deposition of SCMs on surface. Although we observed Tb^{III} chains on surface, they do not have appealing magnetic behaviour, which is the scope of this thesis. To address this point, efforts have to be made to design new NIT ligands with functionalised pending groups that could be more suitable for the deposition process.

2.5. References

[1] L. Bogani, W. Wernsdorfer, *Nat. Mater.* **2008**, *7*, 179–186.

[2] S. Jiang, K. Goß, C. Cervetti, L. Bogani, *Sci. China Chem.* **2012**, *55*, 867–882.

[3] L. Bogani, in *Mol. Nanomagnets Relat. Phenom.* (Ed.: S. Gao), Springer Berlin Heidelberg, Berlin, Heidelberg, **2014**, pp. 331–381.

[4] K. Hymas, A. Soncini, *Phys. Rev. B* **2019**, *99*, 245404.

[5] F.-S. Guo, B. M. Day, Y.-C. Chen, M.-L. Tong, A. Mansikkamäki, R. A. Layfield, *Science* **2018**, *362*, 1400–1403.

[6] D. Gatteschi, A. Cornia, M. Mannini, R. Sessoli, *Inorg. Chem.* **2009**, *48*, 3408–3419.

[7] A. Cornia, M. Mannini, P. Sainctavit, R. Sessoli, *Chem. Soc. Rev.* **2011**, *40*, 3076.

[8] H. Brune, P. Gambardella, in *Fundam. Picoscience*, CRC Press, **2013**, pp. 447–470.

[9] R. J. Holmberg, M. Murugesu, *J. Mater. Chem. C* **2015**, *3*, 11986–11998.

[10] P. Gambardella, A. Dallmeyer, K. Maiti, M. C. Malagoli, W. Eberhardt, K. Kern, C. Carbone, *Nature* **2002**, *416*, 301–304.

[11] P. Gambardella, S. Rusponi, M. Veronese, S. S. Dhesi, C. Grazioli, A. Dallmeyer, I. Cabria, R. Zeller, P. H. Dederichs, K. Kern, C. Carbone, H. Brune, *Science* **2003**, *300*, 1130–1133.

[12] F. Donati, S. Rusponi, S. Stepanow, C. Wackerlin, A. Singha, L. Persichetti, R. Baltic, K. Diller, F. Patthey, E. Fernandes, J. Dreiser, . ljivan anin, K. Kummer, C. Nistor, P. Gambardella, H. Brune, *Science* **2016**, *352*, 318–321.

[13] T. Miyamachi, T. Schuh, T. Märkl, C. Bresch, T. Balashov, A. Stöhr, C. Karlewski, S. André, M. Marthaler, M. Hoffmann, M. Geilhufe, S. Ostanin, W. Hergert, I. Mertig, G. Schön, A. Ernst, W. Wulfhekel, *Nature* **2013**, *503*, 242–246.

[14] C. Hübner, B. Baxevanis, A. A. Khajetoorians, D. Pfannkuche, *Phys. Rev. B* **2014**, *90*, 155134.

[15] L. Bogani, L. Cavigli, M. Gurioli, R. L. Novak, M. Mannini, A. Caneschi, F. Pineider, R. Sessoli, M. Clemente-León, E. Coronado, A. Cornia, D. Gatteschi, *Adv. Mater.* **2007**, *19*, 3906–3911.

[16] M. Mannini, P. Sainctavit, R. Sessoli, C. Cartier dit Moulin, F. Pineider, M.-A. Arrio, A. Cornia, D. Gatteschi, *Chem. - Eur. J.* **2008**, *14*, 7530–7535.

[17] L. Margheriti, D. Chiappe, M. Mannini, P.-E. Car, P. Sainctavit, M.-A. Arrio, F. B. de Mongeot, J. C. Cezar, F. M. Piras, A. Magnani, E. Otero, A. Caneschi, R. Sessoli, *Adv. Mater.* **2010**, *22*, 5488–5493.

[18] A. Hofmann, Z. Salman, M. Mannini, A. Amato, L. Malavolti, E. Morenzoni, T. Prokscha, R. Sessoli, A. Suter, *ACS Nano* **2012**, *6*, 8390–8396.

[19] L. Malavolti, M. Mannini, P.-E. Car, G. Campo, F. Pineider, R. Sessoli, *J. Mater. Chem. C* **2013**, *1*, 2935.

[20] B. Warner, F. El Hallak, N. Atodiresei, P. Seibt, H. Prüser, V. Caciuc, M. Waters, A. J. Fisher, S. Blügel, J. van Slageren, C. F. Hirjibehedin, *Nat. Commun.* **2016**, *7*, 12785.

[21] L. Margheriti, M. Mannini, L. Sorace, L. Gorini, D. Gatteschi, A. Caneschi, D. Chiappe, R. Moroni, F. B. de Mongeot, A. Cornia, F. M. Piras, A. Magnani, R. Sessoli, *Small* **2009**, *5*, 1460–1466.

[22] L. Malavolti, V. Lanzilotto, S. Ninova, L. Poggini, I. Cimatti, B. Cortigiani, L. Margheriti, D. Chiappe, E. Otero, P. Sainctavit, F. Totti, A. Cornia, M. Mannini, R. Sessoli, *Nano Lett.* **2015**, *15*, 535–541.

[23] E. Kiefl, M. Mannini, K. Bernot, X. Yi, A. Amato, T. Leviant, A. Magnani, T. Prokscha, A. Suter, R. Sessoli, Z. Salman, *ACS Nano* **2016**, *10*, 5663–5669.

[24] L. Gragnaniello, F. Paschke, P. Erler, P. Schmitt, N. Barth, S. Simon, H. Brune, S. Rusponi, M. Fonin, *Nano Lett.* **2017**, *17*, 7177–7182.

[25] A. Köbke, F. Gutzeit, F. Röhricht, A. Schlimm, J. Grunwald, F. Tuczek, M. Studniarek, D. Longo, F. Choueikani, E. Otero, P. Ohresser, S. Rohlf, S. Johannsen, F. Diekmann, K. Rossnagel, A. Weismann, T. Jasper-Toennies, C. Näther, R. Herges, R. Berndt, M. Gruber, *Nat. Nanotechnol.* **2020**, *15*, 18–21.

[26] F. Paschke, T. Birk, V. Enenkel, F. Liu, V. Romankov, J. Dreiser, A. A. Popov, M. Fonin, *Adv. Mater.* **2021**, 2102844.

[27] G. G. Condorelli, A. Motta, I. L. Fragalà, F. Giannazzo, V. Raineri, A. Caneschi, D. Gatteschi, *Angew. Chem. Int. Ed.* **2004**, *43*, 4081–4084.

[28] B. Fleury, L. Catala, V. Huc, C. David, W. Zhao Zhong, P. Jegou, L. Baraton, S. Palacin, P.-A. Albouy, T. Mallah, *Chem. Commun.* **2005**, 2020.

[29] G. G. Condorelli, A. Motta, G. Pellegrino, A. Cornia, L. Gorini, I. L. Fragalà, C. Sangregorio, L. Sorace, *Chem. Mater.* **2008**, *20*, 2405–2411.

[30] M. Mannini, F. Bertani, C. Tudisco, L. Malavolti, L. Poggini, K. Misztal, D. Menozzi, A. Motta, E. Otero, P. Ohresser, P. Sainctavit, G. G. Condorelli, E. Dalcanale, R. Sessoli, *Nat. Commun.* **2014**, *5*, 4582.

[31] M. Mannini, F. Pineider, P. Sainctavit, C. Danieli, E. Otero, C. Sciancalepore, A. M. Talarico, M.-A. Arrio, A. Cornia, D. Gatteschi, R. Sessoli, *Nat. Mater.* **2009**, *8*, 194–197.

[32] M. Mannini, F. Pineider, C. Danieli, F. Totti, L. Sorace, P. Sainctavit, M.-A. Arrio, E. Otero, L. Joly, J. C. Cezar, A. Cornia, R. Sessoli, *Nature* **2010**, *468*, 417–421.

[33] F. Pineider, M. Mannini, C. Danieli, L. Armelao, F. M. Piras, A. Magnani, A. Cornia, R. Sessoli, *J Mater Chem* **2010**, *20*, 187–194.

[34] M. Perfetti, F. Pineider, L. Poggini, E. Otero, M. Mannini, L. Sorace, C. Sangregorio, A. Cornia, R. Sessoli, *Small* **2014**, *10*, 323–329.

[35] D. Mitcov, A. H. Pedersen, M. Ceccato, R. M. Gelardi, T. Hassenkam, A. Konstantatos, A. Reinholdt, M. A. Sørensen, P. W. Thulstrup, M. G. Vinum, F. Wilhelm, A. Rogalev, W. Wernsdorfer, E. K. Brechin, S. Piligkos, *Chem. Sci.* **2019**, *10*, 3065–3073.

[36] J. Gómez-Segura, I. Díez-Pérez, N. Ishikawa, M. Nakano, J. Veciana, D. Ruiz-Molina, *Chem Commun* **2006**, 2866–2868.

[37] L. Bogani, C. Danieli, E. Biavardi, N. Bendiab, A.-L. Barra, E. Dalcanale, W. Wernsdorfer, A. Cornia, *Angew. Chem. Int. Ed.* **2009**, *48*, 746–750.

[38] S. Kyatskaya, J. R. Galán Mascarós, L. Bogani, F. Hennrich, M. Kappes, W. Wernsdorfer, M. Ruben, *J. Am. Chem. Soc.* **2009**, *131*, 15143–15151.

[39] L. Spree, F. Liu, V. Neu, M. Rosenkranz, G. Velkos, Y. Wang, S. Schiemenz, J. Dreiser, P. Gargiani, M. Valvidares, C. Chen, B. Büchner, S. M. Avdoshenko, A. A. Popov, *Adv. Funct. Mater.* **2021**, 2105516.

[40] R. Mas-Ballesté, J. Gómez-Herrero, F. Zamora, *Chem. Soc. Rev.* **2010**, *39*, 4220.

[41] W. L. Leong, J. J. Vittal, *Chem. Rev.* **2011**, *111*, 688–764.

[42] S. Stepanow, M. Lingenfelder, A. Dmitriev, H. Spillmann, E. Delvigne, N. Lin, X. Deng, C. Cai, J. V. Barth, K. Kern, *Nat. Mater.* **2004**, *3*, 229–233.

[43] M. Surin, P. Samorì, A. Jouaiti, N. Kyritsakas, M. W. Hosseini, *Angew. Chem. Int. Ed.* **2007**, *46*, 245–249.

[44] D. Olea, R. González-Prieto, J. L. Priego, M. C. Barral, P. J. de Pablo, M. R. Torres, J. Gómez-Herrero, R. Jiménez-Aparicio, F. Zamora, *Chem Commun* **2007**, 1591–1593.

[45] O. Shekhah, H. Wang, S. Kowarik, F. Schreiber, M. Paulus, M. Tolan, C. Sternemann, F. Evers, D. Zacher, R. A. Fischer, C. Wöll, *J. Am. Chem. Soc.* **2007**, *129*, 15118–15119.

[46] M. Koepf, J. A. Wytko, J.-P. Bucher, J. Weiss, *J. Am. Chem. Soc.* **2008**, *130*, 9994–10001.

[47] M. Koepf, F. Chérioux, J. A. Wytko, J. Weiss, *Coord. Chem. Rev.* **2012**, *256*, 2872–2892.

[48] D. Olea, S. S. Alexandre, P. Amo-Ochoa, A. Guijarro, F. de Jesús, J. M. Soler, P. J. de Pablo, F. Zamora, J. Gómez-Herrero, *Adv. Mater.* **2005**, *17*, 1761–1765.

[49] P. Amo-Ochoa, L. Welte, R. González-Prieto, P. J. Sanz Miguel, C. J. Gómez-García, E. Mateo-Martí, S. Delgado, J. Gómez-Herrero, F. Zamora, *Chem. Commun.* **2010**, *46*, 3262.

[50] R. Matsuoka, R. Toyoda, R. Sakamoto, M. Tsuchiya, K. Hoshiko, T. Nagayama, Y. Nonoguchi, K. Sugimoto, E. Nishibori, T. Kawai, H. Nishihara, *Chem. Sci.* **2015**, *6*, 2853–2858.

[51] R. Aoki, R. Toyoda, J. F. Kögel, R. Sakamoto, J. Kumar, Y. Kitagawa, K. Harano, T. Kawai, H. Nishihara, *J. Am. Chem. Soc.* **2017**, *139*, 16024–16027.

[52] L. Bogani, C. Sangregorio, R. Sessoli, D. Gatteschi, *Angew. Chem. Int. Ed.* **2005**, *44*, 5817–5821.

[53] K. Bernot, L. Bogani, A. Caneschi, D. Gatteschi, R. Sessoli, *J. Am. Chem. Soc.* **2006**, *128*, 7947–7956.

[54] K. Bernot, L. Bogani, R. Sessoli, D. Gatteschi, *Inorganica Chim. Acta* **2007**, *360*, 3807–3812.

[55] A. Caneschi, D. Gatteschi, N. Lalioti, C. Sangregorio, R. Sessoli, *J. Chem. Soc. Dalton Trans.* **2000**, 3907–3912.

[56] K. Bernot, L. Bogani, A. Caneschi, D. Gatteschi, R. Sessoli, *J. Am. Chem. Soc.* **2006**, *128*, 7947–7956.

[57] Q. Evrard, F. Houard, C. Daiguebonne, G. Calvez, Y. Suffren, O. Guillou, M. Mannini, K. Bernot, *Inorg. Chem.* **2020**, *59*, 9215–9226.

[58] C. Einhorn, J. Einhorn, J.-L. Luche, *Synthesis* **1989**, *1989*, 787–813.

[59] V. Safarifard, A. Morsali, *Coord. Chem. Rev.* **2015**, *292*, 1–14.

[60] W. de Poel, S. Pintea, J. Drnec, F. Carla, R. Felici, P. Mulder, J. A. A. W. Elemans, W. J. P. van Enckevort, A. E. Rowan, E. Vlieg, *Surf. Sci.* **2014**, *619*, 19–24.

[61] A. L. Weisenhorn, *J. Vac. Sci. Technol. B Microelectron. Nanometer Struct.* **1991**, *9*, 1333.

[62] Y. P. Wu, Y. Yang, Z. H. Yang, N. N. Phouc, F. Ma, B. Y. Zong, J. Ding, *J. Appl. Phys.* **2015**, *118*, 013902.

[63] I. Matolínová, M. Gillet, E. Gillet, V. Matolín, *Nanotechnology* **2009**, *20*, 445604.

[64] P. Amo-Ochoa, M. I. Rodríguez-Tapiador, O. Castillo, D. Olea, A. Guijarro, S. S. Alexandre, J. Gómez-Herrero, F. Zamora, *Inorg. Chem.* **2006**, *45*, 7642–7650.

[65] I. Y. Bagryanskaya, L. V. Politanskaya, E. V. Tretyakov, *Inorg. Chem. Commun.* **2016**, *66*, 47–50.

[66] P. . Campbell, L. . Sinnamon, C. . Thompson, D. . Walmsley, *Surf. Sci.* **1998**, *410*, L768–L772.

[67] H. Poppa, A. G. Elliot, *Surf. Sci.* **1971**, *24*, 149–163.

[68] M. G. Dowsett, R. M. King, E. H. C. Parker, **n.d.**, 8.

[69] W. L. Baun, *Surf. Interface Anal.* **1980**, *2*, 145–147.

[70] C. Morterra, A. Zecchina, S. Coluccia, A. Chiorino, *J. Chem. Soc. Faraday Trans. 1 Phys. Chem. Condens. Phases* **1977**, *73*, 1544.

[71] J. Baltrusaitis, V. H. Grassian, *J. Phys. Chem. B* **2005**, *109*, 12227–12230.

[72] Y. Lykhach, T. Staudt, R. Streber, M. P. A. Lorenz, A. Bayer, H.-P. Steinrück, J. Libuda, *Eur. Phys. J. B* **2010**, *75*, 89–100.

[73] T. Fukuma, Y. Ueda, S. Yoshioka, H. Asakawa, *Phys. Rev. Lett.* **2010**, *104*, 016101.

[74] H. K. Christenson, N. H. Thomson, *Surf. Sci. Rep.* **2016**, *71*, 367–390.

[75] J. . Israelachvili, *J. Colloid Interface Sci.* **1973**, *44*, 259–272.

[76] J. L. Caslavsky, K. Vedam, *J. Appl. Phys.* **1971**, *42*, 516–520.

[77] J. Hu, X.-D. Xiao, D. F. Ogletree, M. Salmeron, *Science* **1995**, *268*, 267–269.

[78] J. Hu, X. -d. Xiao, D. F. Ogletree, M. Salmeron, *Surf. Sci.* **1995**, *344*, 221–236.

[79] M. Odelius, M. Bernasconi, M. Parrinello, *Phys. Rev. Lett.* **1997**, *78*, 2855–2858.

[80] J. D. Rinehart, J. R. Long, *Chem. Sci.* **2011**, *2*, 2078.

[81] D. N. Woodruff, R. E. P. Winpenny, R. A. Layfield, *Chem. Rev.* **2013**, *113*, 5110–5148.

[82] T. T. da Cunha, J. Jung, M.-E. Boulon, G. Campo, F. Pointillart, C. L. M. Pereira, B. Le Guennic, O. Cador, K. Bernot, F. Pineider, S. Golhen, L. Ouahab, *J. Am. Chem. Soc.* **2013**, *135*, 16332–16335.

[83] C. S. Bonnet, J. Massue, S. J. Quinn, T. Gunnlaugsson, *Org. Biomol. Chem.* **2009**, *7*, 3074.

[84] Q.-P. Li, B. Yan, *RSC Adv.* **2012**, *2*, 10840.

[85] W. T. Carnall, P. R. Fields, K. Rajnak, *J. Chem. Phys.* **1968**, *49*, 4447–4449.

[86] K. Binnemans, in *Handb. Phys. Chem. Rare Earths*, Elsevier, **2005**, pp. 107–272.

[87] S. Faulkner, S. J. A. Pope, B. P. Burton-Pye, *Appl. Spectrosc. Rev.* **2005**, *40*, 1–31.

[88] E. R. H. Walter, J. A. G. Williams, D. Parker, *Chem. Commun.* **2017**, *53*, 13344–13347.

2.A. Appendices

2.A.1. Deposition attempts of a SCM by drop-casting

2.A.1.1. Synthesis of [Ln(hfac)$_3$·2H$_2$O]

On one hand, 8 mmol (1 eq.) of $LnCl_3·6H_2O$ was dissolved in 10 mL of H_2O. On the other hand, 24 mmol (3.35 mL, 3 eq.) of Hhfac (hexafluoroacetylacetone) was poured in 100 mL of cold Et_2O. The latter was deprotonated by addition of around 2 mL of aqueous ammonia solution (25 %), giving white smokes. Once they disappeared, the aqueous $LnCl_3$ solution was added and the organic phase was washed several times with water (3 x 50 mL) and separated. The resultant organic solution was dried on Na_2SO_4 and concentrated under reduced pressure, giving a yellow oil. This yellow oil was dried in a dry atmosphere, giving a yellow-white powder (Yield = 64.2 %).

2.A.1.2. Synthesis of homogeneous and pure [Tb(hfac)$_3$(NITPhOPh)]$_n$ microcrystallites

The synthesis of the pure **[Tb(hfac)$_3$(NITPhOPh)]$_n$** powder was already reported elsewhere.[57] 1.3 mmol (106.1 mg, 1.3 eq.) of [Tb(hfac)$_3$·2H$_2$O] was dissolved in 40 mL of boiling heptane (T_b = 98 °C) and the solution concentrated to 12 mL. 1 mmol (32.5 mg, 1eq.) of NITPhOPh was then added with 3 mL of $CHCl_3$ (T_b = 61 °C). The process was thus performed under antisolvent conditions with $CHCl_3$ as solvent and heptane as antisolvent. The obtained deep blue solution was then directly transferred to a 20 mL vial for immediate sonication. Pulsed sonication was performed with a Hielscher UP400 St sonicator using an S24d3 sonotrode operating at a fixed frequency (24 kHz) with a 90 % pulse rate (0.9 s of sonication/0.1 s of silence, ≈ 24 J per pulse) until 150 kJ were delivered. The precipitate was quickly filtered, affording a dark green powder corresponding to crystallites of **[Tb(hfac)$_3$(NITPhOPh)]$_n$** (Yield = 24.2 %).

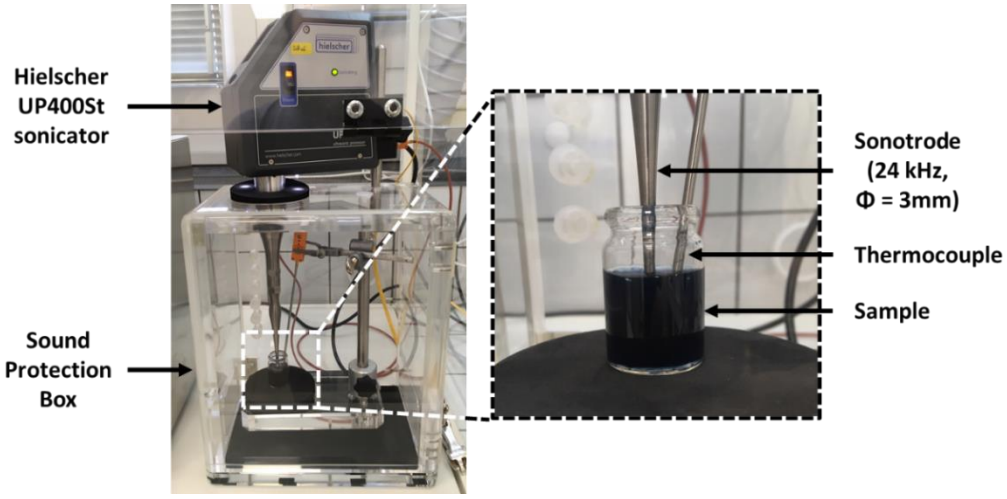

Figure 2.A.14. Pictures of the ultrasonication setup used for this study.

2.A.1.3. Substrate samples preparation

Muscovite mica substrates were cleaved with adhesive tape right before the drop-casting step. A 0.35 mmol·L^{-1} solution of the studied compound in anhydrous cyclohexane (99.5 %, Sigma-Aldrich) was sonicated for 2 min in an ultrasonic bath (Bransonic 3510, 80 W), and 0.5 mL of this solution were dripped on a freshly air-cleaved mica surface (with an adhesive tape). The samples were dried under an N_2 flux, then either directly characterised or kept at 300 K and relative humidity of 90% for 24 h.

2.A.1.4. Atomic Force Microscopy

AFM imaging was performed with a P47-PRO instrument (NT-MDT co. Zelenograd, Moscow, Russia) using an NSC-36 silicon tip (Mikromasch, Sofia, Bulgaria) with a resonance frequency of about 92 kHz. Semi-contact mode was used in order to avoid any deformation or damage to the examined samples. All images were processed using the Gwyddion software.

2.A.2. Deposition of $[Tb(hfac)_3.2H_2O]$

2.A.2.1. Magnetic properties of $[Tb(hfac)_3{\cdot}2H_2O]_n$@mica

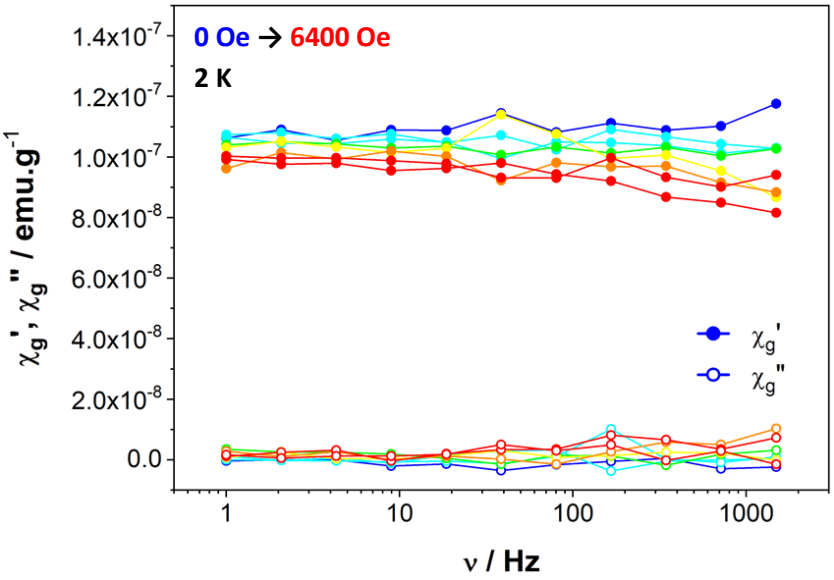

Figure 2.A.15. Frequency dependence of the in-phase (χ_g') and the out-of-phase (χ_g'') mass susceptibilities of the **mica** substrate (m = 11.6 mg) measured at different H_{DC} fields.

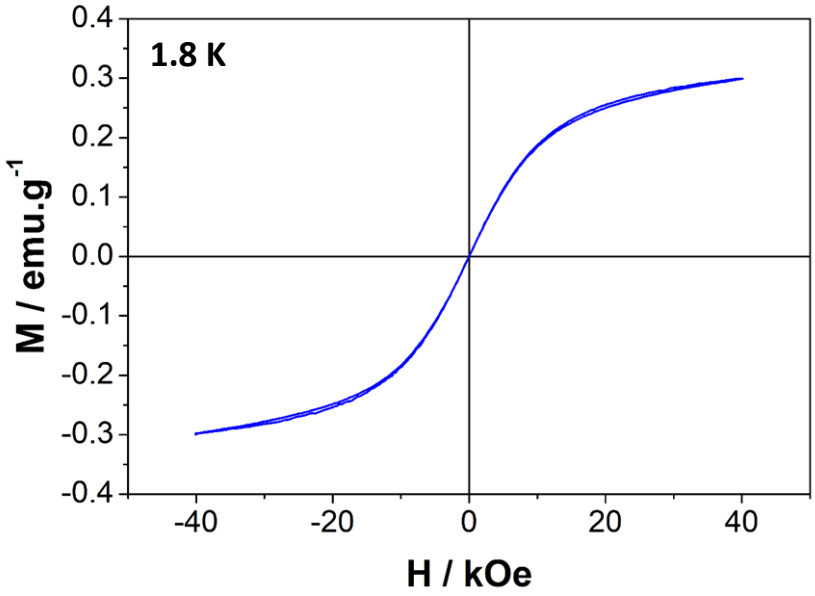

Figure 2.A.16. Magnetisation curve of **mica** substrate (*m* = 11.6 mg) with a magnetic field sweep rate of 15.5 Oe·s^{-1}.

2.A.2.2. Luminescence of [Tb(hfac)$_3$·2H$_2$O]$_n$@mica

Luminescence emission spectra were measured with a Horiba Jobin-Yvon Fluorolog-III fluorescence spectrometer equipped with a 450 W Xe lamp. The emission signal was collected in the 190 - 860 nm range via a Hamamatsu R928 UV-visible photomultiplier. The sample emission was measured directly on the mica substrate (in reflection mode at 90°). The emission lifetime was obtained using the same equipment coupled to an additional time-correlated single-photon counting (TSPC) module and a pulsed Xe source at 312 nm. The measurement of the bulk material was performed using a powder sample holder with a quartz window.

The bulk sample was positioned following the same geometry as used for the mica substrate (in reflection mode at 90°). The emission lifetime was measured using the TSPC module and a pulsed Xe source at 339 nm. The luminescence measurements of the liquid samples were performed using a standard 1 cm quartz cuvette containing a 10^{-5} mol·L^{-1} solution of [Tb(hfac)$_3$·2H$_2$O]. Appropriate filters were used to remove residual lamp excitation, scattered light and associated harmonics. The emission lifetime was measured using the TSPC module and a pulsed Xe source at 312 nm for the water solution and a pulsed Horiba Scientific DeltaDiode DD-340 nm for the $CHCl_3$ solution.

Chapter 3. Chiral Supramolecular Nanotubes of Single-Chain Magnets

3.1. Introduction

We have seen in Chapter 2 that the **[Tb(hfac)$_3$(NITPhOPh)]** coordination polymer was not suitable for the deposition of SCM on surface. We assumed that the pendant phenyl group of the bridging NIT radical provided too strong intermolecular interactions to favour dissociation of the corresponding single chains during sonication, from the crystalline bulk into a dispersed solution.

In this chapter, we have synthesised an NIT radical with a long alkyl chain, the **NITPhOC$_6$**. Co^{II}-based SCMs have already been reported with close NIT linkers, leading to impressive magnetic performances but due to a ferromagnetic 3D ordering (see Part.1.3.3.3) and not to a SCM relaxation.[1–4] In our case, using NIT radical with a longer alkyl chain should prevent such long-range ordering. Coupled with less directional Tb(hfac)$_3$ centres, we expect to obtain a more flexible linear chain and induce more favourable interactions and arrangements with the substrate.[5–8]

In the following part, the resulting coordination polymer **[Tb(hfac)$_3$(NITPhOC$_6$)]$_n$** is extensively characterised from a structural and magnetic point of view.[c]

[c] This study has been published under the reference: F. Houard, Q. Evrard, G. Calvez, Y. Suffren, C. Daiguebonne, O. Guillou, F. Gendron, B. Le Guennic, T. Guizouarn, V. Dorcet, M. Mannini, K. Bernot. 2020. Chiral Supramolecular Nanotubes of Single-Chain Magnets. *Angew. Chem. Int. Ed*. 59, 2, 780-784.

3.2. Synthesis and crystal structure

A novel NIT radical derivative, namely **NITPhOC$_6$** (2-(4'-(hexyloxy)phenyl)-4,4,5,5-tetramethylimidazolin-1-oxyl-3-oxide), has been synthesized following the standard Ullman procedure.[9–11] The condensation between 2,3-bis(hydroxyamino)-2,3-dimethylbutane and 4-(hexyloxy)-benzaldehyde in methanol was maintained at room temperature for 24 hours. The resulting Pre-NITPhOC$_6$, a milky white slurry, was directly oxidised with 1.5 equivalent of $NaIO_4$ in an H_2O/CH_2Cl_2 bi-phasic solution, to avoid further mass loss or degradation (the experimental procedure is detailed in Part.3.A.1.2). This oxidation step led to the corresponding **NITPhOC$_6$** radical, used as a ligand in the following study.

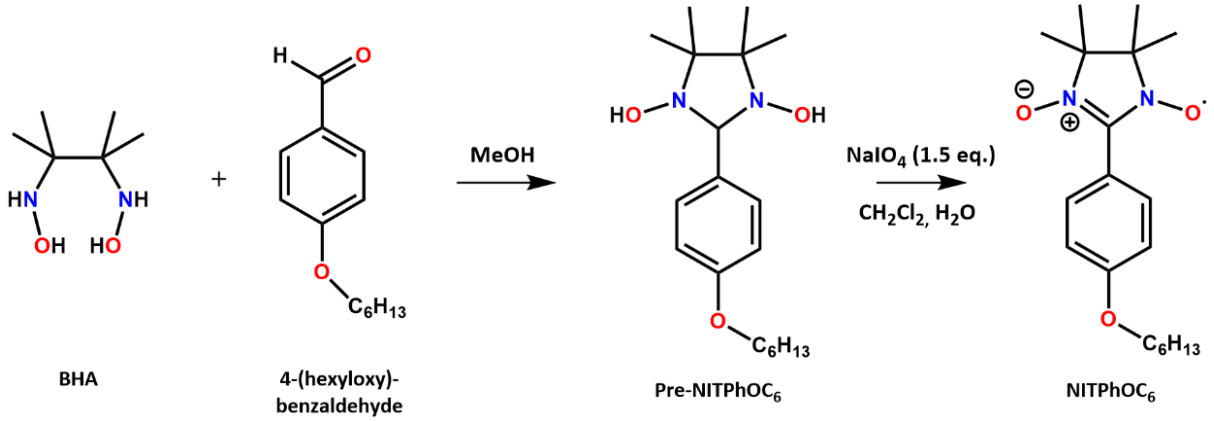

Figure 3.1. Synthetic pathway toward **NITPhOC$_6$** radical.

The use of this alkoxy-benzaldehyde was motivated by the following reasons. First, the phenyl ether ring, being electron-rich, is expected to ensure a main skeleton chain robustness by π-stacking interactions with the electron-poor $hfac^-$ planes (as reported for similar systems).[12–14] Then, the aliphatic hexyl chain, connected in *para*, should act as a spacer between neighbouring coordinated chains to avoid interchain magnetic interactions and thus, a 3D ordering. Last, it could also make the resulting SCM more suitable for the surface deposition process presented in the previous chapter, by controlled fragmentation of SCM crystals into smaller entities through sonication followed by drop-casting of the diluted solution. Indeed, the flexibility and the weak London interactions[15] inherent for alkyl tails are expected to allow a more moderate separation of the coordination polymer from the bulk and potential "anchoring points" with hydrophobic surfaces.

As a reminder, close NIT radical bearing alkoxy phenyl groups have already been synthesised and studied by Ishida *et al.*,[1,4] which differ slightly from the present molecule by the length of the alkyl chain with 4 or 5 carbons (see Part.1.3.3.3). They have successfully synthesized corresponding 1D coordination polymers where the radicals alternate with $Co(hfac)_2$ units, leading to the observation of giant coercivities of around 50 kOe at 6 K. However, it appeared that these results, impressive in any case, were due to the rise of a 3D ordering because of non-negligible interchain interactions.[3] In our case, a longer aliphatic chain combined with bigger and less rigid $Tb(hfac)_3$ moieties should ensure more significant

degrees of freedom to give rise to a large crystallographic asymmetric unit because of the large variety of structural conformations that it could accommodate.

Crystallisation in solvent/antisolvent conditions with layered CH_2Cl_2 (solvent) and *n*-heptane (antisolvent) at 4°C afforded large dark blue single crystals after few days, suitable for single-crystal X-Ray diffraction (Figure 3.2, Table 3.1).

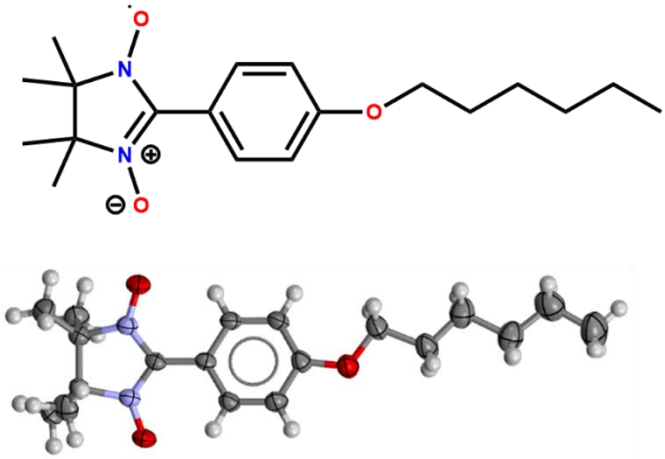

Figure 3.2. Single-crystals observed under optical microscope (x10 and x63 magnification, left) and schematic and ORTEP (thermal ellipsoids at 30 % probability) representation of the molecular structure of **NITPhOC$_6$** (left).

[Tb(hfac)$_3$·2H$_2$O] was dissolved in boiling dry *n*-heptane, and a stoichiometric amount of NITPhOC$_6$ dissolved in a minimum amount of $CHCl_3$ was added during cooling. The mixture was stirred until reaching room temperature and kept for slow evaporation. Long thin cyan needles, of formula **[Tb(hfac)$_3$(NITPhOC$_6$)]$_n$**, were obtained after few days.

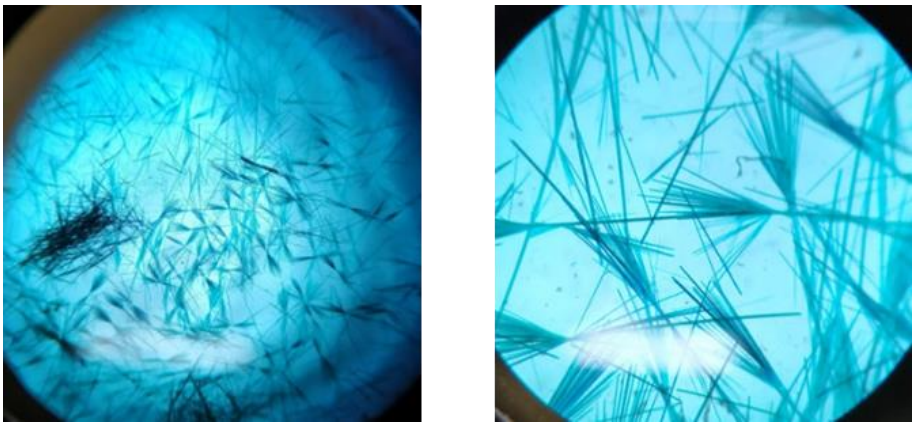

Figure 3.3. Crystals of **[Tb(hfac)$_3$(NITPhOC$_6$)]$_n$** observed under optical microscope (x10 and x63 magnification).

Despite the appreciable dimensions of the single-crystals, several attempts of X-ray diffraction (XRD) measurements (performed by V. Dorcet, Centre de Diffractométrie X, ISCR) were needed to collect a satisfactory diffraction pattern. The main cause is that these single crystals quickly lose their crystallisation solvent once they are removed from the mother solution (highlighted by the fast amorphisation visible on the powder XRD pattern, Figure 3.A.21), and the high degree of disorder of the long aliphatic end-groups further complicated

the quality of the data refinement. To address this issue, we performed a very long data collection (≈ 15h) under N_2 flow at 150K with a single-crystal directly picked from the mother solution with Apiezon grease to avoid solvent removal. A SQUEEZE procedure[16] was run to exclude the contribution of strongly disordered electron densities due to the expected presence of solvent molecules (*n*-heptane and/or chloroform). On the solvent-free data set, only the terbium atoms were refined anisotropically, the -CF_3 groups from $hfac^-$ molecules were rigidified by fixing their C-F bond distance, and the aliphatic chains by fixing the thermal agitation of the terminal carbon atoms.

[Tb(hfac)$_3$(NITPhOC$_6$)]$_n$ crystallises in a hexagonal system, chiral $P6_122$ space group with a large cell volume of V = 54727 Å^3 (Table.1). The asymmetric unit is made of two and a half radicals and two and a half terbium atoms that alternate, with one terbium atom (Tb1) and one radical (central atoms C80, C81, C84 and O23) laying on 2-fold symmetry axes along *a* and *a* + *b* axes respectively. Each Tb^{III} ion is surrounded by eight oxygen atoms, six from the three bidentate $hfac^-$ ligands and two from the bridging nitroxide groups. Tb^{III} coordination polyhedra are slightly distorted triangular dodecahedron D_{2d} for Tb1 and Tb2, and square antiprism D_{4d} for Tb3 (Table 3.A.6). The Tb-O_{rad} distances are in the range 2.33 – 2.51 Å, while the shortest intrachain distance between Tb^{III} ions is 8.39 Å, consistent with values previously observed for similar 4*f* NIT chains. [14,17–24]

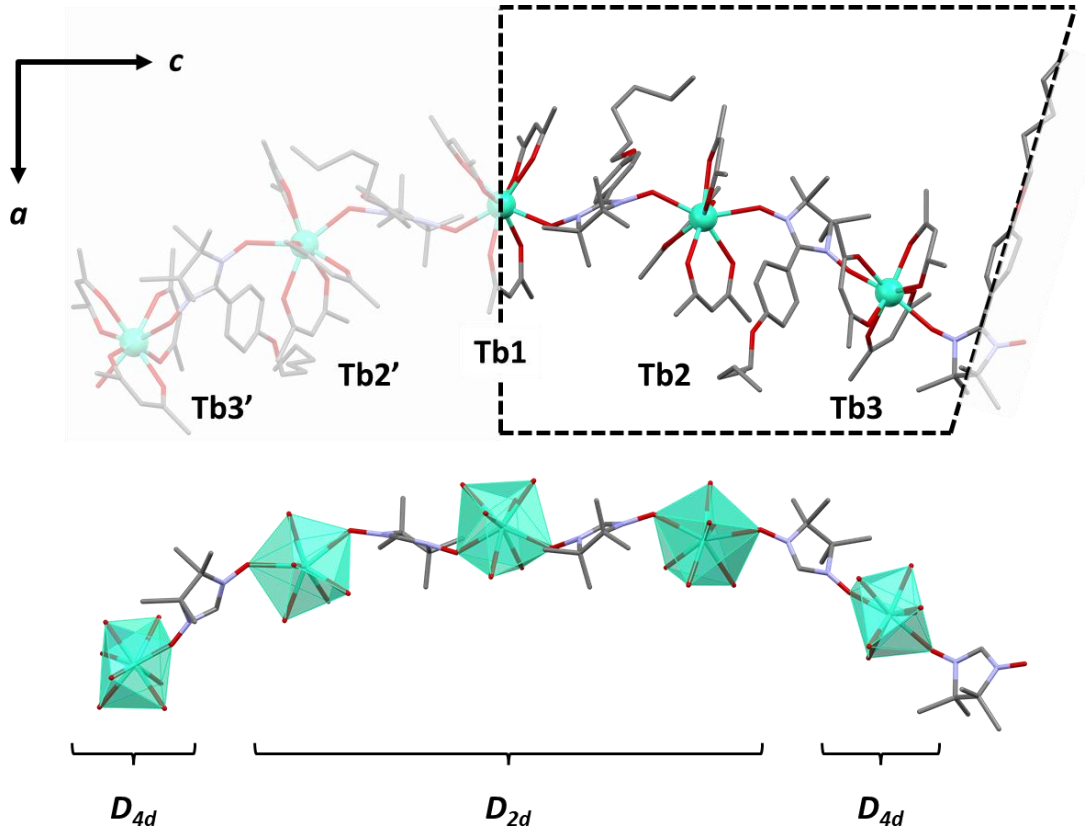

Figure 3.4. Representations of **[Tb(hfac)$_3$(NITPhOC$_6$)]$_n$** molecular structure along the *b*-axis with the asymmetric unit as dotted area (top, with hydrogen and fluorine atoms omitted for clarity) and the simplified magnetic backbone with the related coordination polyhedra (bottom).

Table 3.1. Crystallographic parameters of **NITPhOC$_6$** and **[Tb(hfac)$_3$(NITPhOC$_6$)]$_n$**.

Name	NITPhOC$_6$	[Tb(hfac)$_3$(NITPhOC$_6$)]$_n$
M **(g·mol^{-1})**	333.44	5567.73
Crystal system	Monoclinic	Hexagonal
Space group	P2$_1$/n (N°14)	*P*6$_1$22 (N°178)
a **(Å)**	10.6590(1)	59.187(5)
b **(Å)**	9.2253(1)	59.187(5)
c **(Å)**	19.844(3)	18.039(3)
α **[°]**	90	90
β **[°]**	95.998(8)	90
γ **[°]**	90	120
V **[Å^3]**	1940.6(5)	54726(11)
Z	4	6
T **(K)**	150	150
2ϑ **range**	2.064 - 27.534	2.285 – 20.790
Reflections collected	4445	81037
Indep. reflections	4445	18872
Obs. reflections	1939	15501
Parameters	222	647
R$_1$[d] **[*I* > 2*σ*(*I*)] / *wR$_2$*[e] [*I* > 2*σ*(*I*)]**	7.13 / 21.20	13.44 / 34.88
GOF	0.946	1.574
CCDC Number	1958728	1958799

[d] $\sum(|F_0| - |F_c|)/\sum|F_0|$

[e] $\sqrt{\sum w(|F_0|^2 - |F_c|^2)^2/\sum w(|F_0|^2)^2}$

As expected, π-stacking is observed between the phenyl group of bridging NIT radicals and neighbouring aromatic hfac⁻ planes. One can consider the angle α between the stacking planes and distance $d_{\pi\text{-}\pi}$ that separates their centroid.[25,26] Such interactions are well defined between the hfac⁻ ligands linked to Tb2 and Tb3 and their neighbouring phenyl groups, with slightly tilted face-to-face orientation (α = 5.1 – 9.5°) and small distance ($d_{\pi\text{-}\pi}$ = 3.36 – 3.53 Å), while π- interaction seems weaker for the hfac⁻ linked to Tb1 (α = 20.8° and $d_{\pi\text{-}\pi}$ = 3.78 Å).

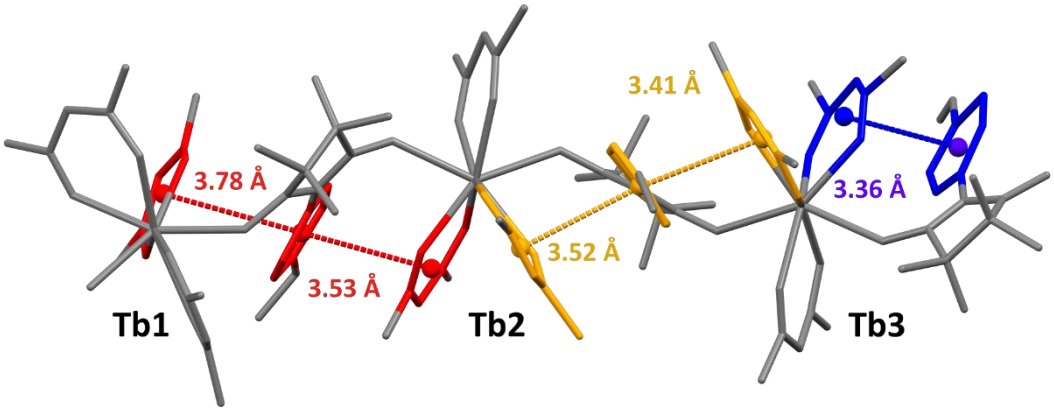

Figure 3.5. Representations of the π- interaction pattern along the simplified asymmetric unit of the **[Tb(hfac)$_3$(NITPhOC$_6$)]$_n$** chain.

The NIT-4*f* chains[27] can be described by the Cx-Ln-Cx angle, where Cx is the central C atom of the tetramethylimidazoline group. Usually, two consecutive angles compensate along the chain direction to give rise to a regular and flat zig-zag chain.[28] In **[Tb(hfac)$_3$(NITPhOC$_6$)]$_n$**, the picture is very different because the Cx-Ln-Cx angles add up to form a curved asymmetric unit. This curvature, combined with the 2-, 3- and 6- fold symmetry axes of the hexagonal space group, creates a left-handed (Λ) helical chain along the *c*-axis.

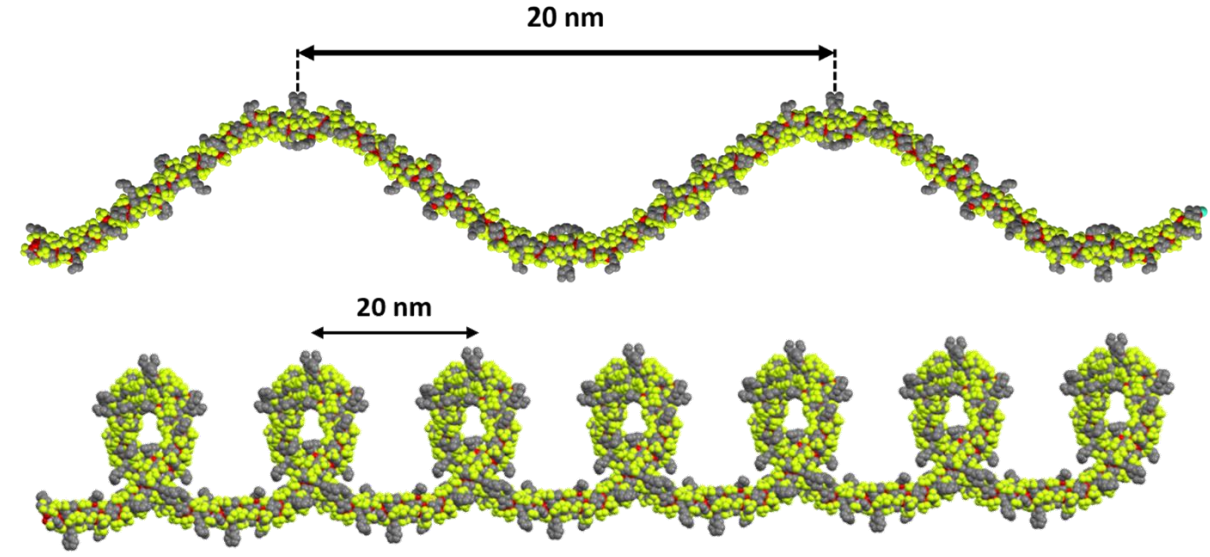

Figure 3.6. Side (top) and perspective (bottom) representations of an isolated left-handed helical chain of **[Tb(hfac)$_3$(NITPhOC$_6$)]$_n$** with atoms represented with their van der Waals radii.

Twelve asymmetric units are necessary to make a full revolution, resulting in a pitch length of almost 20 nm (198 Å). This arrangement is due to the flexibility of the hexyl tail of the **NITPhOC$_6$** radical, which accommodates very different structural conformations along the asymmetric unit, a feature not possible with more rigid NIT radicals.[14]

The crystal packing of these chains is even more peculiar since the long helical pitch makes room for 10 other chains. Overall, 11 chains are wound around each other and give rise to a self-organised chiral tubular superstructure along the *c*-axis. These neighbouring chains are generated by the symmetry axes of the $P6_122$ space group (this space group has 12 symmetry operations but one of the chains lies in a particular position). The resulting structure is a nanotube with an external diameter of 6.8 nm and an inner one of 4.5 nm, filled by disordered *n*-heptane molecules. There is one nanotube per unit cell and so all nanotubes are crystallographically similar, with shortest intermolecular Tb-Tb distance of 10.80 Å.

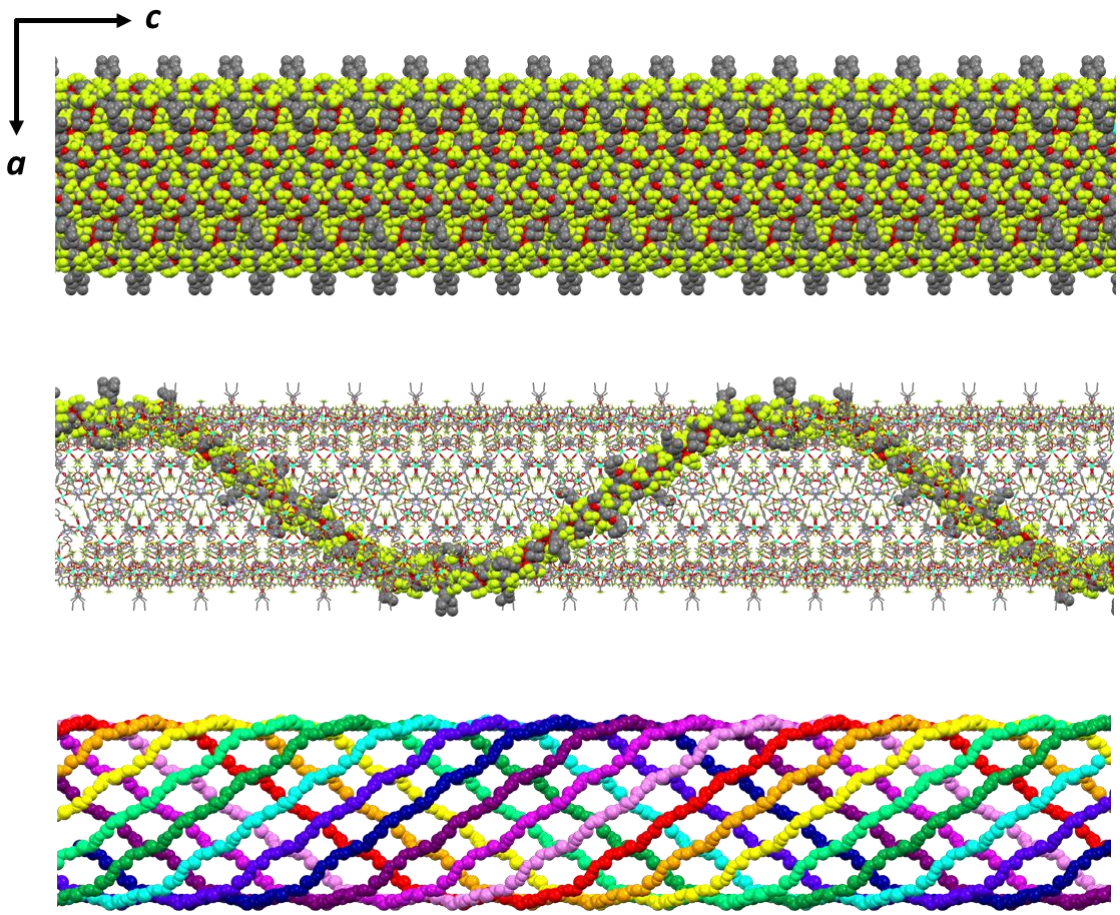

Figure 3.7. Representations of a nanotube of **[Tb(hfac)$_3$(NITPhOC$_6$)]$_n$** along the *b*-axis with chains represented with their van der Waals radii (top and middle), and only magnetic backbone chains with different colours (bottom).

On the tested crystal, the eleven chains are curled clockwise. It could be stressed that this chirality, as in similar chains,[20,29] comes from the spontaneous resolution in the $P6_122$ chiral space group. In the absence of chiral building blocks, the opposite chirality ($P6_522$, N°179) is equally probable but it has not been observed given the complexity of crystal structure data collection and analysis. A statistical study on several crystals from a given batch was not possible given the very long data collection time. Moreover, optical circular dichroism measurements were also considered but too complex to implement with such fragile crystals (see the following Part.3.3).

The evident affinity between the reaction solvent (*n*-heptane) and the aliphatic tail of the radical plays a key role in the thermodynamic stabilisation of these nanotubes. The considerable calculated porosity of 25495 $Å^3$ (44% of cell volume for a 1.2 Å kinetic radius) added to the loss of X-ray diffracting power once dried. It can lead to the hypothesis that the helical arrangement is induced by the heptane molecules trapped within the pores, taking advantage of aliphatic π- and London dispersion interactions.[26]

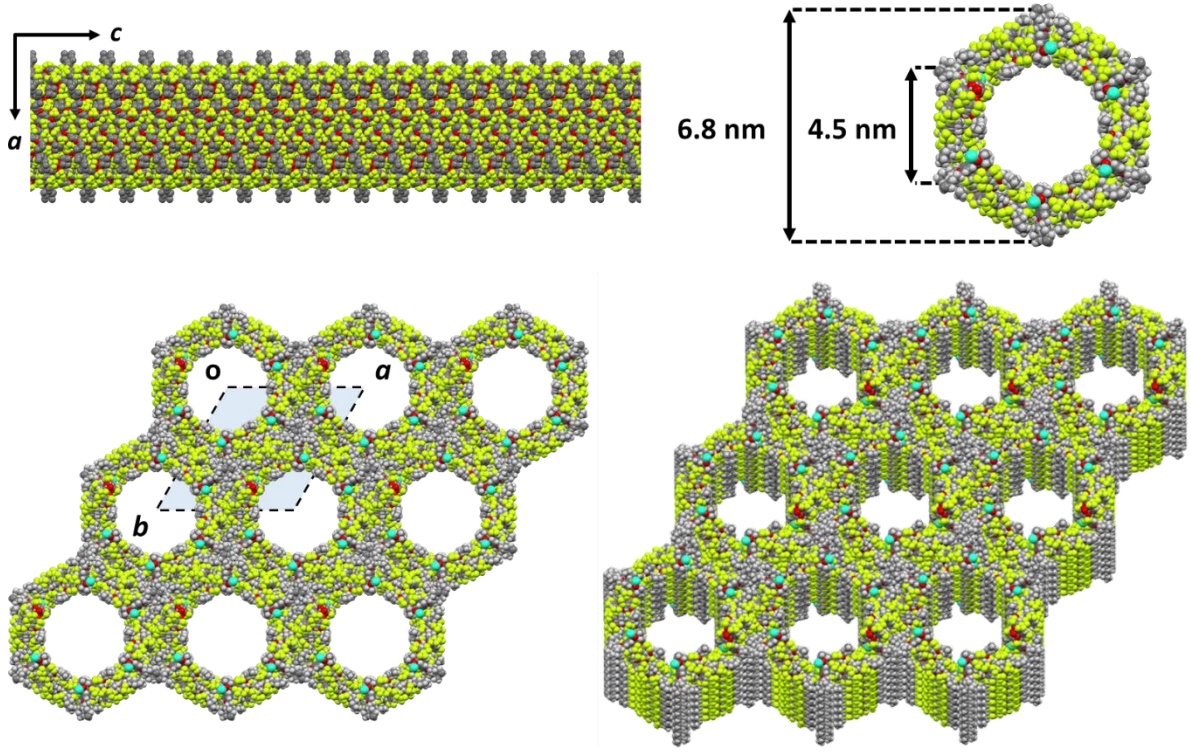

Figure 3.8. Top: Representations of a nanotube of **$[Tb(hfac)_3(NITPhOC_6)]_n$** with chains represented with their van der Waals radii along the *b*- (left) and *c*-axes (right). Bottom: Representations of the resulting packing along the *c*-axis (left) and a perspective view (right).

3.3. Stability: thermal and luminescent measurements

Supporting this assumption, crystals observed *via* Scanning Electron Microscopy (SEM) measurements show a progressive bending of their shape, probably due to forced removal of the solvent molecules within the tubes under long exposure to vacuum. One can note that the crystals are still mechanically robust after SEM measurements, but their diffracting power is lost.

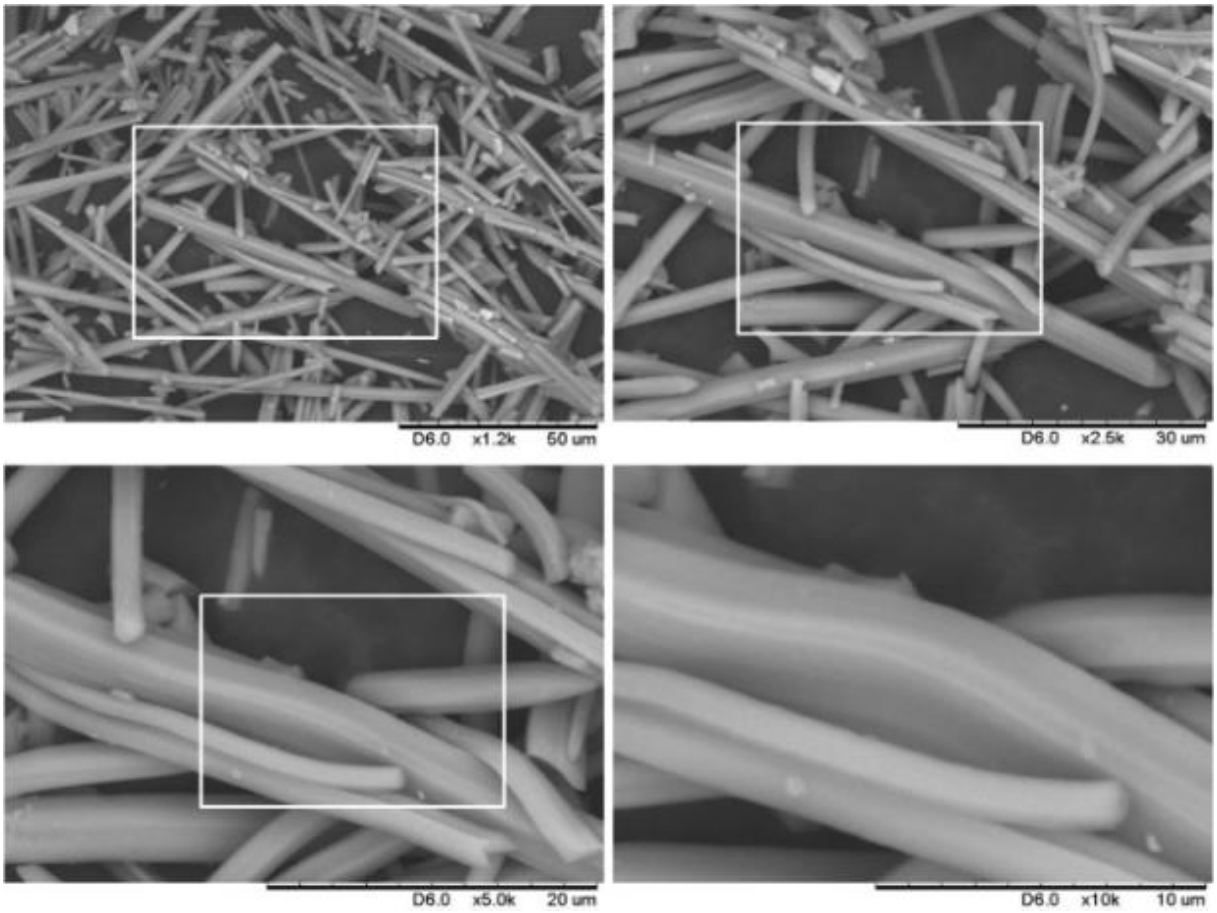

Figure 3.9. SEM images of **[Tb(hfac)$_3$(NITPhOC$_6$)]$_n$** crystals. One can note the crystal deformation caused by solvent loss under operating conditions (progressive zoom from x1.2k to x10k magnification).

To further confirm that the chain structure is conserved upon crystallinity loss, thermogravimetric/thermodifferential analyses (TG-TDA) and coupled TGA-FTIR of exhausted gases were performed on one-minute air-dried samples. The first one reveals a negligible weight loss until the melting of the compound at T_{melt} = 120°. The second shows that no *n*-heptane nor chloroform signatures can be found either, with no vibrational bands in the area of interest (2950-2850 and 1450-1350 cm^{-1}) until melting and decomposition of the sample at higher temperatures. This indicates that the one-minute drying is enough to remove most of the solvent molecules from the pores.

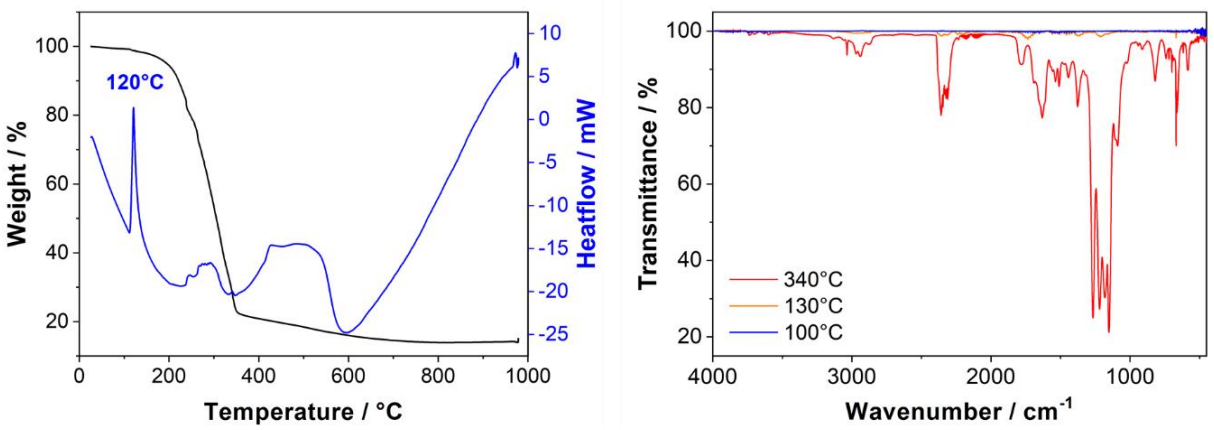

Figure 3.10. Thermogravimetric and thermodifferential analyses (left) and FTIR single spectra of exhausted gazes recorded at different temperatures (right) of **[Tb(hfac)$_3$(NITPhOC$_6$)]$_n$**.

Finally, solid-state luminescence measurements (with the help of Dr. Y. Suffren) with varying temperatures have been performed. We have taken advantage of the strong luminescence properties of the chain's building blocks, [Tb(hfac)$_3$·2H$_2$O] and NIT radicals: the first exhibits a very intense line-shaped green emission (see Figure 2.13), and the second a broad-shaped red emission that is blue-shifted upon Tb(hfac)$_3$ coordination[30] that also quenches the Tb^{III} emission. As expected, **[Tb(hfac)$_3$(NITPhOC$_6$)]$_n$** shows neither any trace of Tb^{III} nor uncoordinated NIT radical emission but a blue-shift of the main emission peaks compared to the radical ones (710 to 705 nm and 772 to 753 nm at 77 K, Figure 3.A.22-Figure **3.A.23**). This indicates that the air-dried samples are free from traces of reactants and that amorphisation does not induce decomposition of the chains. Accordingly, the dried samples are suitable for the following magnetic analyses.

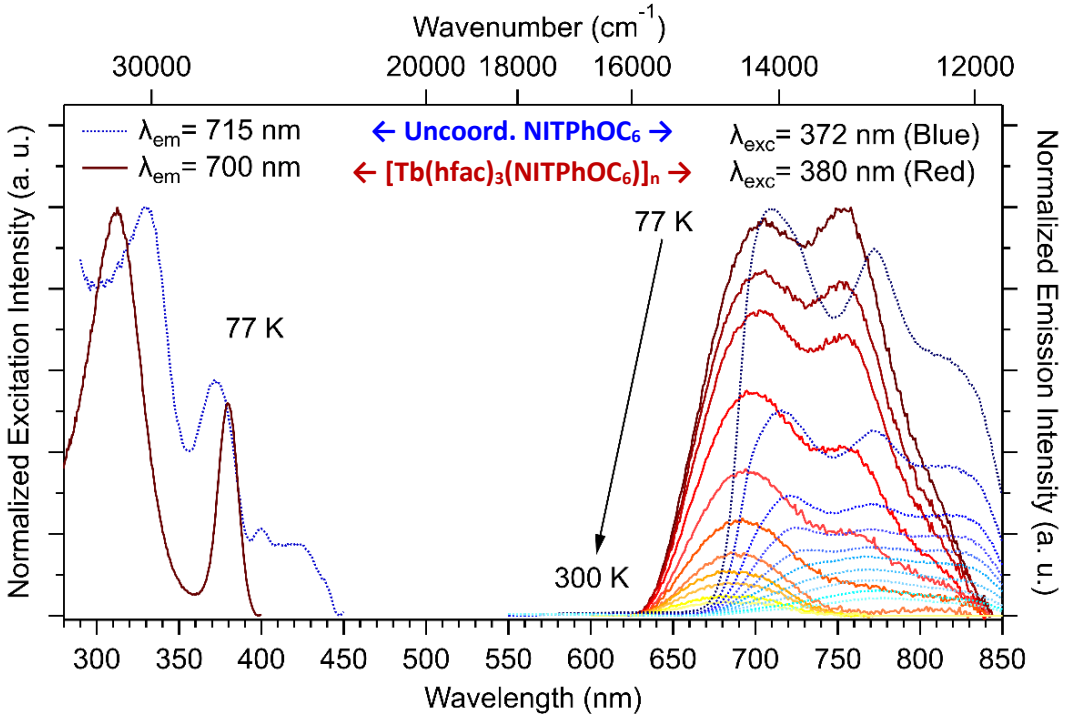

Figure 3.11. Solid-state excitation spectra and emission spectra measured of uncoordinated **NITPhOC$_6$** and **[Tb(hfac)$_3$(NITPhOC$_6$)]$_n$**.

3.4. Magnetic properties

3.4.1. Static (DC) magnetic properties

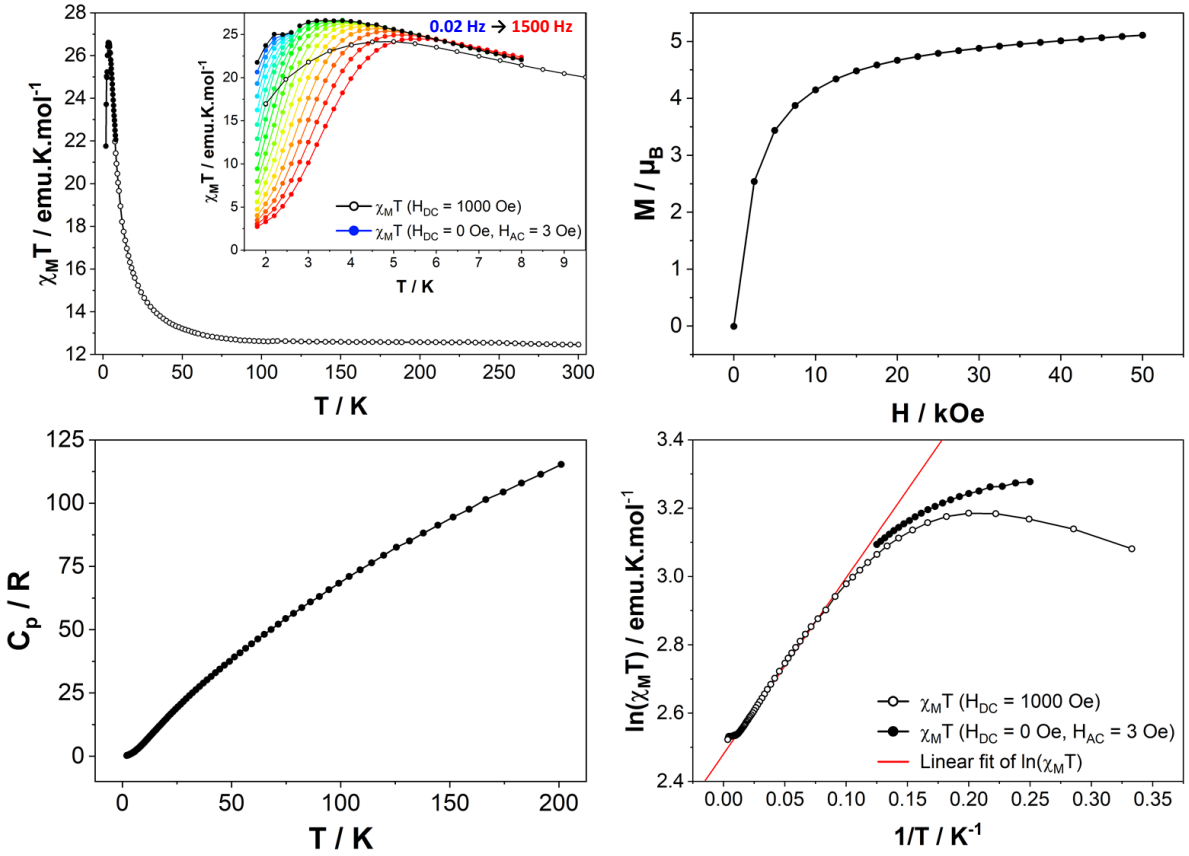

Figure 3.12. Top: Temperature dependence of $\chi_M T$ measured on **[Tb(hfac)$_3$(NITPhOC$_6$)]$_n$** powder with static fields (open circles) and reconstructed from AC data (filled dots) with in inset, a zoom in the low-temperature region with the AC data at different frequencies (left) and field dependence of magnetisation at 2 K (right). Bottom: Specific heat measurement (left) and reciprocal temperature dependence of ln($\chi_M T$), with best fit as a red line (right).

Static magnetic properties have been measured on polycrystalline sample under a static field H_{DC} = 1000 Oe. The temperature dependence of the magnetic susceptibility at room temperature shows a value of $\chi_M T_{(300K)}$ = 12.44 emu·K·mol^{-1}, close to the expected value of $\chi_M T_{(300K)}$ = 12.195 emu·K·mol^{-1} for one isolated radical (g_S = 2, S = ½) and one Tb^{III} ion (g_J = 3/2, J = 6). As the temperature is lowered, a severe increase of $\chi_M T$ is observed below 50 K up to $\chi_M T$ = 24.2 emu·K·mol^{-1} at 3.5 K as a result of the onset of a spin correlation along the chain. Below 3.5 K, $\chi_M T$ drops because of saturation effects. To tackle this, dynamic magnetic measurements (H_{AC} = 3 Oe) have been performed, allowing to reach the highest value for $\chi_M T$ = 26.56 emu·K·mol^{-1} at 3.2 K.

This saturation effect was also observed on the isothermal magnetisation curve at 2 K, with a quick increase of the magnetisation once the magnetic field is applied until progressively tending toward a value of 5.1 μ_B, close to the theoretical saturation M_S = 5.5 μ_B.

Additionally, specific heat studies down to 2 K do not highlight any abrupt anomaly in the specific heat capacity C_P and exclude the presence of 3D magnetic ordering.[31,32]

As a reminder of Chapter 1, NIT-Ln chains can behave as Ising chains and exhibit SCM behaviour if well magnetically shielded: slow magnetic relaxation operates *via* a 1D magnetic relaxation mechanism, more robust than the Orbach one seen on SMMs. Accordingly, Ising one-dimensional systems present an exponential divergence of $\chi_M T$ as the temperature is lowered, such as $\chi_M T = C_{eff}.\exp(\Delta_\xi/k_B T)$, with Δ_ξ the correlation energy required to create a domain wall. It is more suitable to make this assumption when saturation effects are discarded. This is why DC measurements with reconstructed $\chi_M T$ from AC measurements (H_{DC} = 0 Oe, H_{AC} = 3 Oe) have also been considered for $\Delta_{\xi(DC)}$ extraction, with no influence on the linear domain considered however. Values are then C_{eff} = 11.84 emu·K·mol^{-1} and $\Delta_{\xi(DC)}/k_B$ = 5.5 ± 0.5 K (R^2 = 0.9998).

3.4.2. Theoretical description and magnetic coupling

On 3*d*-based chains, straightforward ab initio calculations of intrachain coupling constants have been recently reported[33] but are unlikely to be directly applied on the chains. Indeed, the reliable determination of magnetic interactions on Ln-NIT compounds *via* state-of-the-art wave function-based calculations (CASSCF/DDCI) is challenging even on isolated NIT-Y^{III}-NIT molecules.[34]

Then, the modelling of the magnetic interaction pathways is trickier here because SCM made of NIT radicals and lanthanide ions are known to host nearest (NIT-Ln) and next-nearest (Ln-Ln, and NIT-NIT) neighbour magnetic interactions,[35] the latter being stronger than the former. These numerous magnetic pathways, as well as the three crystallographically different Tb^{III} ions in **[Tb(hfac)$_3$(NITPhOC$_6$)]$_n$**, hamper a precise quantification of the magnetic couplings in the chain.

However, *ab-initio* calculations (performed by B. Le Guennic and F. Gendron, Chimie Théorique Inorganique group, ISCR and detailed in Part.3.A.3.1) on simplified units where methyl groups replaced the hexyl chains, such as [Tb(hfac)$_3$(NITPhOMe)$_2$] represented below. To simplify the discussion, the three different models are labelled $[Tb(1)]^{2-}$, $[Tb(2)]^{2-}$ and $[Tb(3)]^{2-}$ in the following.

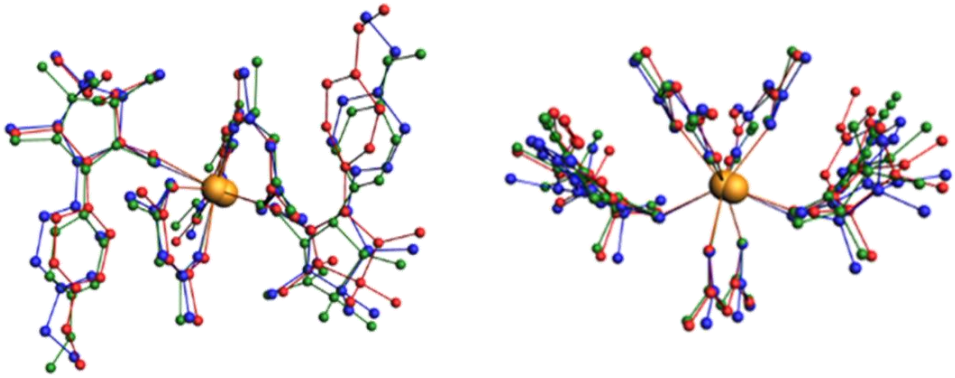

Figure 3.13. Overlay of the three model compounds $[Tb(1)]^{2-}$ (blue), $[Tb(2)]^{2-}$ (green) and $[Tb(3)]^{2-}$ (red).

In the three model compounds, the ground state (GS) and the first excited state (ES1) correspond to pseudo-Kramers doublets that derive formally from the m_J states ± 6 and ± 5 of the $^7F_6$ level, respectively. More precisely, the nature of these states results from an admixture by the crystal-field of the different m_J states such as:

$$|\psi_{GS}\rangle = a\,|6,\pm6\rangle + b\,|6,\pm4\rangle + c\,|6,\pm2\rangle \qquad \text{Eq. 3.1}$$

$$|\psi_{ES1}\rangle = d\,|6,\pm5\rangle + e\,|6,\pm3\rangle + f\,|6,\pm1\rangle \qquad \text{Eq. 3.2}$$

with $a^2 + b^2 + c^2 = 1$ and $d^2 + e^2 + f^2 = 1$.

The calculated values of the square of these coefficients are given in the Table 3.2 below. For the GS, the contribution of the m_J = ± 6 is the dominant one (over 95 %) and remains very similar for the three model compounds. On the other hand, the nature of ES1 differs when going from $[Tb(1)]^{2-}$ to $[Tb(3)]^{2-}$. For the former, ES1 results mainly from the m_J = ± 5 state (96.2 %), whereas for the latter, this contribution strongly decreases to 74.8 % and is strongly mixed with the m_J = ± 3 state (20.5 %).

Table 3.2. Calculated m_J contributions (in per-cent) associated with the GS and ES1 wavefunctions for the model compounds.

	GS			ES1		
	|± 6>	**|± 4>**	**|± 2>**	**|±5 >**	**|±3 >**	**|±1 >**
$[Tb(1)]^{2-}$	98.0	1.6	0.4	96.2	2.0	1.8
$[Tb(2)]^{2-}$	96.4	3.0	0.6	78.6	13.2	8.2
$[Tb(3)]^{2-}$	95.2	4.6	0.2	74.8	20.5	4.7

The calculated relative energies of the states deriving from the $^7F_6$ level of the Tb^{III} ion in the three model compounds are given in the Table 3.3. Calculated relative energies (ΔE in cm-1) and EPR *g-factors* for the lowest states deriving from the ^{7F6} level of the TbIII ion in the three model compounds. below. The modification of the nature of the excited states goes along with a modification of the energetic splitting. In $[Tb(1)]^{2-}$, a relatively small energy gap of 38 cm^{-1} is calculated between the GS and ES1, whereas this energy gap increases to 97 and 144 cm^{-1} for $[Tb(2)]^{2-}$ and $[Tb(3)]^{2-}$, respectively. The overall splitting of the $^7F_6$ level also differs between the three building blocks, with calculated splitting of 555, 598 and 697 cm^{-1} for $[Tb(1)]^{2-}$, $[Tb(3)]^{2-}$ and for $[Tb(2)]^{2-}$, respectively.

Table 3.3. Calculated relative energies (ΔE in cm^{-1}) and EPR *g*-factors for the lowest states deriving from the $^7F_6$ level of the Tb^{III} ion in the three model compounds.

	$[Tb(1)]^{2-}$			**$[Tb(2)]^{2-}$**			**$[Tb(3)]^{2-}$**		
	ΔE	**$g_{\|\|}$**	**$g_{\perp}$**	**ΔE**	**$g_{\|\|}$**	**$g_{\perp}$**	**ΔE**	**$g_{\|\|}$**	**$g_{\perp}$**
GS	0	17.75	0.00	0	17.57	0.00	0	17.57	0.00
ES1	38	14.78	0.00	97	12.77	0.00	144	13.23	0.00
ES2	120	10.88	0.00	134	-	0.00	207	-	0.00
ES3	170	-	0.00	155	8.33	0.00	240	13.49	0.00
ES4	246	10.28	0.00	242	11.47	0.00	263	10.44	0.00
ES5	379	13.46	0.00	400	14.67	0.00	370	14.04	0.00
ES6	555	17.01	0.00	697	17.71	0.00	598	17.65	0.00

The GS of the three Tb compounds exhibits considerable magnetic anisotropy, characterised by extremely large parallel components of the EPR *g*-factors (around 17.6) and perpendicular components equal to zero. For comparison, a pure $m_J = \pm 6$ state would possess a parallel component of 18.0. Despite the very similar magnitude of the $g_{\parallel}$, the three model compounds exhibit very different orientation of their easy axes of magnetisation. In $[Tb(1)]^{2-}$, the easy axis goes along with a NIT-Tb-NIT direction, whereas in $[Tb(2)]^{2-}$ the magnetic axis cross one of the $hfac^-$ ligand. Finally, an intermediate situation is calculated in $[Tb(3)]^{2-}$.

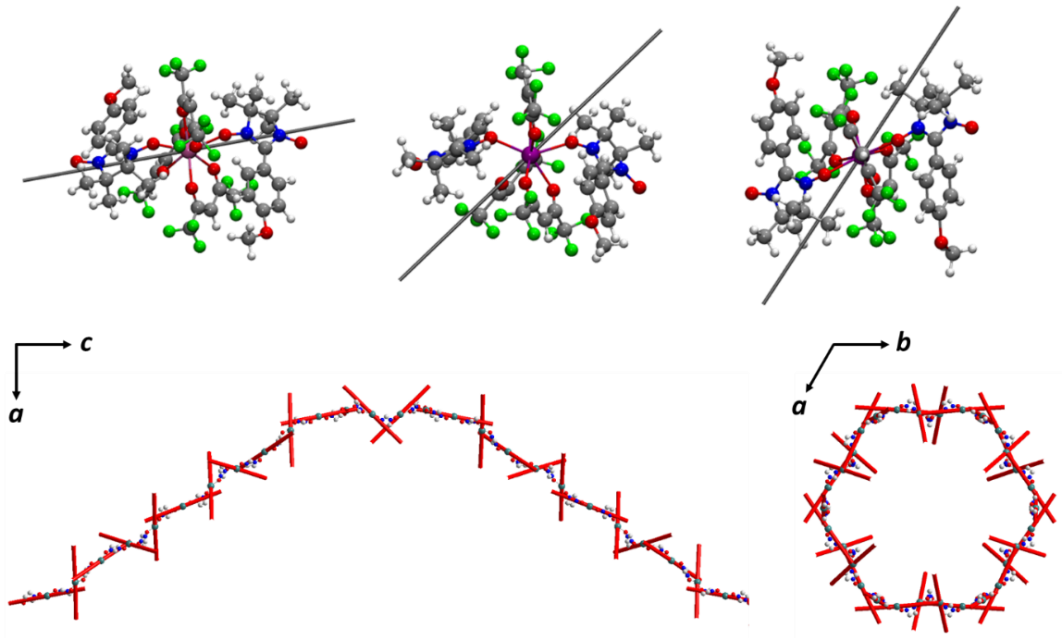

Figure 3.14. Top: Representation of the easy axis of the magnetisation for the GS in $[Tb(1)]^{2-}$ (left), $[Tb(2)]^{2-}$ (middle) and $[Tb(3)]^{2-}$ (right). Bottom: Representation of the easy axes for a chain along the *b*-(left) and *c*-axis (right) of **$[Tb(hfac)_3(NITPhOC_6)]_n$**.

The resulting organisation of these easy magnetic axes, reported above according to the packing of the chain and the nanotube structures of **$[Tb(hfac)_3(NITPhOC_6)]_n$**, do not lie in any particular direction with respect to the molecule.

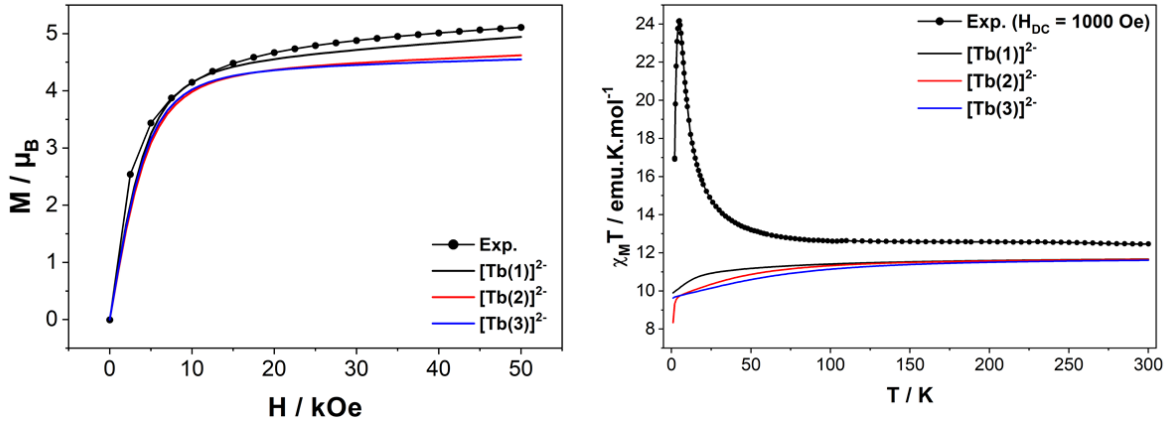

Figure 3.15. Calculated isothermal field dependence of magnetisation at 2 K (left) and temperature dependence of $\chi_M T$ (right) of the isolated models and the **$[Tb(hfac)_3(NITPhOC_6)]_n$** chain.

The calculated $\chi_M T$ susceptibility and the magnetisation for the three model compounds are shown in Figure 3.15. At room temperature, very similar $\chi_M T_{(300K)}$ of 11.67, 11.65 and 11.61 emu·K·mol^{-1} are calculated for $[Tb(1)]^{2-}$, $[Tb(2)]^{2-}$ and $[Tb(3)]^{2-}$, respectively. Due to a smaller GS-ES1 energy gap in $[Tb(1)]^{2-}$, the decrease in magnitude of $\chi_M T$ with T is slightly slower than in the two other compounds. For the same reason, the calculated magnetisation at 2K of $[Tb(1)]^{2-}$ does not reach saturation at 5 Tesla, whereas for $[Tb(2)]^{2-}$ and $[Tb(3)]^{2-}$, the calculated magnetisations converge to 4.5 μ_B.

3.4.3. Dynamic (AC) magnetic properties

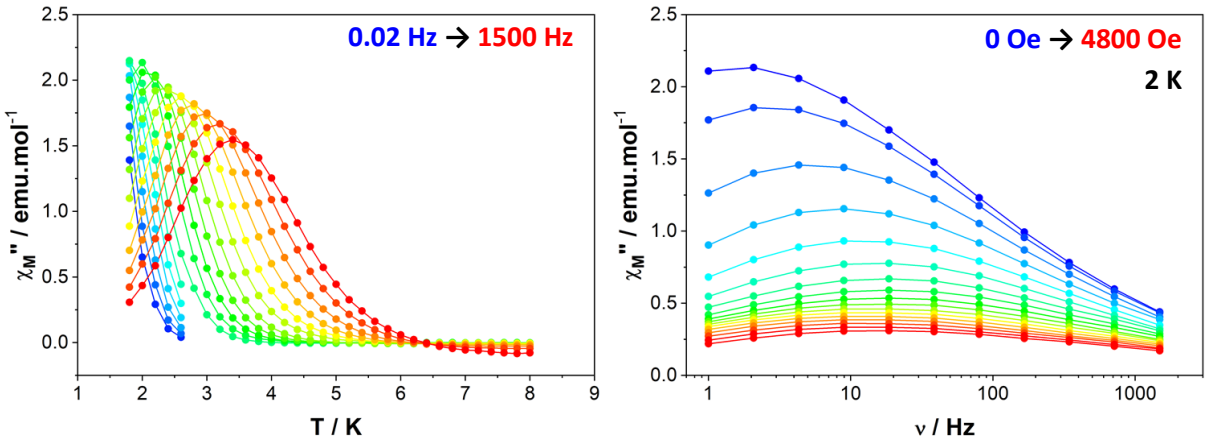

Figure 3.16. Top: Temperature (left) and field (right) dependencies of the out-of-phase (χ_M'') susceptibility of **$[Tb(hfac)_3(NITPhOC_6)]_n$**.

Dynamic susceptibility properties were measured with a H_{AC} = 3 Oe field oscillating at various frequencies. A slow relaxation of the magnetisation, confirming the SCM behaviour of **$[Tb(hfac)_3(NITPhOC_6)]_n$**, is highlighted by the clear temperature dependence of the out-of-phase (χ_M'') susceptibility.

The field dependence at 2 K exhibits the slowest relaxation (*i.e.* the minimal frequency linked to a maximum peak) for an applied field of H_{DC} = 0 Oe. As soon as a field is applied, the magnetic relaxation accelerates, in line with what is expected for an SCM.[37]

Frequency dependence of the magnetic relaxation is observed up to 8 K (see Figure 3.17), from which the corresponding relaxation times τ were extracted using a generalised Debye model and fitted according to an Arrhenius law $\tau = \tau_0.\exp(\Delta_{eff}/k_B T)$ where Δ_{eff} is the effective energy barrier (Table 3.A.7). On the Arrhenius plot, two thermally activated processes are observed, accounting for the presence of distinct finite and infinite regimes. Their energy barriers can be expressed as $\Delta_F = \Delta_A + \Delta_{\xi(AC)}$ and $\Delta_I = \Delta_A + 2.\Delta_{\xi(AC)}$ respectively, with Δ_A the anisotropic magnetic contribution of the Tb^{III} ion.

In this case, the fitted values for the finite regime are Δ_F/k_B = 25.5 ± 0.2 K and τ_F = (2.4 ± 0.3) x 10^{-7} s (R^2 = 0.9998) while the infinite regime is characterised by Δ_I/k_B = 29.6 ± 0.5 K and $\tau_{,I}$ = (3.4 ± 0.5) x 10^{-8} s (R^2 = 0.9983), the crossover occurring at T^* = 2.1 K.

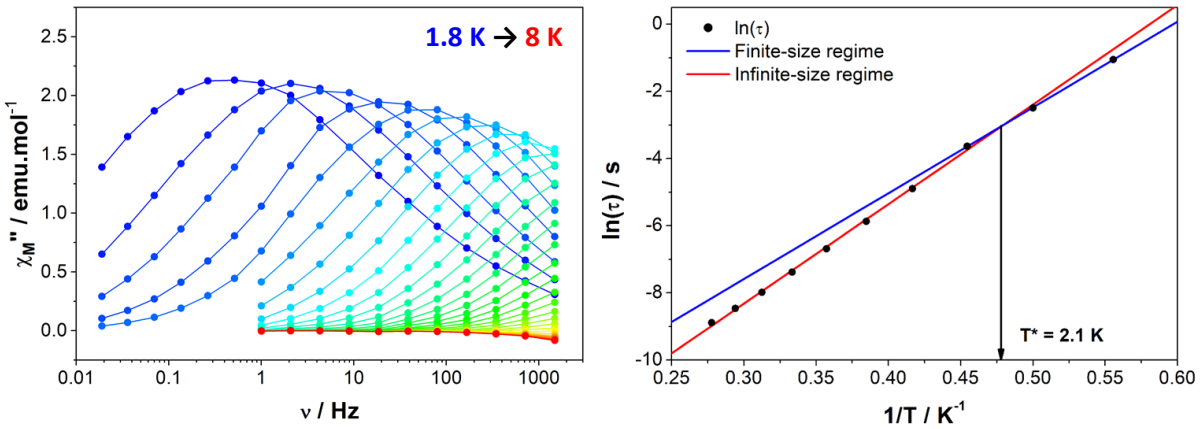

Figure 3.17. Frequency dependence of the out-of-phase susceptibility (left) and the resulting Arrhenius plot of the extracted relaxation times (right).

Then, the correlation energy can be determined by a simple subtraction as $\Delta_{\xi(AC)}/k_B = \Delta_I/k_B - \Delta_F/k_B = 4.1 \pm 0.7$ K, a value close to the one estimated from DC measurements ($\Delta_{\xi(DC)}/k_B = 5.5 \pm 0.5$ K) but more reliable because no external field was applied (preventing any saturation phenomenon).

It is clear that the small value of Δ_ξ makes the fitting of the Arrhenius plot tricky because both finite and infinite regimes have close energy barriers, contrary to what is observed on 3d-based SCMs.[36,37] Accordingly, on such systems, the fitting procedure should be performed very carefully in order to obtain a valuable T^* value.

Finally, for SCMs, $\Delta_{\xi(AC)}$ can be linked to the average number of the correlated magnetic units n with the crossover temperature T^* through $n \approx 2\xi \approx \exp(\Delta_{\xi(AC)}/k_B T^*)$. Given the small values of $\Delta_{\xi(AC)}$ and the large confidence interval, n is included between 5 and 10 units for **[Tb(hfac)$_3$(NITPhOC$_6$)]$_n$**. However, we recall that this value is purely informative as such treatment is valid for chains made of repeating identical magnetic units. This is far more complex to rationalise in our case because of the asymmetric unit made of two and a half Tb^{III} ions and two and a half radicals.

In order to exclude any hypothetical collective SMM contributions to these previous results, doping experiments have been done with Y^{III} ions: the presence of such diamagnetic ions along the chain is expected to hinder the growth of a magnetic correlation, critical for SCMs. Crystals of **[(Tb$_{0.05}$Y$_{0.95}$)(hfac)$_3$(NITPhOC$_6$)]$_n$** have been obtained (which composition was checked by EDS-SEM, Figure 3.A.26) and dynamic SQUID measurement revealed no out-of-phase χ_M'' signal at low temperature (Figure 3.A.27), discarding this hypothesis.

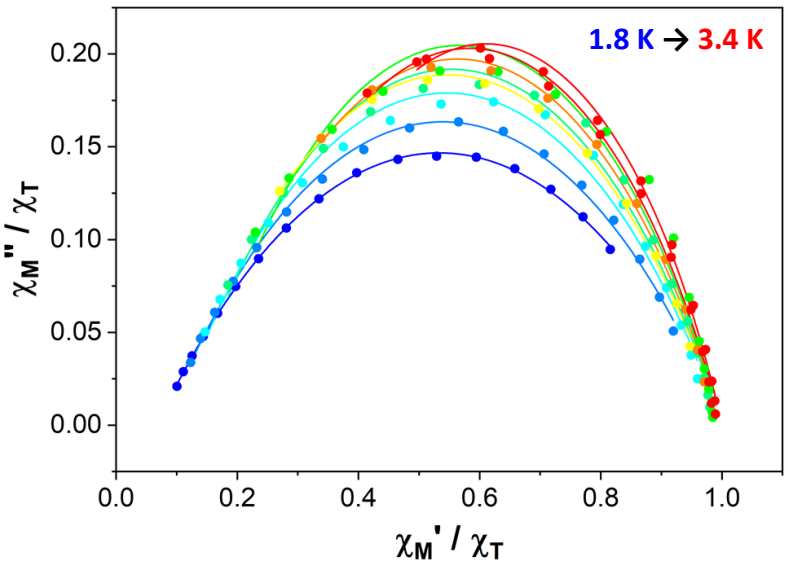

Figure 3.18. Normalised Argand diagram of **[Tb(hfac)$_3$(NITPhOC$_6$)]$_n$** (solid lines represent the best fits with an extended Debye model).

An extended Debye model was applied to determine the distribution of the relaxation times α (Table 3.A.8). As a reminder, the α value for an ideal relaxation dynamic tends towards zero (all the molecules share the same single relaxation time τ) while it is 1 for a totally disordered relaxation scheme. In our case, α is spread from 0.39 at 3.6 K to 0.62 at 1.8 K, and only one semi-circle is observed, ruling out once again the possibility of a collective SMM behaviour stated above. It can be noted that at 1.8 K, almost all the sample relax slowly (1-(χ_S/χ_T) = 93%, where χ_S and χ_T correspond to the adiabatic and the isothermal susceptibility, respectively).

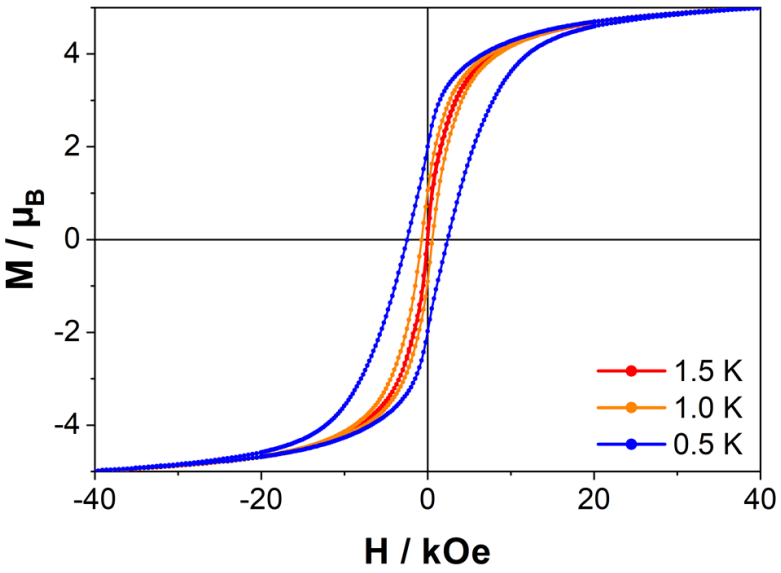

Figure 3.19. Magnetic hysteresis curves of **[Tb(hfac)$_3$(NITPhOC$_6$)]$_n$** measured at different temperatures, with a magnetic field sweep rate of 15.5 Oe·s^{-1}.

Finally, the ability of the **[Tb(hfac)$_3$(NITPhOC$_6$)]** chain to store magnetic information is evaluated by magnetic hysteresis measurements at low temperatures. Within this range of

temperature, the relaxation dynamics is ruled by the finite size regime and the blocking temperature T_B in our operating conditions (magnetic field sweep rate of 15.5 Oe·s^{-1}, with a τ_{exp} = 21.3 s) can be estimated considering the modified Arrhenius equation $T_B = \Delta_F/[k_B.\ln(\tau_{exp}/\tau_F)] = 1.39 \pm 0.02$ K.

This estimated value is in accordance with the clear hysteresis opening observed by lowering the temperature below 1.5 K, with a maximum coercive field of H_C = 2400 Oe and a remanent magnetisation of M_R = 2.09 μ_B (38% of the saturation value) recorded at 0.5 K.

3.5. Conclusion

In this chapter, we have demonstrated that the functionalisation of an aromatic NIT radical with a long aliphatic chain and its coordination with a strongly anisotropic Tb(hfac)$_3$ centre allowed the synthesis of a chiral helical coordination polymer **[Tb(hfac)$_3$(NITPhOC$_6$)]**. The packing of this latter is characterised by the formation of supramolecular porous nanotubes, thermodynamically stabilised by the favourable interactions between the radical alkyl tails and the aliphatic solvent molecules. This feature confers a higher degree of structural stabilisation than linear coordination polymers that fail to exhibit interchain supramolecular interactions. However, it is also strongly dependent on the presence of these crystallisation solvent molecules, as proved by the loss of crystallinity of the dried compound. Nevertheless, this fact did not impact the successful observation of a SCM, characterised by a zero-field slow relaxation of the magnetisation, the presence of typical finite and infinite relaxation regimes, and an appreciable open hysteresis at 0.5 K from molecular origin.

3.6. References

[1] N. Ishii, Y. Okamura, S. Chiba, T. Nogami, T. Ishida, *J. Am. Chem. Soc.* **2008**, *130*, 24–25.

[2] Y. Okamura, T. Nogami, T. Ishida, *Chem. Lett.* **2009**, *38*, 740–741.

[3] T. Ishida, Y. Okamura, I. Watanabe, *Inorg. Chem.* **2009**, *48*, 7012–7014.

[4] Y. Okamura, N. Ishii, T. Nogami, T. Ishida, *Bull. Chem. Soc. Jpn.* **2010**, *83*, 716–725.

[5] J. Gómez-Segura, I. Díez-Pérez, N. Ishikawa, M. Nakano, J. Veciana, D. Ruiz-Molina, *Chem Commun* **2006**, 2866–2868.

[6] D. Bléger, A. Bocheux, D. Kreher, F. Mathevet, A.-J. Attias, G. Metgé, L. Douillard, C. Fiorini-Debuisschert, F. Charra, *Nanoscale* **2013**, *5*, 1452.

[7] T. Inose, D. Tanaka, H. Tanaka, O. Ivasenko, T. Nagata, Y. Ohta, S. De Feyter, N. Ishikawa, T. Ogawa, *Chem. - Eur. J.* **2014**, *20*, 11362–11369.

[8] R. Konnerth, C. Cervetti, A. Narita, X. Feng, K. Müllen, A. Hoyer, M. Burghard, K. Kern, M. Dressel, L. Bogani, *Nanoscale* **2015**, *7*, 12807–12811.

[9] J. H. Osiecki, E. F. Ullman, *J. Am. Chem. Soc.* **1968**, *90*, 1078–1079.

[10] E. F. Ullman, J. H. Osiecki, D. G. B. Boocock, R. Darcy, *J. Am. Chem. Soc.* **1972**, *94*, 7049–7059.

[11] E. V. Tretyakov, V. I. Ovcharenko, *Russ. Chem. Rev.* **2009**, *78*, 971–1012.

[12] A. Caneschi, D. Gatteschi, J. Laugier, P. Rey, R. Sessoli, C. Zanchini, *J. Am. Chem. Soc.* **1988**, *110*, 2795–2799.

[13] A. Caneschi, D. Gatteschi, N. Lalioti, C. Sangregorio, R. Sessoli, *J. Chem. Soc. Dalton Trans.* **2000**, 3907–3912.

[14] L. Bogani, C. Sangregorio, R. Sessoli, D. Gatteschi, *Angew. Chem. Int. Ed.* **2005**, *44*, 5817–5821.

[15] F. Hellman, A. Hoffmann, Y. Tserkovnyak, G. S. D. Beach, E. E. Fullerton, C. Leighton, A. H. MacDonald, D. C. Ralph, D. A. Arena, H. A. Dürr, P. Fischer, J. Grollier, J. P. Heremans, T. Jungwirth, A. V. Kimel, B. Koopmans, I. N. Krivorotov, S. J. May, A. K. Petford-Long, J. M. Rondinelli, N. Samarth, I. K. Schuller, A. N. Slavin, M. D. Stiles, O. Tchernyshyov, A. Thiaville, B. L. Zink, *Rev. Mod. Phys.* **2017**, *89*, 025006.

[16] A. L. Spek, *Acta Crystallogr. Sect. C Struct. Chem.* **2015**, *71*, 9–18.

[17] C. Benelli, A. Caneschi, D. Gatteschi, L. Pardi, P. Rey, *Inorg. Chem.* **1989**, *28*, 275–280.

[18] C. Benelli, A. Caneschi, D. Gatteschi, L. Pardi, P. Rey, *Inorg. Chem.* **1990**, *29*, 4223–4228.

[19] K. Bernot, L. Bogani, A. Caneschi, D. Gatteschi, R. Sessoli, *J. Am. Chem. Soc.* **2006**, *128*, 7947–7956.

[20] X. Liu, Y. Zhang, W. Shi, P. Cheng, *Inorg. Chem.* **2018**, *57*, 13409–13414.

[21] X. Liu, Y.-X. Wang, Z. Han, T. Han, W. Shi, P. Cheng, *Dalton Trans.* **2019**, *48*, 8989–8994.

[22] C. V. Sarmiento, T. A. Araujo, S. G. Reis, M. S. de Souza, R. A. Allão Cassaro, M. A. Novak, M. G. F. Vaz, *RSC Adv.* **2019**, *9*, 30302–30308.

[23] Y.-L. Wang, N. Zhou, Y. Ma, Z.-X. Qin, Q.-L. Wang, L.-C. Li, P. Cheng, D.-Z. Liao, *CrystEngComm* **2012**, *14*, 235–239.

[24] H. Tian, X. Wang, X. Mei, R. Liu, M. Zhu, C. Zhang, Y. Ma, L. Li, D. Liao, *Eur. J. Inorg. Chem.* **2013**, *2013*, 1320–1325.

[25] C. Janiak, *J. Chem. Soc. Dalton Trans.* **2000**, 3885–3896.

[26] K. S. Kim, S. Karthikeyan, N. J. Singh, *J. Chem. Theory Comput.* **2011**, *7*, 3471–3477.

[27] X. Meng, W. Shi, P. Cheng, *Coord. Chem. Rev.* **2019**, *378*, 134–150.

[28] H.-L. Sun, Z.-M. Wang, S. Gao, *Coord. Chem. Rev.* **2010**, *254*, 1081–1100.

[29] R. Sessoli, M.-E. Boulon, A. Caneschi, M. Mannini, L. Poggini, F. Wilhelm, A. Rogalev, *Nat. Phys.* **2015**, *11*, 69–74.

[30] A. Lannes, M. Intissar, Y. Suffren, C. Reber, D. Luneau, *Inorg. Chem.* **2014**, *53*, 9548–9560.

[31] F. Cinti, A. Rettori, M. Barucci, E. Olivieri, L. Risegari, G. Ventura, A. Caneschi, D. Gatteschi, D. Rovai, M. G. Pini, M. Affronte, M. Mariani, A. Lascialfari, *J. Magn. Magn. Mater.* **2007**, *310*, 1460–1461.

[32] E. Bartolomé, J. Bartolomé, S. Melnic, D. Prodius, S. Shova, A. Arauzo, J. Luzón, F. Luis, C. Turta, *Dalton Trans.* **2013**, *42*, 10153.

[33] M. Böhme, W. Plass, *Chem. Sci.* **2019**, *10*, 9189–9202.

[34] J. Jung, M. Puget, O. Cador, K. Bernot, C. J. Calzado, B. Le Guennic, *Inorg. Chem.* **2017**, *56*, 6788–6801.

[35] C. Coulon, R. Clérac, W. Wernsdorfer, T. Colin, A. Saitoh, N. Motokawa, H. Miyasaka, *Phys. Rev. B* **2007**, *76*, 214422–1.

[36] M. Ferbinteanu, H. Miyasaka, W. Wernsdorfer, K. Nakata, K. Sugiura, M. Yamashita, C. Coulon, R. Clérac, *J. Am. Chem. Soc.* **2005**, *127*, 3090–3099.

[37] C. Pichon, N. Suaud, C. Duhayon, N. Guihéry, J.-P. Sutter, *J. Am. Chem. Soc.* **2018**, *140*, 7698–7704.

3.A. Appendices

3.A.1. Synthesis and crystal structure

3.A.1.1. Synthesis of N,N'-2,3 bis(hydroxyamino) 2,3 dimethylbutane, "BHA"

50 mmol of 2,3-dimethyl-2,3-dinitrobutane (8.8 g, 1eq.) was dissolved in a cold solution of THF (150 mL) and water (25 mL). Zn powder (13.5 g, 200 mmol, 4 eq.) was added all at once to this solution, kept in an ice bath. 75 mL of an aqueous solution of NH_4Cl (21.5 g, 400 mol, 8 eq.) was added dropwise for 2 hours. Then stirring was continued overnight in at 12°C, until the blue colour of the solution disappears and the zinc powder is completely whitened. The resulting slurry was filtered, and the carefully washed with cold THF (2 x 100 mL). The solution was evaporated under vacuum until THF ceased to distil off, and the remaining water solvent removed by freeze-drying to avoid the degradation of the resulting Zn(2,3-bis(hydroxyamino)-2,3-dimethylbutane)Cl_2 or Zn(BHA)Cl_2 (Yield = 90.5 %). The white powder was then stored in dark under argon.

3.A.1.2. Synthesis of the $NITPhOC_6$ radical

2.5 mmol (486 µL, 1 eq.) of commercially available 4-(hexyloxy)benzaldehyde was added to 5 mmol (741 mg, 2 eq.) of Zn(BHA)Cl_2 in 50 mL of methanol, and stirred at room temperature for one day. The solution was dried and the remained milky-white waxy solid was dissolved in 50 mL of cold CH_2Cl_2, then 50 mL of an $NaIO_4$ aqueous solution (641.6 mg, 3 mmol, 1.5 eq.) was added. The mixture immediately turned dark blue, the organic phase was washed several times with water (3 x 100 mL) and separated. The resultant organic solution was dried on Na_2SO_4, concentrated under reduced pressure and purified by flash silica gel (40-60 µm, 60 Å) column chromatography eluted with a 3/1 (*v/v*) ether/*n*-pentane solution. A dark blue fraction was collected and concentrated under reduced pressure, resulting of 250.1 mg (0.75 mmol) of fine blue crystalline solid. Yield: 30%.

Single crystals suitable for single crystal XRD were obtained by slow inter-diffusion of 0.05 mmol (16.7 mg) of $NITPhOC_6$ in 7 mL of CH_2Cl_2 layered with 10 mL of *n*-heptane, kept at 4°C. Single-crystals were isolated after few days. Elemental analysis (%) calcd. for $C_{19}H_{29}N_2O_3$: C 68.44; H 8.77; N 8.40. Found: C 68.28; H 8.62; N 8.14.

3.A.1.3. Synthesis of the $[Tb(hfac)_3(NITPhOC_6)]$, "chain"

0.05 mmol (40.8 mg, 1eq.) of $[Tb(hfac)_3{\cdot}2H_2O]$ was dissolved in 40 mL of dry boiling *n*-heptane. The solution was concentrated until the volume reaches 10 mL, then cooled to 75°C. 0.05 mmol (16.7 mg, 1eq.) of $NITPhOC_6$ dissolved in $CHCl_3$ (7 mL) was slowly added under stirring, and the solution was cooled to room temperature. The final mixture was kept for evaporation under dry atmosphere for two days, giving thin light green needles. Yield: 26%.

Elemental analysis (%) calcd. for $TbC_{34}H_{32}N_2O_9F_{18}$: C 36.67; H 2.90; N 2.52. Found: C 36.50; H 2.98; N 2.59.

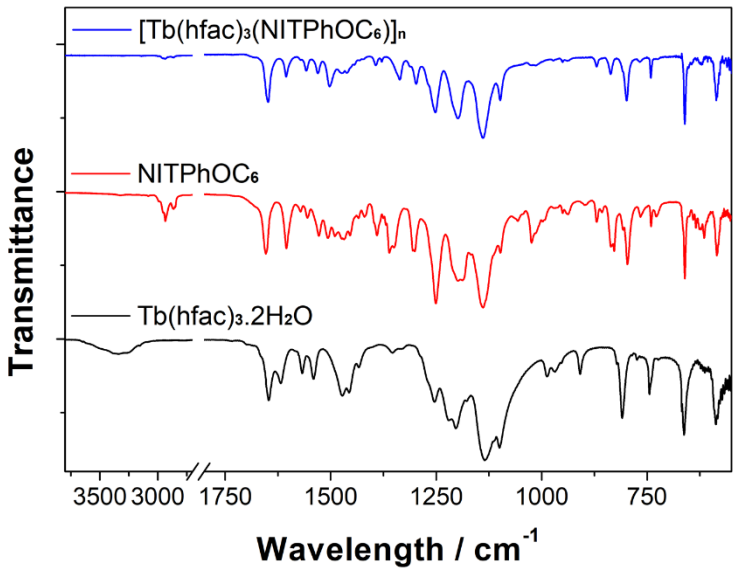

Figure 3.A.20. FTIR spectra of **[Tb(hfac)$_3$·2H$_2$O]**, **NITPhOC$_6$** and **[Tb(hfac)$_3$(NITPhOC$_6$)]$_n$**.

[Tb(hfac)$_3$·2H$_2$O]: 3335 *ν*(O-H), 1646, 1618 and 1565 *ν*(C=C), 1540 *ν*(C-O), 1472 *ν*(C=C), 1253 *ν*(C-F), 1201 *ν*(C-F), 1134 *δ*(C-H)
NITPhOC$_6$: 2995, 2950, 2936 and 2864 *ν*(C-H), 1653 *ν*(C=C), 1603 *ν*(C=C$_{arom}$), 1391, 1360 *ν*(N-O), 1301 *ν*(C-O), 1250 *ν*(C$_{arom}$-O in ether), 1197 *ν*(C-O), 1138 *ν*(C-N)
[Tb(hfac)$_3$(NITPhOC$_6$)]$_n$: 2954 and 2871 *ν*(C-H), 1648 *ν*(C=C), 1603 *ν*(C=C$_{arom}$), 1557, 1530 and 1501 *ν*(C=C), 1335 *ν*(N-O), 1298 *ν*(C-O), 1251 *ν*(C$_{arom}$-O in ether, C-F), 1198 *ν*(C-O, C-F), 1138 *ν*(C-N)

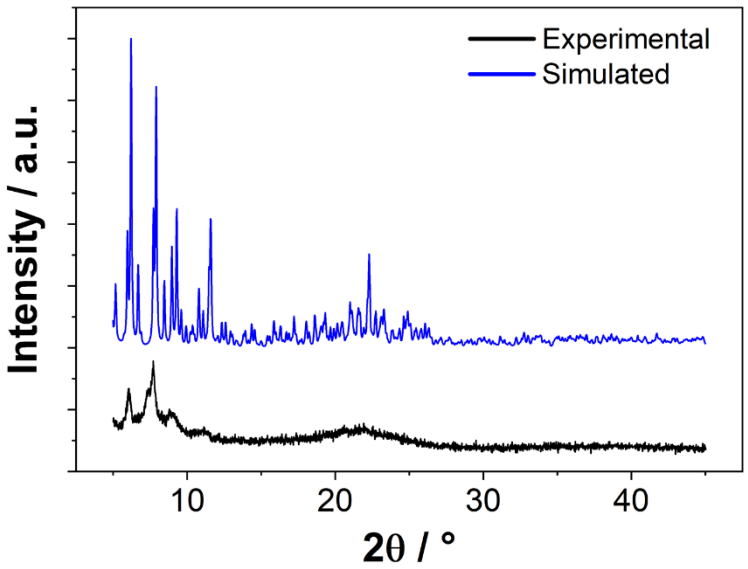

Figure 3.A.21. Powder X-Ray diffraction pattern of experimental and simulated **[Tb(hfac)$_3$(NITPhOC$_6$)]$_n$**.

Table 3.A.4. Selected bond distances (Å) for **[Tb(hfac)$_3$(NITPhOC$_6$)]$_n$**.

Tb1		Tb2		Tb3	
Tb1-O1	2.382	Tb2-O6	2.401	Tb3-O15	2.509
Tb1-O1*	2.382	Tb2-O7	2.373	Tb3-O16	2.328
Tb1-O2	2.359	Tb2-O8	2.359	Tb3-O17	2.317
Tb1-O2*	2.360	Tb2-O9	2.371	Tb3-O18	2.318
Tb1-O3	2.340	Tb2-O10	2.328	Tb3-O19	2.203
Tb1-O3*	2.341	Tb2-O11	2.420	Tb3-O20	2.430
Tb1-O4	2.343	Tb2-O12	2.363	Tb3-O21	2.382
Tb1-O4*	2.343	Tb2-O13	2.401	Tb3-O22	2.347

* = (*x-y,-y,-z*) symmetry operation

Table 3.A.5. Selected angles (°) for **[Tb(hfac)$_3$(NITPhOC$_6$)]$_n$**.

Tb1		Tb2		Tb3	
O1-Tb1-O1*	52.98	O6-Tb2-O7	52.09	O15-Tb3-O16	49.21
O1-Tb1-O2	51.48	O6-Tb2-O8	37.73	O15-Tb3-O17	32.11
O1-Tb1-O2*	15.52	O6-Tb2-O9	53.45	O15-Tb3-O18	14.80
O1-Tb1-O3	28.26	O6-Tb2-O10	51.78	O15-Tb3-O19	44.44
O1-Tb1-O3*	23.19	O6-Tb2-O11	16.25	O15-Tb3-O20	52.07
O1-Tb1-O4	55.37	O6-Tb2-O12	44.18	O15-Tb3-O21	52.01
O1-Tb1-O4*	52.55	O6-Tb2-O13	21.43	O15-Tb3-O22	21.00
O1*-Tb1-O2	15.67	O7-Tb2-O8	53.53	O16-Tb3-O17	52.62
O1*-Tb1-O2*	76.31	O7-Tb2-O9	28.32	O16-Tb3-O18	61.74
O1*-Tb1-O3	23.64	O7-Tb2-O10	20.89	O16-Tb3-O19	51.37
O1*-Tb1-O3*	122.92	O7-Tb2-O11	62.58	O16-Tb3-O20	28.61
O1*-Tb1-O4	53.83	O7-Tb2-O12	102.28	O16-Tb3-O21	22.38
O1*-Tb1-O4*	37.82	O7-Tb2-O13	16.33	O16-Tb3-O22	16.34
O2-Tb1-O2*	22.80	O8-Tb2-O9	54.04	O17-Tb3-O18	54.10
O2-Tb1-O3	53.41	O8-Tb2-O10	18.31	O17-Tb3-O19	20.07
O2-Tb1-O3*	53.28	O8-Tb2-O11	52.65	O17-Tb3-O20	53.77
O2-Tb1-O4	37.96	O8-Tb2-O12	20.34	O17-Tb3-O21	16.84
O2-Tb1-O4*	42.47	O8-Tb2-O13	44.98	O17-Tb3-O22	46.45
O2*-Tb1-O3	53.92	O9-Tb2-O10	53.21	O18-Tb3-O19	49.95
O2*-Tb1-O3*	72.54	O9-Tb2-O11	22.59	O18-Tb3-O20	23.08
O2*-Tb1-O4	42.83	O9-Tb2-O12	16.02	O18-Tb3-O21	29.50
O2*-Tb1-O4*	103.77	O9-Tb2-O13	53.12	O18-Tb3-O22	54.30
O3-Tb1-O3*	50.25	O10-Tb2-O11	28.07	O19-Tb3-O20	18.80
O3-Tb1-O4	52.65	O10-Tb2-O12	51.93	O19-Tb3-O21	56.28
O3-Tb1-O4*	13.12	O10-Tb2-O13	56.04	O19-Tb3-O22	37.83
O3*-Tb1-O4	13.10	O11-Tb2-O12	53.29	O20-Tb3-O21	52.26
O3*-Tb1-O4*	74.80	O11-Tb2-O13	52.39	O20-Tb3-O22	50.99
O4-Tb1-O4*	24.39	O12-Tb2-O13	38.43	O21-Tb3-O22	53.97

* = (*x-y,-y,-z*) symmetry operation

Table 3.A.6. Continuous Shape Measurements (CShM)[38] for **[Tb(hfac)$_3$(NITPhOC$_6$)]$_n$**.

Coordination geometry (site symmetry)	Square antiprism (D_{4d})	Triangular dodecahedron (D_{2d})	Bi-augmented trigonal prism (C_{2v})
Tb1 CShM	1.74	0.51	2.60
Tb2 CShM	1.25	0.45	1.99
Tb3 CShM	0.80	1.16	1.53

3.A.2. Stability: thermal and luminescent measurements

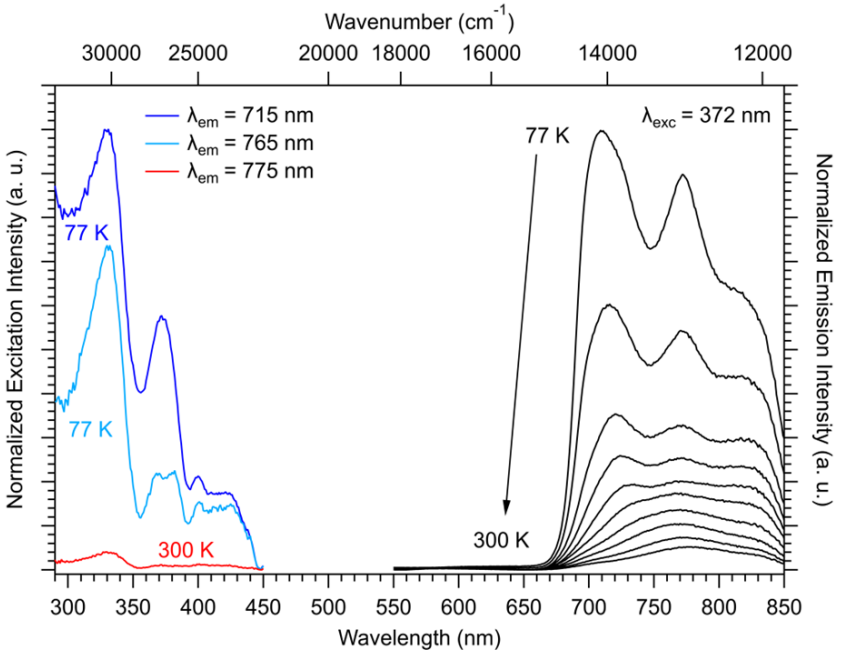

Figure 3.A.22. Solid excitation spectra at 77 K (λ_{em} = 715 or 765 nm), at 300 K (λ_{em} = 775 nm), and emission spectra (λ_{ex} = 372 nm, for the dark curves) between 77 and 300 K of the uncoordinated **NITPhOC$_6$**. The emission data are corrected properly by eliminating the additional emission from the holder used for the measurement (quartz cuvette).

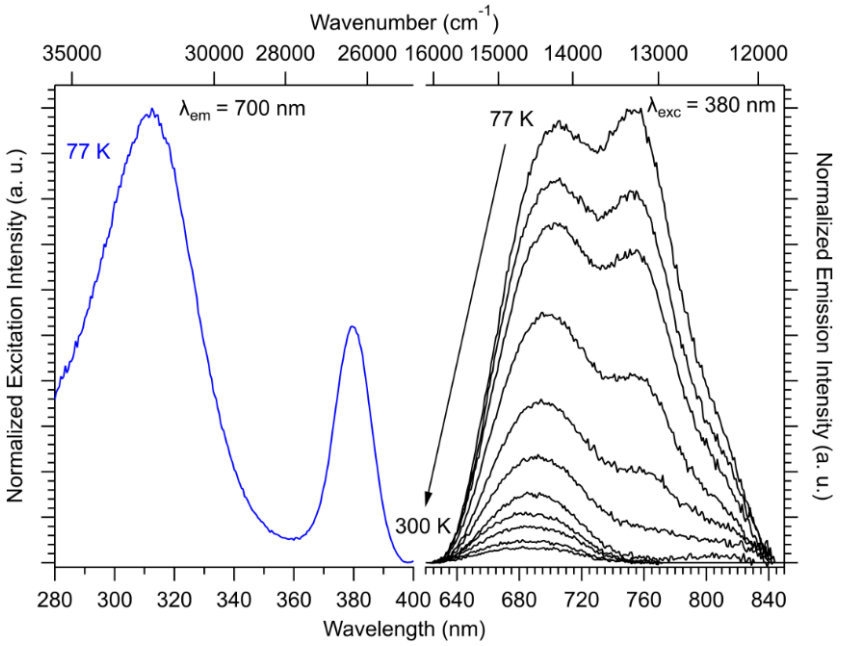

Figure 3.A.23. Solid excitation spectrum at 77 K (λ_{em} = 700 nm), and emission spectra (λ_{ex} = 380 nm) between 77 and 300 K of **[Tb(hfac)$_3$(NITPhOC$_6$)]$_n$**. The emission data are corrected properly by eliminating the additional emission from the holder used for the measurement (quartz cuvette).

3.A.3. Magnetic properties

3.A.3.1. Theoretical description and magnetic coupling: computational details

In order to decrease the computational cost of the wavefunction theory (WFT) calculations, the 3 crystallographically different Tb^{III} units were simplified by shortening the strongly disordered C6 carbon tail to a more rigid methyl one. The hydrogen atom positions of the model structures were optimized by using Kohn-Sham density functional theory (DFT) with the Amsterdam Density Functional (ADF) software package.[39–41] These calculations utilized the scalar all-electron zeroth-order regular approximation (ZORA).[42] The PBE functional (Perdew-Burke-Ernzerhof)[43,44] from the generalized gradient approximation, was employed along with the triple-ζ polarized Slater-type orbital (STO) all-electron basis set with two sets of polarization functions for all atoms (TZ2P).[45]

The WFT calculations were performed with the help of the Molcas 8.2 and OpenMolcas software packages[46] on the di-anionic molecular units $[Tb(1)]^{2-}$, $[Tb(2)]^{2-}$ and $[Tb(3)]^{2-}$ to obtain diamagnetic NIT ligands, and evaluate the magnetic properties arising from the Tb^{III} centres only. In these calculations, the complete active space self-consistent field (CASSCF) approach[47] was used to treat the static correlation effects arising from the partially filled *4f* shell of the Tb^{III} ion. The second-order Douglas-Kroll-Hess scalar relativistic (SR) Hamiltonian[48–51] was used to treat the scalar relativistic effects in combination with the all-electron atomic natural orbital relativistically contracted (ANO-RCC) basis set from the Molcas library.[52–54] The basis sets were contracted to the triple-ζ plus polarization (TZP) quality for the Tb, N and O atoms (Tb = 25s22p15d11f4g2h/8s7p4d3f2g1h; N, O = 14s9p5d3f2g/ 4s3p2d1f), and to the double-z (DZ) quality for the H, C and F atoms (H = 8s4p3d1f/2s; C, F = 14s9p5d3f2g/3s2p). Additionally, the C atoms between the two NO groups of each NIT radical ligands were treated with a basis set contracted to the TZP quality, whereas the O atoms not coordinated to the Tb centres were treated using a basis set contracted to DZ quality. The calculations employed the state-averaged formalism at the SR level by taking into account the 7 septet, the 140 quintet, 588 triplet and the 396 singlet spin states arising from the 8 electrons spanning the seven 4*f* orbitals (i.e. CAS(8,7)). The spin-orbit coupling (SOC) was then introduced within a state interaction among the basis of calculated SR states using the restricted active space state interaction (RASSI) approach.[55] Herein the SOC matrix is diagonalized using the calculated 7 SR septet, 140 SR quintet, the 91st lowest SR triplet and the 77th lowest SR singlet spin states. The EPR *g*-factors were calculated according to Ref.[56] as implemented in the RASSI module of Molcas, whereas the magnetic susceptibility and magnetisation calculations were performed using the Single-Aniso module of Molcas as detailed in Ref.[57].

3.A.3.2. Dynamic (AC) magnetic properties

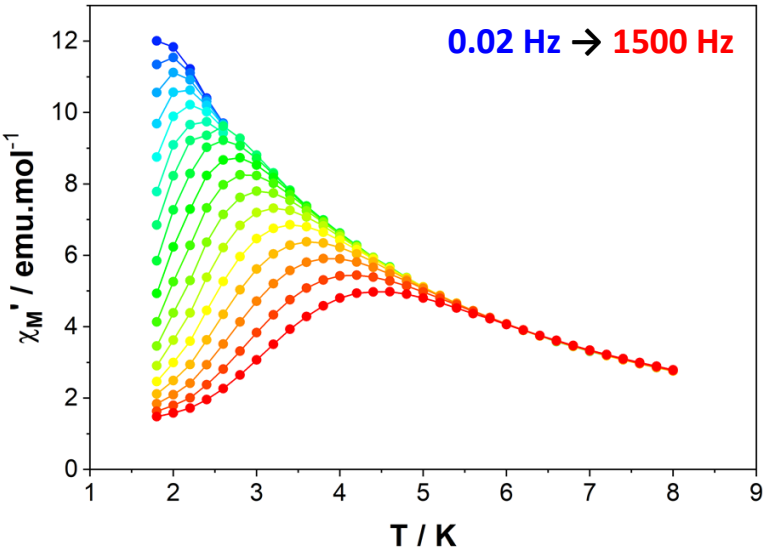

Figure 3.A.24. Temperature dependence of the in-phase (χ_M') susceptibility of **[Tb(hfac)$_3$(NITPhOC$_6$)]$_n$** at various frequencies.

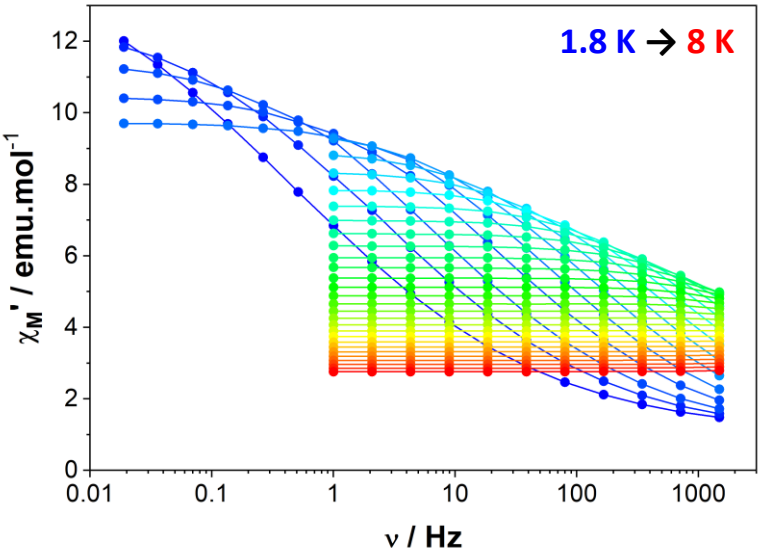

Figure 3.A.25. Frequency dependence of the in-phase (χ_M') susceptibility of **[Tb(hfac)$_3$(NITPhOC$_6$)]$_n$** at various temperatures.

Table 3.A.7. Relaxation times extracted for **[Tb(hfac)$_3$(NITPhOC$_6$)]$_n$**.

T (K)	τ (μs)	R^2	*T* (K)	τ (μs)	R^2
1.8	348573	0.9997	**2.8**	1243	0.9990
2	82754	0.9992	**3**	621	0.9985
2.2	26455	0.9986	**3.2**	342	0.9981
2.4	7466	0.9981	**3.4**	211	0.9977
2.6	2826	0.9986	**3.6**	138	0.9994

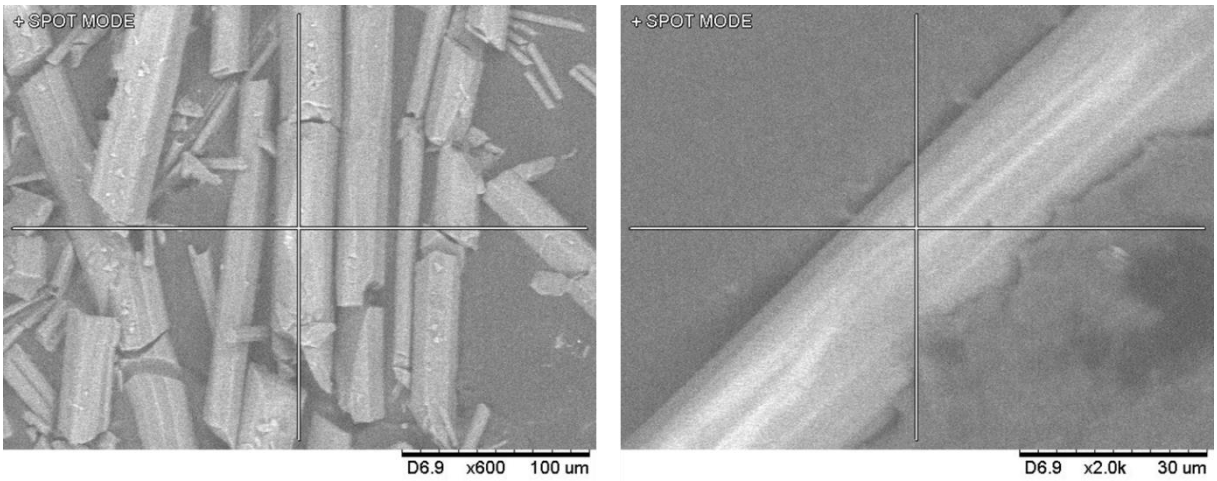

Figure 3.A.26. SEM images of doped **[(Tb$_{0.05}$Y$_{0.95}$)(hfac)$_3$(NITPhOC$_6$)]$_n$** crystals. Respective Tb/Y atomic compositions are 4.6%/95.4% (left) and 6.2%/93.8% (right).

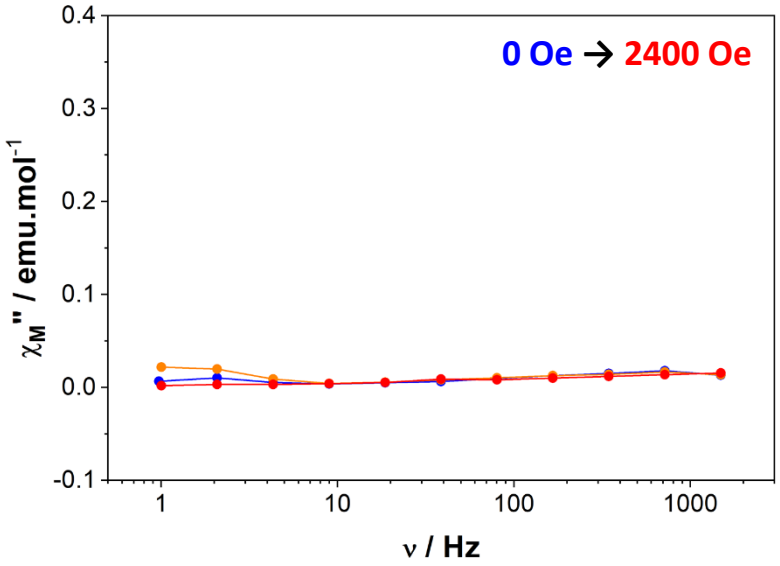

Figure 3.A.27. Field dependence of the out-of-phase susceptibility at 2 K of doped **[(Tb$_{0.05}$Y$_{0.95}$)(hfac)$_3$(NITPhOC$_6$)]$_n$**

Table 3.A.8. Adiabatic (χ_S), isothermal (χ_T) susceptibility values and relaxation times distribution (α) extracted for **[Tb(hfac)$_3$(NITPhOC$_6$)]**.

T (K)	χ_S	χ_T	α	R^2
1.8	0.98	15.10	0.615	0.9997
2.0	0.90	13.87	0.595	0.9991
2.2	0.76	12.93	0.586	0.9992
2.4	0.79	11.61	0.555	0.9982
2.6	0.77	10.70	0.535	0.9989
2.8	0.83	9.90	0.511	0.9994
3.0	1.00	9.17	0.479	0.9988
3.2	1.15	8.57	0.454	0.9988
3.4	1.36	8.04	0.428	0.9988
3.6	1.73	7.52	0.387	0.9984

3.A.4. References

[38] M. Llunell, D. Casanova, J. Cirera, P. Alemany, S. Alvarez, *SHAPE*, **2010**.

[39] G. te Velde, F. M. Bickelhaupt, E. J. Baerends, C. Fonseca Guerra, S. J. A. van Gisbergen, J. G. Snijders, T. Ziegler, *J. Comput. Chem.* **2001**, *22*, 931–967.

[40] C. Fonseca Guerra, J. G. Snijders, G. te Velde, E. J. Baerends, *Theor. Chem. Acc. Theory Comput. Model. Theor. Chim. Acta* **1998**, *99*, 391–403.

[41] E. J. Baerends, T. Ziegler, J. Autschbach, D. Bashford, A. Bérces, F. M. Bickelhaupt, C. Bo, P. M. Boerrigter, L. Cavallo, D. P. Chong, others, *ADF2017*, SCM, Vrije Universiteit, Amsterdam, The Netherlands, **2017**.

[42] E. van Lenthe, E. J. Baerends, J. G. Snijders, *J. Chem. Phys.* **1993**, *99*, 4597–4610.

[43] J. P. Perdew, K. Burke, M. Ernzerhof, *Phys. Rev. Lett.* **1996**, *77*, 3865–3868.

[44] J. P. Perdew, K. Burke, M. Ernzerhof, *Phys. Rev. Lett.* **1997**, *78*, 1396–1396.

[45] E. Van Lenthe, E. J. Baerends, *J. Comput. Chem.* **2003**, *24*, 1142–1156.

[46] F. Aquilante, J. Autschbach, R. K. Carlson, L. F. Chibotaru, M. G. Delcey, L. De Vico, I. Fdez. Galván, N. Ferré, L. M. Frutos, L. Gagliardi, M. Garavelli, A. Giussani, C. E. Hoyer, G. Li Manni, H. Lischka, D. Ma, P. Å. Malmqvist, T. Müller, A. Nenov, M. Olivucci, T. B. Pedersen, D. Peng, F. Plasser, B. Pritchard, M. Reiher, I. Rivalta, I. Schapiro, J. Segarra-Martí, M. Stenrup, D. G. Truhlar, L. Ungur, A. Valentini, S. Vancoillie, V. Veryazov, V. P. Vysotskiy, O. Weingart, F. Zapata, R. Lindh, *J. Comput. Chem.* **2016**, *37*, 506–541.

[47] B. O. Roos, P. R. Taylor, P. E. M. Sigbahn, *Chem. Phys.* **1980**, *48*, 157–173.

[48] M. Douglas, N. M. Kroll, *Ann. Phys.* **1974**, *82*, 89–155.

[49] B. A. Hess, *Phys. Rev. A* **1985**, *32*, 756–763.

[50] B. A. Hess, *Phys. Rev. A* **1986**, *33*, 3742–3748.

[51] A. Wolf, M. Reiher, B. A. Hess, *J. Chem. Phys.* **2002**, *117*, 9215–9226.

[52] P.-O. Widmark, P. Å. Malmqvist, B. O. Roos, *Theor. Chim. Acta* **1990**, *77*, 291–306.

[53] B. O. Roos, R. Lindh, P. Å. Malmqvist, V. Veryazov, P.-O. Wildmark, *J. Phys. Chem. A* **2004**, *105*, 2851–2858.

[54] B. O. Roos, R. Lindh, P.-Å. Malmqvist, V. Veryazov, P.-O. Widmark, *J. Phys. Chem. A* **2005**, *109*, 6575–6579.

[55] P. Å. Malmqvist, B. O. Roos, B. Schimmelpfennig, *Chem. Phys. Lett.* **2002**, *357*, 230–240.

[56] H. Bolvin, *ChemPhysChem* **2006**, *7*, 1575–1589.

[57] L. F. Chibotaru, L. Ungur, *J. Chem. Phys.* **2012**, *137*, 064112.

Chapter 4. Single-Chain Magnet Behaviour in a Finite Linear Hexanuclear Molecule

4.1. Introduction

From Chapter 3, we have demonstrated that the flexibility of the **$[Tb(hfac)_3(NITPhOC_6)]_n$** system could lead to supramolecular helical nanotubes of SCMs. However, such organisation is far from being usual for the [Ln(hfac)$_3$(NITPhO-*R*)] chains, due to the π-interactions pattern between aromatic $hfac^-$ moieties and phenyl groups that impose a more linear growth fashion because of angles that compensate.

In this chapter, we report how the crystallisation conditions can influence the selective obtaining of a new linear complex **$[(Tb(hfac)_3)_6(NITPhOC_6)_5(H_2O)_2]$**, constituted of the same building blocks of the helical **$[Tb(hfac)_3(NITPhOC_6)]_n$**. We will detail and compare how this structural change impacts the magnetic properties of these two compounds.[f]

[f] This study has been published under the reference: F. Houard, F. Gendron, Y. Suffren, T. Guizouarn, V. Dorcet, G. Calvez, C. Daiguebonne, O. Guillou, B. Le Guennic, M. Mannini, K. Bernot. 2021. Single-Chain Magnet Behavior in a Finite Linear Hexanuclear Molecule. *Chem. Sci*. 12, 31, 10613-10621.

4.2. Synthesis and crystal structure

During crystallisation of the supramolecular nanotubes of SCMs (see Chapter 3), plate-like crystals with the same light green colour were observed among the needles characteristic of the chains of **[Tb(hfac)$_3$(NITPhOC$_6$)]$_n$** organised as nanotubes. Preliminary measurements on these crystals show chemical similitudes; they share poorly crystalline diffraction patterns once removed from the mother solution (Figure 4.A.20) and matching FTIR vibrational bands (with an additional broad peak around 3150 cm^{-1} probably due to crystallisation water molecules). These first insights led us to assume that this difference in the crystal's morphology could be due to polymorphism, *i.e.*, a different packing of the previous helical **chain** structure.

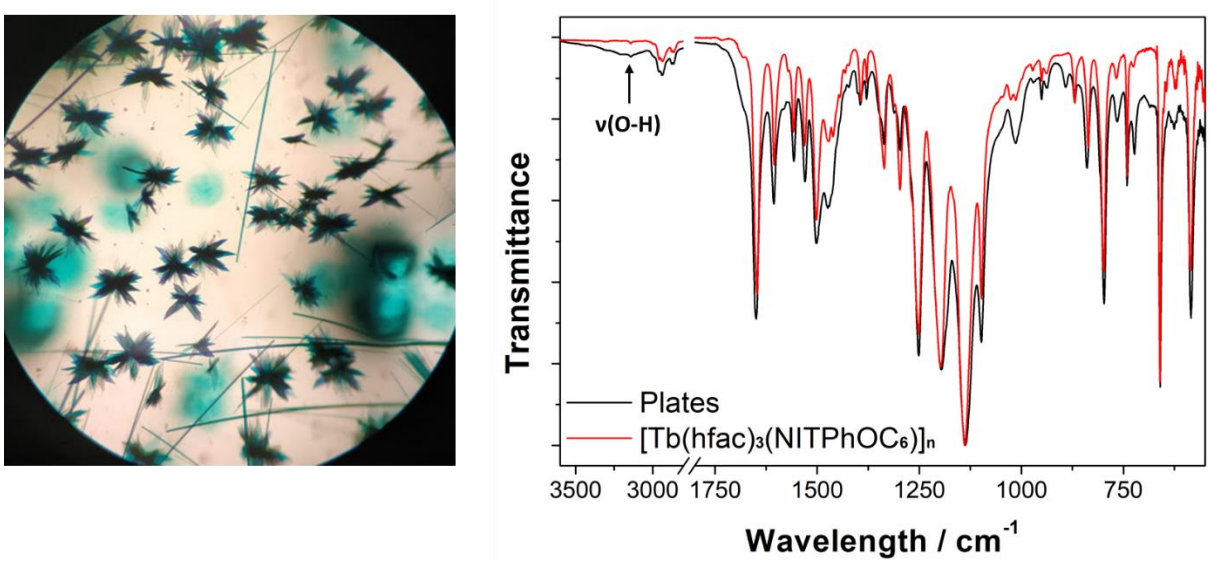

Figure 4.1. Plate and needle crystals observed under optical microscope (x63 magnification, left) and comparative FTIR spectra of the plates and **[Tb(hfac)$_3$(NITPhOC$_6$)]$_n$** (right).

Taking advantage of our previous experience with the previous fragile needles, the best single crystals were measured by single-crystal X-ray diffraction with the same precautions (picked with Apiezon grease from mother solution, N_2 flux at 150 K), which allowed us to determine its molecular structure.

Once again, the presence of strongly disordered electron densities coming from crystallisation solvent molecules was excluded by a SQUEEZE procedure.[1] The same treatments as for the **[Tb(hfac)$_3$(NITPhOC$_6$)]$_n$** were executed: anisotropic refinement of all the atoms and fixing of the relevant free parameters for the more mobile groups of atoms (C-F bond lengths for the -CF_3 groups and thermal agitation coefficients for the terminal carbons of the aliphatic chains).

Hence, it appeared that this evolution of crystal morphology in the mother solution, from needles to plates, came along with drastic changes of the resulting crystal structure depicted thereafter, discarding our first hypothesis of polymorphic structure.

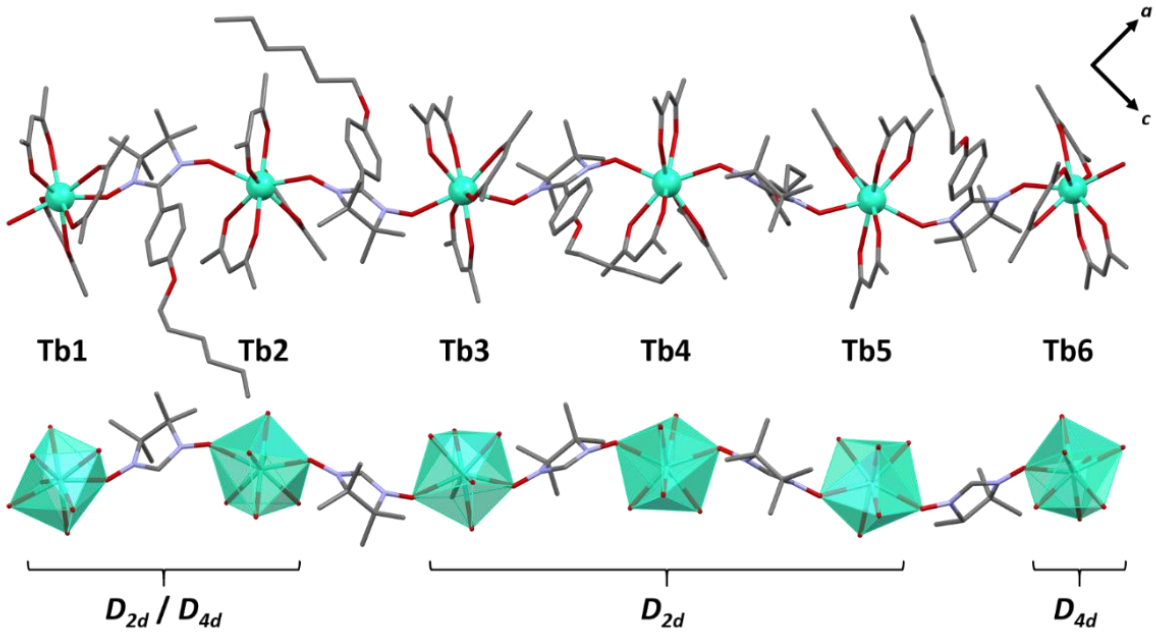

Figure 4.2. Representations of the asymmetric unit along the *b*-axis (top, with solvent molecules, hydrogen and fluorine atoms omitted for clarity) and the simplified magnetic backbone (bottom) of the **hexanuclear** complex.

Indeed, this new structure, of formula **$[(Tb(hfac)_3)_6(NITPhOC_6)_5(H_2O)_2]\cdot CHCl_3.C_7H_{16}$** and called thereafter "**hexanuclear**", crystallises in a monoclinic $P2_1/n$ system (Table 4.1). Its asymmetric structure can be described as a linear alternation of five NIT radicals and six $Tb(hfac)_3$, end-capped by one water molecule on each side. All Tb^{III} ions are eight-fold coordinated by six oxygen atoms from $hfac^-$ ligands and two from bridging nitroxide groups, except for terminal Tb1 and Tb6 ions with one radical substituted by a water molecule. The resulting coordination polyhedra are D_{2d} triangular dodecahedra for Tb1, Tb2, Tb3, Tb4 and Tb5 (the first two are also close to D_4 square antiprism) and D_4 square antiprism for Tb6 (Table 4.A.7). Tb-O_{rad} distances are in the range of 2.36 – 2.41 Å and the shortest intramolecular distance between Tb^{III} ions within the molecule is 8.40 Å, values that are very close to the ones reported for the helical **chain** described in the previous chapter.

The asymmetric unit also includes a chloroform molecule, and more importantly, an *n*-heptane molecule that faces a radical aliphatic tail (Figure 4.A.21). This is in line with our previous assumption of favoured interactions between the radical alkyl groups and the solvent, the latter acting as a scaffold/template for the molecular structure in this case.

As for the helical **chain**, analogous π-stacking arrangements between aromatic $hfac^-$ moieties and phenyl groups are observed, with inter-centroid distances lying in the same range ($d_{\pi\text{-}\pi}$ = 3.48 – 3.97 Å) but with more tilted orientations (α = 9.6 – 24.3°, except for Tb4-Tb5 rings where α = 3.7 – 4.2°) then for the **chain**, indicating potentially weaker π- interactions.

Table 4.1. Crystallographic parameters of **$[(Tb(hfac)_3)_6(NITPhOC_6)_5(H_2O)_2]\cdot CHCl_3.C_7H_{16}$**.

Name	$[(Tb(hfac)_3)_6(NITPhOC_6)_5(H_2O)_2]\cdot CHCl_3.C_7H_{16}$
M **(g.mol^{-1})**	6603.36
Crystal system	Monoclinic
Space group	$P2_1/n$ (N°14)
a **(Å)**	27.995(4)
b **(Å)**	22.437(3)
c **(Å)**	41.691(5)
α **[°]**	90
β **[°]**	94.178(4)
γ **[°]**	90
V **[Å^3]**	26118
Z	4
T **(K)**	150
2ϑ **range**	2.3867– 27.4754
Reflections collected	262314
Indep. reflections	59734
Obs. reflections	44434
Parameters	3379
R_1[g] **[*I* > 2*σ*(*I*)] / wR_2**[h] **[*I* > 2*σ*(*I*)]**	4.72 / 10.39
GOF	1.017
CCDC Number	2076378

[g] $\sum(|F_0| - |F_c|)/\sum|F_0|$

[h] $\sqrt{\sum w(|F_0|^2 - |F_c|^2)^2/\sum w(|F_0|^2)^2}$

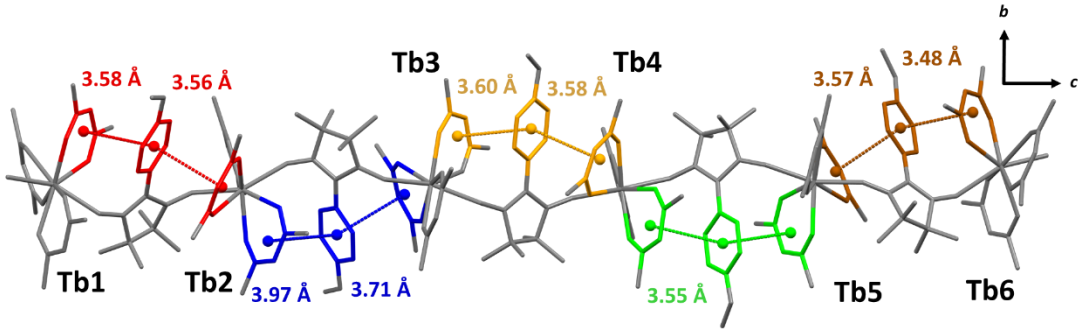

Figure 4.3. Representations of the π- interaction pattern along the simplified asymmetric unit of the **hexanuclear**.

The presence of coordinated water molecules incited us to pay attention to the presence or not of atmospheric moisture during the crystal growth step. After a careful screening of the crystallisation conditions, we observed that moisture triggers the predominance of plates over needles: crystals of **chains** (needles) were mainly obtained under dry conditions (desiccator with a layer of silica gel) while the platelets (**hexanuclear**) grew in humid atmosphere. More surprisingly, batches of crystallised needles (**chains**) exposed to atmospheric moisture afterwards have been observed to turn into platelets irreversibly. These observations supported the hypothesis that coordinating water molecules drive the crystallogenesis, the two crystalline states forming a somewhat bistable system in presence of atmospheric water molecules, with the **hexanuclear** complex being the thermodynamically favoured state.

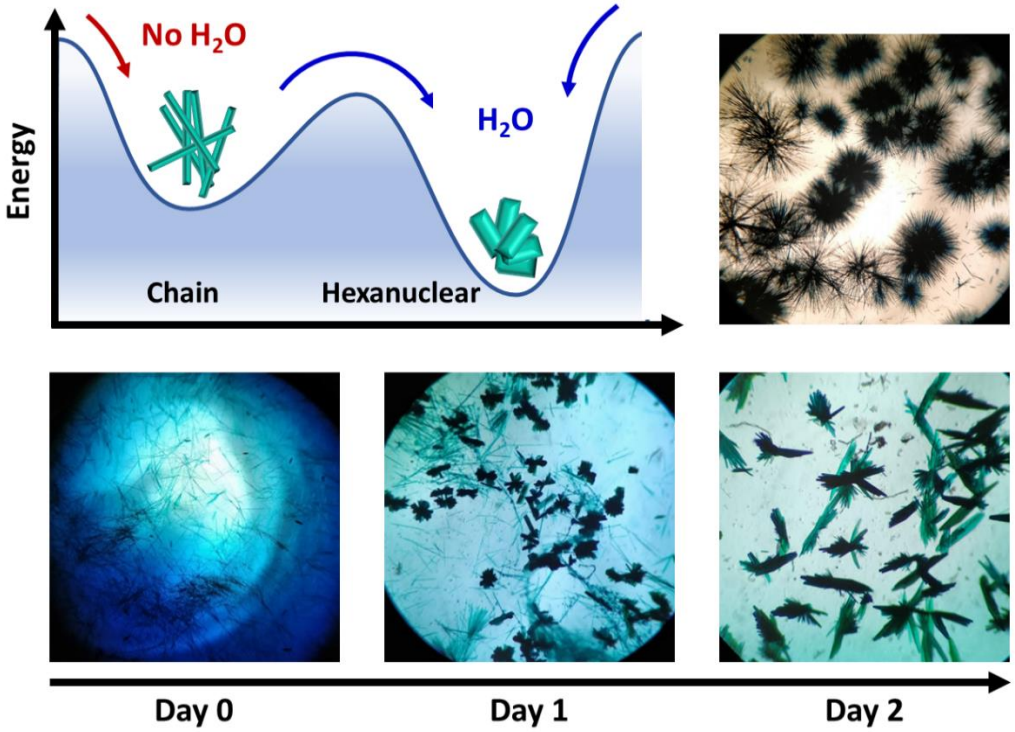

Figure 4.4. Top: Possible crystallisation mechanism of the **hexanuclear** (left) and picture of crystals of **chains** obtained in dry atmosphere (left). Bottom: Observation of the progressive changes observed in the crystallisation batch where needles (**chains**) disappears and plates are formed (**hexanuclears**) under water-saturated conditions.

The terminal water molecules of two consecutive **hexanuclears** interact two by two by hydrogen bonding in a very similar way as the one observed in the crystalline $Tb(hfac)_3$ dihydrate (see also Chapter 2).[2,3] This interaction is tailored by the strong Lewis acidity of the $Tb(hfac)_3$ units that favour interaction between the electron-poor water oxygen atoms of two neighbouring molecules. This induces an intermolecular Tb-Tb distance of 6.05 Å that is shorter than the mean value of the intramolecular one (8.40 Å). These modifications within the Tb-Tb distances could impact the magnetic properties of this polynuclear system and will be a crucial point to address for the investigation of the magnetic properties of the **hexanuclears**.

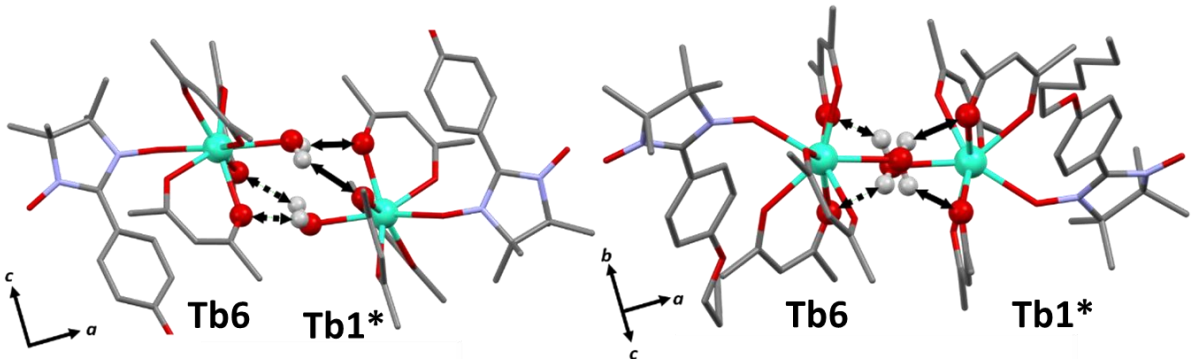

Figure 4.5. Side and top views of hydrogen bonding patterns between two consecutive **hexanuclear** molecules.

Overall, this non-covalent bonding between consecutive units, coupled with the symmetry operations of the $P2_1/n$ space group, generates a supramolecular arrangement of **hexanuclears** along the [502] direction (see Figure 4.6 below). Perpendicularly to this direction, the shortest Tb-Tb interchain distance is 11.33 Å, which excludes any intermolecular magnetic interactions between the molecules as well as long-range magnetic ordering.

It is worth comparing the finite **hexanuclear** molecules obtained here with the previously reported **chains** in Chapter 3. At first glance, one could think that the **chains** form first and that water molecules cut it in particular points to form the finite molecule. However, no obvious "cutting point" can be found on the **chains** using either the symmetry operation of the space group, the number of repeating asymmetric units or the Tb coordination polyhedron.

One can also compare the two crystallisation routes in Figure 4.4:

1) The transformation of **chains** into **hexanuclear** units is not a strictly single-crystal-to-single-crystal transformation because it occurs in the mother solution. So, it is likely that the **chains** decompose, and then the presence of water triggers the crystallisation of the **hexanuclear** compounds;
2) The **hexanuclear** can be obtained directly from the mother solution if the crystallisation is conducted in water-saturated conditions. The **chain** crystals (needles) are not observed but directly the **hexanuclear** units (platelets).

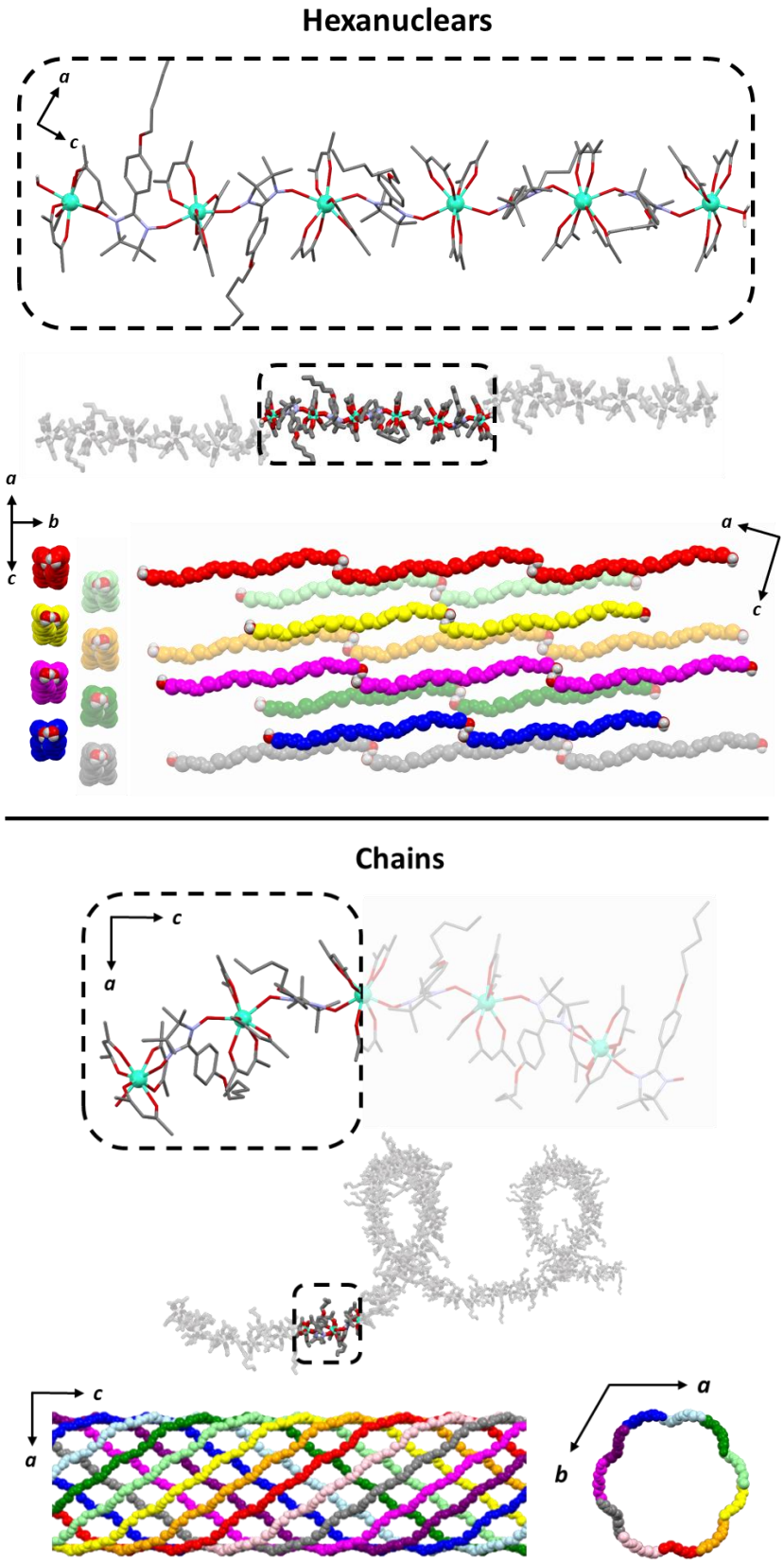

Figure 4.6. Comparison of the **hexanuclears** and the **chains** (from top to bottom with solvent molecules, hydrogen and fluorine atoms omitted): Representations of the molecules with the asymmetric unit as dotted square; Representation of the crystal packing along and perpendicular to the propagation direction of the molecules ([502] direction for the **hexanuclears**, *c*-axis for the **chains**).

The crystal packing is also very different, as represented above. **Hexanuclears** are water bridged along the [502] direction and then further stacked one over the other. This contrasts with what is seen on **chains** where supramolecular interaction between chains induce a helicity and constrain them to be wrapped eleven by eleven to form supramolecular nanotubes that stack further in a hexagonal lattice.

It can be noted that, as far we tested, variation of the stoichiometry, the temperature or humidity conditions does not allow control over the nuclearity of the molecule because as soon as humidity is present during the crystallisation, **hexanuclears** are obtained. This suggests that this species is particularly stable from the thermodynamic point of view. This is rather surprising because linear polynuclear molecules usually tend to form wheels to gain stability[4–6] even when combined in larger edifices.[7]

4.3. Stability: thermal and luminescent measurements

As stated before, and like the **chain**, the **hexanuclears**' single crystals quickly become amorphous when taken off the mother solution. This is due to solvent loss as 10% of the cell volume (V_{void} = 2577 Å^3) is filled with *n*-heptane and chloroform molecules that quickly evaporate. Despite losing their long-range order and diffracting power, crystals are still robust and can be collected easily. Indeed, SEM images show that crystals are still observable under vacuum conditions and do not collapse into a powder. This is probably because the main intermolecular contacts between the **hexanuclear** units are via their H-bonded terminal Tb(hfac)$_3$ moieties and radical alkyl chains, not with the solvent molecules.

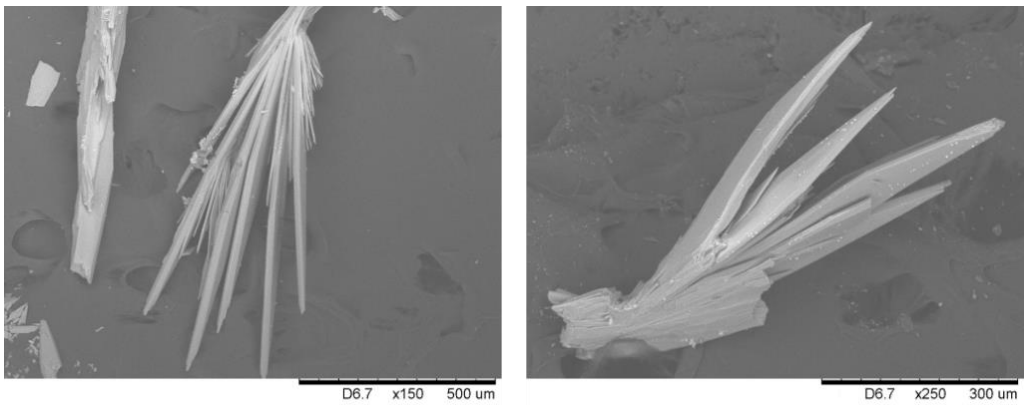

Figure 4.7. SEM images of **hexanuclear** crystals (magnification x150 and x250).

However, coupled FTIR spectroscopy, TGA and TDA analyses have been performed on freshly dried crystals to check if reliable magnetic measurements can be performed on these amorphous compounds. They show that the compound is stable up to 124°C (coordinated water molecules departure or melting as observed for the chains) and that no other significant gas emission is observed below 200°C. This sustains the hypothesis that the fast amorphisation is due to crystallisation solvent loss and that the molecular skeleton of the compound is preserved at room temperature (no gas emission before complete decomposition of the compound at high temperature).

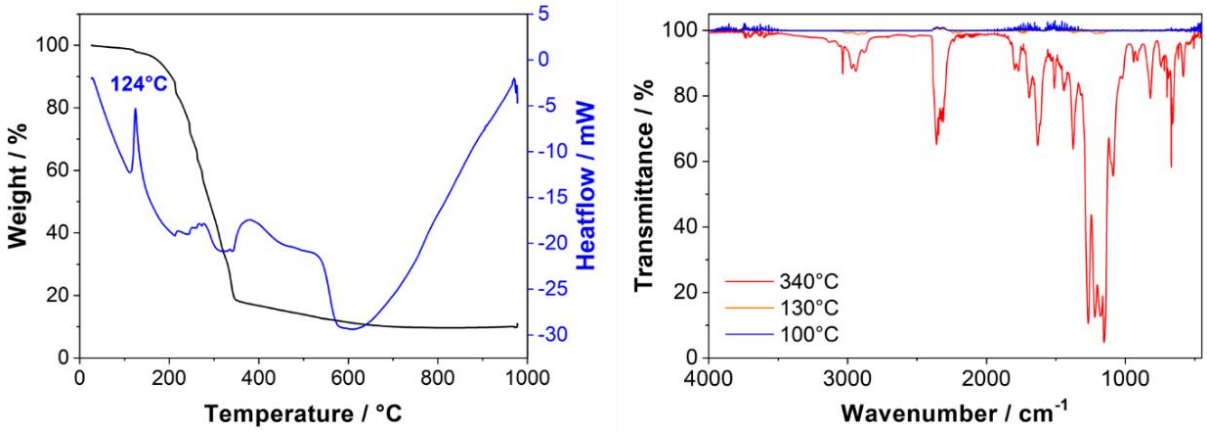

Figure 4.8. Thermogravimetric (TG) and thermodifferential (TD) analyses (left) and FTIR single spectra of exhausted gazes recorded at different temperatures (right) of **hexanuclear**.

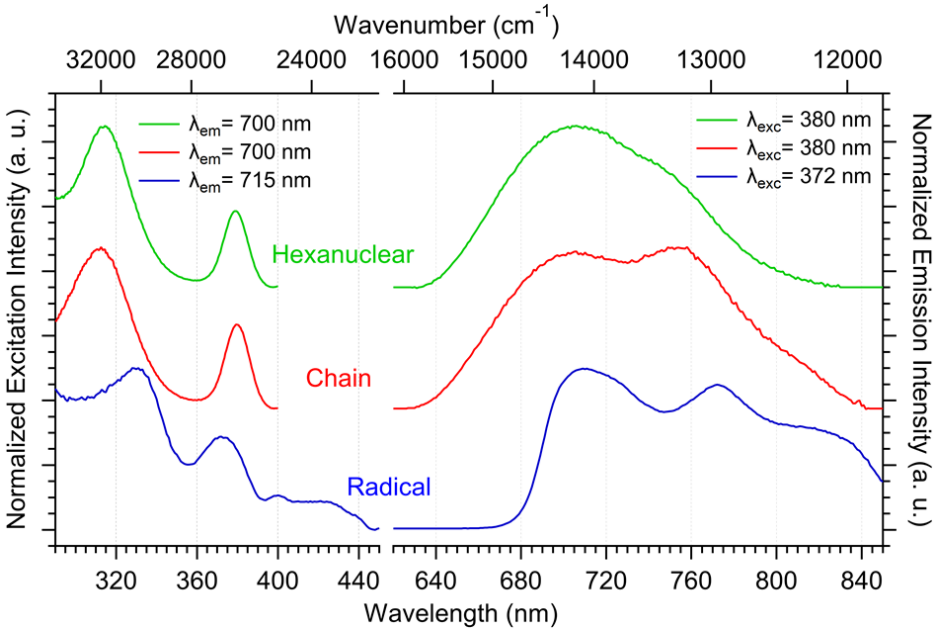

Figure 4.9. Normalised solid-state excitation and emission spectra at 77 K measured for the **hexanuclear**, the **chains** and the uncoordinated **NITPhOC$_6$** radical.

Finally, luminescent measurements were performed to probe to chemical purity of the **hexanuclear**, taking into account the considerations detailed in the previous chapter (see Part.3.3). The intense emission bands related to uncoordinated Tb^{III} complexes should not be observed, and the coordinated radical emission spectrum has to be blue-shifted by metal–ligand charge transfer compared to the coordinated one. These prerequisites are fulfilled regarding the luminescence spectra below, with no emission of the free Tb^{III} ion and a blue-shifted NIT radical emission (from 710 nm to 704 nm). In light of this, slight differences can be noticed compared to the **chain** one. **Hexanuclear** emission spectrum displays only one band with a peak at 704 nm and a small shoulder around 740 - 750 nm, the latter becoming more defined and centred around 755 nm by an increase of the temperature (Figure 4.A.22), probably due to the significant structural changes (packing, Tb^{III} coordination polyhedral, coordinated water molecules).

All these thermal and luminescent investigations unambiguously demonstrate that the **hexanuclears** are preserved upon crystal amorphisation, and that magnetic investigation can be trustily performed.

4.4. Magnetic properties

4.4.1. Static (DC) magnetic properties

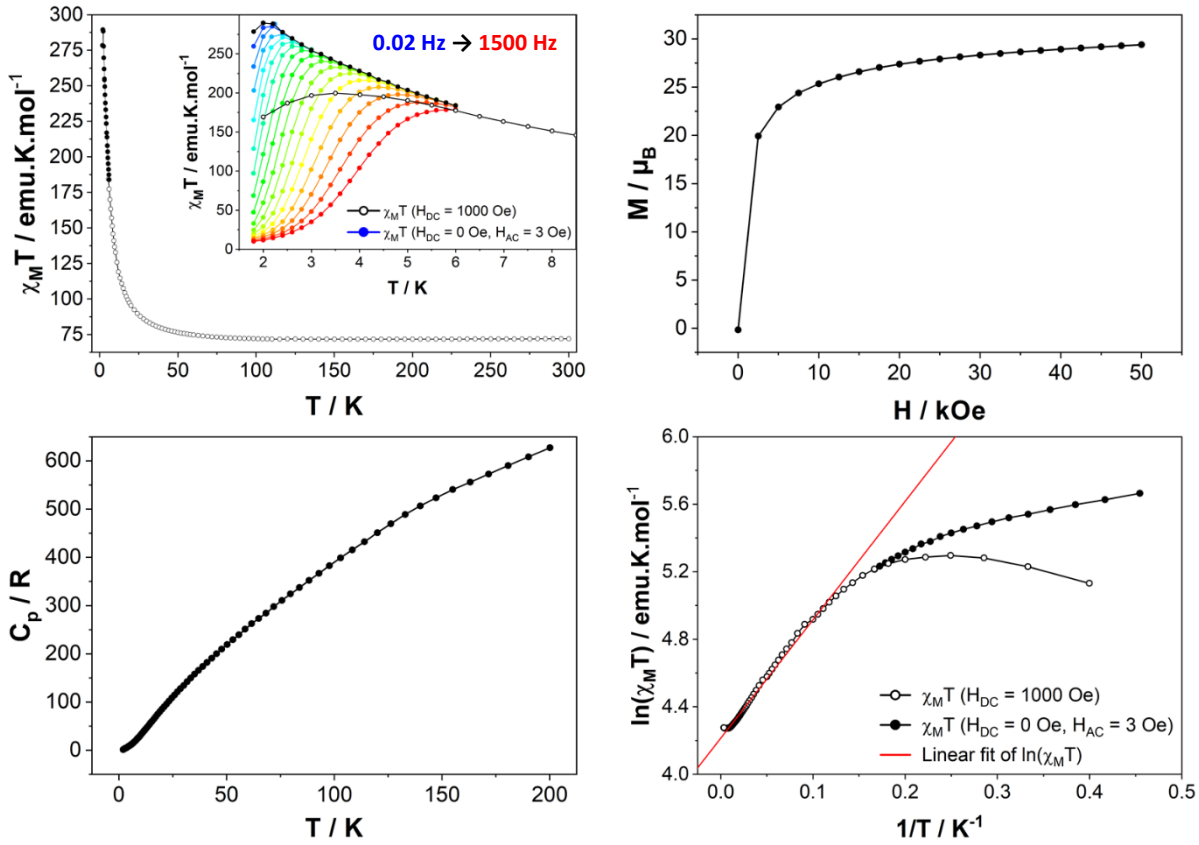

Figure 4.10. Top: Temperature dependence of $\chi_M T$ measured with H_{DC} = 1000 Oe (open circles) and reconstructed from AC measurements with H_{AC} = 3 Oe (filled dots) with in inset, a zoom in the low-temperature region with the AC data at different frequencies (left) and field dependence of magnetisation at 2 K (right). Bottom: Specific heat measurement (left) and reciprocal temperature dependence of ln($\chi_M T$), with best fit as a red line (right).

The temperature dependence of the magnetic susceptibility χ_M was measured on a polycrystalline sample under static field and show a $\chi_M T_{(300K)}$ value of 72.02 emu·K·mol^{-1}, close to the theoretical value $\chi_M T_{(300K)}$ = 72.795 emu·K·mol^{-1} expected for six Tb^{III} ions and five uncoupled NIT radicals. By decreasing the temperature, this value slightly increases until 50 K then sharply reaches a maximum of $\chi_M T_{(DC)}$ = 199.65 emu·K·mol^{-1} at 3.5 K. This increase is followed by an abrupt drop due to saturation effects, highlighted by $\chi_M T_{(AC)}$ values calculated from AC susceptibility measurement. Hence, a more reliable maximum of $\chi_M T_{(AC)}$ = 289.54 emu·K·mol^{-1} is observed at 2 K.

The saturation is also confirmed by the magnetisation curve recorded at 2 K that rises very quickly as a field is applied to reach a value of 29.4 μ_B at 50 kOe, slightly lower than the theoretical saturation value expected on a polycrystalline sample (M_s = 32.0 μ_B). Adding to this, specific heat (C_P) measurement does not stress any divergence of the specific heat capacity C_p up to 2 K in the low-temperature region, as it can be observed in the presence of long-range magnetic ordering. These preliminary results, akin to those reported for the previous helical **chain**, are compatible with a SCM behaviour.

Based on this assumption, the characteristic correlation energy Δ_ξ was extracted from the linear part of the exponential divergence of $\chi_M T$ product. This value was estimated at $\Delta_{\xi(dc)}$ = 6.9 ± 0.1 K (R^2 = 0.9984), comparable to the one observed on the **chain**'s derivative (5.5 ± 0.5 K), with an effective Curie constant C_{eff} = 66.86 emu·K·mol^{-1}. We performed diamagnetic doping of the **hexanuclears** by Y^{III} or Lu^{III} ions to evaluate the dimension of the correlation length statistically. At high doping levels, only needles were obtain, and SEM/EDS measurements showed signs of segregation between **hexanuclear** units made of Tb and others of Y/Lu ions at low doping levels. Consequently, this approach has been dismissed.

4.4.2. Theoretical description and magnetic coupling

As for the previous compound, this system was investigated by B. Le Guennic and F. Gendron (Chimie Théorique Inorganique group, ISCR) and divided into six simplified units with hexyl chains replaced by methyl groups, as [Tb(hfac)$_3$(NITPhOMe)$_2$] for the central Tb^{III} (labelled $[Tb(2)]^{2-}$, $[Tb(3)]^{2-}$, $[Tb(4)]^{2-}$ and $[Tb(5)]^{2-}$) and [Tb(hfac)$_3$(NITPhOMe)(H$_2$O)] for the terminal ones (or $[Tb(1).H_2O]^-$ and $[Tb(6).H_2O]^-$). Besides, to evaluate the presence of magnetic interactions between the consecutive **hexanuclears**, two dimer models were also investigated and are labelled $[Dimer\text{-}Tb(1)]^{2-}$ and $[Dimer\text{-}Tb(2)]^{2-}$, respectively.

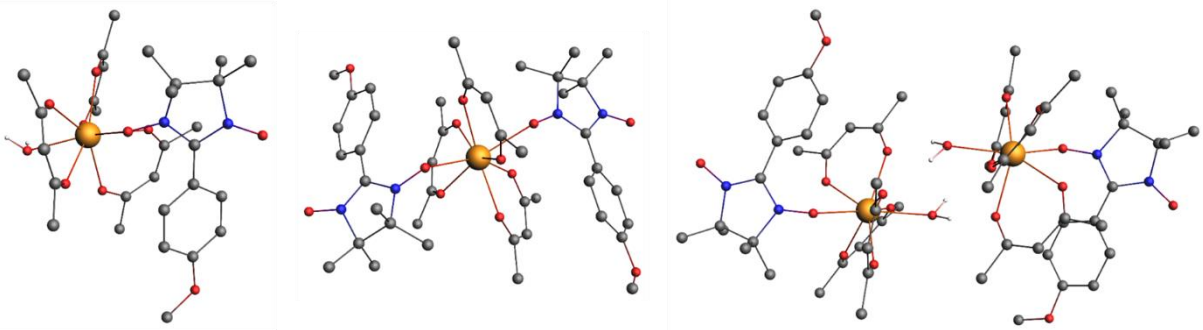

Figure 4.11. Model compounds for $[Tb(1)\text{-}NIT\text{-}H_2O]^-$ (left), $[Tb(2)\text{-}NIT_2]^{2-}$ (middle) and $[Dimer\text{-}Tb(1)]^{2-}$ (right).

In all model compounds, the ground state (GS) corresponds to a non-Kramers doublet that derives formally from the m_J states ± 6 of the $^7F_6$ level. More precisely, the nature of these states results from an admixture by the crystal-field of the different m_J states, described by the following wave-function:

$$|\psi_{GS}\rangle = a\,|6,\pm6\rangle + b|6,\pm5\rangle + c\,|6,\pm4\rangle + d\,|6,\pm3\rangle + e\,|6,\pm2\rangle + f\,|6,\pm1\rangle + g\,|6,0\rangle \quad \text{Eq. 4.1}$$

where $a^2 + b^2 + c^2 + d^2 + e^2 + f^2 + g^2 = 1$.

The calculated values of the square of these coefficients are given in Table 4.2. The $m_J = \pm 6$ state is the dominant contribution, but a sizable one is calculated from the $m_J = \pm 4$ state. Interestingly, the $m_J = \pm 6$ state's contribution to the GS wave function differs significantly between the six model compounds, in agreement with the small differences observed in the first coordination sphere of the Tb^{III} ions (Table 4.A.7). Hence, the $[Tb(2)]^{2-}$ model compound has the lowest $m_J = \pm 6$ contribution (76%) that goes along with the highest $m_J = \pm 4$ one (14%), contrasting with the opposite trend for the $[Tb(1).H_2O]^-$ model (91 % for the $m_J = \pm 6$ contribution and 6.4 % for the $m_J = \pm 4$ states).

Table 4.2. Calculated m_J contributions (in per-cent) associated with the GS wave-function for the six model compounds.

	|± 6>	**|± 5>**	**|± 4>**	**|± 3>**	**|± 2>**	**|± 1>**	**|0>**
[Tb(1)-NIT-H_2O]$^-$	90.7	0.0	6.4	0.6	2.0	0.0	0.3
[Tb(2)-NIT_2]$^{2-}$	76.3	5.8	14.7	1.6	0.8	0.2	0.6
[Tb(3)-NIT_2]$^{2-}$	84.4	2.4	10.5	0.8	1.4	0.4	0.1
[Tb(4)-NIT_2]$^{2-}$	90.0	0.2	7.5	0.2	1.4	0.4	0.3
[Tb(5)-NIT_2]$^{2-}$	88.8	0.2	8.6	0.2	1.4	0.4	0.4
[Tb(6)-NIT-H_2O]$^-$	87.0	0.0	8.4	0.2	3.4	0.0	1.0

The calculated relative energies of the states and the associated EPR *g*-factors (for the states exhibiting a pseudo-spin $S = ½$) are linked with the conclusions stated above. In $[Tb(2)]^{2-}$, a relatively small energy gap of 16 cm^{-1} is calculated between the GS and ES1, leading to the smallest value for the parallel component of the EPR *g*-factors ($g_{\parallel} = 16.58$) whereas this energy gap increases to 85 cm^{-1} for $[Tb(5).H_2O]^-$, with an EPR *g*-factor of 17.26.

The overall splitting of the $^7F_6$ level also differs between the six building blocks of the **hexanuclears**, with calculated splitting of 361 and 388 cm^{-1} for $[Tb(5).H_2O]^-$ and $[Tb(6).H_2O]^-$, respectively, whereas splitting of 431, 470, 486 and 527 cm^{-1}, are calculated for Tb(1), Tb(2), Tb(4), and Tb(3) respectively.

Table 4.3. Calculated relative energies (ΔE in cm^{-1}) and EPR *g*-factors for the lowest states deriving from the $^7F_6$ level of the Tb^{3+} ion in the six model compounds.

	[Tb(1).H_2O]$^-$			**[Tb(2)]$^{2-}$**			**[Tb(3)]$^{2-}$**		
	ΔE	**$g_{\parallel}$**	**$g_{\perp}$**	**ΔE**	**$g_{\parallel}$**	**$g_{\perp}$**	**ΔE**	**$g_{\parallel}$**	**$g_{\perp}$**
GS	0	17.26	0	0	16.58	0.00	0	16.99	0.00
ES1	85	12.62	0	20	17.51	0.00	16	16.64	0.00
ES2	133	-	-	61	11.92	0.00	66	11.39	0.00
ES3	183	10.27	0	100	-	-	105	-	-
ES4	231	15.35	0	159	10.01	0.00	165	10.13	0.00
ES5	287	13.59	0	217	13.40	0.00	282	13.63	0.00
ES6	361	16.32	0	431	17.08	0.00	470	17.24	0.00

	$[Tb(4)]^{2-}$			$[Tb(5)]^{2-}$			$[Tb(6).H_2O]^{-}$		
	ΔE	**$g_{\parallel}$**	**$g_{\perp}$**	**ΔE**	**$g_{\parallel}$**	**$g_{\perp}$**	**ΔE**	**$g_{\parallel}$**	**$g_{\perp}$**
GS	0	17.25	0.00	0	17.19	0.00	0	16.98	0.00
ES1	81	12.90	0.00	60	14.99	0.00	65	-	-
ES2	111	-	-	81	10.53	0.00	101	5.61	0.00
ES3	149	10.47	0.00	116	-	-	184	9.29	0.00
ES4	230	11.71	0.00	187	10.64	0.00	273	16.30	0.00
ES5	369	13.97	0.00	310	13.73	0.00	303	14.28	0.00
ES6	527	17.04	0.00	486	17.16	0.00	388	15.88	0.00

The orientation of the easy axes of the magnetisation for the *GS* of the six model compounds was determined and revealed different orientations. The GS of the model compounds exhibits sizeable magnetic anisotropy, characterised by extremely large parallel components of the EPR *g*-factors (*c.a.* 17) and perpendicular components equal to zero. For comparison, a pure $m_J = \pm 6$ state would possess a parallel component of 18.0.

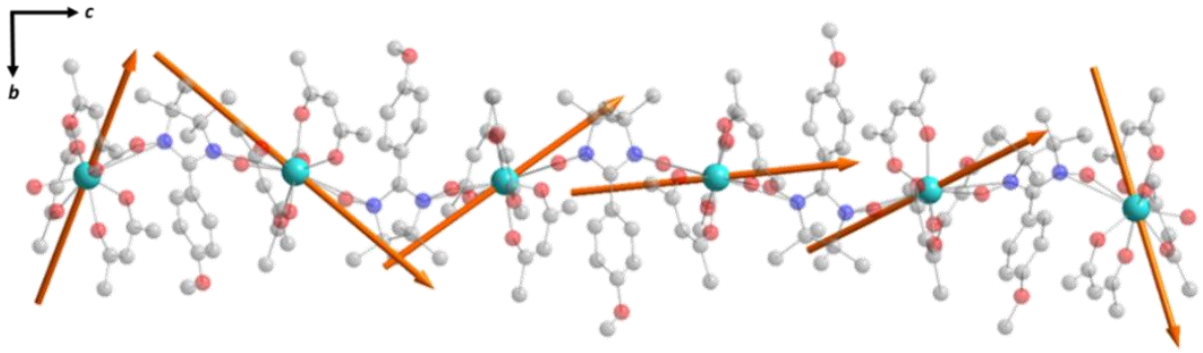

Figure 4.12. Representation of the easy axes of the magnetisation for the Tb^{III} ground state on the model compound of the **hexanuclear**.

For the central Tb^{III} units (Tb2, Tb3, Tb4, Tb5), the easy axis goes mostly along the NIT-Tb-NIT direction as observed on the **chains**. A very different scenario is observed for the terminal Tb1 and Tb6 atoms. As already observed by some of us on mononuclear molecules,[8] Tb1 and Tb6 magnetic axes are perpendicular to the Tb-O (water) direction and the plane of the water molecule. The coordinated water is the driving force for the localisation of the easy-magnetic axes.

The calculated magnetic susceptibilities and magnetisation for the six model compounds are shown in Figure 4.13. At room temperature, very similar $\chi_M T$ values of *c.a.* 11.6 emu·K·mol^{-1} are calculated for all complexes. Due to a non-magnetic ES1 in $[Tb(6).H_2O]^{-}$, the decrease in magnitude of $\chi_M T$ is stronger at very low temperature than in the other compounds. On the other hand, the presence of a very low lying ES1 in $[Tb(2)]^{2-}$ and $[Tb(3)]^{2-}$ leads to calculated magnetisations at 2 K that do not reach saturation at 5 Tesla, whereas for the other model compounds, the calculated magnetisations saturate at 4.5 μ_B.

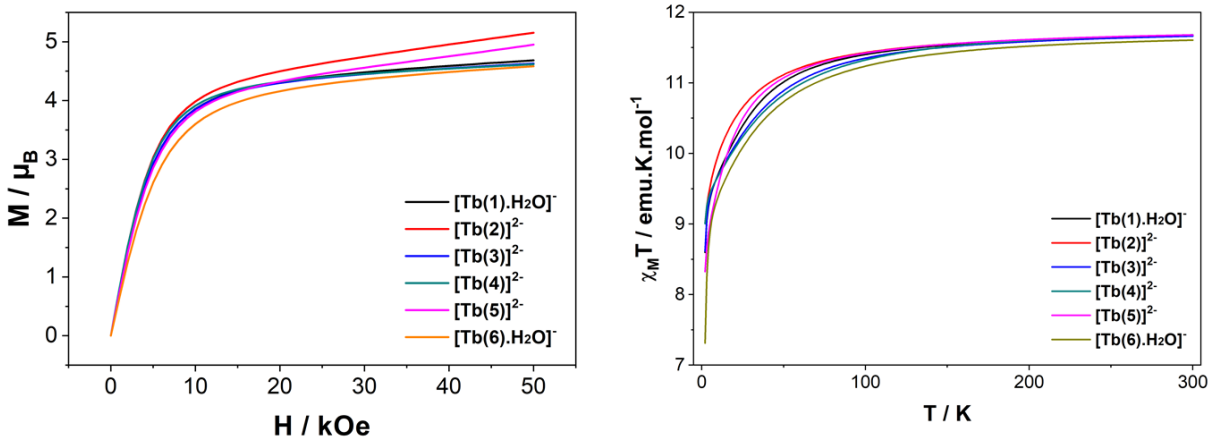

Figure 4.13. Isothermal field dependence of magnetisation at 2 K (left) and calculated temperature dependence of $\chi_M T$ (right) of the isolated models.

Unfortunately, because of the complexity of the structure, the same limiting factors as the ones faced for the **[Tb(hfac)$_3$(NITPhOC$_6$)]$_n$** apply to this **hexanuclear**: a large asymmetric unit with six non-equivalent Tb^{III} centres and the existence of numerous magnetic exchanges (NN and NNN). From the intermolecular point of view, two main interaction pathways can be considered: perpendicular or along the [502] direction. For the first case, the Tb-Tb distance is > 11 Å, so significant magnetic interaction can be discarded. For the second one, Tb-Tb distance is 6.05 Å and **hexanuclear** units are water bridged by the terminal water molecules.

Even if specific heat measurements demonstrate that no 3D magnetic ordering is observed, it is crucial to determine the nature and value of a potential interaction to assess if the compound behaves as an alternating chain of coupled **hexanuclear** units or **hexanuclears** more or less magnetically isolated.

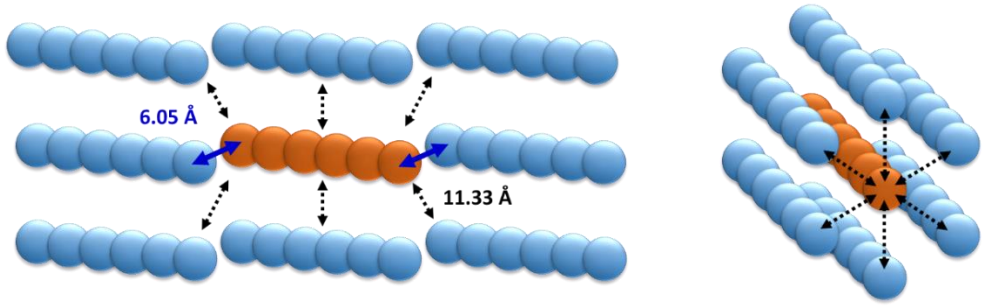

Figure 4.14. . Representation of the intermolecular magnetic interactions between a given **hexanuclear** (red) and its neighbours (blue) parallel or perpendicular to the [502] direction (interaction mediated via the water bridge as full blue arrows and through-space interactions as dotted black arrows).

We used the dimer model to calculate the magnetic susceptibility as a function of the temperature. At low temperature, the decrease of the $\chi_M T$ product is reinforced by a small intramolecular antiferromagnetic interaction between the two Tb^{III} ions. Magnetic exchange is neglected because of the large Tb-Tb distance, and the isotropic dipolar contribution of the AFM interaction is found of *c.a.* J_{inter} = - 0.11 cm^{-1}. This value can be readily understood by the almost collinear orientation of the easy magnetic axes.

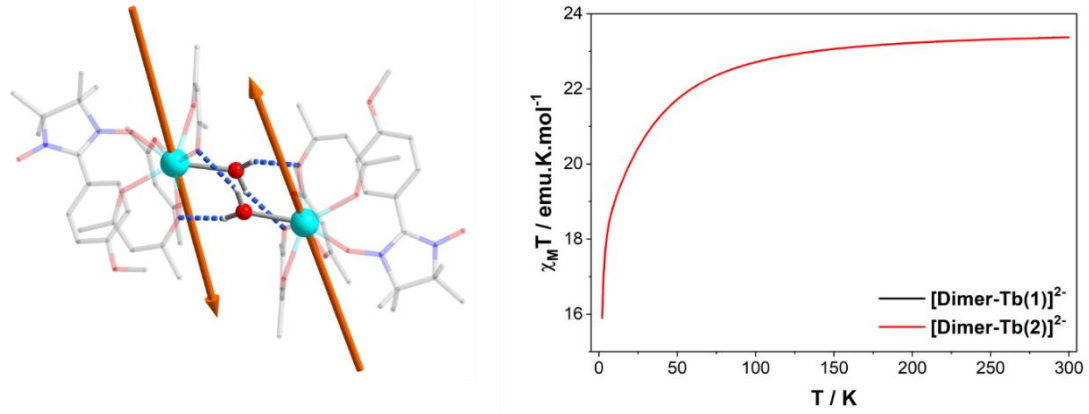

Figure 4.15. Representation of the easy axes of the magnetisation for the Tb^{III} ground state (left) and calculated temperature dependence of $\chi_M T$ (right) of the dimer model that simulates the extremities of the **hexanuclear**.

Hence, if supramolecular interactions are efficient to build SCMs based on 3*d* metal ions,[9,10] it is not the case with 4*f* ions because of the inner character of their orbitals. Accordingly, the very small dipolar coupling observed between Tb1 and Tb6 ions is unlikely to be strong enough to propagate a correlation length beyond the **hexanuclears** because it is several orders of magnitude smaller than the ones operating in the molecule as demonstrated on related NIT based compound. Accordingly, the divergence of the $\chi_M T$ at low temperature can be ascribed to the creation of a correlation length that is confined within each **hexanuclear**.

4.4.3. Dynamic (AC) magnetic properties

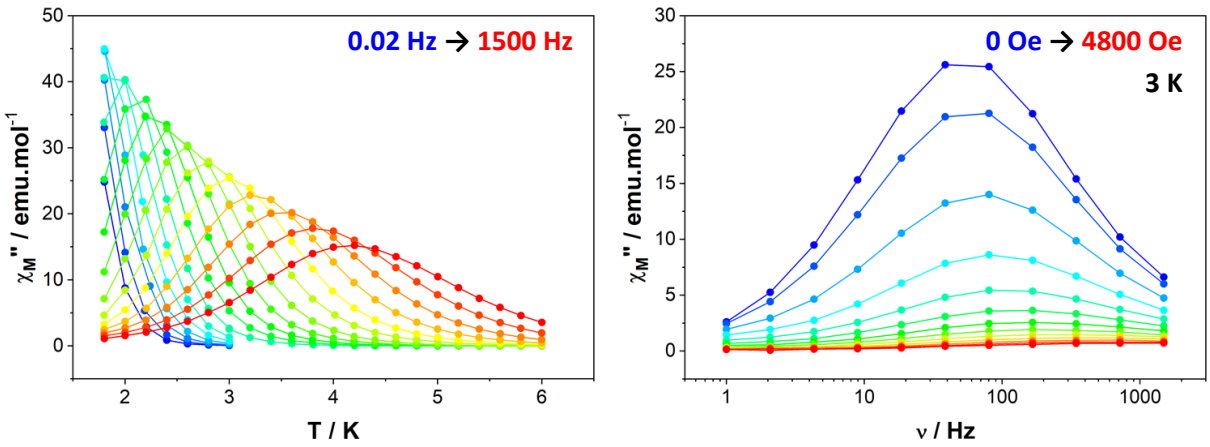

Figure 4.16. Top: Temperature (left) and field (right) dependencies of the out-of-phase (χ_M'') susceptibility of **hexanuclear**.

The comparison between the dynamic magnetic behaviour of the helical **chain** and the **hexanuclear** stresses the parallelism of the two structures from a magnetic point of view. Indeed, the same trends are observed for the temperature dependence of the out-of-phase susceptibility as depicted above, arguing for a slow relaxation of the magnetisation and the decrease of the signal magnitude with under static DC field.

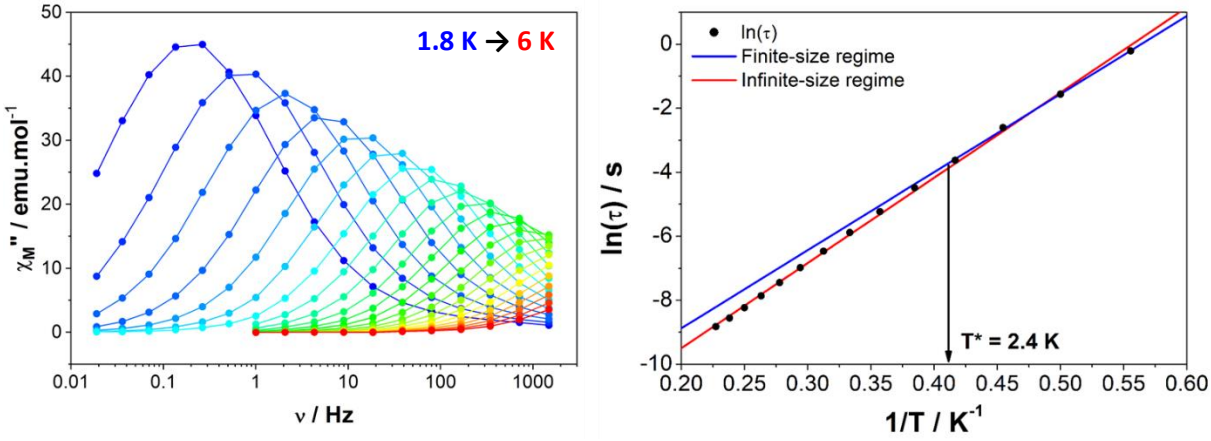

Figure 4.17. Frequency dependence of the out-of-phase susceptibility (left) and the resulting Arrhenius plot of the extracted relaxation times (right) of **hexanuclear**.

The out-of-phase susceptibility χ_M'' shows frequency dependence up to 6 K also, characteristic of slow relaxation of the magnetisation with no broadening as one would observe if the six crystallographically independent Tb^{III} ions were not correlated enough and relaxed independently.

The fitting of the relaxation times τ on the resulting Arrhenius diagram allowed to differentiate the two distinct relaxation processes, compatible with the finite and infinite regimes, whose respective values are Δ_F/k_B = 24.4 ± 0.5 K with τ_F = (1.1 ± 0.2) x 10^{-6} s (R^2 = 0.9988) and Δ_I/k_B = 27.8 ± 0.1 K with τ_I = (2.6 ± 0.1) x 10^{-7} s (R^2 = 0.9999), with a crossover temperature of T^* = 2.4 K. As for the chain, this fitting as to be performed very carefully.

The associated correlation energy $\Delta_{\xi(AC)} = \Delta_I - \Delta_F$ = 3.4 ± 0.6 K is in line with the **chain**' one ($\Delta_{\xi(AC)}$ = 4.1 ± 0.7 K), as expected according to the resemblance of the two systems. The estimated number of correlated units n is included between 3 and 5. It is then clear from these magnetic measurements that the **hexanuclears**, despite being finite molecules, behave as SCM because they are molecules longer than the correlation length Δ_ξ they are hosting.

Interestingly, this difference between molecule length and correlation length is big enough to allow the observation of finite and infinite relaxation regimes in the **hexanuclears**. This shows that spin reversal can occur at an extremity of the molecule (finite regime) and in a central position (infinite regime).

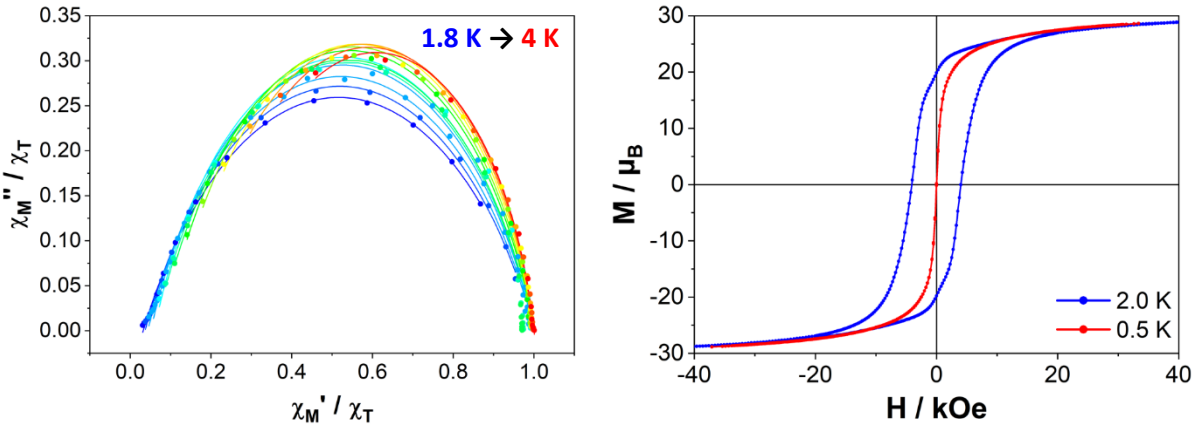

Figure 4.18. Normalised Argand diagram (solid lines represent the best fits with an extended Debye model) (left) and magnetic hysteresis curves of **hexanuclear** measured at 2 K and 0.5 K, with a magnetic field sweep rate of 15.5 Oe·s^{-1} (right).

Only one semi-circle is observed on the Argand diagram above, ruling out the possibility of an SMM behaviour as several relaxations should be observed because the six Tb^{III} ions show different crystal-field splitting and different m_J contributions to the ground-state wave-function (Table 4.2-Table **4.3**). Surprisingly, a lower distribution α of the relaxation times is observed for the **hexanuclear** at 1.8 K than for the **chain** (0.37 *vs* 0.61), highlighting a better collective relaxation behaviour for the finite complex, both samples relaxing quantitatively (97% in this case) at this temperature.

This improvement can also be noted on the magnetic hysteresis curve recorded at low temperature by operating at the same experimental conditions (magnetic field sweep rate of 15.5 Oe·s^{-1} and 0.5 K). Indeed, the coercive field is almost doubled if one compares with the previous **chain** (4100 Oe *vs* 2400 Oe) and the remanent magnetisation (M_R = 19.83 μ_B), which correspond to 62% of the magnetic saturation.

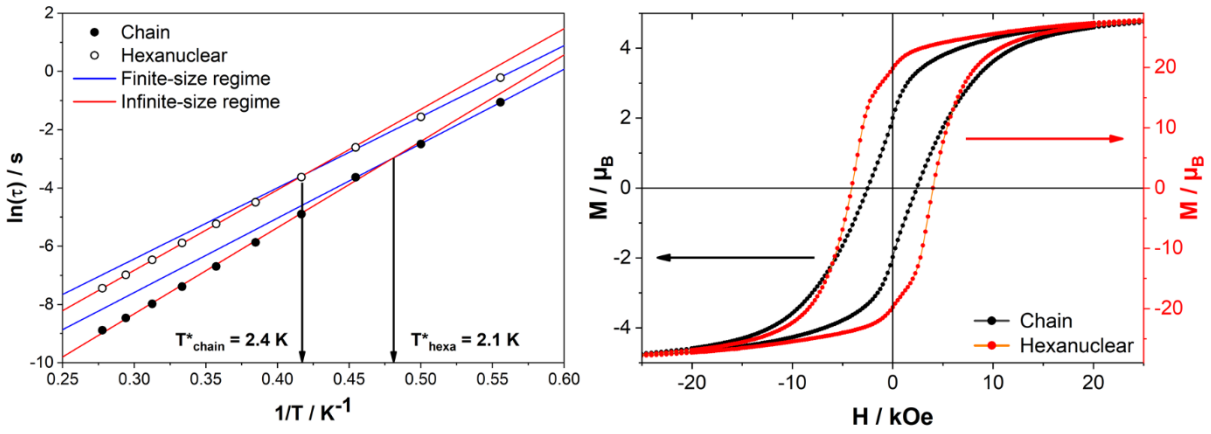

Figure 4.19. Comparison of the Arrhenius plots (left) and the magnetic hysteresis loops (right) between the **chain** and the **hexanuclear**.

Hexanuclears show an enhanced SCM behaviour when compared to **chains**. Indeed, they show a magnetic hysteresis that is steeper with H_C and M_R values almost doubled. A dynamic magnetic relaxation with similar activation energies but slower relaxation times is also observed. The reason for this optimised magnetic behaviour could reside in the quality of the intramolecular magnetic coupling between **chains** and **hexanuclears** because Tb^{III} magnetic anisotropies are almost similar between **chains** and **hexanuclears**. **Chains** are infinitely curled molecules, while **hexanuclears** form linear arrangements of finite molecules. This second arrangement could favour an efficient overlap of magnetic orbitals in the **hexanuclears**.

Table 4.4. Summary of the principal magnetic values for **chains** and **hexanuclear**.

	Chains	**Hexanuclears**
$\Delta_{\xi(dc)}$ **(K)**	5.5 ± 0.5	6.9 ± 0.1
Δ_I/k_B **(K) /** τ_I **(s)**	29.6 ± 0.5 / 3.4 ± 0.5 x10^{-8}	27.7 ± 0.1 / 2.7 ± 0.1 x10^{-7}
Δ_F/k_B **(K) /** τ_F **(s)**	25.5 ± 0.2 / 2.4 ± 0.3 x10^{-7}	24.4 ± 0.5 / 1.1 ± 0.2 x10^{-6}
$\Delta_{\xi(ac)}$ **(K)**	4.1 ± 0.7	3.3 ± 0.6
T^* **(K)**	2.1	2.4
n **(DC ; AC)**	17 ; 5 - 10	18 ; 3 - 5
α **(at 1.8 K)**	0.615	0.374
H_C **(Oe)**	2400	4100
M_R **(**μ_B **/ %**M_{sat}**)**	2.09 / 38%	19.83 / 62%
T_B **(K)**	1.39 ± 0.02	1.34 ± 0.03

4.5. Conclusion

In this chapter, we have reported an extensive investigation of what was a randomly appearing by-product of molecular **chains** and its rational synthesis into stable and pure batches of linear hexanuclear molecules. Its formation is triggered by moisture conditions and the so-called **hexanuclear** shows a SCM behaviour. Indeed, we demonstrated that a finite linear molecule could behave as a SCM if its length is big enough compared to its magnetic correlation length. Additionally, by comparing the **hexanuclears** with their previously reported infinite counterparts, the **chains**, we show that the SCM behaviour is enhanced in the former. This finding is important in the search for temperature and air-stable molecules for new molecular data storage devices.

Indeed, the **hexanuclears** are promising candidates for surface deposition because they combine good chemical stability with a SCM magnetic relaxation. More importantly, such finite molecules should be far simpler to deposit on surfaces than insoluble polymeric chains, which would require their partial destruction to form finite objects with large and uncontrolled length distribution. On the contrary, the use of **hexanuclear**s could be a way to form deposits of monodisperse SCM and enhance their ability to self-organise on the surface (its supramolecular arrangement due to the water molecules being not so different from that of the **[Tb(hfac)$_3$·2H$_2$O]** previously described).

4.6. References

[1] A. L. Spek, *Acta Crystallogr. Sect. C Struct. Chem.* **2015**, *71*, 9–18.

[2] I. Y. Bagryanskaya, L. V. Politanskaya, E. V. Tretyakov, *Inorg. Chem. Commun.* **2016**, *66*, 47–50.

[3] Q. Evrard, G. Cucinotta, F. Houard, G. Calvez, Y. Suffren, C. Daiguebonne, O. Guillou, A. Caneschi, M. Mannini, K. Bernot, *Beilstein J. Nanotechnol.* **2019**, *10*, 2440–2448.

[4] A. Caneschi, D. Gatteschi, J. Laugier, P. Rey, R. Sessoli, C. Zanchini, *J. Am. Chem. Soc.* **1988**, *110*, 2795–2799.

[5] J. Omata, T. Ishida, D. Hashizume, F. Iwasaki, T. Nogami, *Inorg. Chem.* **2001**, *40*, 3954–3958.

[6] G. A. Timco, T. B. Faust, F. Tuna, R. E. P. Winpenny, *Chem. Soc. Rev.* **2011**, *40*, 3067.

[7] G. F. S. Whitehead, F. Moro, G. A. Timco, W. Wernsdorfer, S. J. Teat, R. E. P. Winpenny, *Angew. Chem.* **2013**, *125*, 10116–10119.

[8] G. Cucinotta, M. Perfetti, J. Luzon, M. Etienne, P.-E. Car, A. Caneschi, G. Calvez, K. Bernot, R. Sessoli, *Angew. Chem. Int. Ed.* **2012**, *51*, 1606–1610.

[9] M. Ferbinteanu, H. Miyasaka, W. Wernsdorfer, K. Nakata, K. Sugiura, M. Yamashita, C. Coulon, R. Clérac, *J. Am. Chem. Soc.* **2005**, *127*, 3090–3099.

[10] M. Ding, B. Wang, Z. Wang, J. Zhang, O. Fuhr, D. Fenske, S. Gao, *Chem. - Eur. J.* **2012**, *18*, 915–924.

4.A. Appendices

4.A.1. Synthesis and crystal structure

4.A.1.1. Synthesis of $[(Tb(hfac)_3)_6(NITPhOC_6)_5(H_2O)_2]\cdot CHCl_3.C_7H_{16}$, "hexanuclears"

0.05 mmol (40.8 mg, 1eq.) of $[Tb(hfac)_3\cdot 2H_2O]$ was dissolved in 40 mL of dry boiling *n*-heptane. The solution was concentrated until the volume reaches 10 mL, then cooled to 75°C. 0.05 mmol (16.7 mg, 1eq.) of $NITPhOC_6$ dissolved in $CHCl_3$ (7 mL) was slowly added under stirring, and the solution was cooled to room temperature. The final solution was filtered and kept under evaporation in a sealed dessicator whose bottom was filled with a layer of water, giving green platelets after few days. Yield: 42%.

Elemental analysis (%) calcd. for $Tb_6C_{193}H_{184}N_{10}O_{53}F_{108}Cl_3$: C 35.10; H 2.81; N 2.12. Found: C 37.42; H 3.11; N 2.63.

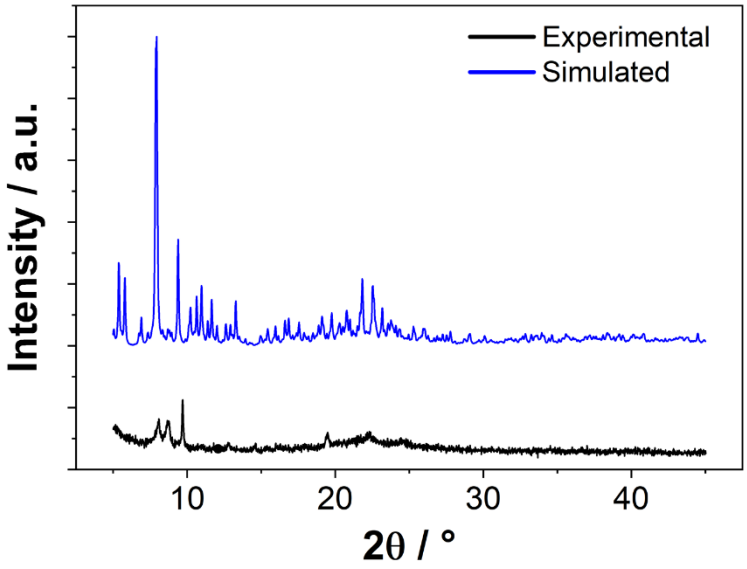

Figure 4.A.20. Powder X-Ray diffraction pattern of experimental and simulated **hexanuclear**.

Table 4.A.5. Selected bond distances (Å) for **hexanuclear**.

Tb1		Tb2		Tb3	
Tb1-O1	2.407	Tb2-O10	2.401	Tb3-O19	2.364
Tb1-O2	2.380	Tb2-O11	2.365	Tb3-O20	2.346
Tb1-O3	2.349	Tb2-O12	2.344	Tb3-O21	2.362
Tb1-O4	2.337	Tb2-O13	2.340	Tb3-O22	2.363
Tb1-O5	2.338	Tb2-O14	2.366	Tb3-O23	2.331
Tb1-O6	2.356	Tb2-O15	2.384	Tb3-O24	2.343
Tb1-O7	2.386	Tb2-O16	2.346	Tb3-O25	2.345
Tb1-O8	2.371	Tb2-O17	2.389	Tb3-O26	2.379

Tb4		Tb5		Tb6	
Tb4-O28	2.371	Tb5-O37	2.374	Tb6-O46	2.391
Tb4-O29	2.367	Tb5-O38	2.329	Tb6-O47	2.360
Tb4-O30	2.364	Tb5-O39	2.347	Tb6-O48	2.395
Tb4-O31	2.365	Tb5-O40	2.376	Tb6-O49	2.371
Tb4-O32	2.325	Tb5-O41	2.338	Tb6-O50	2.350
Tb4-O33	2.373	Tb5-O42	2.359	Tb6-O51	2.325
Tb4-O34	2.345	Tb5-O43	2.363	Tb6-O52	2.357
Tb4-O35	2.388	Tb5-O44	2.385	Tb6-O53	2.411

Table 4.A.6. Selected and angles (°) for **hexanuclear**.

Tb1		Tb2		Tb3	
O1-Tb1-O2	74.34	O10-Tb2-O11	149.75	O19-Tb3-O20	103.15
O1-Tb1-O3	78.59	O10-Tb2-O12	87.47	O19-Tb3-O21	74.65
O1-Tb1-O4	107.74	O10-Tb2-O13	72.03	O19-Tb3-O22	149.27
O1-Tb1-O5	70.79	O10-Tb2-O14	71.91	O19-Tb3-O23	91.74
O1-Tb1-O6	142.64	O10-Tb2-O15	73.22	O19-Tb3-O24	73.56
O1-Tb1-O7	82.14	O10-Tb2-O16	106.43	O19-Tb3-O25	72.88
O1-Tb1-O8	142.63	O10-Tb2-O17	135.77	O19-Tb3-O26	137.53
O2-Tb1-O3	72.29	O11-Tb2-O12	72.77	O20-Tb3-O21	72.60
O2-Tb1-O4	145.18	O11-Tb2-O13	122.89	O20-Tb3-O22	75.39
O2-Tb1-O5	135.89	O11-Tb2-O14	135.09	O20-Tb3-O23	139.08
O2-Tb1-O6	124.44	O11-Tb2-O15	78.91	O20-Tb3-O24	147.26
O2-Tb1-O7	75.64	O11-Tb2-O16	75.15	O20-Tb3-O25	74.55
O2-Tb1-O8	72.90	O11-Tb2-O17	73.94	O20-Tb3-O26	93.02
O3-Tb1-O4	74.15	O12-Tb2-O13	76.74	O21-Tb3-O22	75.74
O3-Tb1-O5	124.40	O12-Tb2-O14	147.80	O21-Tb3-O23	75.14
O3-Tb1-O6	135.28	O12-Tb2-O15	72.05	O21-Tb3-O24	133.94
O3-Tb1-O7	145.97	O12-Tb2-O16	135.45	O21-Tb3-O25	126.21
O3-Tb1-O8	74.75	O12-Tb2-O17	111.46	O21-Tb3-O26	147.73
O4-Tb1-O5	72.75	O13-Tb2-O14	73.53	O22-Tb3-O23	72.79
O4-Tb1-O6	75.73	O13-Tb2-O15	133.68	O22-Tb3-O24	124.06
O4-Tb1-O7	139.03	O13-Tb2-O16	147.71	O22-Tb3-O25	133.32
O4-Tb1-O8	89.66	O13-Tb2-O17	74.12	O22-Tb3-O26	72.66
O5-Tb1-O6	75.21	O14-Tb2-O15	122.15	O23-Tb3-O24	73.43
O5-Tb1-O7	73.60	O14-Tb2-O16	75.45	O23-Tb3-O25	146.23
O5-Tb1-O8	146.53	O14-Tb2-O17	71.80	O23-Tb3-O26	101.27
O6-Tb1-O7	73.74	O15-Tb2-O16	72.09	O24-Tb3-O25	73.41
O6-Tb1-O8	72.90	O15-Tb2-O17	149.67	O24-Tb3-O26	71.90
O7-Tb1-O8	106.37	O16-Tb2-O17	87.82	O25-Tb3-O26	74.16
Tb4		**Tb5**		**Tb6**	
O28-Tb4-O29	74.73	O37-Tb5-O38	105.53	O46-Tb6-O47	75.74
O28-Tb4-O30	71.52	O37-Tb5-O39	73.49	O46-Tb6-O48	72.17
O28-Tb4-O31	148.37	O37-Tb5-O40	148.62	O46-Tb6-O49	109.58
O28-Tb4-O32	93.83	O37-Tb5-O41	91.23	O46-Tb6-O50	73.72
O28-Tb4-O33	72.72	O37-Tb5-O42	71.64	O46-Tb6-O51	83.93
O28-Tb4-O34	104.02	O37-Tb5-O43	73.95	O46-Tb6-O52	143.79
O28-Tb4-O35	137.25	O37-Tb5-O44	136.99	O46-Tb6-O53	145.75
O29-Tb4-O30	73.02	O38-Tb5-O39	73.69	O47-Tb6-O48	71.72
O29-Tb4-O31	125.07	O38-Tb5-O40	73.50	O47-Tb6-O49	143.88
O29-Tb4-O32	73.22	O38-Tb5-O41	138.28	O47-Tb6-O50	138.59
O29-Tb4-O33	133.82	O38-Tb5-O42	73.32	O47-Tb6-O51	72.21
O29-Tb4-O34	147.24	O38-Tb5-O43	145.17	O47-Tb6-O52	120.19
O29-Tb4-O35	70.56	O38-Tb5-O44	89.11	O47-Tb6-O53	80.60
O30-Tb4-O31	134.24	O39-Tb5-O40	76.33	O48-Tb6-O49	76.12

O30-Tb4-O32	145.70	O39-Tb5-O41	75.10	O48-Tb6-O50	122.73
O30-Tb4-O33	124.16	O39-Tb5-O42	122.32	O48-Tb6-O51	140.52
O30-Tb4-O34	75.61	O39-Tb5-O43	135.31	O48-Tb6-O52	141.67
O30-Tb4-O35	75.04	O39-Tb5-O44	149.00	O48-Tb6-O53	77.12
O31-Tb4-O32	72.58	O40-Tb5-O41	72.74	O49-Tb6-O50	73.88
O31-Tb4-O33	76.41	O40-Tb5-O42	134.08	O49-Tb6-O51	142.76
O31-Tb4-O34	72.88	O40-Tb5-O43	125.06	O49-Tb6-O52	77.37
O31-Tb4-O35	74.08	O40-Tb5-O44	74.09	O49-Tb6-O53	76.58
O32-Tb4-O33	77.22	O41-Tb5-O42	148.14	O50-Tb6-O51	77.33
O32-Tb4-O34	138.68	O41-Tb5-O43	75.86	O50-Tb6-O52	74.53
O32-Tb4-O35	99.20	O41-Tb5-O44	104.36	O50-Tb6-O53	137.84
O33-Tb4-O34	73.22	O42-Tb5-O43	73.68	O51-Tb6-O52	72.52
O33-Tb4-O35	149.91	O42-Tb5-O44	74.54	O51-Tb6-O53	112.00
O34-Tb4-O35	92.47	O43-Tb5-O44	71.60	O52-Tb6-O53	70.14

Table 4.A.7. Continuous Shape Measurements (CShM)[11] for **hexanuclear**.

Coordination geometry (site symmetry)	Square antiprism (D_{4d})	Triangular dodecahedron (D_{2d})	Bi-augmented trigonal prism (C_{2v})
Tb1 CShM	0.841	0.777	1.795
Tb2 CShM	0.891	0.825	1.883
Tb3 CShM	1.577	0.234	2.076
Tb4 CShM	1.673	0.265	1.914
Tb5 CShM	1.173	0.460	1.973
Tb6 CShM	0.412	1.775	1.761

[11] M. Llunell, D. Casanova, J. Cirera, P. Alemany, S. Alvarez, *SHAPE*, **2010**.

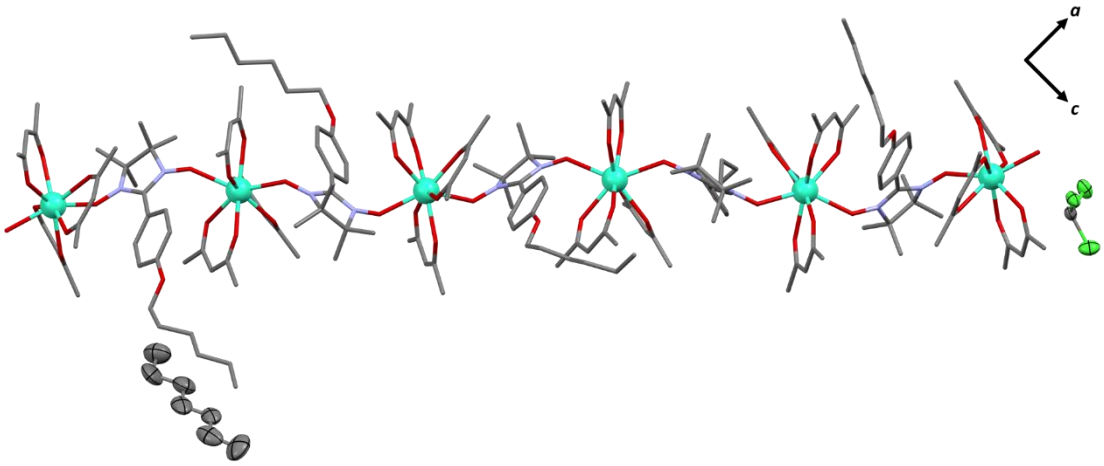

Figure 4.A.21. Representations of the asymmetric unit of the **hexanuclear** along the *b*-axis including the heptane and chloroform crystallisation solvents represented with their thermal ellipsoids (hydrogen and fluorine atoms omitted for clarity).

4.A.2. Stability: thermal and luminescent measurements

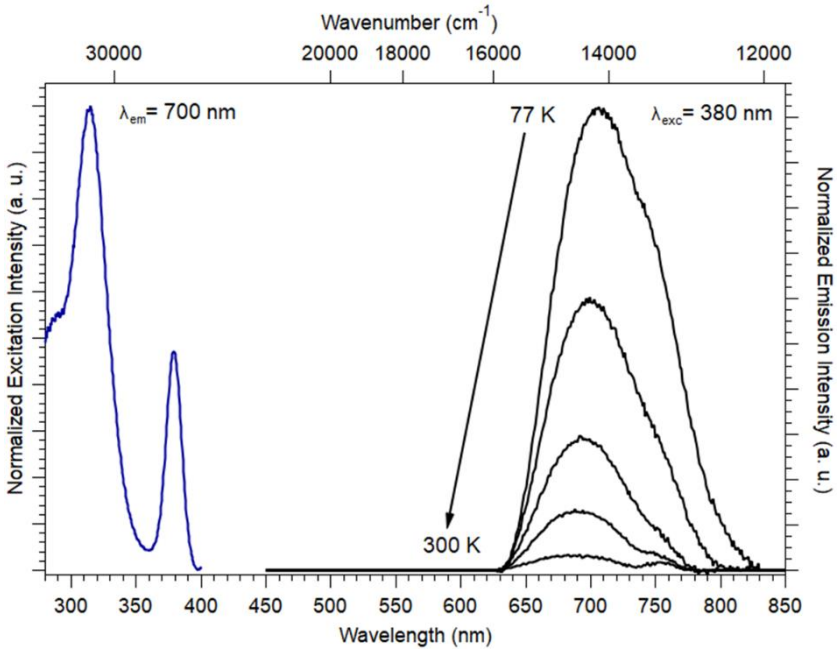

Figure 4.A.22. Solid excitation spectrum at 77 K (λ_{em} = 700 nm), and emission spectra (λ_{ex} = 380 nm) between 77 and 300 K of **hexanuclear**. The emission data are adequately corrected by eliminating the additional emission from the holder used for the measurement (quartz cuvette).

4.A.3. Magnetic properties

4.A.3.1. Dynamic (AC) magnetic properties

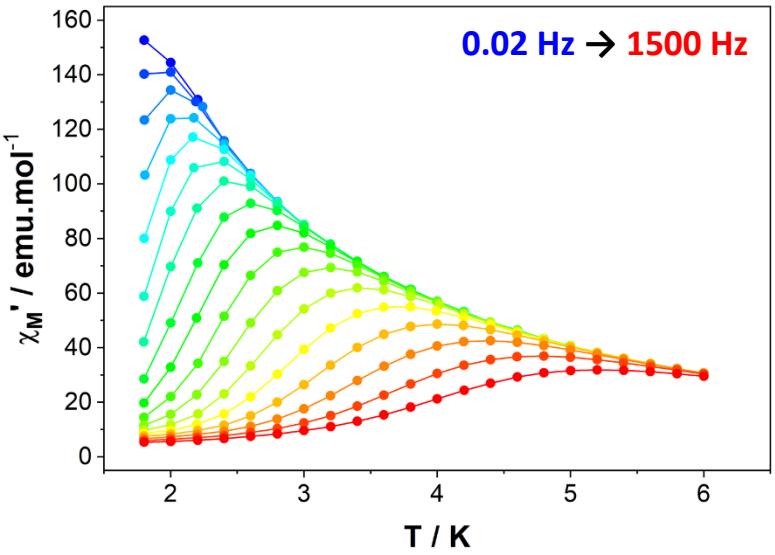

Figure 4.A.23. Temperature dependence of the in-phase (χ_M') susceptibility of **hexanuclear** at various frequencies.

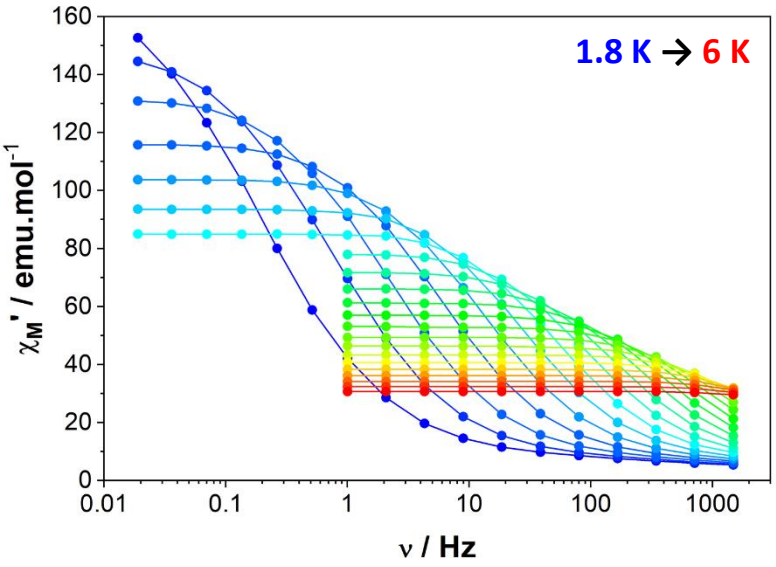

Figure 4.A.24. Frequency dependence of the in-phase (χ_M') susceptibility of **hexanuclear** at various temperatures.

Table 4.A.8. Relaxation times extracted for **hexanuclear**.

T (K)	τ (μs)	R^2	*T* (K)	τ (μs)	R^2
1.8	811019	0.9993	**3.2**	1560	0.9955
2	210663	0.9984	**3.4**	929	0.9958
2.2	73890	0.9967	**3.6**	584	0.9963
2.4	26636	0.9963	**3.8**	384	0.9968
2.6	11276	0.9963	**4.0**	266	0.9975
2.8	5340	0.9961	**4.2**	192	0.9980
3	2781	0.9968	**4.4**	147	0.9986

Table 4.A.9. Adiabatic (χ_S), isothermal (χ_T) susceptibility values and relaxation times distribution (α) extracted for **hexanuclear**.

T (K)	χ_S	χ_T	α	R^2
1.8	5.59	176.00	0.374	0.9982
2.0	5.52	151.47	0.346	0.9977
2.2	5.70	133.77	0.321	0.9946
2.4	5.88	117.29	0.292	0.9895
2.6	6.14	104.68	0.270	0.9874
2.8	5.90	96.08	0.278	0.9937
3.0	6.10	87.56	0.268	0.9971
3.2	6.81	79.09	0.238	0.9905
3.4	7.46	72.36	0.219	0.9900
3.6	8.34	66.53	0.199	0.9900
3.8	9.29	61.51	0.181	0.9934
4.0	10.35	57.13	0.165	0.9951

Chapter 5. Magnetic Metallogels of Supramolecular Nanotubes

5.1. Introduction

The strategy adopted so far relies on the alkyl group carried by the NIT radical, to induce flexibility in the molecular edifices, and obtain new supramolecular crystalline arrangements. In this chapter, we investigate the influence of the size of this aliphatic chain by synthesising two novel NIT radicals, the **NITPhOC$_{10}$** and **NITPhOC$_{18}$**, to modulate the diameter of the nanotubes and its crystallinity. It could also be a way to obtain new supramolecular arrangements of SCMs.

Such an approach has already been used to obtain coordination molecular compounds in the gel state: the coordinated metal ion act here as a node, and the organic ligands form supramolecular structures through weak non-covalent interactions.[1,2] These "metallogels" present both the advantages of gels and coordination compounds: they are easy to shape (which is particularly appealing for surface deposition) and can feature the properties inherent to the metal ion used (redox activity, thermo- or photochromism, luminescence, *etc.*).[3]

Curiously, few studies have been carried out in order to synthesise metallogels with magnetic properties, except for some examples of spin-crossover gels based on 3*d*-alkylated triazole derivatives with thermochromic properties.[4–7] As for the 4*f* ions, they are mainly used for their luminescence properties,[8–14] despite their apparent predisposition to make magnetic molecular materials.

In this chapter, we describe a procedure to obtain metallogels **TbC$_n$** (from **Tb(hfac)$_3$** and **NITPhOC$_n$** (with n = 6, 10, 18). The gelation properties are determined, as well as their magnetic properties. Thanks to Small Angle X-ray Spectroscopy (SAXS) measurements, a 3D structural model is proposed and validated by surface studies.

5.2. Synthesis and gelation properties

Several in-lab observations of soft and translucent amorphous phases, similar to a gel, have caught our attention during the crystallisation step of compounds described in the previous chapters. Indeed, its light cyan colour, identical to the one observed for the crystalline coordination chains and the hexanuclear complexes, seemed to indicate a similar coordination phenomenon between the **Tb(hfac)$_3$** and the **NITPhOC$_6$**.

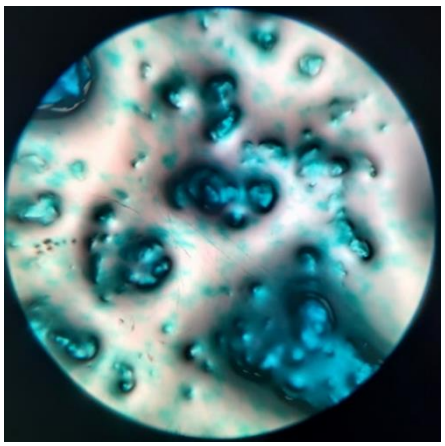

Figure 5.1. Amorphous phase observed under optical microscope (x63 magnification).

Therefore, we have compared the FTIR spectrum of this gel with those reported in the previous chapters, *i.e.*, the **chain** and the **hexanuclear** complex, which show strong correspondences that could result from a similar coordination arrangement (see Figure 5.2).

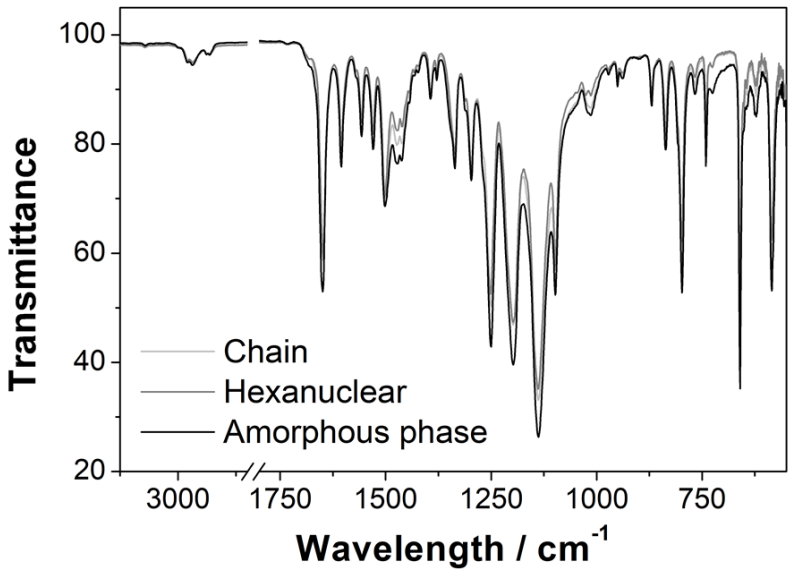

Figure 5.2. Amorphous phase observed under optical microscope (x63 magnification, left) and comparative FTIR spectra of the **chain** and the **hexanuclear** complex with the amorphous phase (right).

Considering no trend has been determined according to external atmospheric factors (temperature, humidity) in the observation of this soft matter, we first tried to obtain it by heating an equimolar amount of Tb^{III} complex and NIT radical in a small volume of *n*-heptane, unsuccessfully leading to the characteristic NIT blue solution once cooled. Therefore, we assumed then that these unfruitful attempts were due to the need for azeotropic removal of the filling water molecules of **[Tb(hfac)$_3$·2H$_2$O]** in boiling *n*-heptane, mandatory for its coordination with NIT radicals.

Following this hypothesis, we applied the usual protocol for crystallogenesis of crystalline counterparts but directly followed by solvent removal under reduced pressure (detailed protocol in Part.5.A.1). This additional step allowed the solution to thicken gradually and to turn from blue to cyan until its complete drying, giving a dark cyan powder, and latterly called **precursor**.

The chemical purity of this powder was probed by luminescence measurements. We recall that the presence of uncoordinated reactants is characterised by observations of a shift for the emission band of the NIT radical and well-defined line-shape bands from the Tb^{III} complex. Hence, the observation of such emission bands at 487, 542, 586, 617 and 650 nm on the luminescent spectra of the solid precursor indicates that a fraction of uncoordinated Tb reactant was still present.

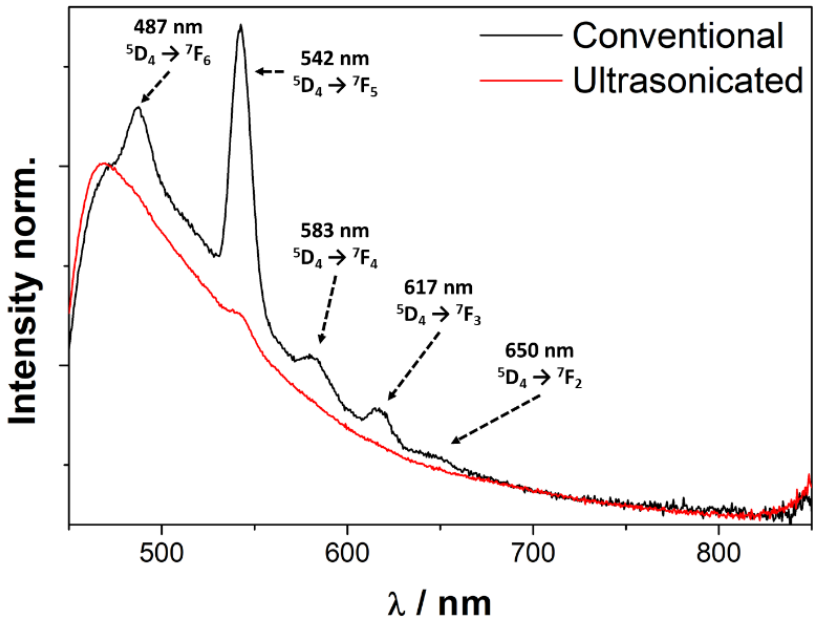

Figure 5.3. Solid-emission spectra (λ_{ex} = 300 nm) at 300 K of non-sonicated ("conventional") and "ultrasonicated" samples of **TbC$_6$ precursor**.

To tackle this, we have added a sonication step to induce a more effective micromixing by ultrasonication before the solvent removal. As demonstrated before in Chapter 2 on a close Tb-NIT radical SCM (the **[Tb(hfac)$_3$(NITPhOPh)]$_n$**),[15] this approach is relevant to prevent the formation of unreacted Tb(hfac)$_3$ particles. Hence, the comparison between the non-sonicated (or "conventional") and the ultrasonicated emission spectra shows a substantial decrease of the main Tb^{III} band intensities, testifying to an improved purity.

The obtained solid powder was dissolved by heating in a small amount of *n*-heptane (C_m = 10 mg·mL^{-1}) in a closed vial then quickly cooled at 4°C. After a few minutes of cooling, the dark blue hot solution formed the expected translucent cyan gel called **TbC$_6$** and depicted in Figure 5.4, which did not flow once the vial was inverted (see the "test-tube inversion method" in Part.5.A.1).

Figure 5.4. Pictures of the "tube inversion" of an *n*-heptane hot solution and a gel of **TbC$_6$** (C_m = 10 mg·mL^{-1}) in 2mL vials (left).

Encouraged by these promising results, and in order to evaluate the impact of the carbon tail length on the gelation properties, NIT radicals with longer aliphatic chains, namely **NITPhOC$_{10}$** and **NITPhOC$_{18}$**, were synthesised (the crystallographic parameters can be found in

Table 5**.A.7**). Longer carbon chain lengths were expected to reinforce the interactions between the bridging radicals with the aliphatic *n*-heptane through London dispersion forces and thus stabilise the gels.[16–18]

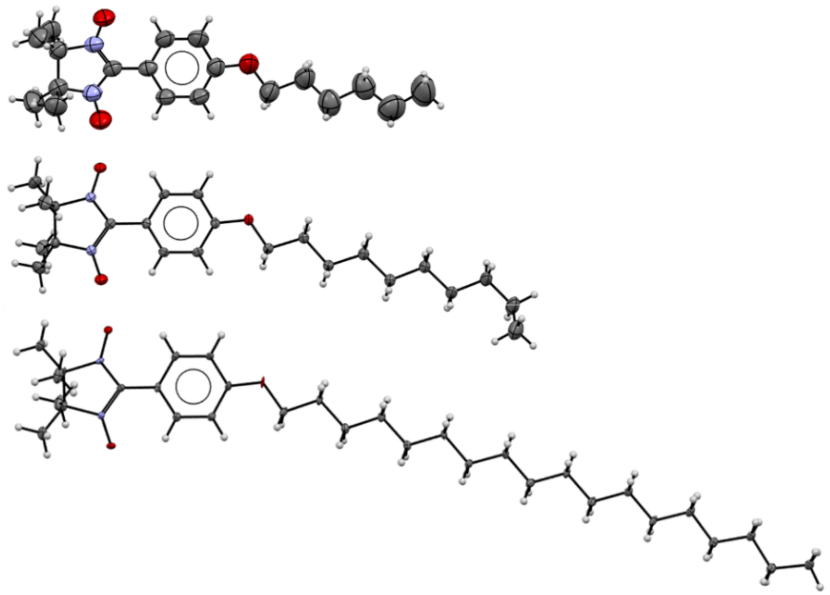

Figure 5.5. ORTEP views (thermal ellipsoids at 50 % probability) of the molecular structures of **NITPhOC$_6$** (top), **NITPhOC$_{10}$** (middle) and **NITPhOC$_{18}$** (bottom).

The same previous gelation protocol, summarised in Figure 5.6, was adopted and gave us similar cyan gels, called thereafter **TbC$_{10}$** and **TbC$_{18}$**, whatever the NIT radical used and whose share the same FTIR vibrational bands (Figure 5.A.30Figure **5.A.31**).

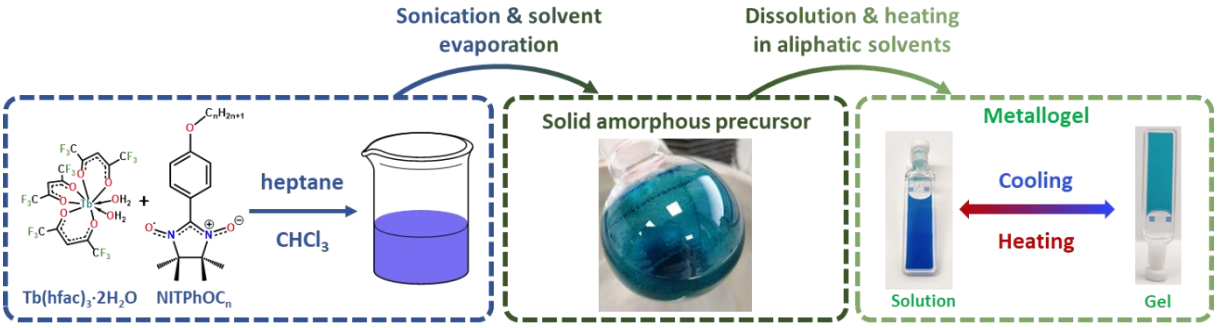

Figure 5.6. Synthetic pathways toward TbC$_n$ metallogels.

Indeed, metallogel formation is governed by the growth of the coordination polymer by dative bonding, but also supramolecular self-assembly through non-covalent interactions between the functional groups (H-bonding, solvophobic, van der Waals, π- interaction …).[19] The latter can be promoted or hindered depending on the nature of the solvent, giving us insights into the driving forces involved in the formation of the metallogel. In other words, the optimal solvent has to avoid competing with the intramolecular interactions cited previously while stabilizing the self-assembled chains.[20] These gelling properties were evaluated toward various usual solvents and summarised in the table below.

Table 5.1. Minimum gelation concentration (in mg·mL^{-1}) of **TbC$_6$**, **TbC$_{10}$** and **TbC$_{18}$**.

Solvent	**TbC$_6$**	**TbC$_{10}$**	**TbC$_{18}$**
n-hexane	10	10	10
n-heptane	8	7	8
n-octane	8	6	8
n-decane	10	4	5
Cyclohexane	S	S	S
Xylenes, Toluene	S	S	S
Ether	S	S	S
Chloroform, DCM	S	S	S
Acetone, Acetonitrile	S	S	S
Methanol, Ethanol	S	S	S
Water	I	I	I

S = Solution, I = Insoluble

Only the linear aliphatic solvents allowed effective gelation of the compounds, with a quenching step at 4°C mandatory to initiate the gelation. The other solvents compete with the formation of coordinate bonds by excessive solubilisation/solvation of the building blocks, thus hindering the formation of a π-stacking assembly between aromatic hfac$^-$ and NIT's phenyl moieties (primarily described in the previous chapters). The gelation ability of the NIT radicals alone was tested in the same way. Still, they were unable to give gels, highlighting the importance of the bridging Tb(hfac)$_3$ complex in the self-assembly process as a "linking node" between the organogelators during the self-aggregation process.[1]

The gelling dynamics and stability also depend on the alkoxy chain length of the radical moiety. Indeed, the **TbC$_6$** forms a gel within minutes, stable at 4°C only for one or two days (followed by the apparition of small crystals within the amorphous matrix). In the meantime, **TbC$_{18}$** gelation requires few hours but can be stored for months at 4°C with no signs of evolution, comforting our assumption that longer carbon chains would improve the gelation ability and stability of the gels.

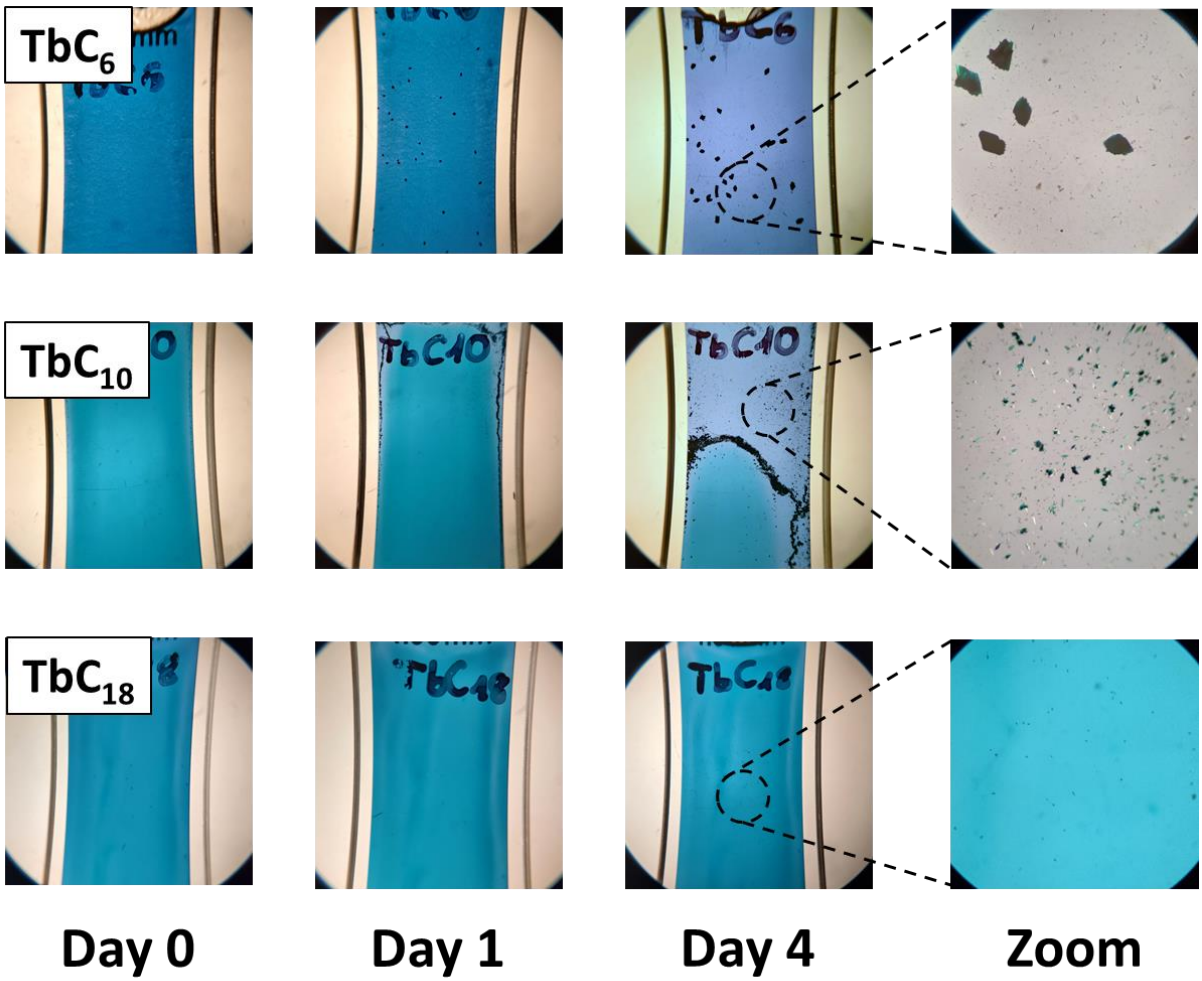

Figure 5.7. Time-dependent evolutions of *n*-heptane gels of **TbC$_6$**, **TbC$_{10}$** and **TbC$_{18}$** (C_m = 10 mg·mL^{-1}) at 4°C under optical microscope (magnification x10 and x63 for the far left zoom images).

The significant colour change associated with the thermo-reversible sol-gel transition was studied by UV-Visible absorption measurements and characterised by a 10 - 20 nm shift toward higher wavelengths of the main absorption band (from 633 - 634 nm for the solutions to 643 - 650 nm for the gels). These changes are induced by the coordination between the Tb(hfac)$_3$ and the NIT moieties, as also observed in luminescence emissions reported for the chains and the hexanuclears in the previous chapters.

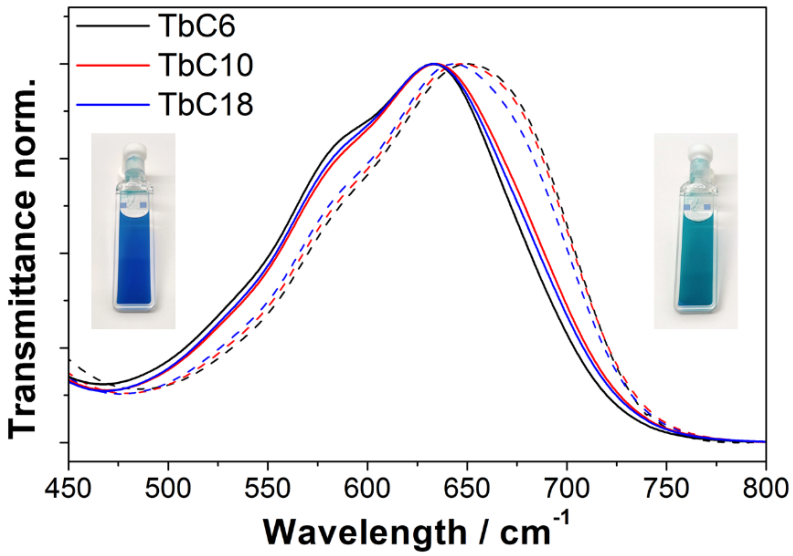

Figure 5.8. UV-visible spectra of hot solutions (dashed lines) and gels (full lines) of **TbC$_n$** in *n*-heptane (C_m = 10 mg·mL^{-1}), with as insets the corresponding images.

EPR spectroscopy measurements can also monitor this sol-gel transition: indeed, nitroxide radicals, being EPR sensitive, have already been used as spin-label to monitor the assembly and gelation dynamics of tuned organogellators.[21–25]

X-band EPR signals of solutions of **NITPhOC$_n$** and **TbC$_n$** were recorded at room temperature and depicted in Figure 5.9. They share the identical spectra with five lines of relative intensity 1:2:3:2:1 due to the hyperfine coupling between the two equivalent ^{14}N nuclei.[26] The *g*-factor and a_n values are also equivalent, irrespectively of the **NITPhOC$_n$** derivative used, and in accordance with those found in the literature for free NIT radicals in solution.[27–29]

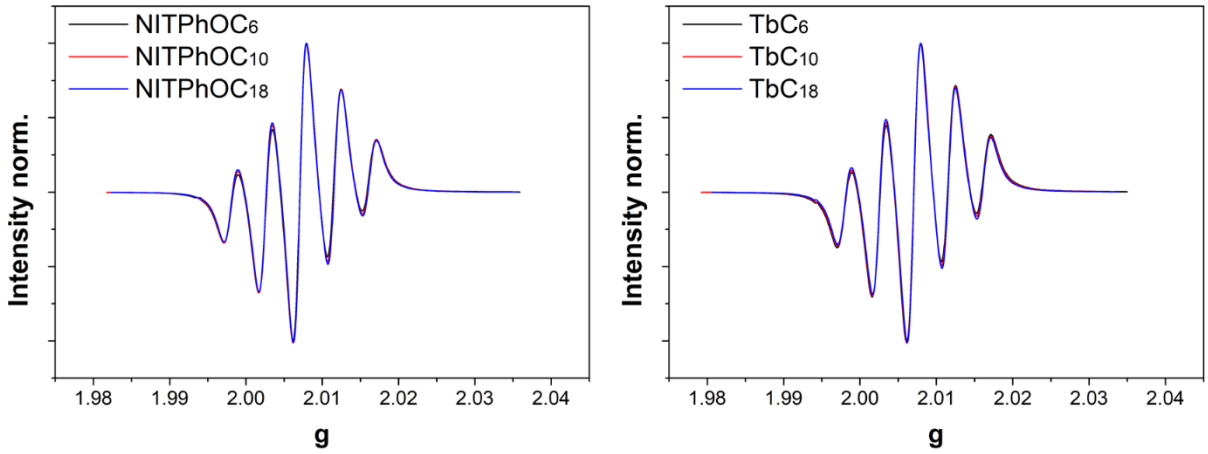

Figure 5.9. X-band spectra of $CHCl_3$ solutions (C_m = 10 mg·mL^{-1}) of **NITPhOC$_n$** (left) and **TbC$_n$** (right).

EPR spectra of both $CHCl_3$ solutions and gels of **TbC$_n$** were recorded with identical experimental conditions to probe the influence of the gelation process on the mobility of the NIT molecules. As represented in Figure 5.10, the signal of the free radicals seems to be totally quenched upon gelation: this indicates a substantial loss of mobility, likely due to coordination of the latter with the Tb(hfac)$_3$ moieties that lead to the formation of a coordinated network.

Interestingly, by strongly increasing the sensitivity of the measurement, a very weak signal appears for the **TbC$_n$** gels with a distorted five-line pattern accounting for the presence of residual free NIT in the trapped solvent, which testifies that most of the solution is converted into a gel.

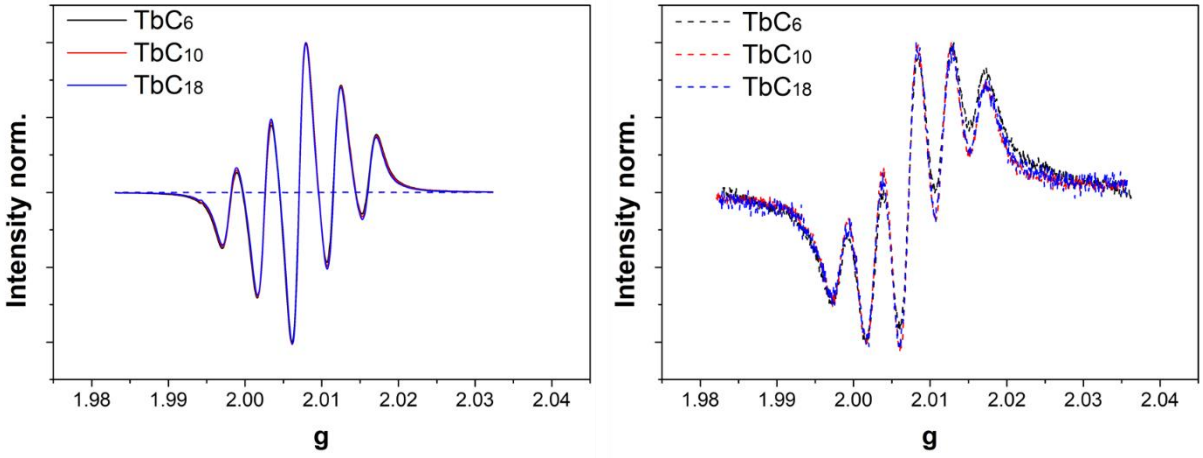

Figure 5.10. X-band EPR spectra of $CHCl_3$ solutions (full lines) and *n*-heptane gels (dashed lines) of **TbC$_n$** (C_m = 10 mg·mL^{-1}) measured in the same experimental conditions, with scaling factor the maximum for each TbCn derivative (left), and a zoom on the *n*-heptane **TbC$_n$** gels spectra (right).

Table 5.2. EPR extracted *g*-factor and hyperfine coupling a_n values for $CHCl_3$ solutions of **NITPhOC$_n$** and **TbC$_n$**, and *n*-heptane gels of **TbC$_n$** (C_m = 10 mg·mL^{-1}).

	Solutions ($CHCl_3$)				**Gels (*n*-heptane)**	
	NITPhOC$_n$		**TbC$_n$**		**TbC$_n$**	
n	***g***	***a_n* (mT)**	***g***	***a_n* (mT)**	***g***	***a_n* (mT)**
6	2.0071	0.76	2.0070	0.77	2.0072	0.75
10	2.0071	0.76	2.0071	0.77	2.0072	0.75
18	2.0071	0.76	2.0071	0.77	2.0073	0.76

5.3. Morphology and structural model

While the previous observations may suggest that a coordination phenomenon between Tb and NIT occurs, legitimate doubts can subsist without additional information about the structure of these gels, particularly the existence of supramolecular organisations as observed in the chains. To this end, we have developed a collaboration with Dr. F. Artzner (Groupe Matière Condensée et Matériaux, Institut de Physique de Rennes) to characterise the morphology of our gels by Small-Angle X-ray Scattering (SAXS) spectroscopy, particularly suitable for soft matter compounds.

5.3.1. Working principles of the SAXS spectroscopy

Indeed, the operating angular range of SAXS spectroscopy (from 0.01° to 5°) allows probing of the structural organisation (from few to hundreds of nanometres) for diverse kinds of nanometric systems (dispersed nanoparticles, colloids, gels, proteins polymers, *etc.*) by a non-destructive mean.

The working principle of a typical SAXS experiment is the following:

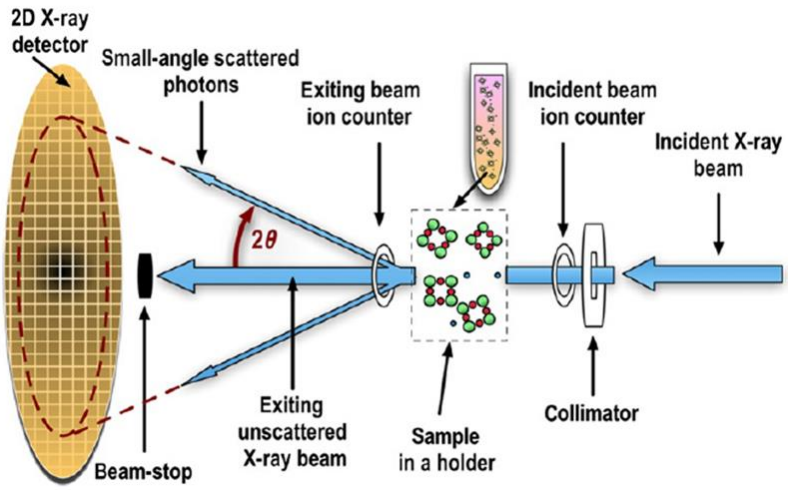

Figure 5.11. Schematic working principle of a SAXS experiment (reproduced from Ref.[30]).

1) First, a monochromatic X-ray beam of given energy is generated by a conventional X-ray tube (with a copper or a molybdenum anode) or a synchrotron facility (to modulate the intensity contrast by tuning the energy beam near the absorption edge of the targeted atom);
2) This beam is then collimated to ensure a sufficient spatial resolution and goes through the sample at variable scattering angles θ;
3) A fraction of the incident photons interacts with the electronic clouds of atoms, giving insights about the statistical spatial fluctuation of the electron density of the objects constituting the dispersed sample by elastic scattering;
4) And finally, the scattering pattern is collected on a 2D X-ray detector.

The theoretical scattered intensity *I(q)* for a single particle will depend on its electron contrast Δ_ρ (the difference of its electronic density with the solvent/matrix one), its volume V_p, and its form factor, *i.e.,* its shape expressed by a pair distribution function *P*(*q*). The summation of this intensity for all the particles of a homogeneous sample is defined by:

$$I(q) \propto \frac{N_p}{V}.(V_p)^2.(\Delta_\rho)^2.P(q) \qquad \text{Eq. 5.1}$$

with N_p being the number of particles and *V* the volume of the sample.

The resulting intensity profile is plotted *versus* the scattering vector *q*, defined by the difference between the final (or scattered) wave vector k_f and the incident one k_i, which is expressed as:

$$q = \frac{4\pi}{\lambda}\sin(\theta) \qquad \text{Eq. 5.2}$$

with being θ the angle of incidence and λ the wavelength of the incident X-ray beam.

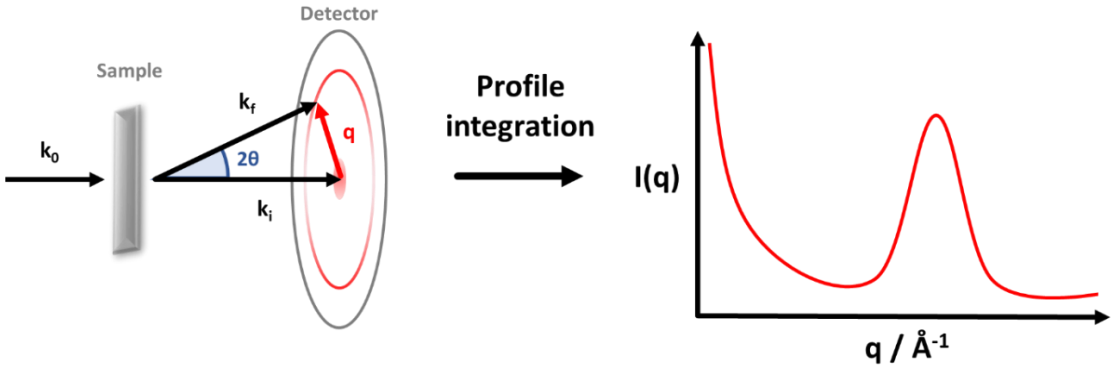

Figure 5.12. Schematic representation of the theoretical scattering process during a SAXS measurement (left) and deduced SAXS intensity profile (right).

Because the collected intensity corresponds to the representation of the scattered structure in the reciprocal space, this vector *q* can be linked to real-space dimension *d* according to the Bragg law by the following expression:

$$d = \frac{2\pi}{q} \qquad \text{Eq. 5.3}$$

By using a conventional Cu anode as an X-ray beam generator (λ = 1.5406 Å) and applying the previous equations, one can estimate the dimensions probed during a SAXS experiment.

Table 5.3. Estimation of the sizes measured during a SAXS experiment with a CuK_α generated X-ray beam.

θ (°)	q (Å^{-1})	d (nm)
0.001	0.00014	4413
0.01	0.0014	441
0.1	0.014	44
1	0.14	4

Hence, given the large range of dimensions investigated, a typical SAXS profile spectra can be divided into three regions which contain specific information each: the low *q* (or Guinier) region gives information about the size of the objects, the intermediate (Fourier) region about their shape, and the high *q* (Porod) related to their surface (and their interface).

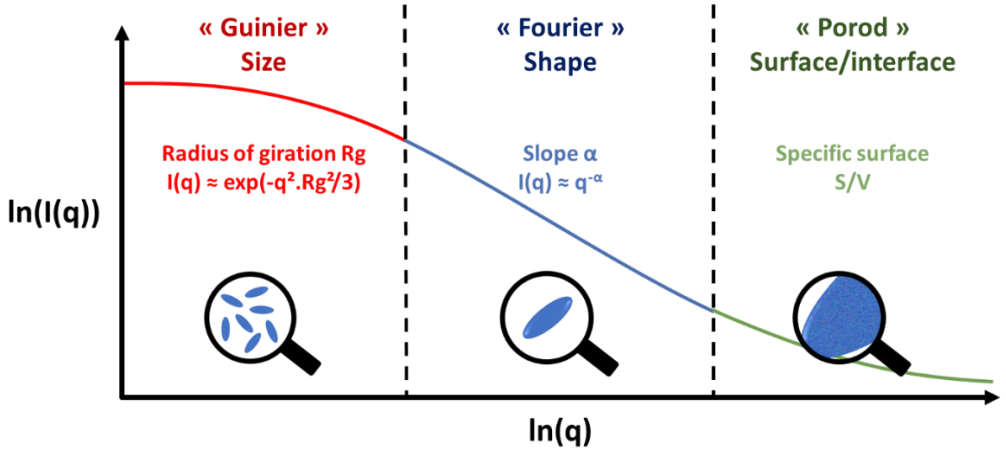

Figure 5.13. Regions of SAXS intensity profiles and their related information.

The Guinier region can be fitted by an exponential expression to determine the radius of gyration R_g, the radius of the typical volume occupied by a mobile particle normalised by its centre of gravity. This value depends on the dispersity of the sample or its degree of aggregations (which can be affected by the concentration). This radius can be linked to the characteristic dimensions of the particles of the known shape by simple relations expressed as:

- Sphere of radius *R* $R_g^2 = {}^3/_5 . R^2$
- Shell (sphere with inner and outer radius R_1 and R_2, respectively) $R_g^2 = {}^3/_5 \cdot \frac{R_2^5 - R_1^5}{R_2^3 - R_1^3}$
- Cylinder of length *h* and radius *R* $R_g^2 = \frac{R^2}{2} + \frac{h^2}{12}$
- Disk (cylinder with $L \rightarrow 0$) $R_g^2 = \frac{R^2}{2}$
- Rod (cylinder with $R \rightarrow 0$) $R_g^2 = \frac{R^2}{2} + \frac{h^2}{12}$
- Triaxial ellipsoid with semiaxes *a*, *b* and *c* $R_g^2 = \frac{a^2 + b^2 + c^2}{2}$

However, for a sample constituted of objects whose geometry is unknown, it is necessary to refer to the next Fourier region.

Indeed, the power-law dependence of the intensity profile curve $I(q) \approx q^{-\alpha}$ in the Fourier region allows the estimation of the shape of the particles such as $\alpha = 1$ for a rod-like object, $\alpha = 2$ for a disk and $\alpha = 3$ for a sphere. Then the curve can be fitted more accurately by an appropriate pair distribution function $P(q)$, an analytical expression directly proportional to the intensity $I(q)$ and specific to each geometry.[31–33]

- Sphere $$A_{sph}^2(qR) = \frac{9}{(qR)^6}[\sin(qR) - qR.\cos(qR)]^2$$
- Shell $$\frac{\left[R_2^3.A_{sph}(qR_2) - R_1^3.A_{sph}(qR_1)\right]^2}{(R_2^3 - R_1^3)^2}$$
- Cylinder $$4\int \frac{J_1^2(qR\sqrt{1-x^2})}{(qR\sqrt{1-x^2})^2}.\frac{\sin^2(qL.x/2)}{(qL.x/2)^2}.dx\,dy$$
- Disk $$\frac{2 - J_1(2qR)/qR}{(qR)^2}$$
- Rod $$\frac{2}{qL}\int \frac{\sin(t)}{t}dt - \frac{\sin^2(qL/2)}{(qL/2)^2}$$
- Triaxial ellipsoid $$\iint A_{sph}^2.[q\sqrt{a^2\cos^2\left(\frac{\pi x}{2}\right) + b^2\sin^2\left(\frac{\pi x}{2}\right)(1-y^2) + c^2y^2}.dx\,dy$$

with J_1 a first kind Bessel function of order 1.

Finally, the Porod region is related to the nanometric dimensions of the particles. The average roughness can be estimated by the power-law $I(q) \approx q^{-(6-d)}$, with d being the fractal dimension of the surface.

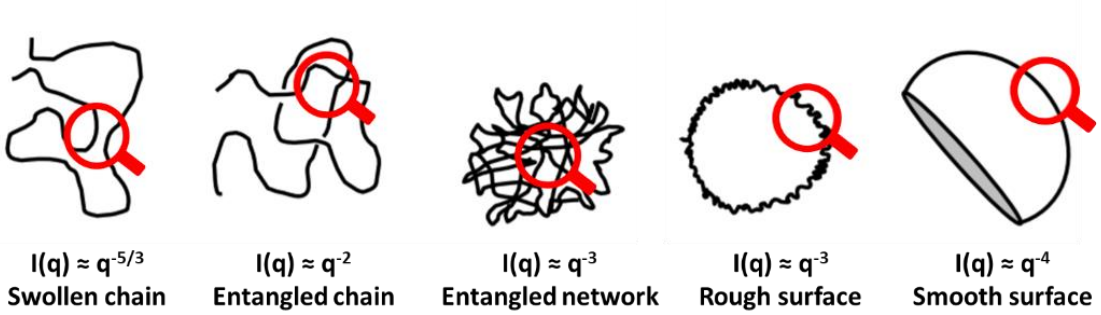

Figure 5.14. Fractal dimension values for some usual particle shapes.

In the case of homogenous particles with well-defined surfaces (d = 2, $I(q) \approx q^{-4}$), one can estimate the specific surface S of the particles by applying a simplified Porod law:

$$I(q) = 2\pi.S.\Delta_\rho^2.q^4 \qquad \text{Eq. 5.4}$$

More complex features proper to this high q region can be investigated, such as the surface of a discrete particle (or a compact aggregate),[32] their roughness,[34,35] the intermolecular interfaces[36–38] or the compactness of a linear polymer or a protein.[39,40]

5.3.2. SAXS measurements of TbC_n gels

In our case, SAXS measurements of fresh **TbC_n** gels in quartz capillaries have been performed (by Dr. F. Artzner, see Part.5.A.1 for experimental details).

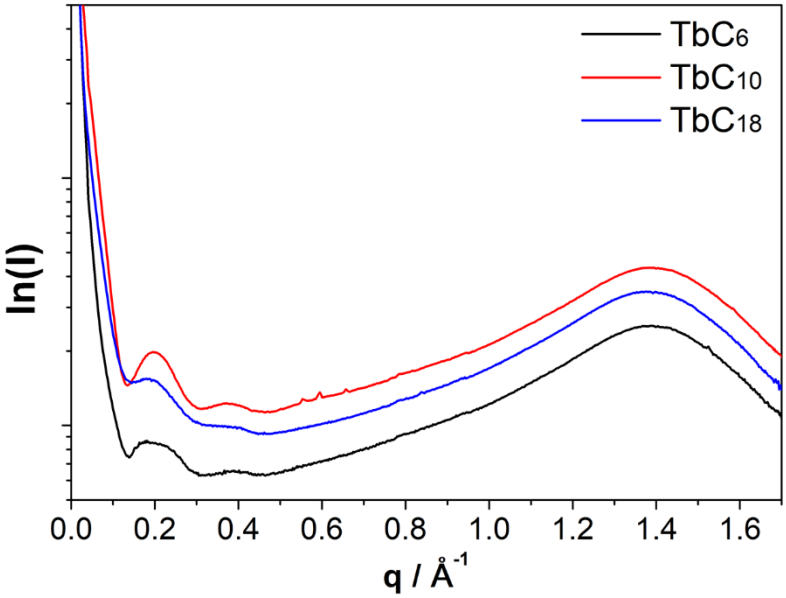

Figure 5.15. SAXS intensity profile spectra of fresh *n*-heptane **TbC_n** gel samples (C_m = 10 mg·mL^{-1}).

The intensity profiles for each derivative of **TbC_n** revealed the presence of two oscillations of similar periods in the low *q* region ($q^{-1} < 0.5$) and a broad one in the high *q* region ($q^{-1} > 0.5$), due to the scattering of the *n*-heptane solvent. Accordingly, the curves are fitted with the following form factor related to a hollow tube:

$$P(q) = 2\pi \int_0^{+\infty} \rho(r) J_0(qr) r.dr \qquad \text{Eq. 5.5}$$

with J_0 a zeroth order Bessel function.

Considering an infinitely thin wall thickness, we can model the electronic density of the wall by a Dirac pulse $\rho(r) = \delta(r\text{-}r_0)$. Eq. 5.5 become:

$$P(q) = 2\pi \int_0^{+\infty} \delta(r - r_0) J_0(qr) r.dr = 2\pi J_0(qr_0) \qquad \text{Eq. 5.6}$$

with r_0 the radius of the tube.

The resulting fitting model is then:

$$I(q) = \frac{P^2}{q^2} \propto \frac{J_0(qr_0)^2}{q^2} \qquad \text{Eq. 5.7}$$

In our case, the best fit of our oscillation curves is obtained for a radius value of r_0 = 1.8 nm, and our tubes have therefore a diameter of $Ø_{gel}$ = 3.6 nm.

These observations are strongly reminiscent of the structure of crystalline nanotubes made of helical chains described in Chapter 3 but with a smaller diameter ($Ø_{crystal}$ = 4.6 nm).

Thus, a reasonable assumption could be that these gels are also made of wrapped helical chains and maintained because of the favouring interaction between the solvent and the aliphatic tails of the NIT radicals.

Interestingly, time-dependent SAXS experiments have been performed to evaluate the stability of each gel and strengthen the observations made by optical microscopy in Figure 5.7. The intensity profiles of the aged **TbC_6** and **TbC_{10}** gels (D+1) show that the oscillations (related to the tubular gel state) disappear to be replaced by sharp peaks due to the scattering of growing crystals within the amorphous gel matrix. In comparison, no changes are reported for the most stable **TbC_{18}** gel.

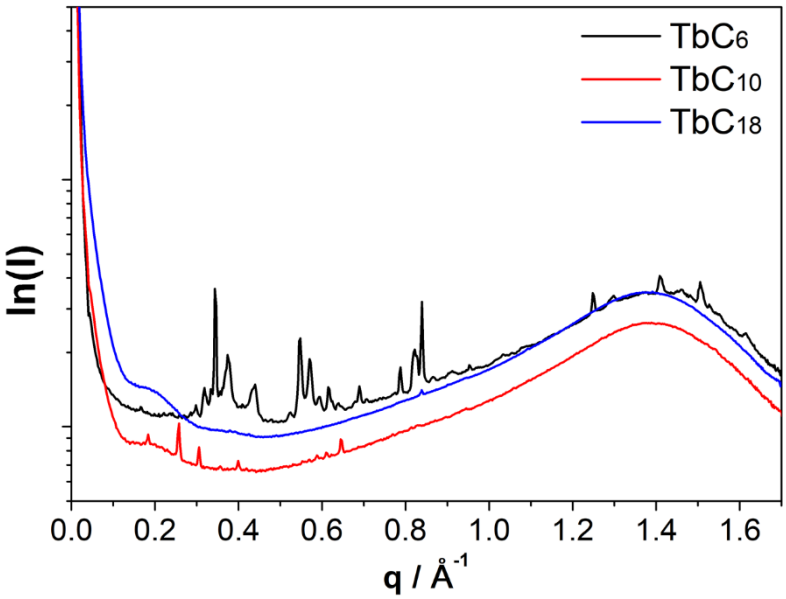

Figure 5.16. SAXS intensity profiles of aged (1 day) of *n*-heptane **TbC_n** gel samples (C_m = 10 mg·mL^{-1}).

However, similarity does not imply equivalence, and if the same supramolecular arrangement seems to occur within the gels, its detailed rationalisation is complex. We recall that SAXS spectroscopy measures a statistical distribution within the sample and then strongly depends on the orientational average of the scattering particles. If it is not an issue for isotropic particles, it is more complicated in our case; the disordered tubes hamper access to additional information, such as distances between Tb^{III} atoms to build a model or the thickness of the tube walls.

5.3.3. Determination of a structural model

Fortunately, the observation of well-aligned fibres obtained during the drying of an *n*-heptane **TbC_{18}** gel sample (C_m = 50 mg·mL^{-1}) against the capillary walls allowed us to extract the parameters needed to address this point. Indeed, a tube can simply be seen as a folded 2D crystal lattice, so the only requirement to build a structural model is to determine the parameters of the unit cell of this crystal lattice.

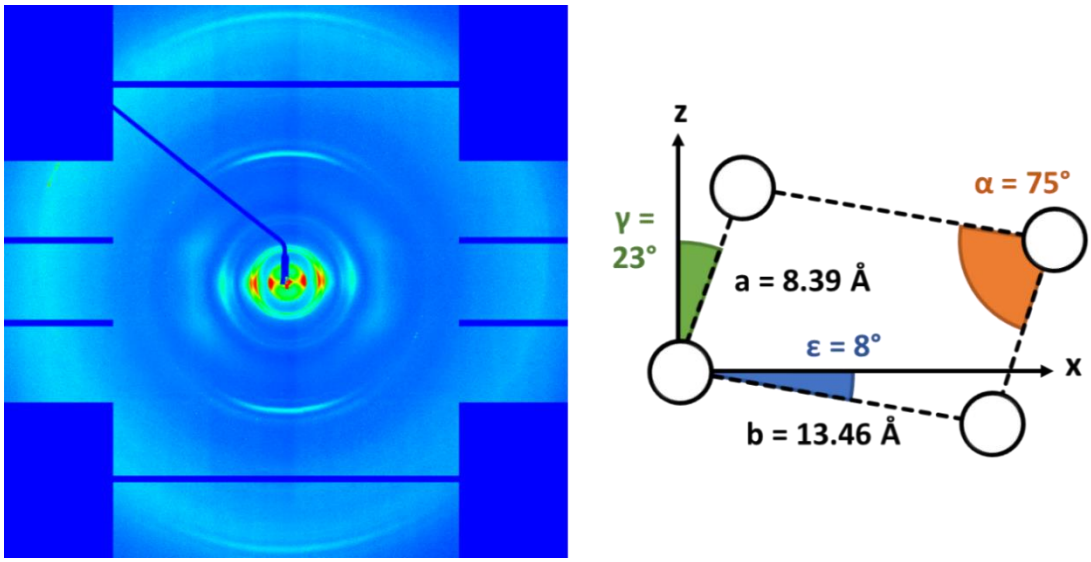

Figure 5.17. SAXS image (left) of a dried *n*-heptane **TbC$_{18}$** sample (C_m = 50 mg·mL^{-1}), with the corresponding monoclinic unit cell (right).

The indexation of the position of diffuse scattering maxima gives *a* = 8.39 Å, *b* = 13.46 Å and *α* = 75°, with *a* at an angle of γ = 23° along the tube axis and *b* at an angle of ε = 8° along its perpendicular plane, as seen on the corresponding monoclinic cell depicted in Figure 5.17 below. The value of the parameter *a* can be unambiguously assigned to the distance of two Tb^{III} ions bridged by one NIT radical, similar to the one reported in the helical **chain** (8.39 Å). The neighbouring chains are slightly more spaced apart by a distance *b* = 13.46 Å. By comparing this distance with the perimeter of the tube $2\pi r_0$, we have estimated that eight chains accommodate to form the tubes compared to eleven for the crystalline ones.

To facilitate the comprehension of this structure, a preliminary overview of the resulting structure can be plotted by implementing these parameters to a 2D Patterson function that stresses the strong similarities between the nanotubes obtained from the **chain** crystals of the Chapter 3 and the ones from the **TbC$_n$** gel derivatives.

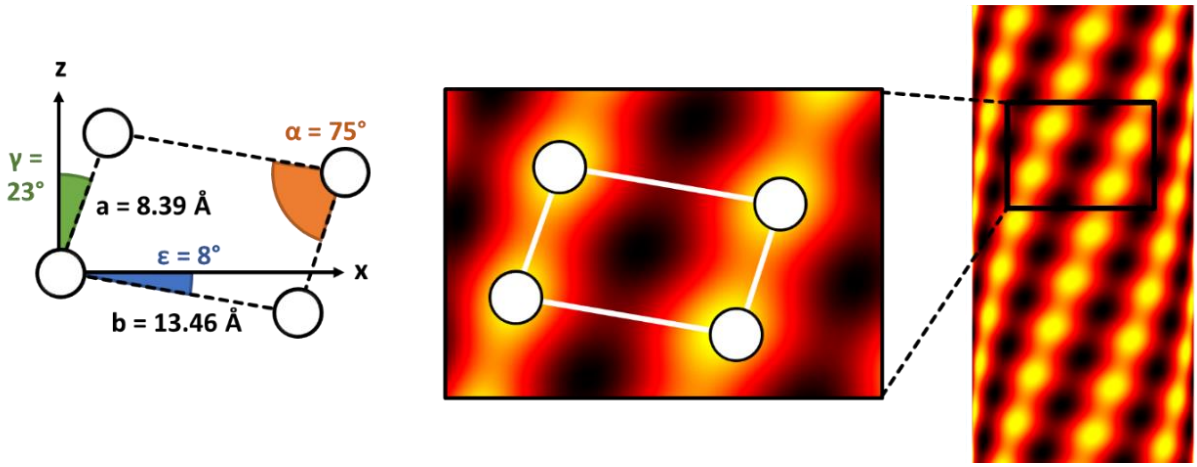

Figure 5.18. Monoclinic unit cell (left), reconstructed 2D Patterson function, indicating the main electron density variation of the unit cell (middle), and enlarged 2D Patterson function of the resulting nanotube.

In order to have a complete representation, we have decided to build a simple 3D structural model of these nanotubes. Because they are made of helical chains, we based our model on the parametric equations of the helix below (Eq. 5.8) to calculate the relative position of each Tb^{III} atom.

$$\begin{cases} x(t) = r_0 \cdot \cos(t) \\ y(t) = r_0 \cdot \theta \cdot \sin(t) \\ z(t) = \dfrac{h}{2\pi} \cdot t \end{cases} \qquad \text{Eq. 5.8}$$

with r_0 being the tube radius, θ the direction of rotation of the helix (θ = +1 for anticlockwise, θ = -1 for clockwise) and h the pitch of the helix.

Our nanotube is constituted of a periodic arrangement of eight helices, so we had to introduce a "shift" between the helices on the unit circle of radius r_0, by adding the equivalent of a "phase difference" φ to the trigonometric terms:

$$\begin{cases} x_i(t) = r_0 \cdot \cos(t + \varphi_i) \\ y_i(t) = r_0 \cdot \theta \cdot \sin(t + \varphi_i) \\ z(t) = \dfrac{h}{2\pi} \cdot t \end{cases} \qquad \text{Eq. 5.9}$$

with $\varphi_i = 2\pi.i/j$, i being the helix' number and j the total number of helices.

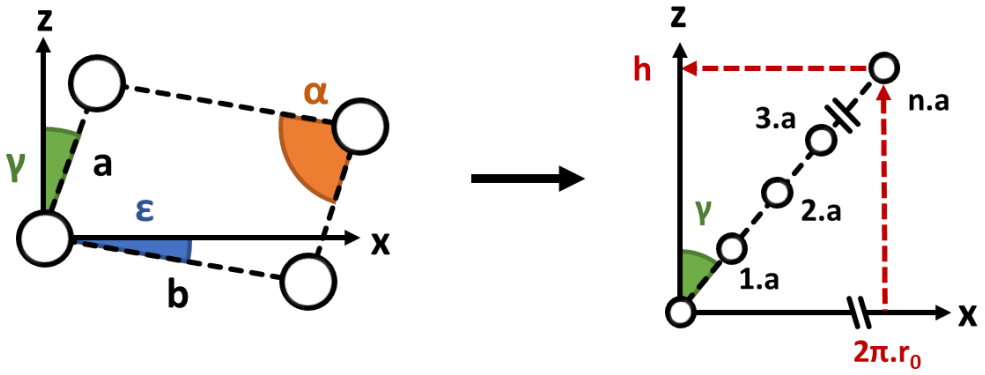

Figure 5.19. Schematic representation of the determination of the value of the pitch h.

Then, the pitch length h can be easily estimated from the 2D monoclinic parameters: it is equivalent to a projection of $n \cdot a$ segments on the unit circle (or the x-axis in Figure 5.19 above), which have to be at least equal to at a complete revolution $2\pi \cdot r_0$. By using the right-angled triangle ratios, we obtain:

$$\tan(\pi - \gamma) = \frac{h}{2\pi \cdot r_0} \qquad \text{Eq. 5.10}$$

$$h = 2\pi \cdot r_0 \cdot \tan(\pi - \gamma) \qquad \text{Eq. 5.11}$$

In our case, the resulting pitch h_{gel} = 26.6 nm (with r_0 = 3.6 nm and γ = 23°) is longer than the one reported for the **chain** crystal (H_{cry} = 19.8 nm), because of a larger interchain space (b = 13.46 Å *vs* 10.80 Å), coupled with a smaller angle along the tube axis (23° *vs* 51°).

An additional difficulty is that the neighbouring chains do not strictly face each other's but are slightly tilted by an angle $\varepsilon = 8°$. We have to determine then the initial position of the first atoms of each chain along the tube axis *z*, *i.e.,* the shift of each helix.

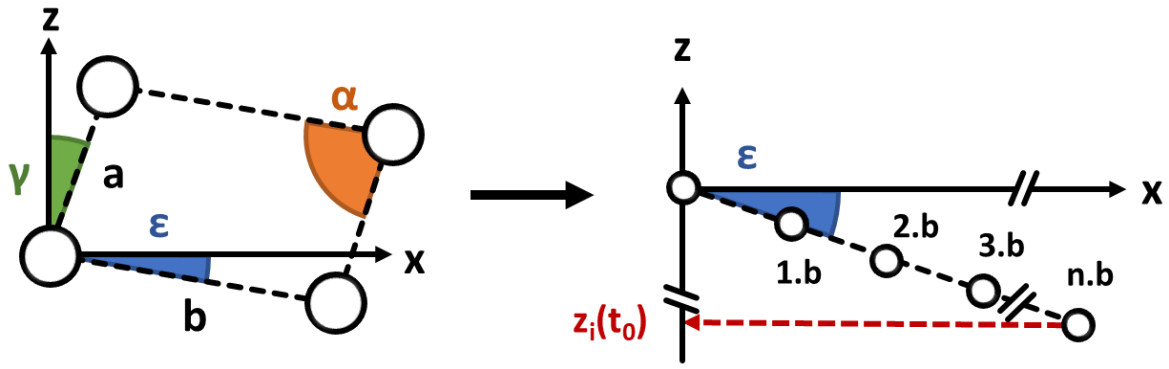

Figure 5.20. Schematic representation of the determination of the relative *z* position of each atom.

Once again, this value is given by a simple trigonometric relation and can be generalised thanks to the periodicity of the system:

$$z_i(t_0) = b \cdot \sin(\varepsilon) \cdot i \qquad \text{Eq. 5.12}$$

The periodic interval between two consecutive intrachain Tb^{III} atoms along *z* is also given by the following relation:

$$z_i(t_{n+1}) = a \cdot \cos(\gamma) \qquad \text{Eq. 5.13}$$

Then, for any helix, the position according to the *z*-axis of the n^{th} atom of the chain will be:

$$z_i(t_n) = n \cdot z_i(t_{n+1}) + z_i(t_0) \qquad \text{Eq. 5.14}$$

$$z_i(t_n) = n \cdot a \cdot \cos(\gamma) + b \cdot \sin(\varepsilon) \cdot i \qquad \text{Eq. 5.15}$$

The parameter *t*, linked to the z(t) position of each atom, is then determined by combining Eq. 5.8 and Eq. 5.15.

$$z_i(t_n) = \frac{h}{2\pi} \cdot t_n = n \cdot a \cdot \cos(\gamma) + b \cdot \sin(\varepsilon) \cdot i \qquad \text{Eq. 5.16}$$

$$t_n = \frac{2\pi}{h} \cdot (n \cdot a \cdot \cos(\gamma) + b \cdot \sin(\varepsilon) \cdot i) \qquad \text{Eq. 5.17}$$

These *t* parameters are finally implemented in the x(t) and y(t) equations from Eq. 5.9 to obtain the coordinates. The resulting model is depicted in Figure 5.21 below, and the relative atom positions are reported in Table 5.A.8.

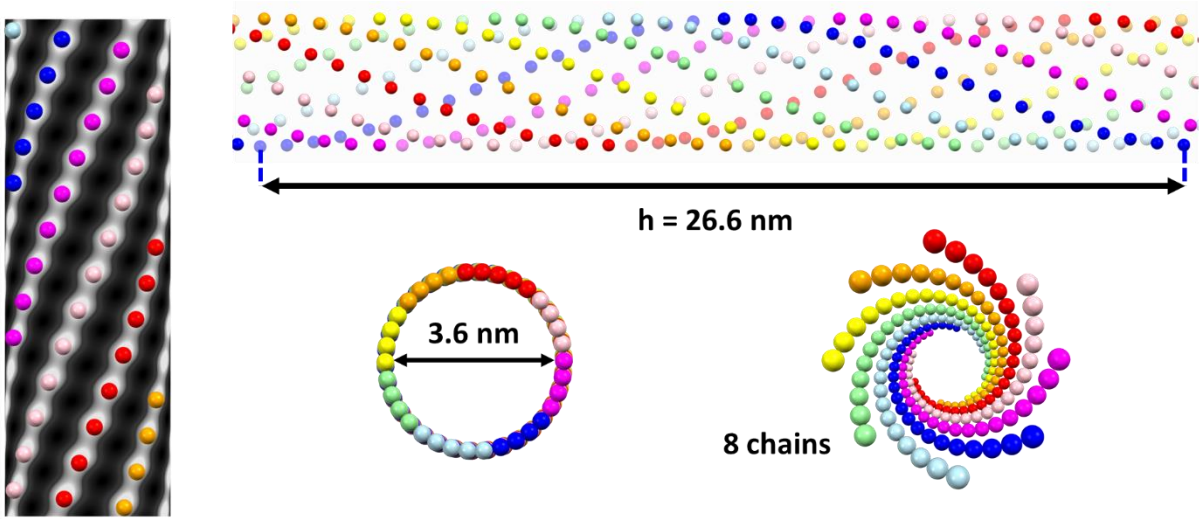

Figure 5.21. Left: Superposition of the 3D model of the **TbC$_{18}$** gel with the 2D Patterson function image (each Tb chain being represented by a different colour). Side representation (top) and views along the tube axis (bottom) of the Tb^{III} tube model of the **TbC$_{18}$** gel.

Additionally, circular dichroism (CD) measurements, performed by Dr. A. Gabbani and Dr. F. Pineider at the LaMM (Firenze), did not evidenced any dichroic contribution in the gels. This is in line with the use of non-chiral building blocks and excludes the possibility of a non-racemic organisation during the self-assembly step. One could also note that this may be a clue that the chirality observed on the **chain** crystal is driven by a spontaneous crystallisation in a chiral space group.

5.4. Magnetic properties

5.4.1. Static (DC) magnetic properties

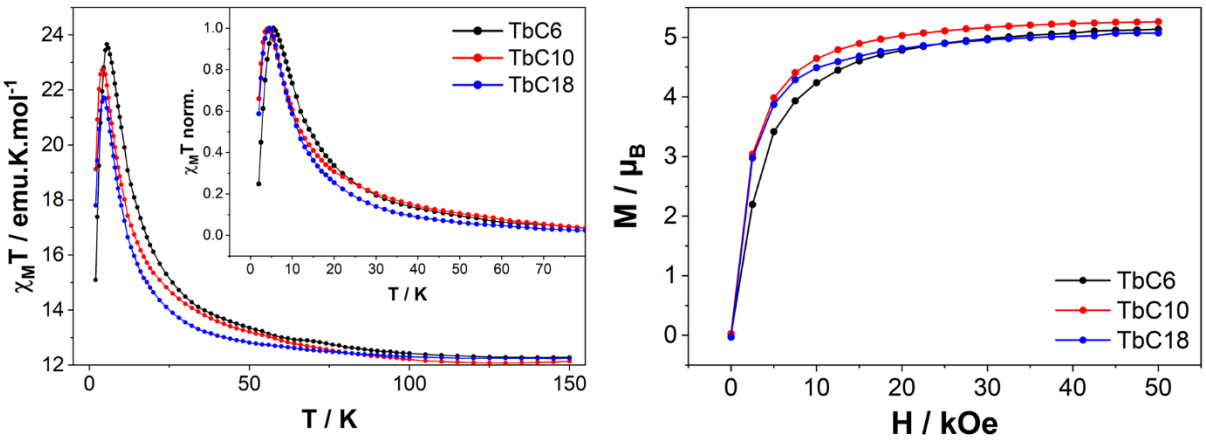

Figure 5.22. Temperature dependence of $\chi_M T$ measured with H_{DC} = 1000 Oe and with inset, a zoom in the low-temperature region of the normalised temperature dependence of $\chi_M T$ (left) and field dependence of magnetisation (right) of *n*-heptane gels of **TbC$_6$**, **TbC$_{10}$** and **TbC$_{18}$** (C_m = 10 mg·mL^{-1}).

Static magnetic properties have been measured on frozen fresh *n*-heptane gels under a static field. The temperature dependence of the product $\chi_M T$ shows a similar behaviour between the **TbC$_6$**, **TbC$_{10}$** and **TbC$_{18}$** gels, with $\chi_M T_{(150K)}$ value of resp. 12.28, 12.13 and 12.25 emu·K·mol^{-1}. These values are close to the theoretical $\chi_M T$ of 12.19 emu·K·mol^{-1} for a free Tb^{III} ion (J = 6, g_J = 3/2) and an uncoupled radical (S = 1/2, g_S = 2) at 300 K. By decreasing the temperature, these values stay constant then increase exponentially below 100 K to reach maxima of 23.66 emu·K·mol^{-1} at 5.5 K (**TbC$_6$**), 22.76 and 21.73 emu·K·mol^{-1} at 4.5 K (for **TbC$_{10}$** and **TbC$_{18}$**, respectively). A sharp decrease follows this increase due to saturation effect, highlighted by AC measurements in Figure 5.A.34Figure **5**.A.36. Besides this, the field dependence of the magnetisation exhibits an abrupt rise starting at the lowest fields and quickly reaching saturation M_{sat} values of 5.1, 5.3 and 5.1 μ_B (for **TbC$_6$**, **TbC$_{10}$** and **TbC$_{18}$** resp.), slightly below the theoretical value of 5.5 μ_B. Noteworthy, measurements conducted on the corresponding xerogels led to similar behaviours described in Figure 5.A.33.

These sharp increases of both the $\chi_M T$ product and the magnetisation can be due either to the rise of ferro- or ferrimagnetic interaction within the tube, or the onset of a magnetic correlation phenomenon along the chains if one takes into account the hypothesis of a SCM behaviour. This latter assumption could be relevant in this case because of the structural features observed in Part.5.3, with consecutive anisotropic Tb^{III} centres linked by radicals and well-spaced chains and the permanence of the molecular nanotube structure in the gels (see SAXS measurements).

5.4.2. Dynamic (AC) magnetic properties

The magnetic relaxation behaviour of the gels was then probed by AC susceptibility measurements with no static external static field. Clear temperature dependence of the out-of-phase (χ_M'') susceptibility signal is observed for each sample, synonym of slow relaxation of their magnetisation.

In-phase and out-of-phase susceptibilities exhibit a noisy but unambiguous frequency dependence below 6 K. The out-of-phase susceptibility curves below 3 K reveal the presence of two relaxing fractions for the gels: a dominant one at higher frequencies (fast relaxation process) and minor and broad contribution at lower frequencies (slow relaxation process). This additional contribution is stressed on the Argand diagrams, with the feature of a tail for the lower temperatures (Figure 5.A.41). However, because of the signal noise, no well-defined peak is distinguishable. Indeed, measurements have been performed with around 100 mg of gels, which correspond to a very small amount of active **TbC$_n$** materials (≈ 1.5 mg).

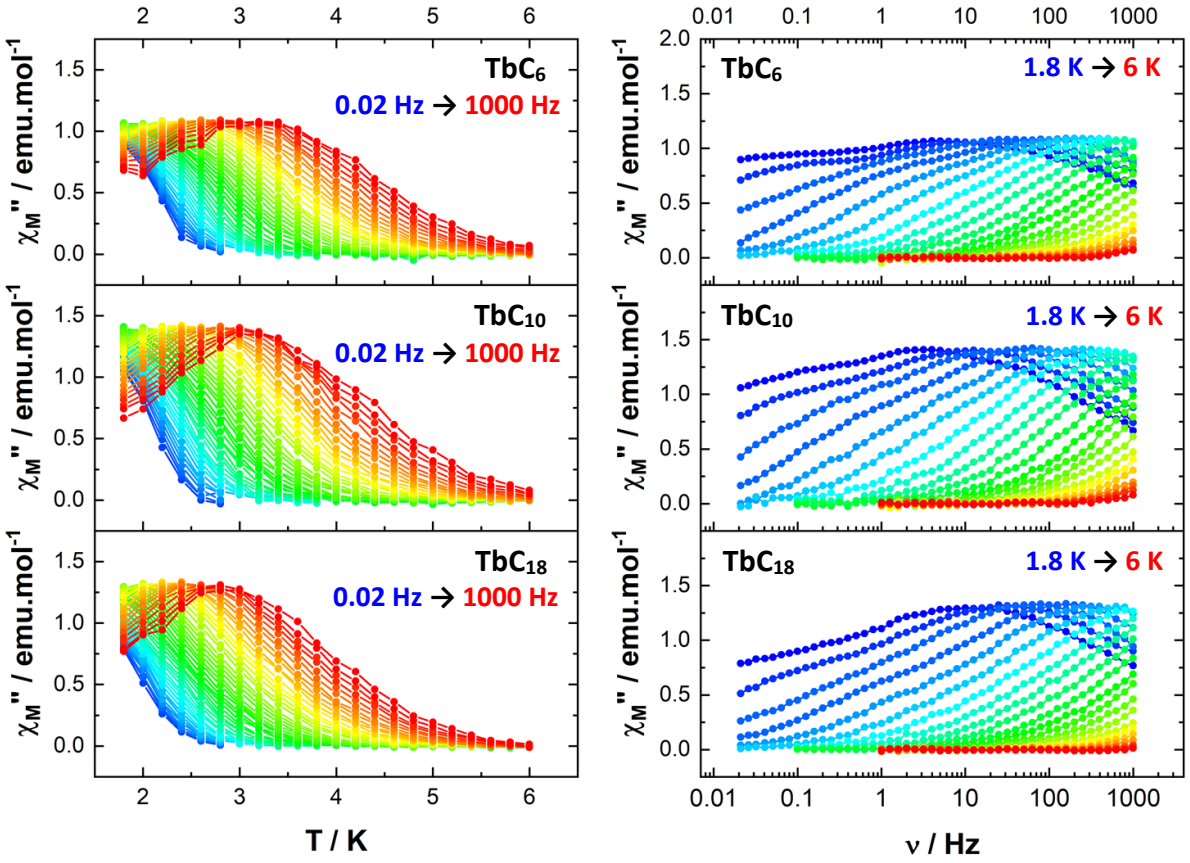

Figure 5.23. Temperature (left) and frequency (right) dependencies of the out-of-phase (χ_M'') susceptibility of *n*-heptane gels of **TbC$_6$**, **TbC$_{10}$** and **TbC$_{18}$** (C_m = 10 mg·mL^{-1}).

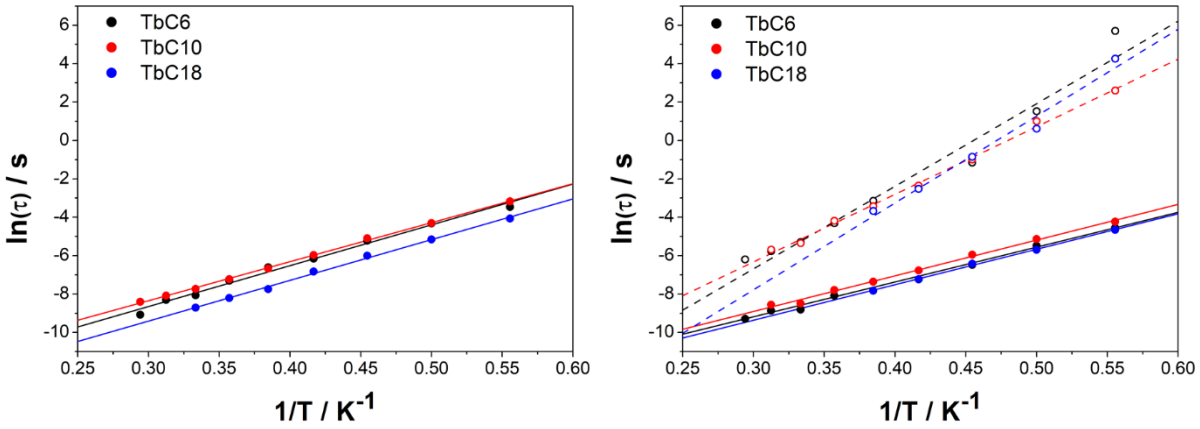

Figure 5.24. Arrhenius plots of the extracted relaxation times with a single (left) and a double (right) relaxation process for *n*-heptane gels of **TbC$_6$**, **TbC$_{10}$** and **TbC$_{18}$** (C_m = 10 mg·mL^{-1}), with filled dots as fast mode and open circles as slow mode.

Regardless, characteristic relaxation times τ were deduced using both single and double relaxation Debye models then fitted *via* an Arrhenius law $\tau = \tau_0.\exp(\Delta_{eff}/k_BT)$. The effective energy barrier Δ_{eff} and the pre-exponential factor τ_0 values extracted are listed in Table 5.4 below.

Table 5.4. Characteristic values extracted from the Arrhenius plots of the *n*-heptane gels of **TbC_6**, **TbC_{10}** and **TbC_{18}** (C_m = 10 mg·mL^{-1}) considering a single relaxation process.

	Single relaxation process		
	TbC_6	**TbC_{10}**	**TbC_{18}**
Δ_{eff}/k_B **(K)**	21.3 ± 0.8	20.3 ± 0.2	22.2 ± 0.5
τ_0 **(s)**	(3.0 ± 1.1) x 10^{-7}	(5.3 ± 0.5) x 10^{-7}	(1.4 ± 0.4) x 10^{-7}
R^2	0.9893	0.9989	0.9965

Table 5.5. Characteristic values extracted from the Arrhenius plots of the *n*-heptane gels of **TbC_6**, **TbC_{10}** and **TbC_{18}** (C_m = 10 mg·mL^{-1}) considering a double relaxation process.

	Double relaxation process					
	TbC_6		**TbC_{10}**		**TbC_{18}**	
	Slow	**Fast**	**Slow**	**Fast**	**Slow**	**Fast**
Δ_{eff}/k_B **(K)**	43.0 ± 3.0	18.1 ± 0.7	35.2 ± 0.9	18.6 ± 0.5	45.2 ± 3.7	18.5 ± 0.4
τ_0 **(s)**	(3.1 ± 0.9) x 10^{-9}	(4.5 ± 1.4) x 10^{-7}	(4.7 ± 2.0) x 10^{-8}	(5.1 ± 1.2) x 10^{-7}	(5.3 ± 4.4) x 10^{-10}	(3.4 ± 0.7) x 10^{-7}
R^2	0.9555	0.9895	0.9958	0.9950	0.9741	0.9979

Suppose one takes into account only a single relaxation mode for the gel samples (Table 5.4). In that case, the energy barrier Δ_{eff} and the pre-exponential τ_0 values are close for each gel, and in the same order of magnitude as the ones reported earlier for the chain and the hexanuclear. This would not be surprising as the main magnetic pathway is the same, with similar organisation and equal Tb-NIT distances as deduced from the SAXS measurements.

However, the presence of two simultaneous relaxation processes has already been reported in the literature, while only one should be expected for SCM systems.[41–43]

The first hypothesis could be that interchain interactions give rise to ferromagnetic order between neighbouring chains, as reported on similar Co-based systems.[42,44,45] This ferromagnetic contribution can be suppressed by applying a static H_{DC} field during AC susceptibility measurements (Figure 5.A.42). If the vanishing of this slow contribution is not evident for the gel and xerogels samples, their magnetic behaviour is an argument favouring a SCM behaviour, with an out-of-phase signal at zero H_{DC} field that decreases while increasing its intensity.

A second hypothesis could be the simultaneous presence of short and long chains, both ruled by the finite-size regime.[41,46] If these chains differ only by their size, the activation energy barrier Δ_{eff} should remain the same. This assumption does not apply here if one considers the values extracted from the double relaxation fitting in Table 5.5 with slow and fast Δ_{eff} values ranging from simple to double. Such a difference in magnitude observed for the xerogel samples (Table 5.A.10) is not even compatible with the presence of both finite- and infinite-size regimes if we compare the values obtained for the **chains** and the **hexanuclears**.

The last hypothesis is that gels are not composed strictly of chains weaved into nanotubes, but that some traces of closely related molecules are present whose signature is visible only at low temperature. Indeed, Ln-NIT systems are known to give rise to $[Ln\text{-}NIT]_n$ chains but also [NIT-Ln-NIT] complexes,[47,48] that can behave as SMM with Δ_{eff} and τ_0 values comparable as the one observed here. It is very likely that a small amount of chains decomposes during the gelation process to give these isolated molecules. To validate this hypothesis, [NIT-Ln-NIT] complexes based on $NITPhOC_6$, $NITPhOC_{10}$ and $NITPhOC_{18}$ should be synthesised, and their magnetic properties compared with the low T signature observed here. We are currently working along this line.

Finally, magnetic hysteresis measurements were performed at 0.5 K. Both gels and xerogel powders act as effective magnets with open hysteresis loops in our operating conditions (magnetic field sweep rate of 15.5 $Oe \cdot s^{-1}$). To the best of our knowledge, it is the first time that a magnetic hysteresis loop from a molecular origin has been reported for a family of metallogels, expanding the family of molecular magnetic materials.

In the case of the gels, the opening of the loop seems to follow a trend **TbC_6** > **TbC_{10}** > **TbC_{18}** for the gels with the best performance attributed to the **TbC_6** gel, with a coercive field of H_C = 3440 Oe and a remnant magnetisation of M_R = 2.49 μ_B. This trend is nevertheless not observed for the xerogel powders, whose nearly stacked open hysteresis with the same pinched shapes testify to the preservation of the coordination organisation that confer these magnetic properties after drying.

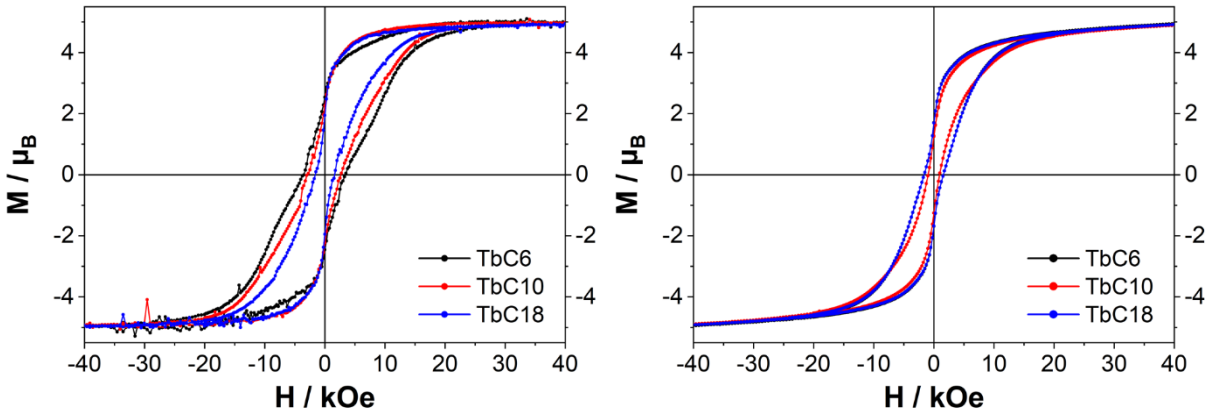

Figure 5.25. Magnetic hysteresis curves of *n*-heptane gels (C_m = 10 $mg \cdot mL^{-1}$) (left) and xerogels (right) of **TbC_6**, **TbC_{10}** and **TbC_{18}** measured at 0.5 K.

Table 5.6. Coercive fields H_C and remanent magnetisations M_R reported for the **TbC_6**, **TbC_{10}** and **TbC_{18}** gels and xerogels at 0.5 K.

		H_C (Oe)	M_R (μ_B / $\%M_{sat}$)
TbC_6	**Gel**	3440	2.49 / 50 %
	Xerogel	1600	1.70 / 34 %
TbC_{10}	**Gel**	2780	2.23 / 45 %
	Xerogel	1000	1.27 / 26 %
TbC_{18}	**Gel**	1610	1.94 / 39 %
	Xerogel	1600	1.71 / 34 %

5.5. Surface deposition by spin-coating

In order to confirm the nanotube dimensions estimated by SAXS measurements, thin films of **TbC_n** gels were prepared by spin-coating of drop-casted hot *n*-heptane solutions of **TbC_n** (the detailed protocol can be found in Part.5.A.1) and characterised by AFM measurements (with the help of Dr. G. Cucinotta and Prof. M. Mannini, LAMM, Firenze).

We firstly tried to drop-cast very diluted (C_m = 1 mg·mL^{-1}) hot **TbC_n** solutions. This concentration value should be sufficient to lead to the self-assembly of the nanotubes described above, but also low enough to allow the observation of the latter isolated on the surface.

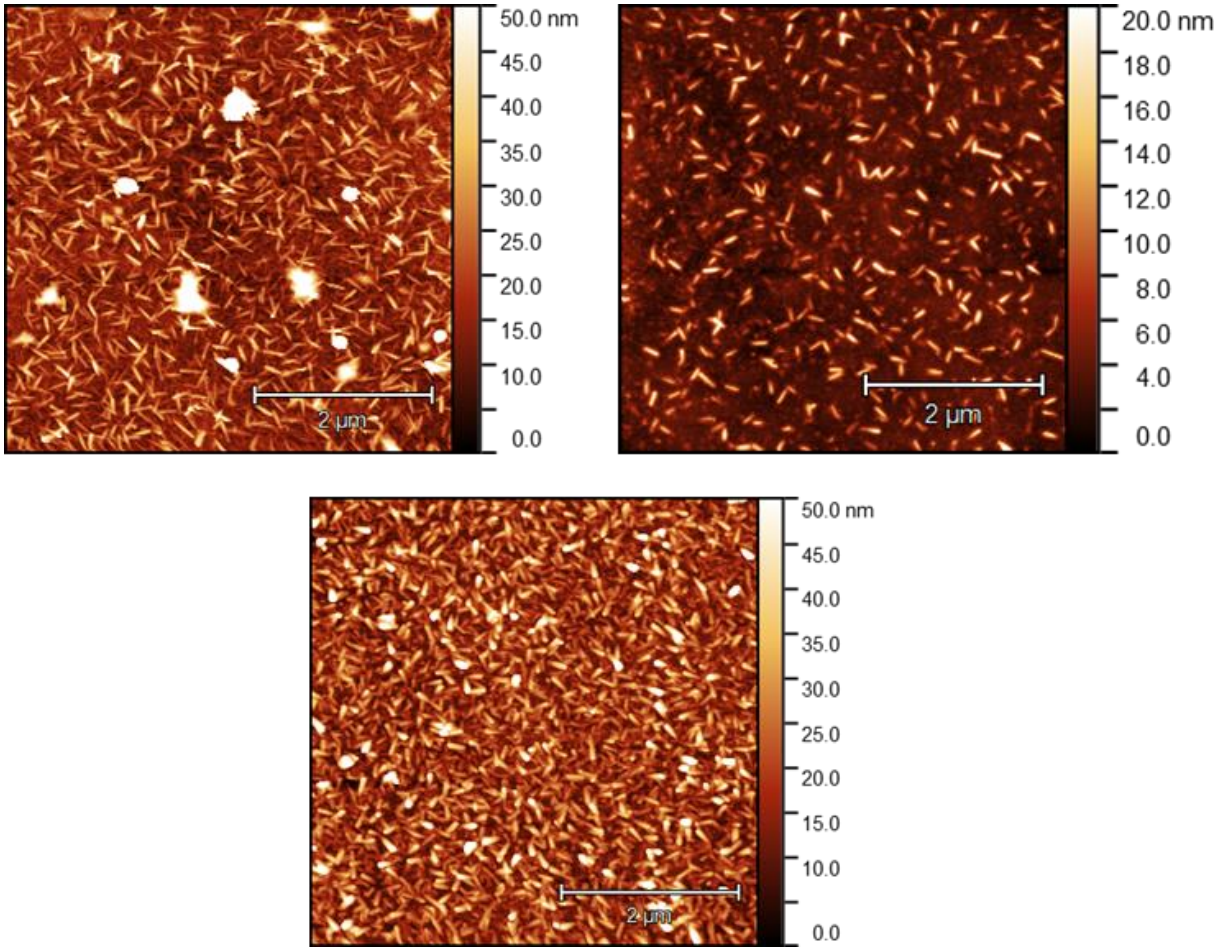

Figure 5.26. AFM topography images of 1.0 mg·mL^{-1} *n*-heptane solutions of **TbC_6** (left), **TbC_{10}** (right) and **TbC_{18}** (bottom).

Unfortunately, only small straight crystals of tens of nanometres height were observed after several attempts, too large to correspond to a single nanotube with a diameter of few nanometres. Noteworthy, these AFM images recall to a smaller extent the measurements conducted on **$[Tb(hfac)_3.NITPhOPh]_n$** crystals drop-casted on mica surface (see Part.2.2.3), which lead to the observation of small crystallites. In this case, because our starting materials are solutions, the presence of these crystals is probably due to an on-surface crystallisation process.

New deposition tests have been performed with solutions of higher concentration (C_m = 2 mg·mL^{-1}) to evaluate the latter's impact on the formation of either crystals or nanotubes. From this concentration, networks of entangled fibres are visible for each 2 mg·mL^{-1} **TbC$_n$** gels derivatives, resulting from a self-assembly organisation with noticeable differences depending on the aliphatic chain length.

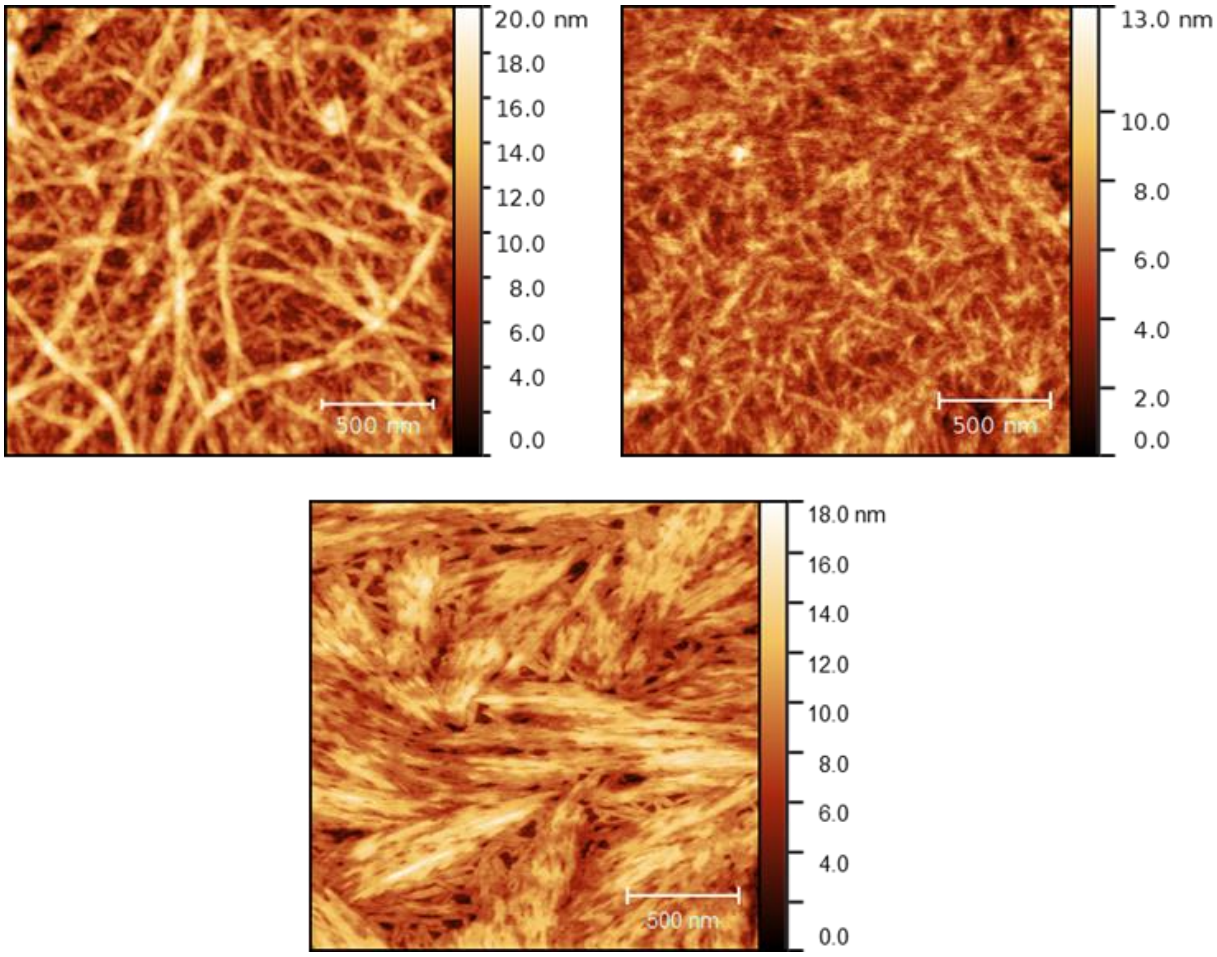

Figure 5.27. AFM topography images of 2 mg·mL^{-1} *n*-heptane gels of **TbC$_6$** (left), **TbC$_{10}$** (right) and **TbC$_{18}$** (bottom).

TbC$_6$ shows homogeneous and well-defined tubular structures, long of several hundreds of nanometres to few micrometres, but with no definite handedness. A rough estimation of few tens of nanometres of diameter, confronted with the values deducted by SAXS experiments for one tube, indicate that such fibres are made of wrapping of several tubular units. Similar conclusions hold for the thin film of **TbC$_{10}$** gel, although the fibres appear smaller and randomly distributed. Finally, for the **TbC$_{18}$** thin film, the fibres seem organised in dense brush-like bundles of small fibres. Interestingly, smaller structures can be seen on darker areas, which could correspond to isolated fibres on the silicon surface.

Anyway, these AFM images show the strong influence of the aliphatic chain length from the NIT radical on the resulting morphologies observed on surface, despite the chemical and structural similarities deducted from the previous SAXS study.

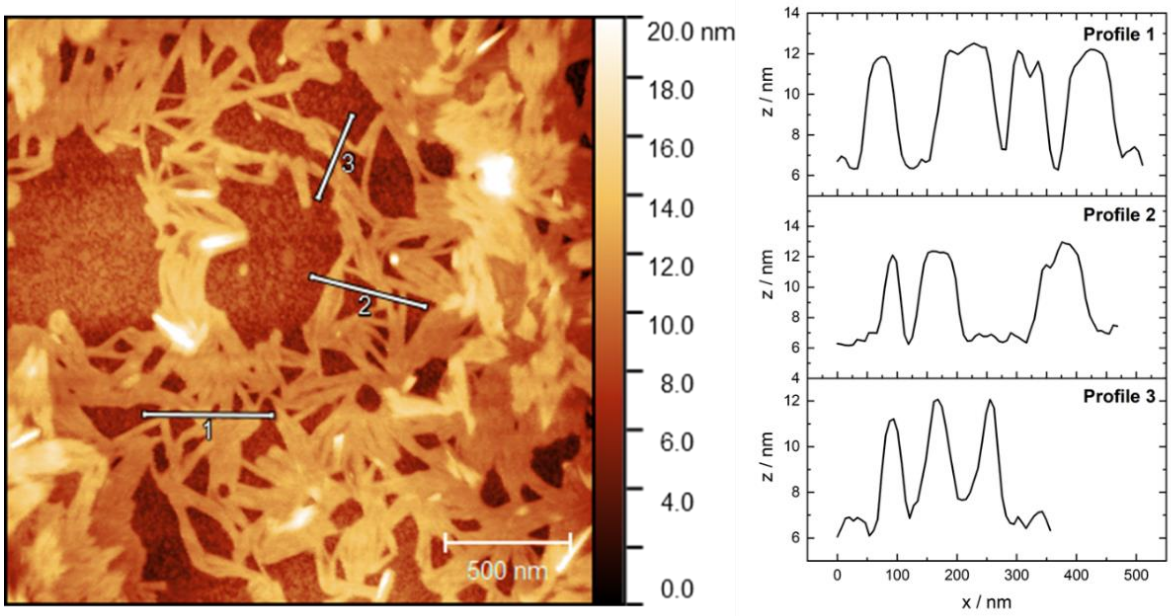

Figure 5.28. AFM topography image of a 1.7 mg·mL^{-1} *n*-heptane gel of **TbC$_{18}$** and relative height profiles.

We have then screened the concentrations between these two values to observe single nanotubes. For the **TbC$_{18}$** thin film at a concentration of C_m = 1.7 mg·mL^{-1}, isolated fibres were successfully observed on the silicon substrate (the dark area), allowing the determination of their dimension. Even though their width cannot be perfectly estimated because of the convolution of the AFM tip, they share a common height of around 6 nm, of the same order of magnitude as the diameters of the tubular objects determined by SAXS measurements thus suggesting that we successfully deposited *one* layer of SCMs.

It is worth of noticing that this is however just the first and essential step in the direction of achieving the *controlled* deposition of SCM on surface, if the nanotubular structure seems preserved, it does not ensure that it is the case of magnetic properties. In the near future, it will be planned experiments on these deposits by X-ray Circular Magnetic Dichroism at ultra-low temperature, as soon as the unique setup available worldwide will be again accessible.[49] This synchrotron based experiment will permit to evaluate if the SCM behaviour observed in bulk will persist at the nanoscale.

5.6. Conclusion

In this chapter, we have established and optimised a protocol to obtain a new kind of soft-matter magnetic compounds from $Tb(hfac)_3$ and aliphatic NIT building blocks. Gelation and stability studies have stressed the importance of the interactions between aliphatic solvents and the alkyl chains from the bridging NIT radicals. SAXS measurements have allowed insights into the structural organisation of these gels, that self-assembly into large nanotubes as for the **chains**. Because of these similar arrangements, slow relaxation of the magnetisation of SCM origin and open hysteresis loops have been measured, which is unprecedented for metallogels. We have also demonstrated that such nanotubular structures can be deposited and observed on surface, thanks to enhanced supramolecular interactions.

This metallogel approach could be a promising way to synthesise new functional materials from known crystalline systems and extend their field of application, taking advantage of the properties of gels. It is actually also a way to bypass the difficulties inherent to the deposition of crystalline coordination polymers and SCM, in particular, on surface.

5.7. References

[1] F. Fages, *Angew. Chem. Int. Ed.* **2006**, *45*, 1680–1682.

[2] J. W. Steed, *Chem Soc Rev* **2009**, *38*, 506–519.

[3] H. Wu, J. Zheng, A. Kjøniksen, W. Wang, Y. Zhang, J. Ma, *Adv. Mater.* **2019**, *31*, 1806204.

[4] K. Kuroiwa, T. Shibata, A. Takada, N. Nemoto, N. Kimizuka, *J. Am. Chem. Soc.* **2004**, *126*, 2016–2021.

[5] O. Roubeau, A. Colin, V. Schmitt, R. Clérac, *Angew. Chem. Int. Ed.* **2004**, *43*, 3283–3286.

[6] P. Grondin, O. Roubeau, M. Castro, H. Saadaoui, A. Colin, R. Clérac, *Langmuir* **2010**, *26*, 5184–5195.

[7] P. Grondin, D. Siretanu, O. Roubeau, M.-F. Achard, R. Clérac, *Inorg. Chem.* **2012**, *51*, 5417–5426.

[8] S. Bhowmik, S. Banerjee, U. Maitra, *Chem. Commun.* **2010**, *46*, 8642.

[9] H. Kim, J. Young Chang, *RSC Adv* **2013**, *3*, 1774–1780.

[10] C. Kim, K. Y. Kim, J. H. Lee, J. Ahn, K. Sakurai, S. S. Lee, J. H. Jung, *ACS Appl. Mater. Interfaces* **2017**, *9*, 3799–3807.

[11] J. Y. R. Silva, L. L. da Luz, F. G. M. Mauricio, I. B. Vasconcelos Alves, J. N. de S. Ferro, E. Barreto, I. T. Weber, W. M. de Azevedo, S. A. Júnior, *ACS Appl. Mater. Interfaces* **2017**, *9*, 16458–16465.

[12] Z. Li, Z. Hou, H. Fan, H. Li, *Adv. Funct. Mater.* **2017**, *27*, 1604379.

[13] F. Chen, Y.-M. Wang, W. Guo, X.-B. Yin, *Chem. Sci.* **2019**, *10*, 1644–1650.

[14] A. Sebastian, M. K. Mahato, E. Prasad, *Soft Matter* **2019**, *15*, 3407–3417.

[15] Q. Evrard, F. Houard, C. Daiguebonne, G. Calvez, Y. Suffren, O. Guillou, M. Mannini, K. Bernot, *Inorg. Chem.* **2020**, *59*, 9215–9226.

[16] J. Cui, Y. Zheng, Z. Shen, X. Wan, *Langmuir* **2010**, *26*, 15508–15515.

[17] F.-K. Zhan, S.-M. Hsu, H. Cheng, H.-C. Lin, *RSC Adv.* **2015**, *5*, 48961–48964.

[18] H.-K. Yang, H. Zhao, P.-R. Yang, C.-H. Huang, *Colloids Surf. Physicochem. Eng. Asp.* **2017**, *535*, 242–250.

[19] A. Noro, M. Hayashi, Y. Matsushita, *Soft Matter* **2012**, *8*, 6416.

[20] Y. Lan, M. G. Corradini, R. G. Weiss, S. R. Raghavan, M. A. Rogers, *Chem. Soc. Rev.* **2015**, *44*, 6035–6058.

[21] P. Terech, R. Ramasseul, F. Volino, *J. Colloid Interface Sci.* **1983**, *91*, 280–282.

[22] P. Terech, *J. Colloid Interface Sci.* **1985**, *107*, 244–255.

[23] M. Kveder, M. Andreis, J. Makarević, M. Jokić, B. Rakvin, *Chem. Phys. Lett.* **2006**, *420*, 443–447.

[24] M. Mannini, S. Cicchi, D. Berti, A. Caneschi, A. Brandi, L. Lascialfari, L. Sorace, *ChemPlusChem* **2013**, *78*, 149–156.

[25] Y. Takemoto, T. Yamamoto, N. Ikuma, Y. Uchida, K. Suzuki, S. Shimono, H. Takahashi, N. Sato, Y. Oba, R. Inoue, M. Sugiyama, H. Tsue, T. Kato, J. Yamauchi, R. Tamura, *Soft Matter* **2015**, *11*, 5563–5570.

[26] N. Hogg, *Free Radic. Biol. Med.* **2010**, *49*, 122–129.

[27] A. Collauto, M. Mannini, L. Sorace, A. Barbon, M. Brustolon, D. Gatteschi, *J. Mater. Chem.* **2012**, *22*, 22272.

[28] R. Kakavandi, S.-A. Savu, L. Sorace, D. Rovai, M. Mannini, M. B. Casu, *J. Phys. Chem. C* **2014**, *118*, 8044–8049.

[29] L. Poggini, G. Cucinotta, L. Sorace, A. Caneschi, D. Gatteschi, R. Sessoli, M. Mannini, *Rendiconti Lincei Sci. Fis. E Nat.* **2018**, *29*, 623–630.

[30] T. M. Stawski, L. G. Benning, in *Methods Enzymol.*, Elsevier, **2013**, pp. 95–127.

[31] L. A. Feĭgin, D. I. Svergun, *Structure Analysis by Small-Angle X-Ray and Neutron Scattering*, Springer US, **1987**.

[32] G. Beaucage, H. K. Kammler, S. E. Pratsinis, *J. Appl. Crystallogr.* **2004**, *37*, 523–535.

[33] B. Shao, S. Wan, C. Yang, J. Shen, Y. Li, H. You, D. Chen, C. Fan, K. Liu, H. Zhang, *Angew. Chem. Int. Ed.* **2020**, *59*, 18213–18217.

[34] C. G. Sonwane, S. K. Bhatia, N. J. Calos, *Langmuir* **1999**, *15*, 4603–4612.

[35] P. K. Chattopadhyay, N. C. Das, S. Chattopadhyay, *Compos. Part Appl. Sci. Manuf.* **2011**, *42*, 1049–1059.

[36] S. Tan, D. Zhang, E. Zhou, *Polymer* **1997**, *38*, 4571–4575.

[37] Z. H. Li, Y. J. Gong, D. Wu, Y. H. Sun, J. Wang, Y. Liu, B. Z. Dong, *Surf. Interface Anal.* **2001**, *31*, 897–900.

[38] S. Chibowski, M. Wiśniewska, A. . Marczewski, S. Pikus, *J. Colloid Interface Sci.* **2003**, *267*, 1–8.

[39] R. P. Rambo, J. A. Tainer, *Biopolymers* **2011**, *95*, 559–571.

[40] A. G. Kikhney, *FEBS Lett.* **2015**, 8.

[41] M. G. F. Vaz, R. A. A. Cassaro, H. Akpinar, J. A. Schlueter, P. M. Lahti, M. A. Novak, *Chem. - Eur. J.* **2014**, *20*, 5460–5467.

[42] X. Liu, X. Feng, K. R. Meihaus, X. Meng, Y. Zhang, L. Li, J. Liu, K. S. Pedersen, L. Keller, W. Shi, Y. Zhang, P. Cheng, J. R. Long, *Angew. Chem. Int. Ed.* **2020**, *59*, 10610–10618.

[43] X. Huang, K. Wang, J. Han, J. Xie, L. Li, J.-P. Sutter, *Dalton Trans.* **2021**, *50*, 11992–11998.

[44] N. Ishii, Y. Okamura, S. Chiba, T. Nogami, T. Ishida, *J. Am. Chem. Soc.* **2008**, *130*, 24–25.

[45] Y. Okamura, N. Ishii, T. Nogami, T. Ishida, *Bull. Chem. Soc. Jpn.* **2010**, *83*, 716–725.

[46] L. Bogani, R. Sessoli, M. G. Pini, A. Rettori, M. A. Novak, P. Rosa, M. Massi, M. E. Fedi, L. Giuntini, A. Caneschi, D. Gatteschi, *Phys. Rev. B* **2005**, *72*, 064406.

[47] K. Bernot, F. Pointillart, P. Rosa, M. Etienne, R. Sessoli, D. Gatteschi, *Chem. Commun.* **2010**, *46*, 6458.

[48] J. Jung, M. Puget, O. Cador, K. Bernot, C. J. Calzado, B. Le Guennic, *Inorg. Chem.* **2017**, *56*, 6788–6801.

[49] J.-P. Kappler, E. Otero, W. Li, L. Joly, G. Schmerber, B. Muller, F. Scheurer, F. Leduc, B. Gobaut, L. Poggini, G. Serrano, F. Choueikani, E. Lhotel, A. Cornia, R. Sessoli, M. Mannini, M.-A. Arrio, P. Sainctavit, P. Ohresser, *J. Synchrotron Radiat.* **2018**, *25*, 1727–1735.

5.A. Appendices

5.A.1. Procedures

Gelation properties and "test tube inversion method"

Gelation properties were evaluated by introducing a precise amount of the targeted compound and a volume of solvent needed to reach the required weight concentration in a 2 mL vial. This vial was then closed and heated with a heat gun until the complete dissolution of the compound and homogenisation of the solution. The solution was cooled to 4°C for several minutes to hours, depending on the gelation dynamics of the compound and the concentration. The effective gelation of the sample was tested by inverting the vial: if the gel does not flow after one minute, then the test is positive.

Electron Paramagnetic Resonance

Fresh solution and gel samples were prepared inside quartz tubes. EPR spectra were recorded on a Bruker EMX–8/2.7 (X–band) spectrometer at room temperature.

Small Angle X-ray Spectroscopy

Fresh gel samples were prepared inside quartz capillaries. SAXS experiments were performed at room temperature, using X-ray patterns collected with a Pilatus 300k (Dectris, Grenoble, France) mounted on a GeniX 3D (Xenocs, Sassenage, France) microsource X-ray generator operating at 30 W with a monochromatic Cu(K_α) radiation is of λ = 1.541 Å. The sample-to-detector distance is 270 mm, and the diffraction patterns were recorded for reciprocal spacing $q = 4\pi \times \sin(\theta)/\lambda$ in a range of repetitive distances from 0.015 $Å^{-1}$ (418 Å) to 1.77 $Å^{-1}$ (8 Å). Images were transformed into graphics using a home-developed program.

Atomic Force Microscopy studies

AFM studies were performed on cleaned silicone substrates (Si/Cz <100>, n-doped, 2-5 Ω.cm, Virginia Semiconductors) on which 10 µL of gel solutions were dropped and spin-coated at 2000 rpm for 60 seconds. Fresh samples then were kept at 4°C for 2min, dried under a dry N_2 flux for 15 seconds and mounted on the AFM sample holder. Samples were measured in semicontact mode to avoid deterioration of the soft film, with an SPM Solver P47 Pro (NT-MDT Spectrum Instrument) and HQ:NSC36/Al BS silicon tips (cantilever B, 130 kHz, 2 $N.m^{-1}$, MikroMasch). Results and imaging were processed using Gwyddion software.

5.A.2. Synthesis and gelation properties

5.A.2.1. Syntheses of the NITPhOC$_n$ radicals (n = 10 and 18)

NITPhOC$_{10}$

2-(4'-(decyloxy)phenyl)-4,4,5,5-tetramethylimidazolin-1-oxyl-3-oxide

2.5 mmol (685 µL, 1 eq.) of commercially available 4-(decyloxy)benzaldehyde was added to 5 mmol (741 mg, 2 eq.) of Zn(BHA)Cl_2 in 50 mL of methanol, and stirred at room temperature for one day. The solution was dried and the remaining milky-white waxy solid was dissolved in 50 mL of cold CH_2Cl_2, then 50 mL of a $NaIO_4$ aqueous solution (641.6 mg, 3 mmol, 1.5 eq.) was added. The mixture immediately turned dark blue, the organic phase was washed several times with water (3 x 100 mL) and separated. The resultant organic solution was dried on Na_2SO_4, concentrated under reduced pressure and purified by flash silica gel (40-60 µm, 60 Å) column chromatography eluted with a 3/1 (*v/v*) ether/*n*-pentane solution. A dark blue fraction was collected and concentrated under reduced pressure, resulting of 350.6 mg (0.91 mmol) of fine blue crystalline solid. Yield: 36%. Single crystals suitable for single-crystal XRD were obtained by slow inter-diffusion of 0.05 mmol (19.5 mg) of NITPhOC$_{10}$ in 7 mL of CH_2Cl_2 layered with 10 mL of *n*-heptane, kept at 4°C. Single-crystals were isolated after few days. Elemental analysis (%) calcd. for $C_{23}H_{37}N_2O_3$: C 70.91; H 9.57; N 7.19. Found: C 71.37; H 9.59; N 7.29.

NITPhOC$_{18}$

2-(4'-(octadecyloxy)phenyl)-4,4,5,5-tetramethylimidazolin-1-oxyl-3-oxide

2.5 mmol (936 mg, 1 eq.) of commercially available 4-(octadecyloxy)benzaldehyde was added to 5 mmol (741 mg, 2 eq.) of Zn(BHA)Cl_2 in 50 mL of methanol, and stirred at room temperature for three days. The solution was dried and the remaining milky-white waxy solid was dissolved in 50 mL of cold CH_2Cl_2, then 50 mL of a $NaIO_4$ aqueous solution (641.6 mg, 3 mmol, 1.5 eq.) was added. The mixture immediately turned dark blue, the organic phase was washed several times with water (3 x 100 mL) and separated. The resultant organic solution was dried on Na_2SO_4, concentrated under reduced pressure and purified by flash silica gel (40-60 µm, 60 Å) column chromatography eluted with a 3/1 (*v/v*) ether/*n*-pentane solution. A dark blue fraction was collected and concentrated under reduced pressure, resulting in 313.6 mg (0.625 mmol) of fine blue crystalline solid. Yield: 25%. Single crystals suitable for single-crystal XRD were obtained by slow inter-diffusion of 0.05 mmol (25.5 mg) of NITPhOC$_{18}$ in 7 mL of CH_2Cl_2 layered with 10 mL of *n*-heptane, kept at 4°C. Single-crystals were isolated after few days. Elemental analysis (%) calcd. for $C_{23}H_{37}N_2O_3$: C 70.91; H 9.57; N 7.19. Found: C 71.37; H 9.59; N 7.29.

Table 5.A.7. Crystallographic parameters of **NITPhOC$_{10}$** and **NITPhOC$_{18}$**.

Name	NITPhOC$_{10}$	NITPhOC$_{18}$
M **(g.mol^{-1})**	389.54	501.75
Crystal system	Monoclinic	Monoclinic
Space group	P2$_1$/c (N°14)	P2$_1$/n (N°14)
a **(Å)**	8.4606(8)	7.4068(13)
b **(Å)**	31.157(3)	44.744(8)
c **(Å)**	9.0987(9)	8.8243(17)
α **[°]**	90	90
β **[°]**	111.456(4)	94.435(7)
γ **[°]**	90	90
V **[Å^3]**	2232.3(4)	2915.7(9)
Z	4	4
T **(K)**	150	150
2ϑ **range**	2.492 - 27.513	2.359 - 27.216
Reflns collected	5088	9894
Indep. reflns	5088	6097
Obs. reflns	4200	3869
Parameters	253	325
R$_1$[i] **[*I* > 2*σ*(*I*)] / *wR$_2$*[j] [*I* > 2*σ*(*I*)]**	7.75 / 20.69	17.88 / 46.94
GOF	0.880	1.769

5.A.2.2. Syntheses of [Tb(hfac)$_3$(NITPhOC$_n$)] (n = 6, 10, 18), "*TbC$_n$ precursors*"

0.1 mmol (81.6 mg, 1eq.) of [Tb(hfac)$_3$·2H$_2$O] was dissolved in 40 mL of dry boiling *n*-heptane. The solution was concentrated until the volume reached 10 mL, then cooled to 75°C. 0.1 mmol of NITPhOC$_n$ (33.3 mg, 38.9 mg and 50.1 mg for *n* = 6, 10, 18, resp.) dissolved in 3 mL of $CHCl_3$ was quickly added under stirring, and the obtained deep blue solution was then directly transferred to a 20 mL vial for immediate sonication. Pulsed sonication was performed with a Hielscher UP400 St sonicator using an S24d3 sonotrode (fixed frequency 24 kHz, diameter 3 mm) with a 90 % pulse rate (0.9 s of sonication/0.1 s of silence, ≈ 24 J per pulse) until 75 kJ were delivered. The final mixture was dried under reduced pressure at room temperature, giving a dark green powder for the TbNITPhOC$_6$ (TbC$_6$, yield: 59%) and TbNITPhOC$_{10}$ (TbC$_{10}$, yield: 60%), and a dark green latex-like solid for the TbNITPhOC$_{18}$ (TbC$_{18}$, yield: 65%).

[i] $\sum(|F_0| - |F_c|)/\sum|F_0|$

[j] $\sqrt{\sum w(|F_0|^2 - |F_c|^2)^2/\sum w(|F_0|^2)^2}$

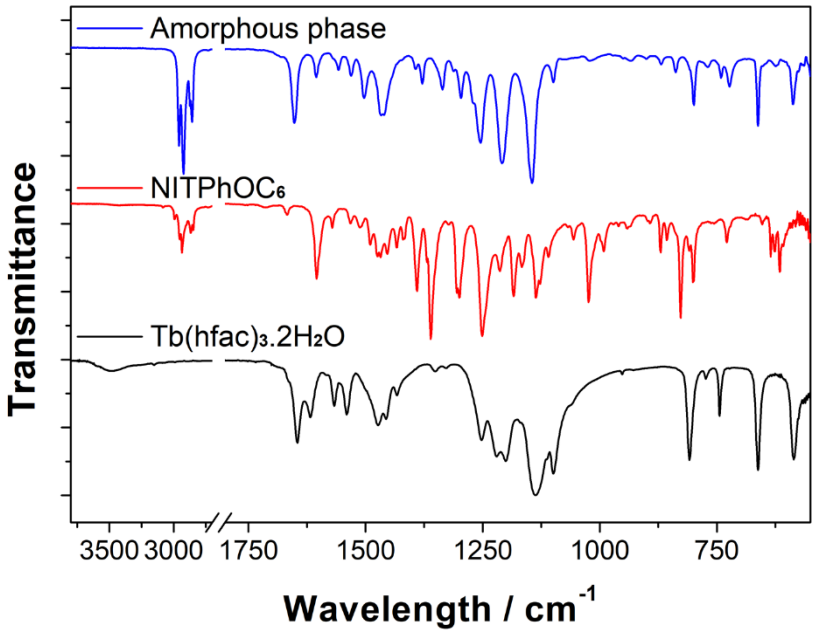

Figure 5.A.29. Comparative FTIR spectra of **[Tb(hfac)$_3$·2H$_2$O]**, **NITPhOC$_6$** and resulting amorphous phase.

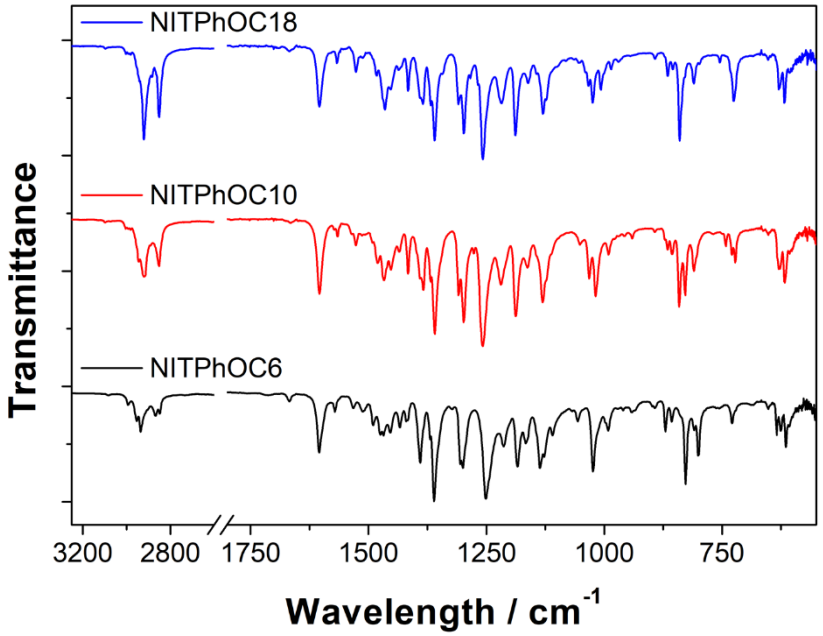

Figure 5.A.30. Comparative FTIR spectra of the **NITPhOC$_6$**, **NITPhOC$_{10}$** and **NITPhOC$_{18}$**.

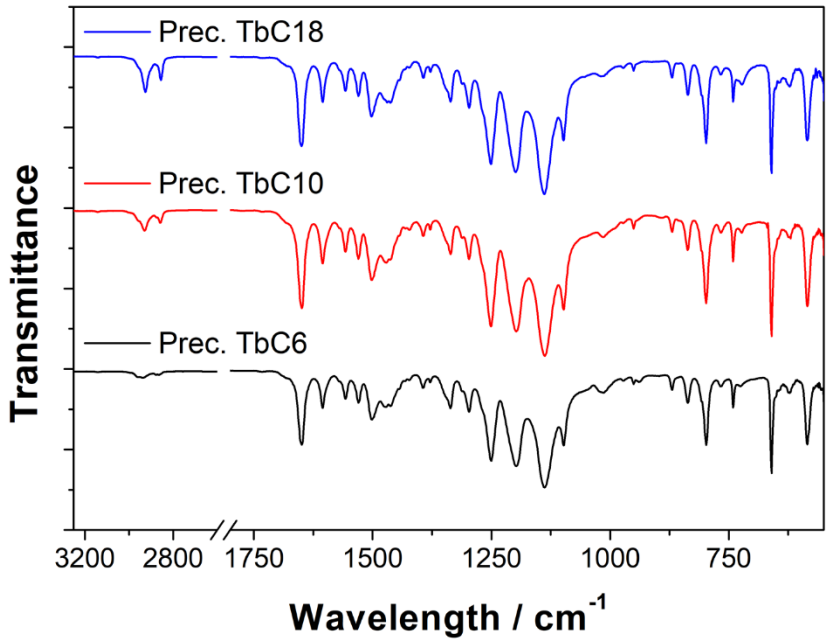

Figure 5.A.31. Comparative FTIR spectra of precursors of **TbC_6**, **TbC_{10}** and **TbC_{18}**.

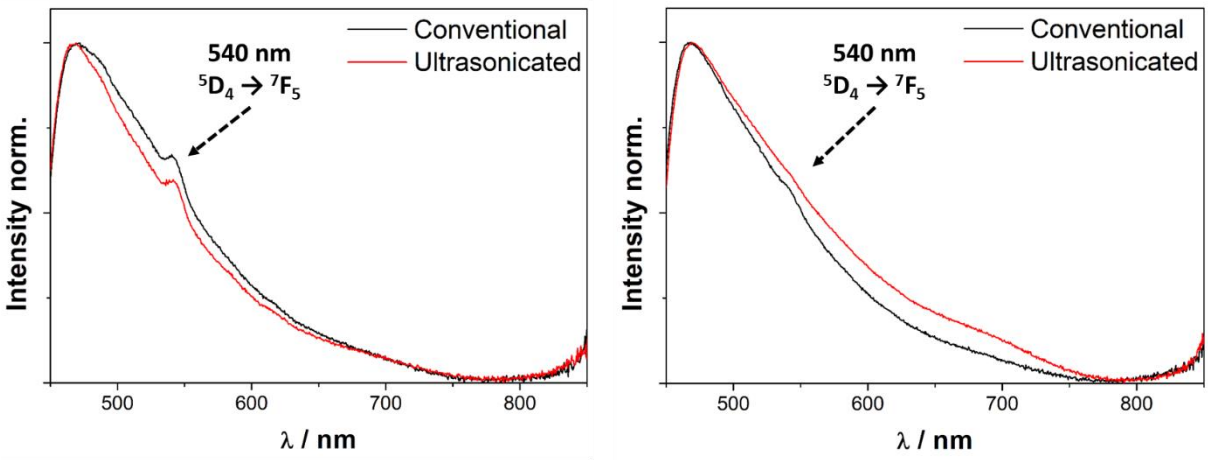

Figure 5.A.32. Solid-emission spectra (λ_{ex} = 300 nm) at 300 K of non-sonicated ("conventional") and "ultrasonicated" samples of **TbC_{10}** (left) and **TbC_{18}** (right) **precursors**.

5.A.3. Morphology and structural model

Table 5.A.8. Relative positions of the Tb^{III} atoms of a nanotube reconstructed from the structural model described in Part.5.3.3, for a unit cell of parameters $a = b = 36$ Å, $c = 283.42$ Å, $\alpha = \beta = \gamma = 90°$.

Helix n°1			Helix n°2			Helix n°3			Helix n°4		
x(t)	y(t)	z(t)	x(t)	y(t)	z(t)	x(t)	y(t)	z(t)	x(t)	y(t)	z(t)
1.000	0.500	0.027	0.869	0.838	0.024	0.544	0.998	0.020	0.196	0.897	0.016
0.992	0.591	0.044	0.802	0.899	0.040	0.453	0.998	0.036	0.129	0.836	0.032
0.967	0.678	0.060	0.724	0.947	0.056	0.364	0.981	0.052	0.075	0.763	0.048
0.927	0.760	0.076	0.640	0.980	0.072	0.279	0.948	0.068	0.034	0.682	0.064
0.873	0.833	0.092	0.550	0.997	0.088	0.201	0.901	0.084	0.009	0.594	0.080
0.807	0.895	0.108	0.460	0.998	0.105	0.134	0.840	0.101	0.000	0.504	0.097
0.730	0.944	0.125	0.370	0.983	0.121	0.078	0.768	0.117	0.008	0.413	0.113
0.646	0.978	0.141	0.285	0.951	0.137	0.036	0.687	0.133	0.032	0.325	0.129
0.557	0.997	0.157	0.206	0.905	0.153	0.010	0.600	0.149	0.071	0.243	0.145
0.466	0.999	0.173	0.138	0.845	0.169	0.000	0.510	0.165	0.124	0.170	0.161
0.376	0.984	0.189	0.082	0.774	0.185	0.007	0.419	0.182	0.190	0.107	0.178
0.290	0.954	0.206	0.039	0.693	0.202	0.029	0.331	0.198	0.267	0.058	0.194
0.212	0.908	0.222	0.011	0.607	0.218	0.068	0.249	0.214	0.351	0.023	0.210
0.142	0.849	0.238	0.000	0.516	0.234	0.120	0.175	0.230	0.440	0.004	0.226
0.085	0.779	0.254	0.006	0.426	0.250	0.186	0.111	0.246	0.530	0.001	0.242
0.041	0.699	0.270	0.027	0.337	0.266	0.261	0.061	0.262	0.620	0.015	0.259
0.013	0.613	0.287	0.065	0.254	0.283	0.345	0.025	0.279	0.706	0.045	0.275
0.001	0.523	0.303	0.116	0.180	0.299	0.433	0.004	0.295	0.785	0.089	0.291
0.005	0.432	0.319	0.181	0.115	0.315	0.524	0.001	0.311	0.855	0.148	0.307
0.025	0.343	0.335	0.256	0.064	0.331	0.614	0.013	0.327	0.913	0.218	0.323
0.061	0.260	0.351	0.339	0.027	0.347	0.700	0.042	0.343	0.957	0.297	0.340
0.112	0.184	0.367	0.427	0.005	0.364	0.780	0.086	0.360	0.986	0.384	0.356
0.176	0.119	0.384	0.518	0.000	0.380	0.850	0.143	0.376	0.999	0.474	0.372
0.250	0.067	0.400	0.608	0.012	0.396	0.909	0.213	0.392	0.996	0.564	0.388
0.333	0.029	0.416	0.695	0.039	0.412	0.955	0.292	0.408	0.976	0.653	0.404
0.421	0.006	0.432	0.775	0.082	0.428	0.985	0.377	0.424	0.940	0.737	0.420
0.511	0.000	0.448	0.846	0.139	0.445	0.999	0.467	0.441	0.890	0.813	0.437
0.602	0.010	0.465	0.906	0.208	0.461	0.997	0.558	0.457	0.827	0.878	0.453
0.689	0.037	0.481	0.952	0.286	0.477	0.978	0.647	0.473	0.753	0.931	0.469
0.769	0.079	0.497	0.983	0.371	0.493	0.943	0.731	0.489	0.671	0.970	0.485
0.841	0.135	0.513	0.998	0.461	0.509	0.894	0.808	0.505	0.583	0.993	0.501
0.902	0.202	0.529	0.997	0.552	0.525	0.832	0.874	0.522	0.492	1.000	0.518
0.949	0.280	0.546	0.980	0.641	0.542	0.759	0.928	0.538	0.402	0.990	0.534
0.981	0.365	0.562	0.946	0.726	0.558	0.677	0.968	0.554	0.315	0.964	0.550
0.998	0.455	0.578	0.898	0.803	0.574	0.589	0.992	0.570	0.234	0.923	0.566

Helix n°5			Helix n°6			Helix n°7			Helix n°8		
x(t)	y(t)	z(t)	x(t)	y(t)	z(t)	x(t)	y(t)	z(t)	x(t)	y(t)	z(t)
0.008	0.588	0.012	0.078	0.232	0.008	0.369	0.017	0.004	0.729	0.056	0.000
0.000	0.497	0.028	0.133	0.160	0.024	0.459	0.002	0.020	0.806	0.104	0.016
0.009	0.407	0.044	0.201	0.100	0.040	0.550	0.002	0.036	0.872	0.166	0.032
0.034	0.319	0.060	0.278	0.052	0.056	0.639	0.020	0.052	0.927	0.239	0.049
0.074	0.238	0.077	0.363	0.019	0.073	0.724	0.053	0.069	0.967	0.321	0.065
0.129	0.165	0.093	0.452	0.002	0.089	0.801	0.101	0.085	0.992	0.409	0.081
0.196	0.103	0.109	0.543	0.002	0.105	0.868	0.162	0.101	1.000	0.499	0.097
0.272	0.055	0.125	0.633	0.018	0.121	0.923	0.234	0.117	0.992	0.590	0.113
0.357	0.021	0.141	0.718	0.050	0.137	0.965	0.315	0.133	0.968	0.677	0.130
0.446	0.003	0.157	0.796	0.097	0.154	0.990	0.402	0.150	0.928	0.759	0.146
0.537	0.001	0.174	0.864	0.157	0.170	1.000	0.493	0.166	0.874	0.832	0.162
0.627	0.016	0.190	0.920	0.229	0.186	0.993	0.583	0.182	0.807	0.894	0.178
0.712	0.047	0.206	0.962	0.309	0.202	0.970	0.671	0.198	0.731	0.944	0.194
0.791	0.093	0.222	0.989	0.396	0.218	0.931	0.754	0.214	0.647	0.978	0.210
0.859	0.152	0.238	1.000	0.486	0.235	0.878	0.827	0.231	0.558	0.997	0.227
0.916	0.223	0.255	0.994	0.577	0.251	0.812	0.890	0.247	0.467	0.999	0.243
0.960	0.303	0.271	0.972	0.665	0.267	0.736	0.941	0.263	0.377	0.985	0.259
0.988	0.390	0.287	0.934	0.748	0.283	0.653	0.976	0.279	0.291	0.954	0.275
1.000	0.480	0.303	0.882	0.823	0.299	0.564	0.996	0.295	0.212	0.909	0.291
0.995	0.571	0.319	0.817	0.886	0.315	0.473	0.999	0.312	0.143	0.850	0.308
0.974	0.659	0.336	0.742	0.937	0.332	0.383	0.986	0.328	0.086	0.780	0.324
0.937	0.742	0.352	0.659	0.974	0.348	0.297	0.957	0.344	0.042	0.700	0.340
0.886	0.818	0.368	0.570	0.995	0.364	0.218	0.913	0.360	0.013	0.614	0.356
0.822	0.882	0.384	0.480	1.000	0.380	0.148	0.855	0.376	0.001	0.524	0.372
0.748	0.934	0.400	0.389	0.988	0.396	0.089	0.785	0.393	0.005	0.433	0.389
0.665	0.972	0.417	0.303	0.959	0.413	0.044	0.706	0.409	0.025	0.344	0.405
0.577	0.994	0.433	0.223	0.916	0.429	0.015	0.620	0.425	0.061	0.261	0.421
0.486	1.000	0.449	0.152	0.859	0.445	0.001	0.530	0.441	0.112	0.185	0.437
0.396	0.989	0.465	0.093	0.790	0.461	0.004	0.439	0.457	0.175	0.120	0.453
0.309	0.962	0.481	0.047	0.712	0.477	0.023	0.350	0.473	0.249	0.067	0.470
0.228	0.920	0.498	0.016	0.626	0.494	0.058	0.266	0.490	0.332	0.029	0.486
0.157	0.864	0.514	0.001	0.536	0.510	0.108	0.190	0.506	0.420	0.006	0.502
0.097	0.795	0.530	0.003	0.445	0.526	0.170	0.124	0.522	0.510	0.000	0.518
0.050	0.717	0.546	0.021	0.356	0.542	0.244	0.071	0.538	0.601	0.010	0.534
0.018	0.632	0.562	0.055	0.272	0.558	0.326	0.031	0.554	0.688	0.037	0.550

5.A.4. Magnetic properties

5.A.4.1. Static (DC) magnetic properties

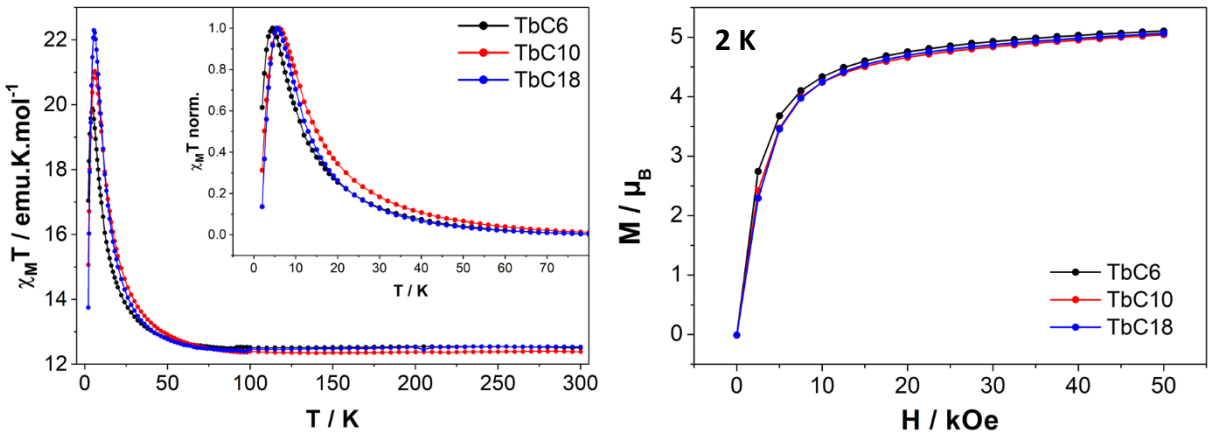

Figure 5.A.33. Temperature dependence of $\chi_M T$ measured with H_{DC} = 1000 Oe and with inset, a zoom in the low-temperature region of the normalised temperature dependence of $\chi_M T$ (left) and field dependence of magnetisation (right) of xerogels of **TbC$_6$**, **TbC$_{10}$** and **TbC$_{18}$**.

The values of the susceptibly product $\chi_M T_{(300K)}$ at room temperature of the **TbC$_6$**, **TbC$_{10}$** and **TbC$_{18}$** xerogels are resp. 12.50, 12.38 and 12.53 emu·K·mol^{-1}. Akin to the gels, they are close to the theoretical $\chi_M T_{(300\ K)}$ = 12.19 emu·K·mol^{-1} for a free Tb^{III} ion (J = 6, g_J = 3/2) and an uncoupled radical (S = 1/2, g_S = 2). These $\chi_M T$ reach maxima of 19.88 emu·K·mol^{-1} at 4.5K (**TbC$_6$**), 21.04 at 6.0 K (**TbC$_{10}$**) and 22.30 emu·K·mol^{-1} at 5.5 K (**TbC$_{18}$**).

Their saturation M_{sat} values are 5.1, 5.0 and 5.1 μ_B (for **TbC$_6$**, **TbC$_{10}$** and **TbC$_{18}$** resp.), slightly below the theoretical value of 5.5 μ_B.

5.A.4.2. Dynamic (AC) magnetic properties

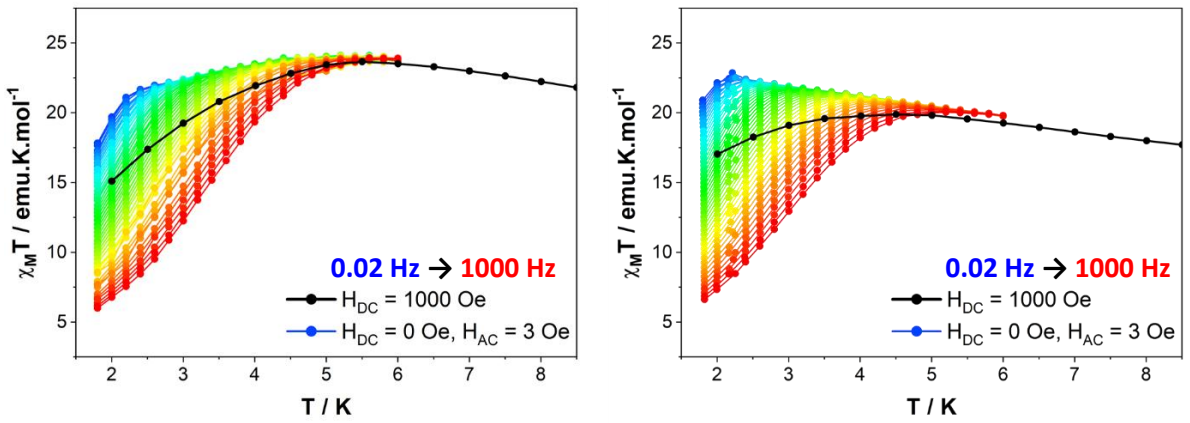

Figure 5.A.34. Temperature dependence of $\chi_M T$ measured with H_{DC} = 1000 Oe (open circles) and reconstructed from AC measurements with H_{AC} = 3 Oe (filled dots) at different frequencies for *n*-heptane gel (C_m = 10 mg·mL^{-1}) (left) and xerogel (right) of **TbC$_6$**.

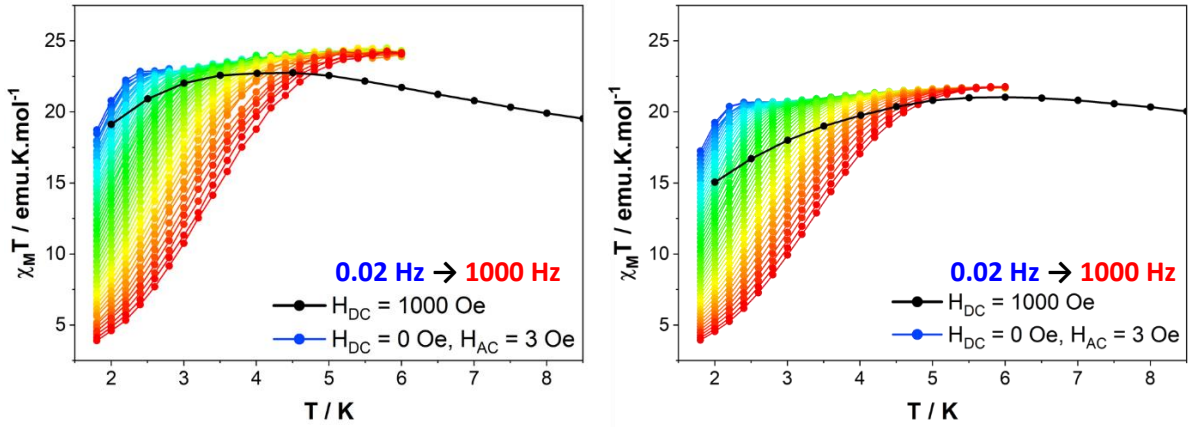

Figure 5.A.35. Temperature dependence of $\chi_M T$ measured with H_{DC} = 1000 Oe (open circles) and reconstructed from AC measurements with H_{AC} = 3 Oe (filled dots) at different frequencies for *n*-heptane gel (C_m = 10 mg·mL^{-1}) (left) and xerogel (right) of **TbC$_{10}$**.

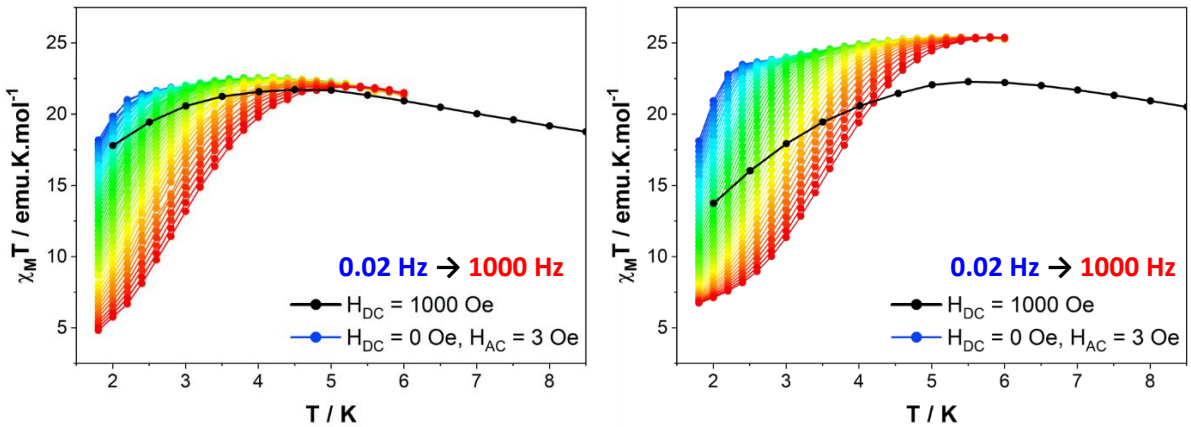

Figure 5.A.36. Temperature dependence of $\chi_M T$ measured with H_{DC} = 1000 Oe (open circles) and reconstructed from AC measurements with H_{AC} = 3 Oe (filled dots) at different frequencies for *n*-heptane gel (C_m = 10 mg·mL^{-1}) (left) and xerogel (right) of **TbC$_{18}$**.

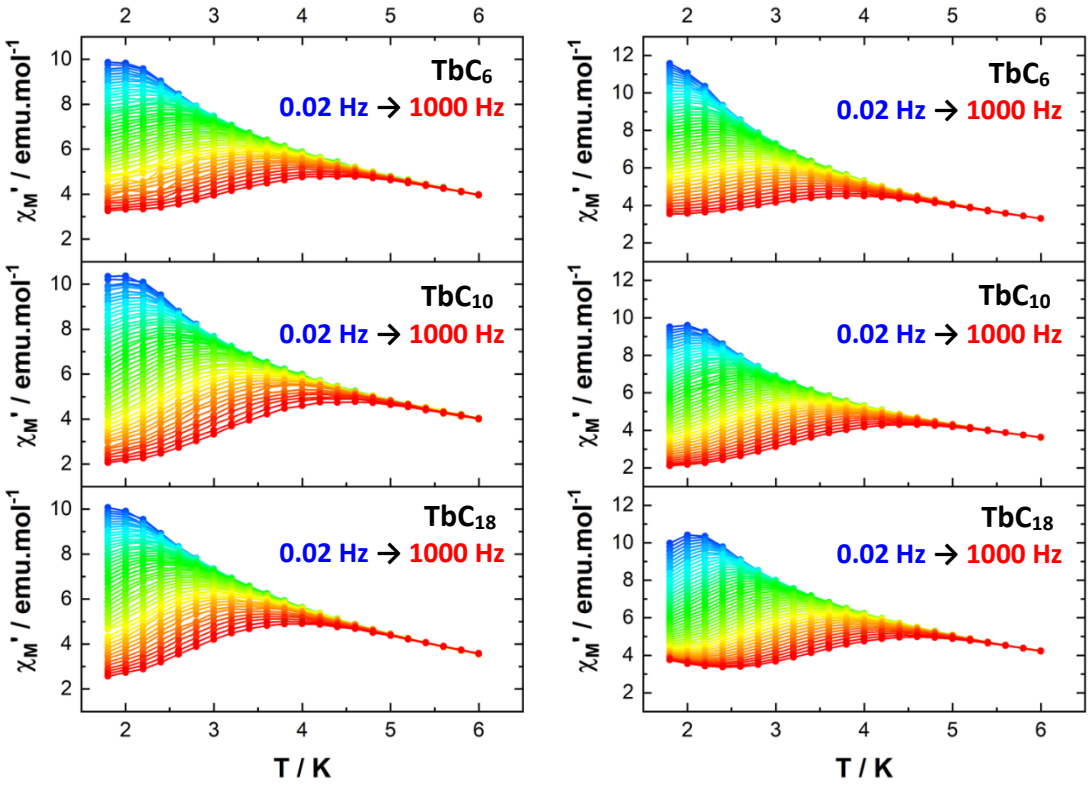

Figure 5.A.37. Temperature dependence of the in-phase (χ_M') susceptibility at different frequencies for *n*-heptane gel (C_m = 10 mg·mL^{-1}) (left) and xerogel (right) of **TbC$_6$**, **TbC$_{10}$** and **TbC$_{18}$**.

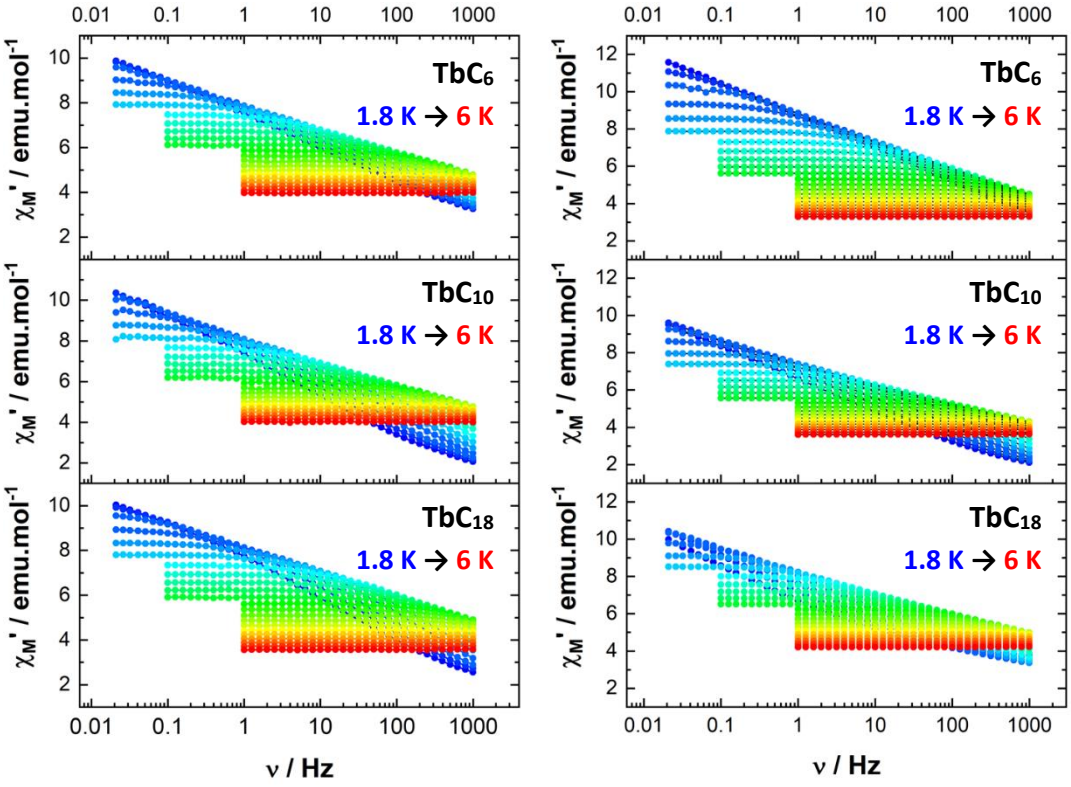

Figure 5.A.38. Frequency dependence of the in-phase (χ_M') susceptibility at different frequencies for *n*-heptane gel (C_m = 10 mg·mL^{-1}) (left) and xerogel (right) of **TbC$_6$**, **TbC$_{10}$** and **TbC$_{18}$**.

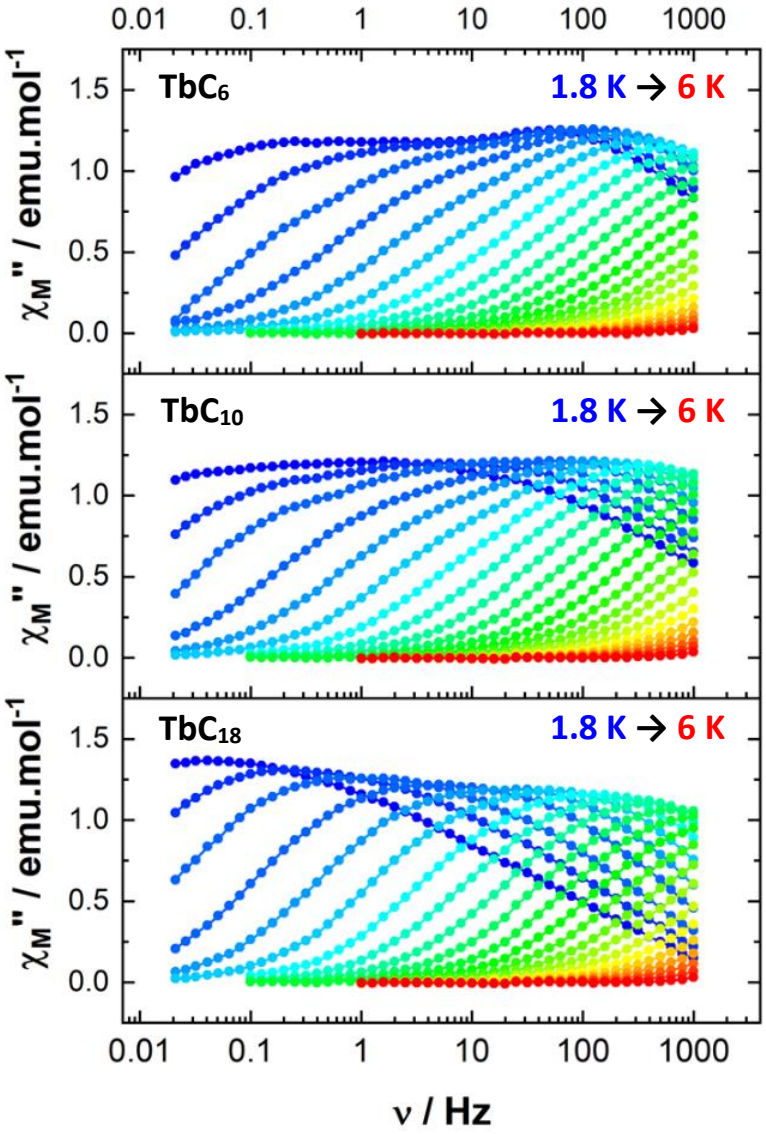

Figure 5.A.39. Frequency dependencies of the out-of-phase (χ_M'') susceptibility at different temperatures of xerogels of **TbC$_6$**, **TbC$_{10}$** and **TbC$_{18}$** (C_m = 10 mg·mL^{-1}).

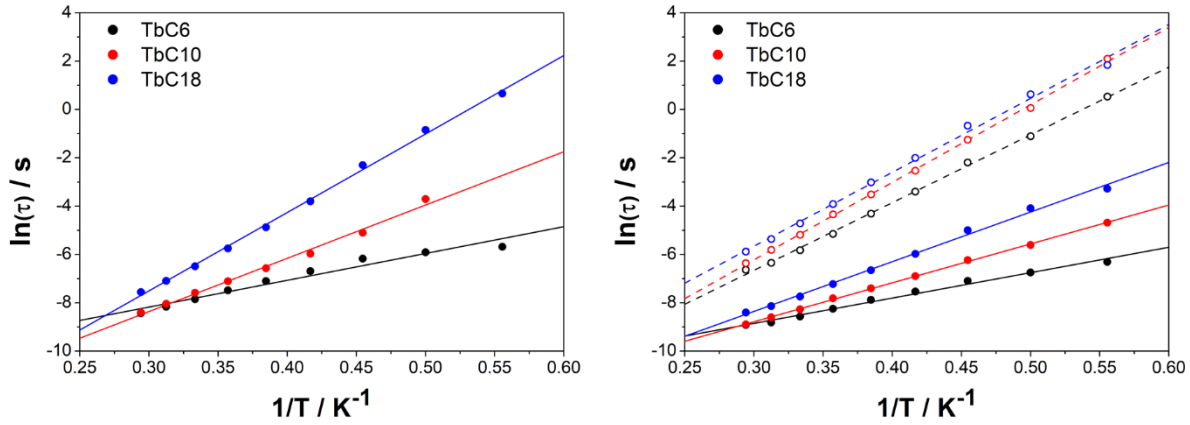

Figure 5.A.40. Arrhenius plots of the extracted relaxation times of xerogels of **TbC_6**, **TbC_{10}** and **TbC_{18}** with fast (filled dots) and low (open circles) relaxation times.

Table 5.A.9. Characteristic values extracted from the Arrhenius plots of the xerogels of **TbC_6**, **TbC_{10}** and **TbC_{18}**, considering a single relaxation process.

	Single relaxation process		
	TbC_6	**TbC_{10}**	**TbC_{18}**
Δ_{eff}/k_B **(K)**	11.1 ± 0.8	22.0 ± 0.8	32.5 ± 0.6
τ_0 **(s)**	(1.0 ± 0.4) x 10^{-5}	(3.2 ± 1.1) x 10^{-7}	(4.9 ± 1.0) x 10^{-7}
R^2	0.9554	0.9912	0.9976

Table 5.A.10. Characteristic values extracted from the Arrhenius plots of the xerogels of **TbC_6**, **TbC_{10}** and **TbC_{18}**, considering a double relaxation process.

	Double relaxation process					
	TbC_6		**TbC_{10}**		**TbC_{18}**	
	Slow	**Fast**	**Slow**	**Fast**	**Slow**	**Fast**
Δ_{eff}/k_B **(K)**	28.0 ± 0.4	10.5 ± 0.4	32.1 ± 0.3	16.1 ± 0.1	30.6 ± 0.7	20.5 ± 0.5
τ_0 **(s)**	(2.9 ± 0.5) x 10^{-7}	(6.1 ± 1.0) x 10^{-6}	(1.3 ± 0.2) x 10^{-7}	(1.2 ± 0.1) x 10^{-7}	(3.6 ± 1.2) x 10^{-7}	(5.0 ± 1.1) x 10^{-7}
R^2	0.9982	0.9890	0.9993	0.9993	0.9957	0.9956

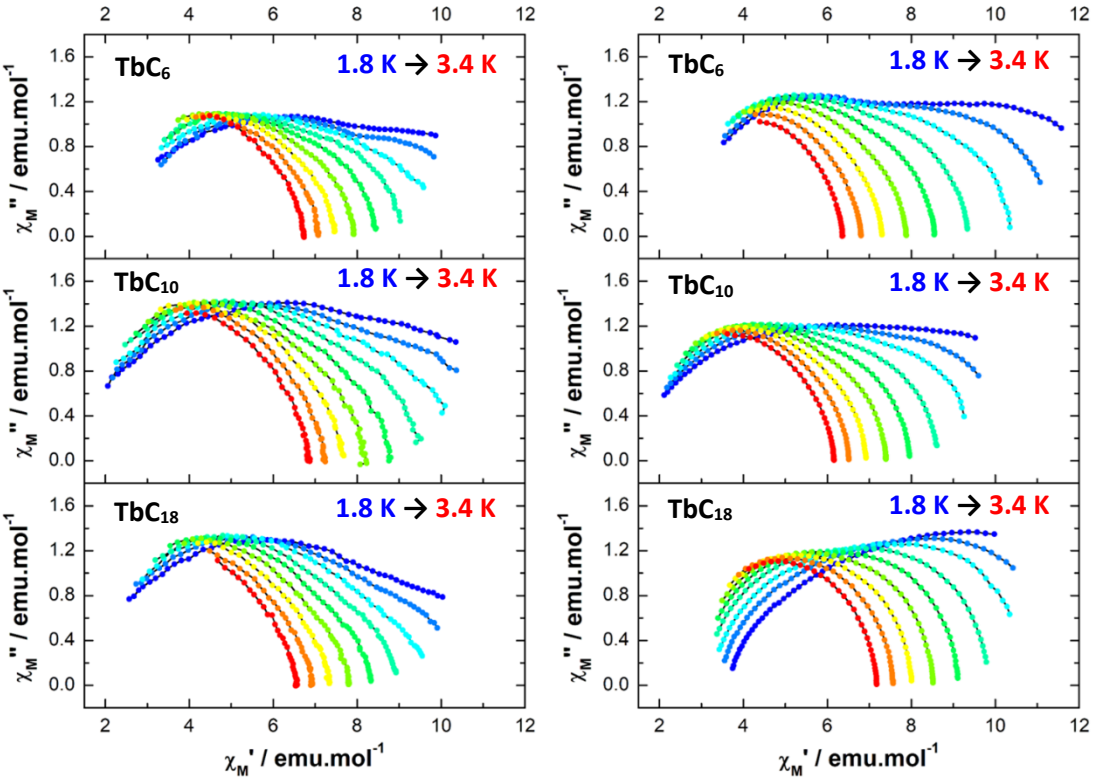

Figure 5.A.41. Argand diagrams at different temperatures for *n*-heptane gel (C_m = 10 mg·mL^{-1}) (left) and xerogel (right) of **TbC$_6$**, **TbC$_{10}$** and **TbC$_{18}$**.

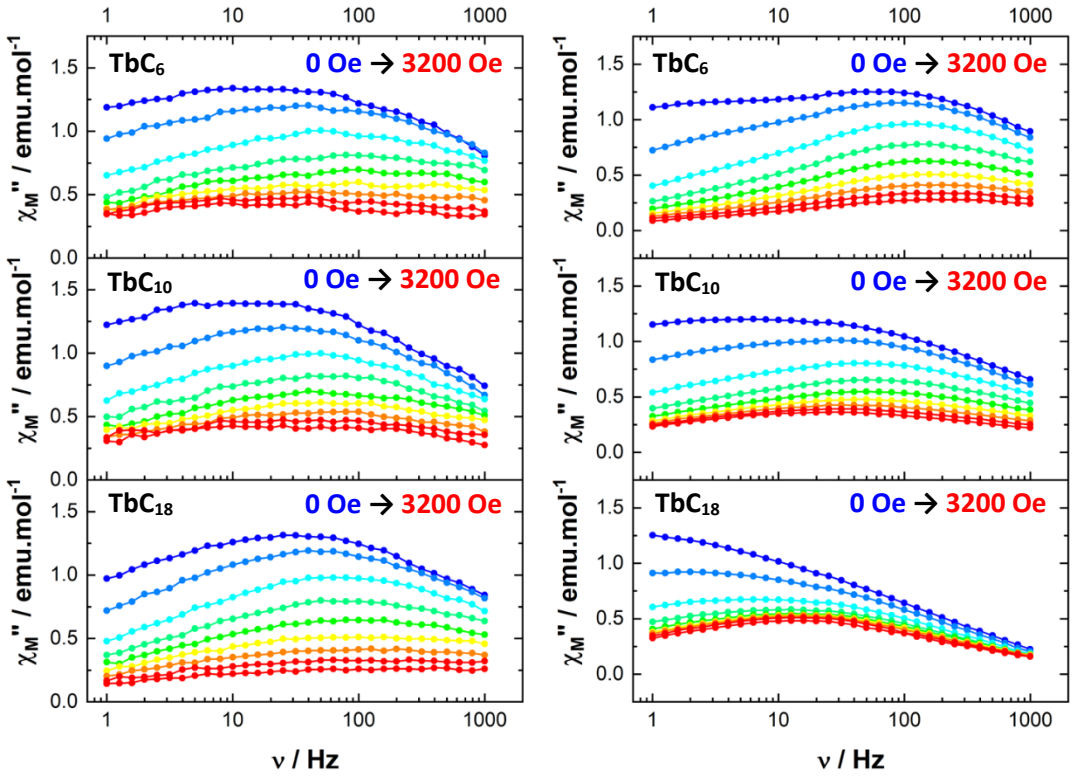

Figure 5.A.42. Frequency dependence of the out-of-phase (χ_M'') susceptibility at different fields H_{DC} fields measured at 2 K for *n*-heptane gel (C_m = 10 mg·mL^{-1}) (left) and xerogel (right) of **TbC$_6$**, **TbC$_{10}$** and **TbC$_{18}$**.

Conclusion

This thesis sought to develop a new approach to the surface deposition of Single-Chain Magnets. We have targeted a particular family of SCMs consisting of highly anisotropic 4*f* lanthanide ions and organic NIT radicals, which can be easily functionalised at this end. A new family of SCM have been synthesised, and their structural and magnetic properties have been reported.

We first investigated a deposition method with an already known SCM, the **$[Tb(hfac)_3(NITPhOPh)]_n$**. The aim was to disperse its constituting single-chains in a solvent by sonication, which would then be deposited on the surface by drop-casting. However, the resulting objects observed by AFM did not correspond to expected isolated chains but large crystallites. Nevertheless, by attempting to reproduce an *in-situ* coordination phenomenon by studying the separate deposition of the corresponding building blocks, we obtained a polymeric arrangement of **$[Tb(hfac)_3{\cdot}2H_2O]_n$** on mica. This deposit has been characterised and shows magnetic and luminescent properties comparable to those of the crystalline phase.

Considering that the molecular packing of **$[Tb(hfac)_3(NITPhOPh)]_n$** was too rigid and compact for a sufficiently gentle dissociation step, we synthesized a new bridging **$NITPhOC_6$** radical. By substituting the phenyl group with an aliphatic chain, we provide more flexibility and spacing to the coordination polymer to dissociate the single-chains from the crystal more easily. Thanks to these additional degrees of freedom, the resulting **$[Tb(hfac)_3(NITPhOC_6)]_n$** (**chains**) coordination polymer grows in helices, with a consequent pitch of 20 nm. These helices organise themselves in a supramolecular manner, favoured by weak interactions with the aliphatic solvent, to form cylindrical nanotubes. The magnetic properties of this coordination polymer were determined by static and alternative susceptibility measurements. Although these chains are woven together, they are nevertheless sufficiently spaced to be isolated from the magnetic point of view. They exhibit a SCM behaviour with an open hysteresis.

Curiously, crystals with different morphology were observed during the crystallization of the **chains**. What we thought was a polymorph turned out to be a finite linear complex, **$[(Tb(hfac)_3)_6(NITPhOC_6)_5(H_2O)_2]$** (**hexanuclears**), end-capped by water molecules. The presence of the latter allowed us to isolate the experimental parameters to obtain either the chains or the hexanuclears selectively. Although these two systems are chemically close, their magnetic properties can differ dramatically: the former is an infinite chain, structurally prone to magnetic correlation and SCM behaviour, while the latter is a finite complex, albeit linked to its neighbours by H-bonds. Magnetic measurements, however, revealed SCM behaviour close to the chains, as the characteristic correlation length is confined within the molecule.

Finally, to obtain new supramolecular organisations, we wanted to investigate further the influence of the size of the aliphatic chain carried by the NIT radical. By coordinating $Tb(hfac)_3$

moieties with **NITPhOC$_n$** (n = 6, 10, 18), we have established a protocol to obtain the corresponding **TbC$_n$** metallogels. The latter, studied by SAXS, revealed a nanotube organisation similar to that observed for the chains. Thanks to the information provided by this technique, we were able to establish a 3D model of these nanotubes. The analogy between the crystal and the gels is confirmed with the magnetic characterisations as the gels showed features compatible with a SCM behaviour, such as the divergence of the $\chi_M T$ at low temperature, and slow relaxation of the magnetisation leading to an open hysteresis at low temperature. Taking advantage of this gel state, we were able to deposit and observe single fibres, whose characteristic sizes estimated by AFM correspond to those determined by SAXS for a single nanotube thus indicating that the adopted strategy can allow the deposition of a single layer of these objects. This strategy will require to be further optimised for instance developing a protocol for the alignment of SCMs and also to be associated with a careful magnetic characterisation that however requires to have access to a unique instrumentation that unfortunately will be available only after the end of this PhD thesis.

As a summary, we have demonstrated that the functionalisation of the NIT radical could induce dramatic structural changes and open the way to a new class of supramolecular magnetic materials, “the supramolecular nanotubes of SCMs”. Taking advantage of these results, we have adopted a "crystal-to-gel" approach to bypass the limitations imposed by the crystalline state of coordination polymers for their surface deposition. This has allowed us to obtain coordination mettalogel magnets, absent from the scientific literature until now.

Further investigations are needed to gain deeper understandings of these compounds and their potentialities. Indeed, the NIT radicals here have been functionalized with single aliphatic chains. It is easy to imagine that introducing new functions (amides, thiols, *etc.*) could promote new supramolecular organisations and better affinity with surfaces, and permit a controlled arrangement of these objects on surface.

Moreover, our studies so far have been focused on the Tb^{III} ion in order to compare the different compounds. However, they can be extended to other 4*f* ions to modulate the magnetic response while preserving the structures. Co^{II} can also be considered for new molecular organisations and improved magnetic performance, because of its enhanced magnetic coupling with the NIT radicals.

Furthermore, the porosity of the nanotubes and their large diameter, whether crystals or gels, can also lead to inclusion studies. Small magnetic or luminescent molecules can be considered to obtain multifunctional materials.

Finally, the study of the **TbC$_n$** gels has been extended to their deposition on surface. If the nanotubes seem to have been preserved during the deposition process in the case of **TbC$_{18}$**, we have no clues about their magnetic properties. To do this, it would be necessary to measure these deposits using specific characterisation techniques for objects on the surface that are the state of the art of the magnetic characterisation either using averaged surface measurements based on synchrotron experiments, or using local probes such as scanning probe based spectroscopies.

Methods

Single crystal X-ray diffraction

Fresh single crystals were mounted on a Bruker D8 Venture. Crystal data collection was performed with MoKα radiation (λ = 0.70713 Å). Crystal structures were solved using SHELXT[1] and refined with SHELXL[2] via the WINGX program.[3]

Unless explicitly indicated, all non-hydrogen atoms were refined anisotropically, hydrogen atoms bound to organic ligands located at ideal positions, and a SQUEEZE procedure was used to remove disordered solvent molecules if required.[4]

Powder X-ray diffraction

Experimental diffraction patterns have been collected with a Panalytical X'pert Pro diffractometer, equipped with an X'Celerator detector. Typical recording conditions were 45 kV, 40 mA for CuK_α (λ = 1.542 Å) in θ/θ mode. Calculated patterns from single-crystal measurements were simulated using the Mercury program from CCDC.

Fourier Transformed Infra-Red spectroscopy

FTIR studies were performed with a Perkin Elmer Frontier UATR spectrometer on as-synthesised powders (from 4000 to 550 cm^{-1}, res. 1 cm^{-1}).

STA-coupled FTIR studies were performed in a ceramic crucible between room temperature and 950°C under N_2 atmosphere with the same spectrometer (from 4000 to 550 cm^{-1}, res. 2 cm^{-1}), coupled to a Perkin Elmer Simultaneous Thermal Analyzer STA6000 at a heating rate of 20°C min^{-1} thanks to a Perkin Elmer Transfer Line TL8000.

UV-Visible spectroscopy

UV-Visible absorption spectra of solutions and gels were recorded with a Jasco-V670 (from 800 to 350 nm, 400 $nm.min^{-1}$, res. 1 nm) in 1mm Hellma 110-QS cuvettes.

SEM and EDS

Measurements were performed with a Hitachi TM-1000 Tabletop microscope (version 02.11 (Hitachi High-Technologies, Corporation Tokyo Japan) with an EDS analysis system (SwiftED-TM, Oxford Instruments, Link INCA). The instrument is equipped with a silicon drift detector with an energy resolution of 165 eV. Samples were put on carbon discs, stuck on a graphite stub fixed at 7 mm from the beam, with a measurement angle of 22°, and observed using an electron beam accelerated at 15 kV under high vacuum.

Thermal analyses

Thermogravimetric and thermodifferential (TGA/TDA) analyses were performed with a Perkin-Elmer PyrisDiamond analyzer in a platinum crucible between room temperature and 950°C under N_2 atmosphere with a heating rate of 5°C. min^{-1}. The compounds were maintained at 1000°C under air atmosphere for one hour to ensure complete combustion.

Elemental analyses

Elemental analyses (CHNS) were realized with a Thermo Fischer FlashEA 1112 analyser.

Liquid and solid states luminescence measurements

Solid and liquid excitation and emission spectra were measured using a Horiba-Jobin Yvon Fluorolog-III spectrofluorimeter, equipped with a three slit double grating excitation and emission monochromator with dispersions of 2.1 nm/mm (1200 grooves/mm). The steady-state luminescence was excited by unpolarized light from a 450 W Xenon CW lamp and detected at a 90° angle for diluted solution measurements and solid-state measurement by a red-sensitive Hamamatsu R928 photomultiplier tube (sensitivity 190 - 860 nm). Spectra were corrected for both the excitation source light intensity variation (lamp and grating) and the emission spectral response (detector and grating). Appropriate filters were used to remove the residual excitation laser light, Rayleigh scattered light and associated harmonics from spectra. The excitation/emission spectra recordings were realized on samples placed directly into quartz cuvette or mounted directly onto copper plates using conductive silver glue and cooled in an optical cryostat capable of reaching temperature down to 77 K through a continuous nitrogen liquid flow and a nitrogen atmosphere inside the sample chamber (OptistatCF, Oxford Inst.).

Specific heat measurements

Specific heat capacity was measured with a Quantum Design PPMS between 2 and 200 K on microcrystalline powder pressed in pellet, with a layer of Apiezon M grease to ensure sufficient thermal contact between the puck and the sample.

Magnetic studies

Magnetic studies were performed using a Quantum Design MPMS SQUID magnetometer equipped with a reciprocating sample option (RSO) sample holder and a ^{3}He insert for hysteresis measurements below 1.5 K. Ground powder of precursors was pressed into pellets to avoid in-field crystallite orientation, and fresh gels were transferred in gelatine capsules and frozen at 100 K (the freezing point of the *n*-heptane being 182 K) to avoid further degradations. Powder measurements were corrected from diamagnetic contributions as calculated with Pascal's constants and the gel ones by subtracting the diamagnetic contributions of the tube, Teflon, grease and solvent measured in the same conditions.

To follow the dynamics of the considered system, one has to perform dynamics (or AC) susceptibility measurements by applying a small oscillating field H_{AC}. Under such conditions, the susceptibility χ can be decomposed as:

$$\chi = \chi'(\omega) - i.\chi''(\omega) \qquad \text{Eq. A.1}$$

with χ' the in-phase susceptibility and χ'' the out-of-phase susceptibility.

When the frequency of the oscillating field is low compared to the characteristic relaxation time τ of the system, there is no phase lag of the magnetisation. This is the *isothermal* regime, and the susceptibility is then χ_T. In contrast, if the frequency ω is too high, the system will not be able to follow the too fast oscillating field, and the measured *adiabatic* susceptibility is then χ_S. Taking into account these two parameters, the susceptibility χ can be expressed as:

$$\chi = \chi_S + \frac{\chi_T - \chi_S}{1 + i\omega\tau} \qquad \text{Eq. A.2}$$

By combining Eq. A.1 and Eq. A.2, we can express the two components of the susceptibility as:

$$\chi' = \chi_S + \frac{\chi_T - \chi_S}{1 + \omega^2\tau^2} \qquad \text{Eq. A.3}$$

$$\chi'' = \chi_S + \frac{(\chi_T - \chi_S)\omega\tau}{1 + \omega^2\tau^2} \qquad \text{Eq. A.4}$$

However, in real systems, all the spins do not relax exactly at the same time, and this distribution α of the relaxation times τ imposes to rewrite the Eq. A.2 above as:

$$\chi = \chi_S + \frac{\chi_T - \chi_S}{1 + (i\omega\tau)^{1-\alpha}} \qquad \text{Eq. A.5}$$

The expression of the susceptibility components become then:

$$\chi' = \chi_S + (\chi_T - \chi_S)\frac{1 + (\omega\tau)^{1-\alpha}\sin\left(\pi\alpha/2\right)}{1 + 2(\omega\tau)^{1-\alpha}\sin\left(\pi\alpha/2\right) + (\omega\tau)^{2-2\alpha}} \qquad \text{Eq. A.6}$$

$$\chi'' = (\chi_T - \chi_S)\frac{(\omega\tau)^{1-\alpha}\cos\left(\pi\alpha/2\right)}{1 + 2(\omega\tau)^{1-\alpha}\sin\left(\pi\alpha/2\right) + (\omega\tau)^{2-2\alpha}} \qquad \text{Eq. A.7}$$

By using these last two equations, one can extract the relaxation times τ of the system from the in-phase χ' and the out-of-phase χ'' susceptibility signals measured by AC susceptibility measurements, as well as the distribution α from the Argand diagram.

References

[1] G. M. Sheldrick, *Acta Crystallogr. Sect. Found. Adv.* **2015**, *71*, 3–8.
[2] G. M. Sheldrick, *Acta Crystallogr. Sect. C Struct. Chem.* **2015**, *71*, 3–8.
[3] L. J. Farrugia, *J. Appl. Crystallogr.* **2012**, *45*, 849–854.
[4] A. L. Spek, *Acta Crystallogr. Sect. C Struct. Chem.* **2015**, *71*, 9–18.

List of publications

1. Q. Evrard, G. Cucinotta, F. Houard, G. Calvez, Y. Suffren, C. Daiguebonne, O. Guillou, A. Caneschi, M. Mannini, K. Bernot. Self-assembly of a terbium(III) 1D coordination polymer on mica. *Beilstein J. Nanotechnol.* **2019**. 10, 2440–2448.

2. F. Houard, Q. Evrard, G. Calvez, Y. Suffren, C. Daiguebonne, O. Guillou, F. Gendron, B. Le Guennic, T. Guizouarn, V. Dorcet, M. Mannini, K. Bernot. Chiral Supramolecular Nanotubes of Single-Chain Magnets. *Angew. Chem. Int. Ed*. **2020**. 59, 2, 780-784.

3. Q. Evrard, F. Houard, C. Daiguebonne, G. Calvez, Y. Suffren, O. Guillou, M. Mannini, K. Bernot. Sonocrystallisation as an Efficient Way to Control the Size, Morphology, and Purity of Coordination Compound Microcrystallites: Application to a Single-Chain Magnet. *Inorg. Chem*. **2020**. 59. 13, 9215–9226**.**

4. Y. Pointel, F. Houard, Y. Suffren, C. Daiguebonne, F. Le Natur, S. Freslon, G. Calvez, K. Bernot, O. Guillou. High Luminance of Heterolanthanide-Based Molecular Alloys by Phase-Induction Strategy. *Inorg. Chem*. **2020**. 59, 15, 11028–11040.

5. F. Houard, F. Gendron, Y. Suffren, T. Guizouarn, V. Dorcet, G. Calvez, C. Daiguebonne, O. Guillou, B. Le Guennic, M. Mannini, K. Bernot. Single-Chain Magnet Behavior in a Finite Linear Hexanuclear Molecule. *Chem. Sci.* **2021**.12, 31, 10613-10621.

6. F. Houard, K. Bernot, M. Mannini, G. Cucinotta, Metallogels de nanotubes supra-moléculaires pour le dépôt sur surfaces de composés moléculaires, dont des chaines-aimants. *French patent under review*. **2021.**

Résumé étendu

Avec la multiplication des données générées par les activités humaines (numérisation de l'industrie, démocratisation d'Internet, cloud-computing et big data), le problème du stockage de ces données sur des supports physiques se pose. Une des limites des technologies actuelles réside dans la densité de stockage, dictée par la taille des domaines magnétiques utilisés pour encoder les bits. Il suffirait donc de réduire la taille de ces domaines pour augmenter la capacité de stockage de ces disques durs. Cependant, cette approche de nanométrisation ("top-down") se heurte aux limites du superparamagnétisme. En dessous d'un certaine taille critique, la barrière énergétique limitant le passage d'une orientation du moment magnétique à un autre (ou inversion d'aimantation) devient comparable à l'énergie thermique, les particules magnétiques ne peuvent plus conserver leur aimantation et le stockage d'informations devient impossible.

Partant de ce constat, les magnétochimistes ont adopté l'approche inverse : synthétiser des édifices moléculaires, dont les dimensions sont bien moindres que les domaines magnétiques, à partir de ions métalliques magnétiques (éléments 3*d* et/ou 4*f*) coordinés judicieusement par des ligands organiques tout en préservant leurs propriétés magnétiques. Cette approche "bottom-up" est à la base d'un domaine de la chimie de coordination, à savoir le magnétisme moléculaire.

Ainsi, de nombreuses molécules-aimants (ou « Single-Molecule Magnets » en anglais) ont été synthétisées au cours des 30 dernières années, présentant des phénomènes de relaxation lente de leur aimantation à basse température. Cela permet dans certains cas d'observer une hystérèse magnétique, point crucial pour le stockage d'informations. Les progrès dans la compréhension de ces phénomènes ont permis de synthétiser des molécules-aimants plus performantes, dont les températures de blocage de l'aimantation sont proches de la température d'évaporation de l'azote liquide. Par ailleurs, de nombreux phénomènes d'origine quantique ont également été mis en évidence, ouvrant la voie à des applications potentielles en spintronique.

Parallèlement aux molécules-aimants, des polymères de coordination magnétiques unidimensionnels, appelés chaînes-aimants (ou "Single-Chain Magnets" en anglais), ont également été synthétisées. Ces chaînes magnétiques sont caractérisées par l'alternance de centres magnétiques fortement anisotropes reliés entre eux par des ligands organiques. Un phénomène de corrélation s'établit entre les porteurs de spin à basse température, conduisant à une aimantation spontanée. L'avantage de telles chaînes est qu'en plus de permettre une aimantation rémanente, elles sont moins soumises aux phénomènes de relaxation « parasites » présents dans les molécules aimant (notamment par l'effet tunnel).

L'un des points restreignant de potentielles applications industrielles reste néanmoins le dépôt de ces molécules sur un support physique. En effet, si les propriétés de ces molécules

ont d'abord été mesurées sur des cristaux et des poudres, qu'en est-il des propriétés d'une molécule-aimant isolée sur une surface ? Existe-t-il de nouveaux phénomènes dus aux interactions avec la surface ? Plusieurs méthodes ont déjà été mises en œuvre avec succès pour les molécules-aimants, comme le dépôt par sublimation ou par greffage chimique, avec leurs avantages et leurs limites. Cependant, aucune tentative n'a encore aboutie pour ce qui est des chaînes-aimants, ce qui fut l'objectif de cette thèse ; la synthèse d'une nouvelle famille de chaînes-aimants et leur dépôt sur surfaces.

Sur la base de travaux antérieurs dans notre laboratoire, nous avons choisi d'étudier des systèmes composés d'ions lanthanides 4*f*, caractéristés par une forte anisotropie magnétique, liés par des ligands nitronyl-nitroxides (NIT), radicaux stables jouant le rôle de relais de l'information magnétique et surtout aisément fonctionnalisables.

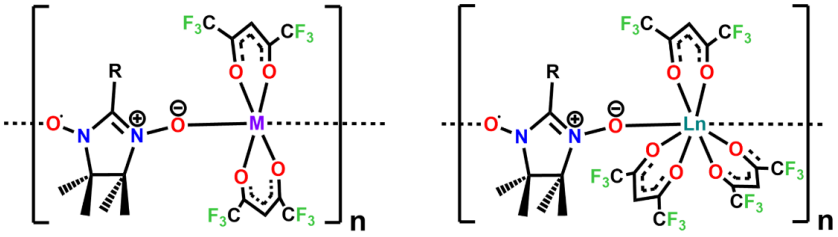

Figure 1. Représentations schématiques des modes de coordinations généralement observés pour des chaînes-aimants de type 3*d*- (gauche) ou 4*f*-NIT (droite).

Nous avons d'abord étudié une méthode de dépôt avec une chaîne-aimant déjà connue, le **[Tb(hfac)$_3$(NITPhOPh)]$_n$**. L'objectif était de dissocier et disperser dans un solvant par sonication les chaines isolées constituant le cristal, et de les déposer par drop-casting.. Cependant, les objets résultants observés par microscopie ne correspondaient pas aux chaînes isolées attendues mais à de grands cristallites. Néanmoins, en essayant de reproduire un phénomène de coordination *in-situ* en étudiant séparément le dépôt des constituants **NITPhOPh** et **[Tb(hfac)$_3$·2H$_2$O]** de cette chaine, nous avons obtenu un arrangement polymérique de ce dernier sur mica. Ce dépôt a été caractérisé et présente des propriétés magnétiques et luminescentes comparables à celles de la phase cristalline.

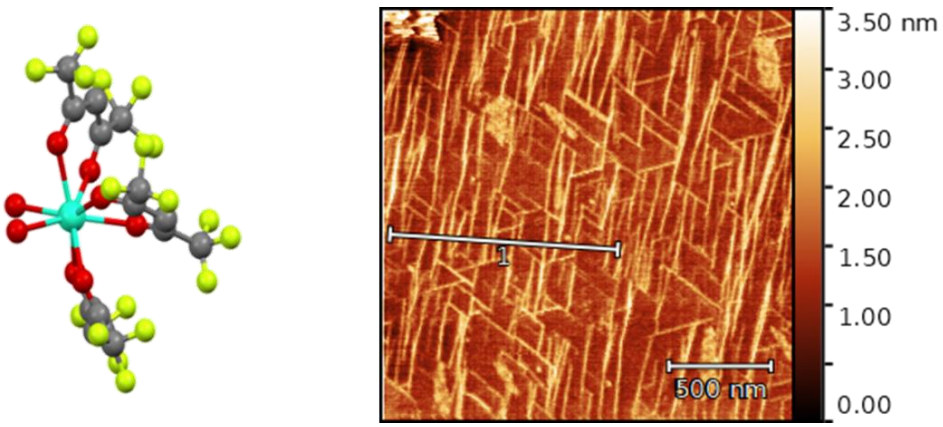

Figure 2. Représentation de la structure moléculaire du **[Tb(hfac)$_3$·2H$_2$O]** (gauche) et image obtenue par AFM d'une surface de mica couverte de chaînes de **[Tb(hfac)$_3$·2H$_2$O]** (droite).

Partant de l'hypothèse que l'empilement moléculaire de **[Tb(hfac)$_3$(NITPhOPh)]$_n$** était trop rigide, nous avons alors synthétisé un nouveau radical **NITPhOC$_6$** pontant. En substituant le groupe phényl par une chaîne aliphatique, nous apportons plus de flexibilité et d'espacement au polymère de coordination pour dissocier plus facilement les chaînes qui constituent le cristal. Grâce à ce degré de liberté supplémentaire, le polymère de coordination **[Tb(hfac)$_3$(NITPhOC$_6$)]$_n$** qui en résulte croît en hélice. Ces dernières s'organisant en nanotubes cylindriques par interactions supramoléculaire faibles, grâce aux interactions faibles avec le solvant aliphatique. Les propriétés magnétiques de cette chaîne ont été déterminées par des mesures de susceptibilité statique et alternative. Bien que ces chaînes soient organisées spatialement entre-elles, elles sont néanmoins suffisamment espacées pour être isolées d'un point de vue magnétique. Elles présentent ainsi un comportement chaînes-aimants avec une courbe d'hystérése magnétique ouverte à basse température.

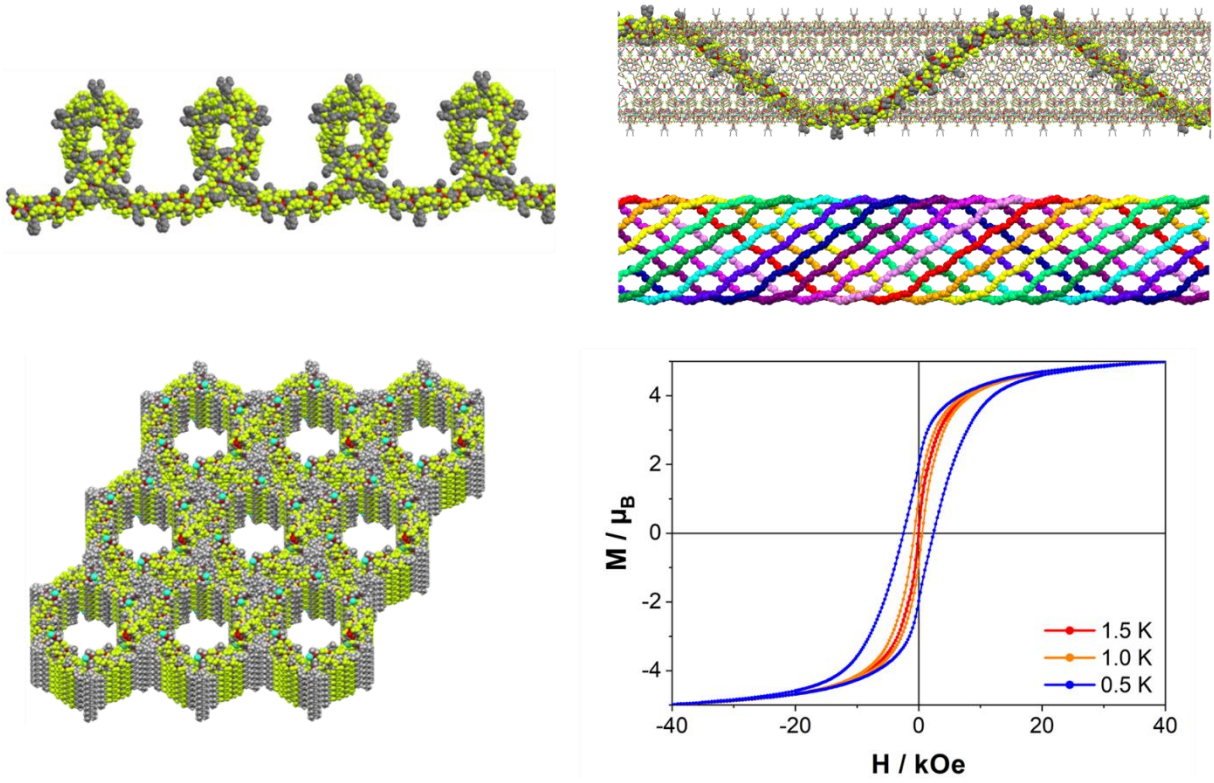

Figure 3. Haut : Représentations d'une chaîne en hélice isolée de **[Tb(hfac)$_3$(NITPhOC$_6$)]$_n$** (gauche) et de l'arrangement de ces dernières en tube (droite). Bas : Représentations de l'empilement cristallin de nanotubes de **[Tb(hfac)$_3$(NITPhOC$_6$)]$_n$** (gauche) et courbes d'hystérèses magnétiques correspondantes mesurées à différentes températures (droite).

Curieusement, des cristaux de morphologie différente ont également été observés lors de la cristallisation du **[Tb(hfac)$_3$(NITPhOC$_6$)]$_n$**. Ce que nous pensions être un polymorphe s'est avéré être un complexe hexanucléaire linéaire, **[(Tb(hfac)$_3$)$_6$(NITPhOC$_6$)$_5$(H$_2$O)$_2$]**. La présence de molécules d'eau nous a permis d'isoler les paramètres expérimentaux pour obtenir sélectivement soit **[Tb(hfac)$_3$(NITPhOC$_6$)]$_n$**, soit **[(Tb(hfac)$_3$)$_6$(NITPhOC$_6$)$_5$(H$_2$O)$_2$]**. Cependant, bien que ces deux systèmes soient chimiquement proches, leurs propriétés magnétiques peuvent grandement différer : le premier correspond à une chaîne infinie, structurellement

favorable à l'observation d'un phénomène de corrélation magnétique et *de facto* au comportement de chaîne-aimant, tandis que le second est un complexe fini, bien que lié à ses voisins par des liaisons H. Les mesures magnétiques ont toutefois révélé un comportement de chaînes-aimants comparable au polymère hélicoïdale, car la longueur de corrélation est confinée à l'intérieur de la molécule.

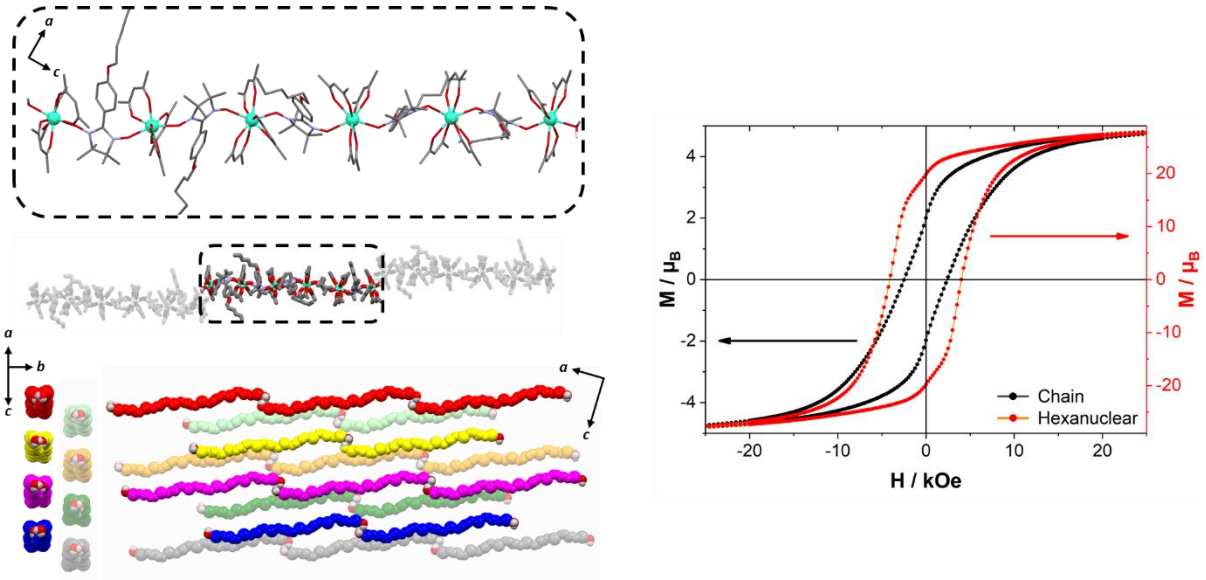

Figure 4. Gauche : Représentations de l'unité asymétrique de **[(Tb(hfac)$_3$)$_6$(NITPhOC$_6$)$_5$(H$_2$O)$_2$]** (haut), et de l'empilement cristallin avec les molécules voisines qui en résulte (milieu et bas). Droite : comparaison entre les courbes d'hystérèses magnétiques de la chaîne **[Tb(hfac)$_3$(NITPhOC$_6$)]$_n$** (en noir) et du complexe **[(Tb(hfac)$_3$)$_6$(NITPhOC$_6$)$_5$(H$_2$O)$_2$]** (en rouge) mesurées à 0.5 K.

Finalement, nous avons étudié l'influence de la taille de la chaîne aliphatique portée par le radical NIT, pour obtenir de possibles organisations supramoléculaires. En faisant réagir du Tb(hfac)3 avec les radicaux **NITPhOC$_n$** (n = 6, 10, 18), nous avons établi un protocole pour obtenir les métallogels **TbC$_n$** correspondants.

Figure 5. Photographies de solutions (sur la partie gauche des images) et de gels (droites) de **TbC$_n$**.

Ces derniers, étudiés par SAXS, ont révélé une organisation tubulaire similaire à celle observée pour les chaînes hélicoïdales cristallines. Grâce aux informations fournies par cette technique, nous avons pu établir un modèle 3D de ces nanotubes. L'analogie entre le cristal et les gels a également été confirmée par des caractéristiques magnétiques compatibles avec un comportement SCM, ainsi qu'une une courbe d'hystérèse magnétique ouverte.

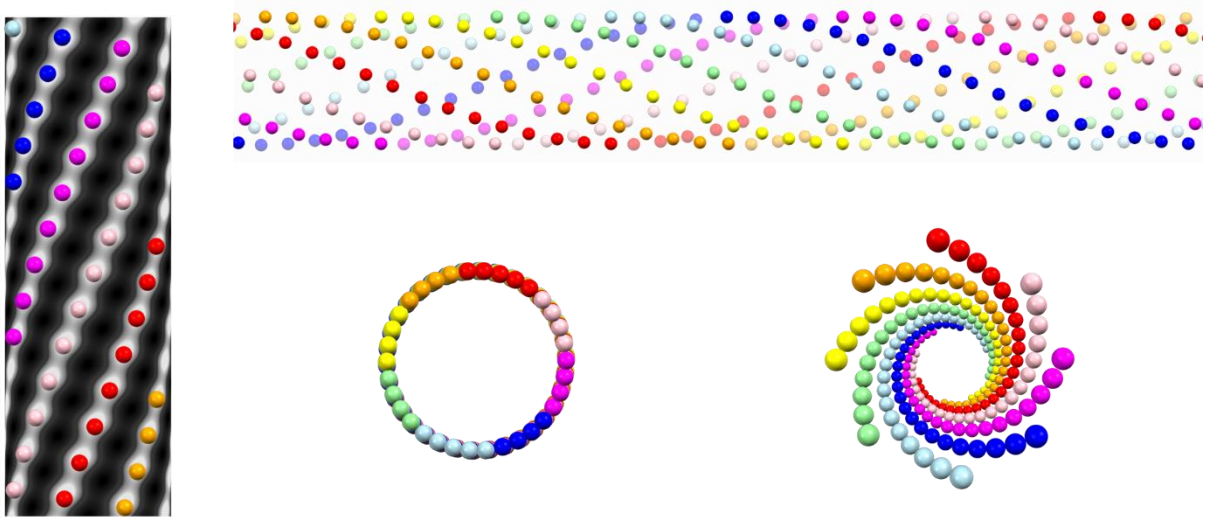

Figure 6. Représentations du modèle structural développé pour le gel de **TbC_{18}** à partir des mesures de SAXS.

Profitant des avantages que présentent ces gels (mise en forme aisée, transition sol-gel réversible), nous avons pu déposer et observer des fibres par spin-coating, dont les tailles caractéristiques estimées par AFM correspondent à celles déterminées par SAXS pour des nanotubes isolés.

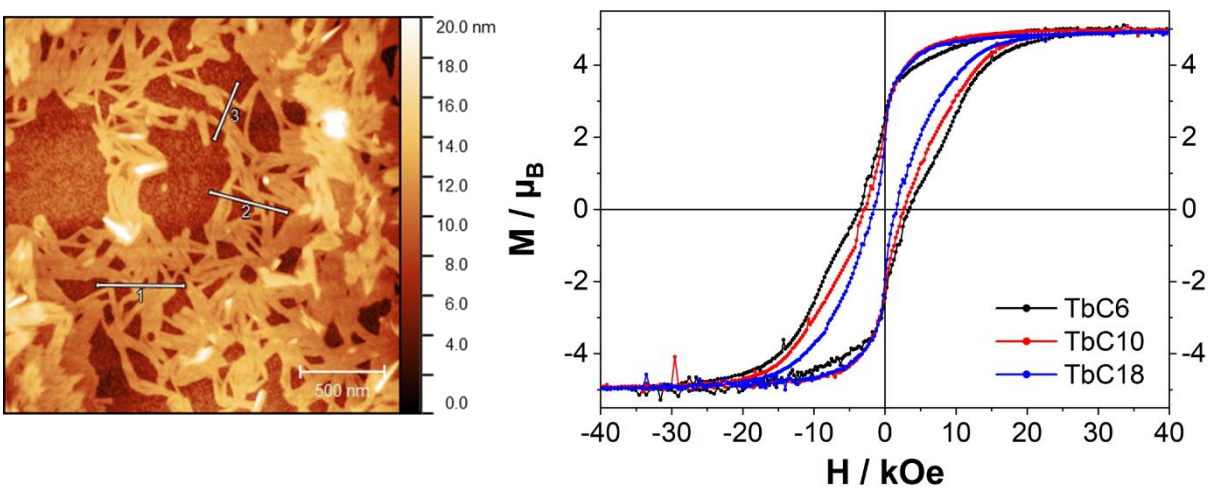

Figure 7. Image obtenue par AFM d'une surface de silicium couverte de fibres de **TbC_{18}** (gauche) et courbes d'hystérèses magnétiques des métallogels **TbCn** mesurées à 0.5 K.

En résumé, nous avons démontré que la fonctionnalisation du radical NIT avec des chaines alkyls de tailles différentes pouvait induire des changements structuraux importants et ouvrir la voie à une nouvelle classe de matériaux magnétiques supramoléculaires, des nanotubes supramoléculaires de chaînes-aimants. Tirant parti de ces résultats, nous avons adopté une approche "cristal-gel" pour contourner les limitations imposées par l'état cristallin des polymères de coordination quant à leur dépôt en surface. Ceci nous a permis d'obtenir des "gel-aimants" à partir de polymères de coordination, absents de la littérature scientifique jusqu'à présent, et de développer un protocole de dépôt sur surface, qui fait l'objet d'une demande de brevet en cours.

INSA de RENNES
Service des Formations

AVIS DU JURY SUR LA REPRODUCTION DE LA THESE SOUTENUE

Titre de la thèse:
Experimental approaches toward the deposition of SCMs on surface

Nom Prénom de l'auteur : HOUARD FELIX

Membres du jury :
- Monsieur BERNOT Kévin
- Monsieur ANDRUH Marius
- Monsieur AROMI Guillem
- Madame GUILLOUX-VIRY Maryline
- Madame MARVAUD Valérie
- Madame PICHON Céline
- Monsieur MANNINI Matteo

Président du jury : Maryline GUILLOUX-VIRY

Date de la soutenance : 06 Décembre 2021

Reproduction de la these soutenue

☒ Thèse pouvant être reproduite en l'état
☐ Thèse pouvant être reproduite après corrections suggérées

Fait à Rennes, le 06 Décembre 2021

Signature du président de jury

Le Directeur,

Pr. M'Hamed DRISSI

DOCTORAT MATIERE BRETAGNE MOLECULES LOIRE ET MATERIAUX

INSA RENNES

Titre : **Approches expérimentales pour le dépôt de chaînes-aimants sur surface**

Mots clés : Chimie de Coordination, Magnétisme Moléculaire, Lanthanides, Chaines-Aimants, Nanotubes Moléculaires

Résumé : Parmi les défis technologiques induits par la consommation exponentielle de données numériques, se trouve celle de leur stockage et de la part croissante de besoins énergétiques que cela représente. En ce sens, un besoin de miniaturisation des dispositifs de stockage magnétique s'impose. Pour faire face à ces enjeux, la communauté du magnétisme moléculaire a synthétisé de nombreuses des molécules magnétiques par chimie de coordination. Parmi cette grande famille de molécules se trouve les chaînes-aimants, des polymères de coordination unidimensionnels pouvant présenter une hystérèse magnétique et donc un effet mémoire.

Dans cette thèse, nous nous intéressons au dépôt sur surface de ces chaines-aimants, étape nécessaire à la réalisation de dispositifs de stockage physiques. Nous avons ciblé une famille particulière de chaînes-aimants, constituée d'ions lanthanides présentant une forte anisotropie magnétique et de radicaux organiques nitronyl-nitroxides. En fonctionnalisant ces derniers avec des fonctions alkyles, une nouvelle famille de nanotubes de chaînes-aimants supramoléculaires a été synthétisée, dont les propriétés structurales et magnétiques sont comparées. Tirant parti de ces résultats, une approche "cristal-gel" a permis d'obtenir des gels de chaînes-aimants, et de les déposer sur surfaces.

Title: **Experimental approaches toward the deposition of SCMs on surface**

Keywords: Coordination Chemistry, Molecular Magnetism, Lanthanides, Single-Chain Magnets, Molecular Nanotubes

Abstract: Among the technological challenges caused by the exponential consumption of digital data is that of its storage and the growing share of energy requirements that this represents. In this sense, there is a need for miniaturisation of magnetic storage devices. To face these challenges, the molecular magnetism community has synthesised numerous magnetic molecules by coordination chemistry. Among this large family of molecules are Single-Chain Magnets (SCMs), one-dimensional coordination polymers that can exhibit magnetic hysteresis and thus a memory effect.

In this thesis, we are investigating the surface deposition of these magnetic chains, a necessary step for the realisation of storage devices. We have targeted a particular family of SCMs, consisting of 4f lanthanide ions with high magnetic anisotropy and organic nitronyl nitroxide radicals. By functionalizing the latter with alkyl functions, a new family of supra-molecular nanotubes of SCMs have been synthesized, whose structural and magnetic properties are compared. Taking advantage of these results, a "crystal-gel" approach has made it possible to obtain gels of SCMs and to deposit them on surfaces.